Cold Repair of Orthotropic Steel Decks using Carbon Fiber-Reinforced Polymer

An experimental and numerical study into the bond behaviour of adhesive carbon fiber-reinforced polymer-steel joints for the Cold Repair method

MSc Thesis

J.S. Mulders

December 2024, Delft

TU Delft

ARUP

Cold Repair of Orthotropic Steel Decks using Carbon Fiber-Reinforced Polymer

An experimental and numercal study into the bond behaviour of adhesive carbon fiber-reinforced polymer-steel joints for the Cold Repair method

By

J.S. Mulders

in partial fulfilment of the requirements for the degree of

Master of Science

in Civil Engineering

at the Delft University of Technology, Faculty of Civil Engineering and Geosciences.

Student number: 4718232

Thesis committee:	Dr. M. Pavlović	TU Delft
	Dr. O. Karpenko	TU Delft
	Dr.ir. F.P. van der Meer	TU Delft
	ir. M. Rikken	Arup
	ir. F. Csillag	Arup

Abstract

Orthotropic steel decks (OSDs) offer structural advantages but are highly sensitive to fatigue cracking, mainly initiated from trough-to-deck plate welds at the intersection between the trough and crossbeam. To mitigate existing fatigue cracks, a high strength concrete (HSC) overlay repair method was developed, which addresses two types of fatigue cracks but does not completely prevent root-weld crack propagation. To avoid damaging the HSC overlay by applying heating in traditional repair methods, the 'Cold Repair' method was developed, using a steel angle adhered to the trough-to-deck plate exterior. Recent studies suggest increased effectiveness with a carbon fiber-reinforced polymer (CFRP) angle, created by vacuum infusing carbon fiber fabrics with epoxy reason onto the OSD. However, limited knowledge exists on the use of fiber-reinforced polymer (FRP) to strengthen OSDs and control root crack growth in these weld details. This presents challenges in understanding its behaviour, material properties and design.

This study investigates CFRP-steel adhesive joints through experimental and numerical analyses. Thick-adherend shear tests (TASTs) were conducted to study the adhesive bond's shear strength, and the failure mechanisms of these adhesive joints subjected to shear loading. Component-level three-point bending tests evaluated bond behaviour under bending loads and the structural performance of OSD strip components strengthened with a CFRP angle. Finite element (FE) models were developed to simulate the adhesive FRP-steel joint, employing both linear tied and non-linear tie-break interface conditions. Experimental and numerical results were compared to assess the FE models' accuracy.

A comparative analysis was also performed between a full-bridge model, provided by supervising company Arup, and the component-level model developed in this thesis. Significant differences in boundary conditions, loading conditions, element formulation, and the scaling of global dimensions (apart from thicknesses) complicated precise comparisons. The component-level model used tie-break interface conditions to model adhesive interface failure, whereas the full-bridge model employed tied interface conditions, which limited its ability to predict failure.

TASTs results identified debonding between steel and primer -applied to enhance the adherend-adhesive bond- as the primary failure mode. In four samples, this debonding occurred alongside delamination of the first glass-fiber layer. The design value of the average shear bond strength was determined to be 5.42 kN. Component-level three-point bending tests consistently showed crack initiation at the outer edge of the horizontal adhesive bond at a load level of around 82 kN. Crack initiation was followed by linear behaviour up to the onset of yielding of the deck plate, after which full debonding of the horizontal leg of the Cold Repair occurred at an average load of 110 kN.

Numerical studies revealed that linear numerical modelling provides a sufficient approach to model the Cold Repair method up to the point of failure. Developed non-linear numerical models do not contribute to additional reliability of the Cold Repair method, as they were unable to accurately match observed failure behaviour and because adhesive bond failure occurs suddenly. Nonetheless, the additional capacity observed in component strips suggests that non-linear numerical modelling could extend the capacity of the Cold Repair method if its design allows for damage. To improve the accuracy of adhesive bond failure modelling, further experiments, including fracture mechanics tests, are recommended to determine essential adhesive properties, such as fracture toughness.

Preface

This thesis concludes my Master of Civil Engineering at the Technical University of Delft. Over the course of November 2023 to December 2024, I have worked on researching and writing the thesis *Cold Repair of Orthotropic Steel Decks using Carbon Fiber-Reinforced Polymer*. As this thesis has come to an end, I would like to express my sincere gratitude to those, who have contributed to this realisation.

In the first place, I would like to thank my university supervisors, Dr. Marko Pavlović, Dr. Olena Karpenko and Dr.ir. Frans van der Meer, for guiding and helping me over the course of this master's thesis. Your critical view helped me to improve my work and made me feel inspired and determined after every meeting.

As I have had the wonderful opportunity to perform this thesis in collaboration with Arup, my utmost gratitude goes to my company supervisors, Maarten Rikken and Fruzsina Csillag. Your both practical and theoretical knowledge helped me greatly and your enthusiasm and confidence in this project kept me going. Thank you so much for providing this opportunity and your time and energy.

I would also like to thank Arup, where I have felt very welcome and supported from the first day. A special thanks goes to Rupert Gibson, who has spent hours in guiding me through LS-DYNA. It was a pleasure being part of such an amazing team.

Special thanks are due to Fred Schilperoort and Giorgos Stamoulis for their assistance with the lab experiments. Moreover, I would like to express my sincere gratitude to the wonderful team of Takke Breukelen and Delft Infra Composites. Without your contribution, this thesis would not have been possible. A special thanks goes to Paul Honing for showing me the wonderful world of composites and for providing the samples for testing.

Above all, I would like to thank my family, friends, housemates and boyfriend, Stijn, for their unconditional love, patience, support and encouragement. Without you, it would not have been possible. Thank you.

Jill Mulders

Delft, December 2024

Table of Contents

Abstract **iv**

Preface **v**

Table of Contents **vi**

List of Symbols **viii**

List of Abbreviations **ix**

List of Figures **x**

List of Tables **xiv**

1. Introduction **1**

1.1 Background 1

1.2 Objectives 3

1.3 Methodology 5

1.4 Outline of Thesis 7

2. Literature Study **8**

2.1 Orthotropic Steel Decks 8

2.2 Fiber-reinforced Polymer 13

2.3 Cold Repair Method 17

2.4 Finite Element Modelling of Adhesive Joints 21

2.5 Summary 22

3. Thick-adherend Shear Tests and Numerical Model **23**

3.1 Introduction 23

3.2 Thick-adherend Shear Tests 23

3.3 Finite Element Modelling of Adhesive Joints in LS-DYNA 37

3.4 Finite Element Model of Thick-adherend Shear Tests 41

3.5 Discussion of TAST Numerical Models 47

3.6 Results 53

3.7 Discussion 61

3.8 Summary 63

4. Component Experiments and Numerical Model **64**

4.1 Introduction 64

4.2 Component Experiments 64

4.3 Finite Element Model of Component Experiments 76
4.4 Discussion of Component-level Numerical Models 79
4.5 Results 83
4.6 Comparison between Component-level and Full-bridge Numerical Model 89
4.7 Discussion 96
4.8 Summary 96
5. Conclusions and Recommendations for Future Research 97
5.1 Conclusions 97
5.2 Recommendations for Future Research 98
Bibliography 99
A Experimental Results of TASTs 103
B Numerical Results of TAST FE Models 118
C Determination of Design Values Bond Strength for Thick-adherend Shear Tests 124
D Experimental Results of Component-level Experiments 125
E Numerical Results of Component-level FE Models 131
F Determination of Design Values Bond Strength for Component-level Tests 139

List of Symbols

Roman upper case letters:

A	crack area represented by the element
CN	stiffness of adhesive interface
CT2CN	tangential / normal stiffness ration
ERATEN	normal energy rate
ERATES	shear energy rate
F	ultimate load
F_I	ultimate load for mode I behaviour
FS	static friction coefficient
FD	dynamic friction coefficient
G_{IC}	energy release rate for mode I
G_{ii}	shear modulus of the considered direction
NFLS	normal bond failure stress in interface
PARAM	additional parameter, dependent on the tie-break option
SFLS	shear bond failure stress in interface
E_i	elastic modulus in the considered i direction

Roman lower case letters:

t	thickness
u_i	displacement in the considered i direction
$u_{I,ini}$	displacement at the end of the uncrack stage
$u_{I,ult}$	displacement at the end of the crack development state
f_{bond}	average bond strength

Greek letters:

σ_{design}	design value of bond stress
σ_n	peel stress of the interface
σ_s	shear stress of the interface
σ_{ij}	components of the stress tensor
φ_i	rotation over considered i axis
ν	poisons ratio
τ_{ij}	components of the shear stress tensor

List of Abbreviations

2D	Two-dimensional
3D	Three-dimensional
ASTM	American Society for Testing Materials
B-K exponent	Benzeggagh-Kenane exponent
CFRP	Carbon Fiber-reinforced Polymer
CR	Cold Repair
CZM	Cohesive Zone Modelling
DOF	Degrees of Freedom
DCB	Double Cantilever Beam
DLS	Double-lap shear
ENF	End Notched Flexure
FEM	Finite Element Method
FRP	Fiber-reinforced Polymer
GFRP	Glass Fiber-reinforced Polymer
HSC	High Strength Concrete
OSD	Orthotropic Steel Deck
QI	Quasi-isotropic
SLS	Single-lap shear
TAST	Thick-adherend Shear Test
UD	Uni-directional

List of Figures

Figure 1.1: Fatigue crack propagation in trough-to-deck welds [59, 61] 1
Figure 1.2: Cold Repair method [9] 2
Figure 1.3: Implementation of Cold Repair method using steel on Galecopper bridge [8] 2
Figure 1.4: Flow-chart of the thesis 6
Figure 2.1: Orthotropic Steel Deck [10] 8
Figure 2.2: Types of Longitudinal Stiffeners for Orthotropic Steel Decks [16] 9
Figure 2.3: Van Brienenoord bridges, Rotterdam [20] 10
Figure 2.4: Moerdijk Railway bridge, Moerdijk [62] 10
Figure 2.5: Galecopper bridge, Utrecht [63] 10
Figure 2.6: Lek bridge, Hagestein [65] 11
Figure 2.7: Moerdijk bridge, Moerdijk [66] 11
Figure 2.8: Common fatigue cracks at rib-to-deck welded connection details of OSDs [67] 12
Figure 2.9: Typical stress-strain curves for different types of fibers [27] 14
Figure 2.10: Example of laminate lay-up [31] 15
Figure 2.11: Adhesive joint loading modes [68] 18
Figure 2.12: Failure modes in a bonded joint [13] 18
Figure 2.13: FRP laminate failure modes [37] 19
Figure 2.14: Strengthening of OSD with FRP angles: (a) FRP angles; (b) strengthened specimen [6] 20
Figure 2.15: Transverse position of GFRP angle (in meters) [5] 20
Figure 2.16: CZM: (a) Local approach (b) Continuum approach [41] 22
Figure 3.1: SLS and DLS test [69] 23
Figure 3.2: Thick-adherend lap shear test specimen [45] 24
Figure 3.3: Thick-adherend shear test specimen with 30 mm overlap length; dimensions in [mm] 25
Figure 3.4: Thick-adherend shear test specimen with 60 mm overlap length; dimensions in [mm] 25
Figure 3.5: Thick-adherend shear test specimen with 90 mm overlap length; dimensions in [mm] 26
Figure 3.6: Notch zone sample TAST 30-3: (a) left side and (b) right side 26
Figure 3.7: FRP-steel plate (a) after vacuum infusion and (b) during post-infusion 27
Figure 3.8: Dry patch on TAST samples (a) 30-1, (b) 60-3 and (c) 90-3 27
Figure 3.9: TASTs: testing set-up 28
Figure 3.10: TASTs: surface that is measured by 2D DIC 28
Figure 3.11: Primer-steel failure (TAST 30-2) 29
Figure 3.12: Micrographs of primer-steel failure 30
Figure 3.13: Primer-steel failure combined with delamination of GFRP layer (TAST 60-1) 30
Figure 3.14: Micrographs of primer-steel failure combined with delamination of GFRP 30
Figure 3.15: Delamination of CFRP (TAST 90-3) 31
Figure 3.16: Micrographs of delamination of CFRP 31

Figure 3.17: Failure behaviour of TAST 30-4 31
Figure 3.18: DIC digital extensometers 32
Figure 3.19: Time-displacement curves for different relative distances of TAST 30-2 33
Figure 3.20: Relative load-displacement curves of TAST with overlap length 30 mm 33
Figure 3.21: Relative load-displacement curves of TAST with overlap length 60 mm 34
Figure 3.22: Relative load-displacement curves of TAST with overlap length 90 mm 34
Figure 3.23: Crack initiation in TAST samples 35
Figure 3.24: Mean relative load-displacement curves of TAST 36
Figure 3.25: Relative load-displacement curves of TASTs with and without visible dry patches 37
Figure 3.26: Principle of contact treatment in LS-DYNA [40] 37
Figure 3.27: Softening behaviour for mode I crack opening in Dycoss Discrete Crack model [47] 38
Figure 3.28: 3D representation of softening model in Dycoss Discrete Crack model [47] 38
Figure 3.29: Geometry of preliminary adhesive interface sensitivity study 39
Figure 3.30: Load-displacement curve of model versions 11.1 and 14.2 40
Figure 3.31: Geometry and boundary conditions of 3D FE models of TASTs 42
Figure 3.32: Geometry and boundary conditions of 2D FE model of TAST with overlap length of 30 mm 44
Figure 3.33: Load-displacement curves of 2D mesh sensitivity study 45
Figure 3.34: Load - relative displacement curves of mesh sensitivity study of 3D FE models of TAST with 30 mm overlap length 45
Figure 3.35: Load - relative displacement curves for 2D and 3D FE models of TAST - 0.5 mm mesh 46
Figure 3.36: Prescribed displacement of FE models 47
Figure 3.37: Relative distance of TAST FE model with overlap of 30 mm 48
Figure 3.38: Load-displacement curves of FEM and experimental results for TAST 30-2 48
Figure 3.39: Load-displacement curves of FEM and experimental results for TAST 60-3 49
Figure 3.40: Load-displacement curves of FEM and experimental results for TAST 90-5 49
Figure 3.41: Influence of reduction FRP stiffness for TAST 30-2 50
Figure 3.42: Influence of reduction FRP stiffness for TAST 60-3 51
Figure 3.43: Influence of reduction FRP stiffness for TAST 90-5 51
Figure 3.44: FE models with and without penetrated notches 52
Figure 3.45: Load-displacement curves of FE models with and without penetrated notches 52
Figure 3.46: Strain in global Z-direction TAST 30-2 at F = 13.6 kN 53
Figure 3.47: Strain in global Y-direction TAST 30-2 at F = 13.6 kN 54
Figure 3.48: Strain in principal direction TAST 30-2 at F = 13.6 kN 54
Figure 3.49: Strain in global Z-direction TAST 60-2 at F = 20.0 kN 55
Figure 3.50: Strain in global Y-direction TAST 60-2 at F = 20.0 kN 55
Figure 3.51: Strain in principal direction TAST 60-2 at F = 20.0 kN 56
Figure 3.52: Strain in global Z-direction TAST 90-5 at F = 20.5 kN 56
Figure 3.53: Strain in global Y-direction TAST 90-5 at F = 20.5 kN 57

Figure 3.54: Strain in principal direction TAST 90-5 at F = 20.5 kN 57
Figure 3.55: Deformed shapes of TAST FE models (magnified 50x) 60
Figure 4.1: Component-level three-point bending test: specimen geometry 64
Figure 4.2: Component-level three-point bending test: test set-up 65
Figure 4.3: Laminate lay-up component samples 65
Figure 4.4: Observed failure for specimen COMP-3 67
Figure 4.5 Global load-displacement curves of component-level three-point bending tests 69
Figure 4.6: Mean load-displacement curve of component tests 69
Figure 4.7: Load-displacement curve of COMP-3.1 70
Figure 4.8: Load-strain curves for strain gauge 1 71
Figure 4.9: Load-strain curves for strain gauge 2 71
Figure 4.10: Inset of load-strain curves for strain gauge 2 72
Figure 4.11: Digital extensometers DIC component-level tests 73
Figure 4.12: Load-strain curves of vertical leg of Cold Repair 74
Figure 4.13: Crack opening close to edge horizontal leg Cold Repair 74
Figure 4.14: Crack opening in the middle of horizontal leg of Cold Repair 75
Figure 4.15: Major strain plots of COMP-7 76
Figure 4.16: Geometry and boundary conditions of 3D FE model of component-level three-point bending test 77
Figure 4.17: Applied load of component-level FE model 78
Figure 4.18: Load-displacement curves of FEM and experimental results for COMP-7 79
Figure 4.19: Inset of load-displacement curves of FEM component tests 80
Figure 4.20: Contact force curves of adhesive interface deck plate – horizontal leg of component FE models 81
Figure 4.21: 3D FE model of OSD component with and without Cold Repair and attached trough-deck connection 81
Figure 4.22: Load-displacement curves of FE models with and without Cold Repair and component tests 82
Figure 4.23: Load-displacement curves of FE models with and without tied trough-deck joint 83
Figure 4.24: Strain in principal direction for DIC COMP 7 and FEM tie-break variation A at F = 60 kN 84
Figure 4.25: Strain in principal direction for DIC COMP 7 and FEM tie-break variation A at F = 104 kN 84
Figure 4.26: Strain in principal direction for DIC COMP 7 and FEM tie-break variation A at F = 119 kN 85
Figure 4.27: Position of horizontal and vertical adhesive interface of component-level FE model 86
Figure 4.28: Failure of the adhesive interface between Cold Repair and OSD in FEM 86
Figure 4.29: Debonding of adhesive interface between deck plate and horizontal leg of Cold Repair 87
Figure 4.30: Local y-directional stress in trough leg with and without Cold Repair 87
Figure 4.31: Axial and bending stress distribution in trough leg along the length of the trough 88
Figure 4.32: Deformed shape of FE model with and without CR (magnified 30x) 88

Figure 4.33: Geometry and boundary conditions FE model Second Van Brienenoord bridge (Arup) 90
Figure 4.34: Elements in FE model Second Van Brienenoord bridge without Cold Repair (Arup) 90
Figure 4.35: Geometry Cold Repair in full-bridge model (Arup) 91
Figure 4.36: Comparison of loading condition on unstrengthened OSD component 92
Figure 4.37: Tandem load cases applied in full-bridge model (Arup) 93
Figure 4.38: Peel bond stress contour plot under characteristic TS cases of bridge model (Arup) 93
Figure 4.39: Shear bond stress contour plot under characteristic TS cases of bridge model (Arup) 94
Figure 4.40: Peel bond stress contour plot at F = 60 kN of strip model in MPa 94
Figure 5.1: FE models of composite laminate plate (c) solid layers (SL) – cohesive zone layer (CZ) - SL and (d) SL - CZ - SL - CZ - SL - CZ – SL (black solid lines are cohesive layers) 98

List of Tables

Table 1.1: Characteristics of component-level models Arup and thesis 5
Table 3.1: Failure mechanisms of TASTs 28
Table 3.2: Failure load for TAST specimens 32
Table 3.3: Mean failure load and stiffness for TAST series 36
Table 3.4: Difference in global stiffness for TAST samples with and without visible dry patches 37
Table 3.5: Tie-break contact properties of option 6 for model version 14.2 40
Table 3.6: Tie-break contact properties of option 9 for model version 11.1 41
Table 3.7: Overview of FE types in TAST model 43
Table 3.8: Linear-elastic material properties of steel 43
Table 3.9: Material properties of UD and ±45 CFRP plies 43
Table 3.10: Material properties of CFRP laminate 44
Table 3.11: Local behaviour comparison for 2D and 3D FE models of TAST - 0.5 mm mesh 46
Table 3.12: Deviation between TAST FE models and experimental data 50
Table 3.13: Average stress of TAST specimens based on failure load 59
Table 3.14: Average and peak bond stress from TAST FE models 59
Table 3.15: Average shear stress of TAST samples at failure 60
Table 3.16: Design values bond strength based on TASTs 61
Table 3.17: Shear comparative evaluation between performed TASTs and comparative studies 62
Table 4.1: Description of plies in laminate lay-up component samples 66
Table 4.2: Micrographs of failure for component three-point bending tests 68
Table 4.3: Load at debonding of component-level three-point bending tests 70
Table 4.4: Yield strains for steel deck plate in component-level tests 73
Table 4.5: Load levels at which crack initiation of component-level tests is observed 75
Table 4.6: Overview of FE types in component-level FE model 77
Table 4.7: Properties of tie-break contact definition of component FE models 78
Table 4.8: Deviation between component FE models and experimental data 80
Table 4.9: Bond stress at outer edge of horizontal leg of CR for component specimens 89
Table 4.10: Values peak bond strength based on comp
onent-level tests at ratio peel / shear of 1 / 2.4 and mesh size of 6 mm 89
Table 4.11: Elements with corresponding element type in FE model Van Brienenoord bridge without Cold Repair 91
Table 4.12: Values for assumed bond strength and design values of bond stress (Arup) 95
Table 4.13: Design values of average bond strength from TASTs 95

1. Introduction

This chapter presents an overview of the background and outline of this thesis. It introduces the topic by providing a background on the Cold Repair Method. This is followed by the objectives of this thesis. The chapter concludes with the followed methodology and outline of the thesis.

1.1 Background

This section provides relevant background information regarding the Cold Repair method. It presents a brief description of orthotropic steel decks, highlighting their challenges. Furthermore, it introduces the concept of the Cold Repair method.

1.1.1 Orthotropic Steel Decks

Orthotropic steel decks (OSDs) are widely used in long-span bridge engineering due to their reduction in dead weight compared to concrete bridge decks. This aspect results in relatively small loads on the substructure, which is highly suitable for large-span and movable bridges. However, despite their benefits, OSDs display a vulnerability to fatigue cracking caused by the relatively high ratio of load-resistance to self-weight compared to concrete bridge decks. This results in high stress ranges under traffic loads, especially at welded joints, which could= lead to fatigue cracking [1–3].

Since the early 1970s, fatigue cracks have been observed in OSDs during their service life. One of the most frequently observed occurrences in OSDs are fatigue cracks at the trough-to-deck welded connections. There are four different crack initiation types, as displayed in Figure 1.1. In the Netherlands, the most observed fatigue cracks are in the deck plate at the intersection of crossbeam and trough, indicated by crack type *a* and *b* in Figure 1.1. Since crack propagation of type *a* and *b* trough the deck plate could damage bridge performance and asphalt pavement leading to decreased traffic safety, these cracks are most harmful [2, 4–6].

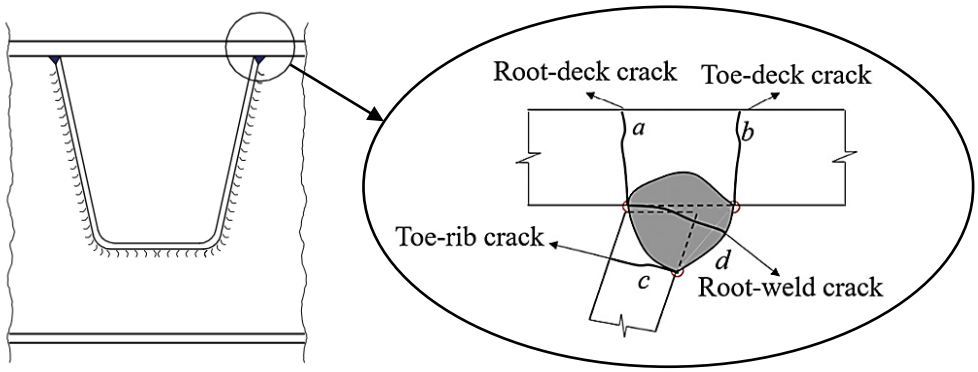

Figure 1.1: Fatigue crack propagation in trough-to-deck welds [58, 60]

To mitigate fatigue cracking in existing bridges with OSDs, several bridge decks are strengthened with a high strength concrete (HSC) overlay. For this method, the asphalt layer will be removed and replaced with an epoxy layer followed by a layer of HSC. This reinforced HSC layer increases the bending stiffness of the OSD and will increase the distribution of vehicle loads, resulting in lower stress ranges in rib-to-deck welds. This repair method mainly contributes to limiting crack propagation of cracks *a* and *b*, while also reducing sensitivity to crack propagation of cracks *c* and *d*. The main issue with crack *d* is that it is typically only detected during renovation inspections, which means there is a risk that a relatively large crack may go unnoticed and could further propagate [7].

A traditional repair method that focuses on resolving crack *d*, includes removing the existing weld and applying a new weld. However, in cases where an OSD is strengthened by applying a HSC overlay, the heating that is required in the welding process will burn the epoxy layer of the strengthened steel deck plate and result in a potential risk for long term damage [8].

1.1.2 Cold Repair Method

As applying heating to resolve weld crack propagation results in potential damage, Arup conducted a study into the 'Cold Repair' method. The Cold Repair method, in literature also described as 'angle steel reinforcement method', consists of a bent steel plate, also referred to as a steel angle, that is attached to the trough-deck plate detail by making use of an adhesive, as displayed in Figure 1.2. This local strengthening technique is researched with the intention of replacing the function of the trough-to-deck plate weld, therefore reducing occurring stresses in the weld and limiting crack propagation. In 2014, the Cold Repair method is applied to the Galecopper bridge as a pilot by Arup and Takke Breukelen, as displayed in Figure 1.3 [8].

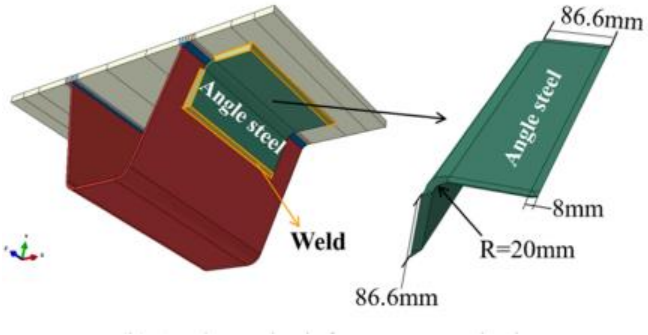

Figure 1.2: Cold Repair method [9]

Figure 1.3: Implementation of Cold Repair method using steel on Galecopper bridge [8]

A review of the production and implementation process resulted in a discussion about the possibility of including fiber-reinforced polymer (FRP) for the strengthening solution. Based on the experience and expertise of involved parties, the decision was made to focus on an FRP composite angle produced by vacuum infusion of fiber fabrics with epoxy resin. The application process would be similar to the Cold Repair method using steel, where the FRP angle would be attached to the bottom of a trough-deck plate detail by an adhesive, in this case by vacuum infusion. The following expected considerations were established:

- **Increased design freedom**. Since the proposed production method includes vacuum infusion of fiber fabrics, the material is flexible and free of form before vacuum infusion is executed. Compared to a steel angle with relatively high stiffness, this is an advantage since, in the field, the geometry of the trough-deck plate detail can vary.
- **Reduced stress in epoxy**. Due to the reduced stiffness of FRP compared to steel, occurring stresses in the epoxy interface between FRP and OSD will be reduced.
- **Better accommodation of imperfections**. As described in the first point, prior to the vacuum infusion process, FRP is quite flexible and can therefore take imperfections in the geometry of the orthotropic steel deck into account, as opposed to a bent steel plate. Since OSDs, especially in longitudinal stiffeners, can have quite large imperfections due to frequent dynamic loading, the epoxy adhesive could have a varying thickness over the surface of the strengthening angle. This introduces a weakness in the design.

- **Increased preparation costs**. As described in section 2.2.6, the production process of described FRP consists of impregnating fiber fabrics with epoxy resin by the process of vacuum infusion. Since this is a manual process and the fiber fabrics need to be prepared by hand, in contrast to a steel angle, preparation costs will increase when an FRP angle will be implemented [8].

1.1.3 Cold Repair Method Study conducted by Arup

The use of CFRP for the Cold Repair method is relatively new and has not been extensively applied. While there is supportive literature that shows the potential of FRP to improve fatigue performance of steel structures and welded connections [6, 10–14], there are several uncertainties and risks involved with respect to its behaviour, material properties and design. For this reason, Arup, in collaboration with contractor Takke Breukelen, is conducting research that aims to design the Cold Repair method using FRP to delay the root-weld crack growth. The study includes three phases, which are:

- **Phase 1 - Methodology / Approach**: establishing design principles and scope of Cold Repair method.
- **Phase 2 - Design**: preliminary design of Cold Repair and in a later stage, development of a detailed design. The designs are based on a linear numerical analysis.
- **Phase 3 - Material and feasibility tests**: conducting several material tests to determine material properties of Cold Repair. In addition, Takke Breukelen will carry out a feasibility test to determine construction time and quality [15].

From phase 1, the decision was made to use carbon fiber-reinforced polymer (CFRP) in the design of the Cold Repair as they exhibit higher strength and tensile properties than other fibers. This thesis provides an expansion of Arup's study into the Cold Repair method, and mainly contributes to phase 2 and 3.

1.2 Objectives

This section presents the objectives of the thesis. Firstly, a brief description of subtopics and research objectives is provided, followed by research questions.

In short, this thesis includes two series of lab experiments, accompanied by two series of numerical models. This means that the thesis contains two main topics, each divided in two sub-topics, as will be outlined in section 1.3.

1.2.1 Experimental testing

Since there are several knowledge gaps regarding behaviour and capacity of the adhesive FRP-steel joint, also referred to as FRP-steel bond, thick-adherend shear tests (TASTs) subject to static load will be performed. These tests, also referred to as small-scale tests or experiments, aim to provide more insight into the bond behaviour and to determine the shear capacity of the adhesive bond. Moreover, the experimental results will be used to provide a discussion and validation of the corresponding numerical model.

In addition to TASTs, static three-point bending tests on component-level will be performed. These components will consist of a trough-deck plate strip element of an OSD, strengthened with FRP angle. The main objectives of these experiments are to provide a discussion and validation of the corresponding numerical study and to determine the static capacity and failure behaviour of strip component.

1.2.2 Numerical Study

Two series of numerical models will be constructed, corresponding to the test series. The development of the numerical model on small-scale level, referring to the TASTs, will provide insight into material models and modelling approaches for the adhesive bonded joint. These will be applied as input parameters and modelling principles for the numerical model on component-level.

Furthermore, the component-level model aims to study to what extent the model can simulate physical behaviour observed during experiments and what modelling techniques could be implemented to model this behaviour. More specifically, this numerical study has the goal to implement non-linear interface conditions for the FRP-steel bond. This contrasts with the full-bridge model provided by Arup, as this model implements linear interface conditions.

In addition, as the numerical model of the component-level three-point bending tests includes a similar geometry of the Cold Repair design to the full-bridge model provided by Arup, a comparison between these models will be performed. This comparison mainly focuses on the contribution of non-linear interface conditions as opposed to linear interface conditions.

Further characteristics of numerical studies will be described in section 0. In conclusion, this thesis aims to study what the contribution of a non-linear numerical analysis and small-scale shear and component-level bending tests, will be.

1.2.3 Research Questions

The main objective of this thesis is translated to a main research question and can be formulated as follows:

"To what extent can non-linear numerical modelling and small-scale and component-level experiments contribute to obtaining an increased reliability of the Cold Repair method using Carbon Fiber-reinforced Polymer angles for delaying the root-weld crack growth of trough-deck plates of orthotropic steel decks?"

To be able to answer this main research question, multiple sub-questions will be required. They are formulated as follows:

- What are the governing failure mechanism and ultimate load capacity obtained in thick-adherend shear experiments?
- How can a finite element model be built to sufficiently resemble the governing failure behaviour obtained in the small-scale shear lab experiments?
- What is the governing failure mechanism and ultimate load capacity obtained in component three-point bending experiments?
- How can a finite element model be built to sufficiently resemble the governing failure mechanisms obtained in the component lab experiments?
- To what extent can a full-bridge model, provided by Arup, and the component-level model give comparable results, and can the full-bridge model represent the behaviour observed in experiments?

1.3 Methodology

To answer the research questions stated in section 1.2.3, a numerical study, which includes the development and application of finite element (FE) models, and an experimental study, which includes small-scale shear and component-level bending tests, will be performed.

The FE models will be computed in LS-DYNA and will be implicit and explicit models, based on the modelling approaches. All models that are part of the scope of this thesis will be static models, which means that fatigue and dynamic loads are not considered.

The FE small-scale model resembles a TAST specimen, like the TAST specimens that will be tested in laboratory. The model will consist of a steel and CFRP strip, both modelled as solid elements, with an adhesive interface. For the interface, several modelling approaches, including tied contact definitions, and several tie-break surface-to-surface options, will be analysed. The loading case will be similar to the testing set-up and will be limited to static loading.

The FE component-level model includes a trough-deck component of an OSD. The model will consist of three elements:

- The steel trough and deck plate of the OSD,
- The epoxy layer which is the adhesive bond (adhesive interface) between the steel and the CFRP
- The CFRP angle, also referred to Cold Repair, itself.

The characteristics of the component-level models built by Arup and within this thesis are displayed in Table 1.1.

Table 1.1: Characteristics of component-level models Arup and thesis

Model type	Modelled by	OSD element type	Interface element type	Cold Repair element type
Full-bridge model	Arup	2D, linear elastic	Linear tied interface condition	3D, linear-elastic orthotropic
Component-level strip model	Jill	3D, linear elastic	Linear and non-linear interface condition	3D, linear-elastic orthotropic

A general overview of this thesis is illustrated in Figure 1.4.

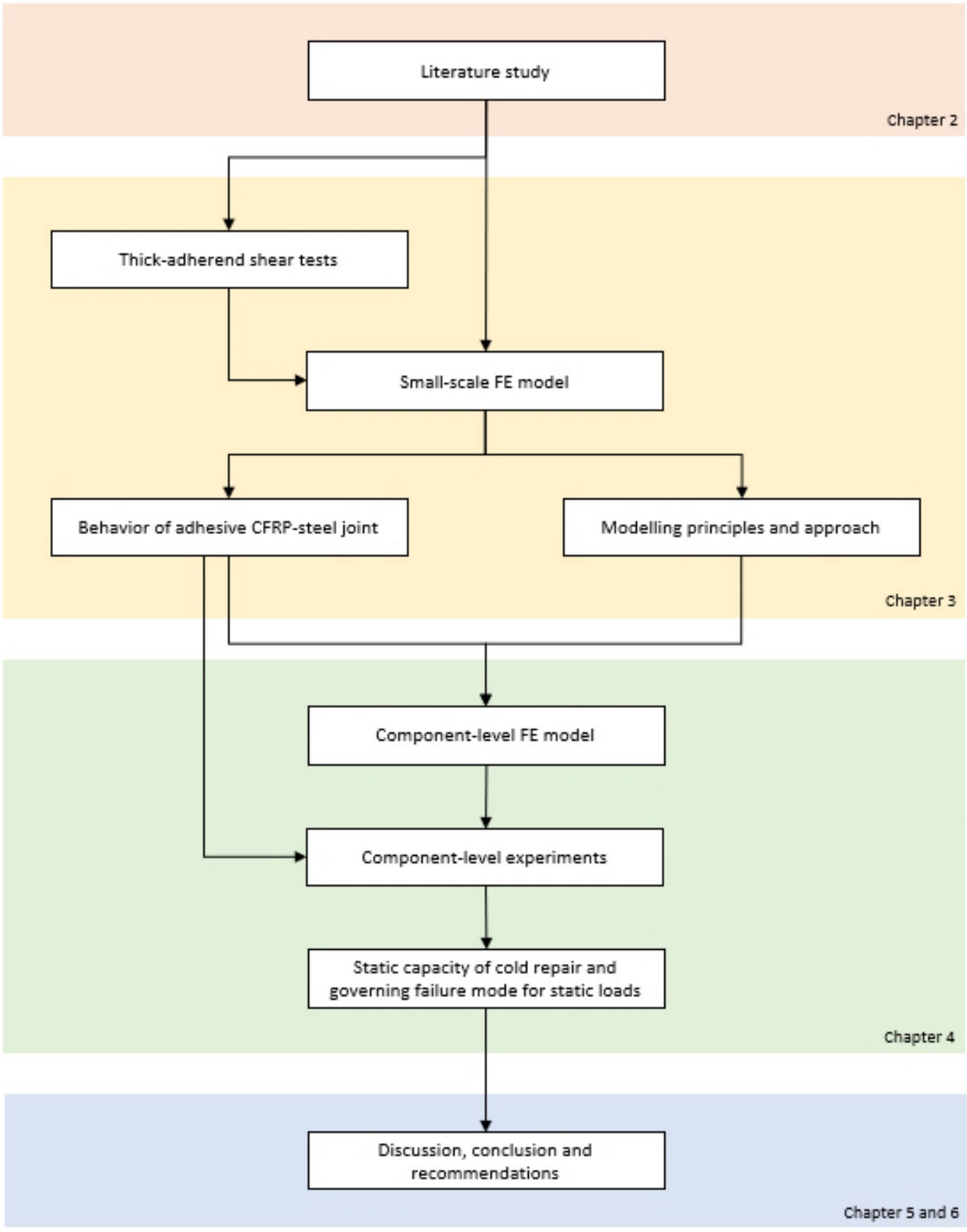

Figure 1.4: Flow-chart of the thesis

1.4 Outline of Thesis

Chapter 1 serves as a introduction to the thesis topic, describing the context of the research problem, illustrating the main objectives of the thesis and describing the methodology in order to answer presented research questions.

Chapter 2 provides a summary of the literature study into the field of thesis research, focusing on OSDs, FRP, the Cold Repair method and finite element modelling (FEM) approaches of simulating adhesive joints.

Chapter 3 is devoted to TASTs and corresponding FE models. The set-up and results of both experimental and numerical studies are presented, followed by a discussion of corresponding FE models. Design values of the shear bond strength are derived.

In Chapter 4, the component-level tests, and accompanying FE model are presented. This chapter describes the set-up and results of experiments and numerical analyses. Moreove, a comparison between the component-level numerical model and full-bridge model will be provided.

In Chapter 5, research conclusions are presented, and recommendations for future research related to this topic are provided.

2. Literature Study

This chapter presents an overview of important topics for the research, based on a literature study. Firstly, it introduces orthotropic steel decks (OSDs) and fiber-reinforced polymers (FRP). This is followed by an introduction of the Cold Repair method, an overview of FEM of adhesive joints and concluded by a summary. an overview of FEM of adhesive joints, introducing several modelling techniques.

2.1 Orthotropic Steel Decks

This section of the literature study provides an overview of OSDs, their application in various bridge types and challenges related to fatigue behaviour.

2.1.1 Introduction

OSDs are a type of steel decks widely used in long-span bridge engineering. The term ‘orthotropic’ refers to a structure or material that has different properties in three mutually perpendicular directions. These steel decks have mostly been developed in Germany and the United States after World War II. Initially, one of the main reasons to design OSDs was the poor steel supply and inexpensive labour since fabricating OSDs is labour-intensive and the application of longitudinal stiffeners saves material. Additional properties, including benefits and challenges, are described later in this section [1, 16].

An OSD consists of a steel deck plate supported in two mutually perpendicular directions by longitudinal, also known as ribs or troughs, and transverse stiffeners, also known as crossbeams. OSDs can be fabricated either with continuous troughs or with continuous crossbeams; the former is preferred with respect to the transfer of loads. An example of an OSD is displayed in Figure 2.1. Traffic loads are distributed from the deck plate to the longitudinal stiffeners, from there to the crossbeams and from the crossbeams to the main girders [1, 16, 17].

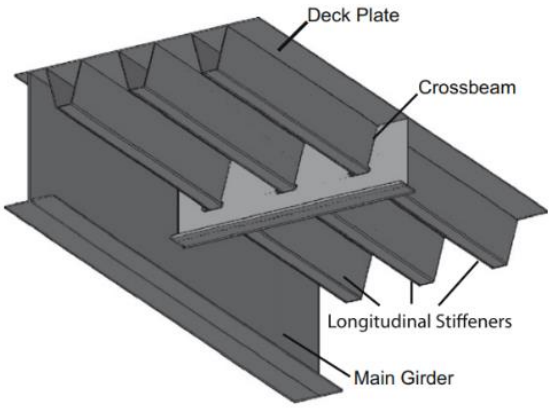

Figure 2.1: Orthotropic Steel Deck [10]

Longitudinal stiffeners can be either closed or open stiffeners, depending on the traffic load and for this reason, bridge type. The different types of longitudinal stiffeners are illustrated in Figure 2.2.

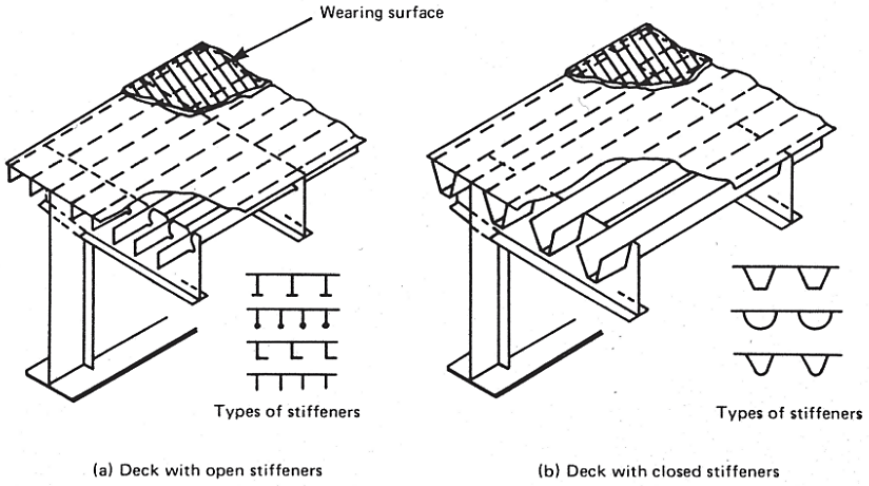

Figure 2.2: Types of Longitudinal Stiffeners for Orthotropic Steel Decks [16]

Open stiffeners are applied to the first generation of orthotropic steel bridge decks, which are mainly constructed after World War II in Europe. The mechanical behaviour of OSDs with open stiffeners can be described as individual beams with very little interaction, resulting in a low longitudinal stiffness and therefore limited spans. When these bridges were constructed, traffic loads were less concentrated which resulted, in combination with limited spans, in a substantial transverse load compared to the longitudinal load [1, 10, 16].

Since open stiffeners have a negligible stiffness in transverse direction, closed stiffeners, also known as ribs or troughs, were introduced. This type of stiffeners has several advantages compared to the application of open stiffeners:

- Increased torsion stiffness. This results in a better accommodation for eccentric loads, therefore increasing the effective width of the bridge deck.
- Increased bending resistance. This results in an increased longitudinal stiffness, therefore making longer spans possible.
- Since only the outer part of the stiffener is in direct contact with weather influence, closed stiffeners are less sensitive to corrosion and results in a reduction of the painting surface.

Trapezoidal closed stiffeners have a larger bending stiffness than round ribs and are more frequently applied. On the other hand, round closed stiffeners have a larger torsion stiffness. A combination of the two types of ribs, as well as trapezoidal and round ribs, is displayed in Figure 2.2 (b) [1, 10, 16].

Nowadays, the main reason for the application of an OSD is the reduction of dead weight compared to bridges with concrete decks. This aspect results in relatively small loads on the substructure and is highly beneficial for large-span and movable bridges. A disadvantage of OSDs is the extensive amount of required labour for fabrication, resulting in high fabrication costs. The increasing application of OSDs in the past was largely driven by inexpensive labour, but today's high labour costs result in a significant challenge with respect to the economical aspect of OSDs [1, 10].

2.1.2 Application of Orthotropic Steel Decks in the Netherlands

OSDs can be and have been applied to many types of steel bridges. This section presents several examples of applications of OSDs in the Netherlands.

In the Netherlands, for main spans greater than two hundred metres, mainly steel bridges are applied. An example of a large-span steel arch bridge is the Van Brienenoord bridge, displayed in Figure 2.3. The Van Brienenoord bridge, also known as the eastern Van Brienenoord bridge, is the first bridge with a span of this length, which is 287 metres, to be constructed in the Netherlands, and is located in Rotterdam where it crosses the New Meuse. The tied-arch bridge, meaning that the deck functions as a tie between the arch ends, was opened in 1964 and is the most heavily used bridge in the country. Traffic increases resulted in construction of the second Van Brienenoord bridge, also known as western Van Brienenoord bridge, in 1989, with a span of 295 metres, also displayed in Figure 2.3 [1, 18–20].

Figure 2.3: Van Brienenoord bridges, Rotterdam [20]

A second example of a steel bridge with an OSD is a truss girder bridge. One of the first modern Warren truss girder bridges, which are bridges where a truss system consisting of only diagonal members is applied, is the Moerdijk Railway bridge, opened in 1955. The bridge, that crosses Hollands Diep, is displayed in Figure 2.4. The upper bracing is applied to reduce the number of members of the truss girders [1].

Figure 2.4: Moerdijk Railway bridge, Moerdijk [61]

A commonly used type of bridges in the Netherlands is a cable-stayed bridge. The Galecopper bridge, constructed in 1971 near Utrecht, is an example and displayed in Figure 2.5. It is built as a replacement of an arch bridge, resulting in a doubling of traffic capacity. To ensure continuous traffic flow during construction of the new bridge, the decision was made to build two separate bridges, the second bridge being finished in 1975 [1].

Figure 2.5: Galecopper bridge, Utrecht [62]

A fourth type of bridge that is constructed with an OSD is a plate girder bridge. This bridge type is considered the most uncomplicated and consists of two or more plate girders, which fulfil the function of main girders, and a deck system. An example of a plate girder bridge is the Lek bridge near Hagestein, also known as Hagesteinse bridge, displayed in Figure 2.6. This bridge has a total span of 740 metres with a main span of 160 metres [1, 21].

Figure 2.6: Lek bridge, Hagestein [63]

A fifth and final type of bridge where an OSD is applied in the Netherlands, is a box girder bridge. A box girder bridge is a bridge type in which the main structural memberis one or more closed sections, in other words, a box girder. An example of a box girder bridge in the Netherlands is the Moerdijk traffic bridge, which crosses the Hollands Diep near Moerdijk. The bridge, displayed in Figure 2.7, is located next to the Moerdijk Rail bridge, as displayed in Figure 2.4. The Moerdijk traffic bridge replaced the second Moerdijk bridge in 1976, which was one of the first bridges that displayed the insufficiency to increasing traffic [1].

Figure 2.7: Moerdijk bridge, Moerdijk [64]

2.1.3 Fatigue Behaviour of Orthotropic Steel Decks

In previous section, several advantages of OSDs are described. However, they also have challenges and drawbacks, with fatigue crack propagation being the major challenge. One of the main reasons for the high number of OSD applications is the improvement of the ratio of load-resistance to self-weight compared to for example a concrete girder bridge deck. However, this property does result in high stress ranges under traffic loads caused by a high number of vehicles, especially at welded joints. This is related to significant stress concentrations in welded joints, due to high temperatures in the welding process. In addition, increasing traffic loads in the last decades result in a higher number of load cycles and higher loads in general. This combination causes sensitivity to fatigue cracking in OSDs, mainly initiating from trough-to-deck weld connections [2, 22, 23].

Since the early 1970s, fatigue cracks have been observed in OSDs during their service life. To specify, fatigue cracks at the rib-to-deck welded connections, also known as trough-to-deck welded connections, are one of the most frequently observed occurrences in OSDs. Fatigue cracks can occur at two locations, either at the intersection between crossbeam, also known as diaphragm, and longitudinal stiffener, also known as rib or through, or between crossbeams in midspan. Crack initiation at the intersection between crossbeam and trough is observed significantly more than in midspan. Both locations are displayed in Figure 2.8 [4, 23].

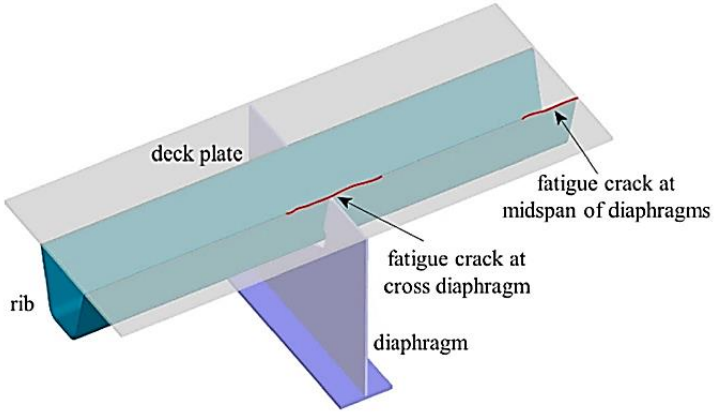

Figure 2.8: Common fatigue cracks at rib-to-deck welded connection details of OSDs [65]

At these two locations, there are four different crack initiation types, as displayed in Figure 1.1. In the Netherlands, the most observed fatigue cracks are located in the deck plate at the intersection of crossbeam and trough, indicated by crack type *a* and *b* in Figure 1.1. For example, deck plate cracks caused by cyclic loading of heavy vehicles were observed in the Second Van Brienenoord bascule bridge in 1997, only 7 years after the bridge opened. Since crack propagation of type *a* and *b* trough the deck plate could damage bridge performance and asphalt pavement leading to decreased traffic safety, these cracks are most harmful [2, 4–6].

2.1.4 High Strength Concrete Overlay for Orthotropic Steel Decks

To mitigate fatigue cracking in existing bridges with OSDs in the Netherlands, Rijkswaterstaat started a project group called ‘Problematiek Stalen Rijdekken’, translated to ‘Problems Steel Bridge Decks’, in 1998. The goal of this project group was to increase understanding regarding orthotropic steel bridge decks and to come up with solutions to strengthen the lifetime of these bridge decks [7].

This resulted in the development of a concept to mitigate deck plate crack propagation, which is the application of a high strength concrete (HSC) overlay. This reinforced high strength concrete layer increases the bending stiffness of the OSD and will increase the distribution of vehicle loads, resulting in lower stress ranges in rib-to-deck welds. These properties will result in an extension of the fatigue life of the orthotropic steel bridge deck. This innovative approach was applied in a pilot that included strengthening of the Caland bridge near Rotterdam, Moerdijk bridge near Moerdijk and Lek bridge near Hagestein. The pilot was considered successful [7].

In 2006, Rijkswaterstaat started ‘Project Renovatie Bruggen’, translated to ‘Project Renovation Bridges’, in 2006. A joint venture between Royal Haskoning DHV, Arup and Greisch was created to further develop this project in 2009. Within this project, the decision was made to start renovation of eight steel bridges in main roads in the Netherlands. These bridges were mainly constructed in the 1960s and 1970s and all displayed fatigue cracks in the deck plate. Since the pilot of the Caland bridge, Moerdijk bridge and Lek bridge near Hagestein was successful, ‘Project Renovation Bridges’ included extension of the fatigue lifetime of these eight bridges with 30 years by applying a high strength concrete overlay. The following bridges were included in the project:

- Muider bridge, part of highway A1 near Muiden

- Beek bridge, part of highway A2 near Beek
- Scharberg bridge, part of highway A76 near Elsloo
- Galecopper bridge, part of highway A12 near Utrecht
- Tacitus bridge, part of highway A50 near Ewijk
- Kreekrak bridge, part of highway A58 near Reimerswaal
- Suurhoff bridge, part of highway A15 near Rotterdam
- Second Van Brienenoord bridge, part of highway A16 in Rotterdam

Since the start of 'Project Renovation Bridges', all bridges within the scope of the project except for the Suurhoff bridge and second Van Brienenoord bridge, also known as western Van Brienenoord bridge, were strengthened by applying a HSC overlay. During the timeframe of the project, the decision was made to change the renovation scope for the Suurfhoff bridge and second Van Brienenoord bridge. Eventually, alternative renovation techniques were researched and developed for these two bridges [7, 24].

2.2 Fiber-reinforced Polymer

This section of the literature study provides an overview of FRP. It introduces their properties, advantages and challenges compared to steel, as well as practical examples of their application.

2.2.1 Introduction to FRP

FRP, is, as the term suggests, a composite material. A composite material is defined as a "material structure that consists of at least two macroscopically identifiable materials that work together to achieve a better result". Macroscopically identifiable materials are those that do not dissolve into one another and remain distinguishable on a macro level, meaning that they can be detected with the human eye [25].

In this thesis, the described composites, or FRP, are produced of a type of fiber, also known as the reinforcement, combined with a resin or matrix, commonly referred to as polymer. After production, both components retain their chemical, physical and mechanical properties. The properties of a composite are determined by:

- Mechanical properties of the fibers
- Mechanical properties of the resin
- Ratio of fiber to resin, also referred to as fiber volume fraction
- Geometry and orientation of fibers [25, 26].

2.2.2 Fibers

The strength and stiffness of FRP composites are mainly provided by fibers since they have a high ultimate strength and a relatively high stiffness. However, fibers can only provide tensile properties along the fibers' length, resulting in a unidirectional strength similar to fibers in a rope. Various types of fibers can be applied, including natural fibers, such as jute, and polyester fibers. However, glass, aramid and carbon fibers are most common. This thesis primarily focuses on carbon fibers, and, to a lower extent, on glass fibers [25, 27].

Carbon fibers have, compared to other common fibers, a higher tensile strength, stiffness, fatigue performance. They also have an excellent stiffness-to-weight ratio and high toughness, making them very advantageous. However, carbon fiber-reinforced polymers, often referred to as CFRP, are more expensive than other fiber types and have a lower compressive than tensile strength, low impact resistance and brittle behaviour. There are various types of carbon fibers with varying properties; prevalent types are high-modulus (HM) or high-strength (HS) carbon fibers [25, 27].

Glass fibers, often referred to as GFRP, offer good chemical resistance, a relatively high tensile strength and impact resistance and are less expensive than other fiber types. However, they have an inferior fatigue properties and modulus of elasticity compared to carbon fibers. Similarly to carbon fibers, there are various types of glass fibers, yet E-glass and S-glass fibers are most frequently applied. A comparison of the stress-strain properties of high-strength carbon, aramid, S-glass and E-glass fibers, as well as an epoxy reason for comparison, is displayed in Figure 2.9 [25, 27].

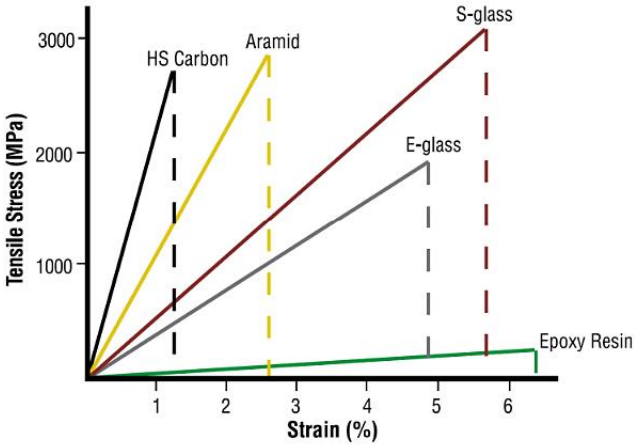

Figure 2.9: Typical stress-strain curves for different types of fibers [26]

In FRP composites, there are several forms in which fibers can be included in the material. These forms can be categorized by discontinuous- and continuous-fiber product forms, where discontinuous-fiber product forms include chopped fibers created by mechanically chopping rovings, yarns or tows. Continuous-fiber product forms include continuous strands, yarns, rovings, reinforced mats and fabrics. FRP composites included in this thesis consist of fiber fabrics. For this reason, a more elaborate description of this product form is provided [25, 27].

Fiber fabrics are defined as “a manufactured assembly of long fibers to produce a flat sheet of one or more layers of fibers” [26]. The layers are bound by mechanical interlocking, which is a method where the rough fibers’ surface holds the fibers in the desired orientation, or with a binding material. Fabrics can applied to manufacture FRP laminates, as will be described in section 2.2.5. The fabrics are characterized by fiber orientation, with three main categories:

- Unidirectional. In this fabric, most fibers are oriented in one direction.
- 0/90° and ±45°, also known as cross ply or biaxial. This fabric consists of a combination of fibers in 0° and 90° orientation or, if rotated 45 degrees of fibers in +45° and -45°.
- Multiaxial. This fabric consists of one or more layers of fibers, bound by a stitching thread. This fabric type provides more design freedom in fiber orientation, since several fiber directions can be combined into one fabric to produce, for example ± 45° fabrics [26, 28].

2.2.3 Resin

The matrix, resin or polymer, has four major functions:

- Fixing the fibers in desired geometrical arrangement
- Distribution of load to and between fibers

- Prevention of fiber-buckling
- Protecting the fibers from environmental influences.

In addition, the matrix provides additional toughness and resistance to damage caused by impact and abrasion. The matrix properties also determine the composite's maximum service temperature, which is the highest temperature at which the material retains its load-bearing capacities, resistance to moisture, thermal stability and sensibility to UV radiation. [26, 27, 29].

Epoxy resins are a type of thermoset polymers, which means that they set after curing and cannot be softened by heating, and most widely used for high-performance composites with either high-modulus (HM) or high-strength (HS). This type of matrix material has a good combination of strength, adhesion, fatigue resistance, low shrinkage, and processing versatility and possess a low moisture absorption capacity. However, this resin is relatively expensive compared to other polymers. In this thesis, epoxy resin will be applied in the design and manufacturing of the FRP [25, 27].

2.2.4 Orthotropic Properties of FRP

In general, materials are classified as either isotropic or anisotropic, where isotropic materials have equal properties in all directions and anisotropic materials have different properties in all directions. Within the material category anisotropic materials, composites consist of a subcategory that is characterized as orthotropic. Like for OSDs, FRP composites have properties that are different in three perpendicular directions. This material property is caused by the strong influence of the fiber direction on the strength and stiffness [25].

For example, a unidirectional (UD) fabric is relatively strong and stiff in longitudinal direction, which is parallel to the fiber, meaning that it can withstand relatively high loads in the axial direction. However, this type of fabric is weaker in transverse direction, which is perpendicular to the fiber. On the other hand, a ± 45° fabric, also referred to as a biaxial fabric, has a relatively high shear capacity [30].

2.2.5 FRP Laminates

As described in section 2.2.2, FRP composites can consist of fiber fabrics combined with a resin. A single layer of fiber fabric is commonly referred to as a ply and can be stacked with other plies containing fibers in equal directions to form a lay-up, in which case it will be referred to as a lamina, or with plies containing fibers in different directions, in which case it will be referred to as a laminate [25].

As fiber orientation directly affects the mechanical properties of a composite material, the design of a laminate is related to the direction of the applied load. In general, the majority of plies in a laminate will be oriented in the load-carrying direction, to ensure a high strength in this direction. However, for the stability of a laminate, it is necessary to combine plies in different directions. Many circumstances require a material to perform in more than one direction, in which case a laminate with different fiber orientations is desired. In such a case, a quasi-isotropic laminate can be applied, which consists of an equal number of plies in 0°, 90° and ± 45° direction and performs well in all directions. An example of a laminate with 0°, 90° and ± 45° plies is displayed in Figure 2.10 [25, 30] .

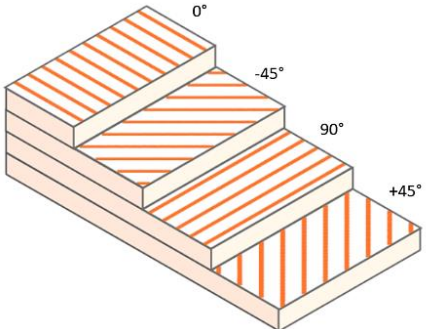

Figure 2.10: Example of laminate lay-up [30]

2.2.6 Production processes of FRP

The production process of an FRP influences the mechanical properties and can be described by three steps, which are:

- **Step 1**: Arrange the fibers in their designated place and orientation. This is done either by hand or by machine.
- **Step 2**: Impregnate the fibers with resin.
- **Step 3**: Cure the resin to finalize the composite product.

The production process can be categorized as either open mould, meaning that the mould is not covered with film or another mould, or closed mould. The mould is required to achieve the desired shape of the composite product. The four most important production processes in civil engineering applications are:

- **Hand lay-up**. This is an open mould process where fiber fabrics are added and impregnated using a brush or roller to remove excess resin. Since this process is performed layer by layer, it is labour intensive and therefore not applied to large components.
- **Filament winding**. This open mould process is used to create various hollow sections by spinning fiber fabrics around a rotating mandrel. With this process, the thickness can be controlled, and an outstanding fiber density can be achieved.
- **Vacuum infusion**. This closed mould process uses vacuum pressure to impregnate fiber fabrics and provides a high design freedom, making this process suitable for production of bridge decks, plates and freeform beams. In this thesis, the composites used in experimental tests and FE modelling are produced by vacuum infusion.
- **Pultrusion**. Since this closed mould process is continuous, it is cost-effective if a high number of elements needs to be produced. Continuous fabrics are pulled through a resin bath and then extruded into the desired shape. The produced components have excellent unidirectional properties, however strength in other directions is relatively low [25, 31].

2.2.7 Performance of FRP Compared to Steel

In general, FRP has several advantages when compared to steel, with the main advantages being:

- **Lightweight**. FRP composites have a lower density than steel, which results in a reduction of dead weight. For example, a unidirectional GFRP composite has a density of 2000 kg/m^3 while in general, steel has a density of 7850 kg/m^3 [32].
- **High tensile strength**. FRP composites have a relatively high tensile strength compared to steel. For example, the tensile strength of a unidirectional GFRP ranges from 1140 to 1725 MPa while the ultimate strength of steel ranges from 360 to 770 Mpa [32].
- **Fatigue resistant**. When compared to steel, FRP provides a better fatigue resistance which is beneficial for bridge applications [33].
- **Corrosion and chemically resistant**. FRP's contain a higher corrosion and chemical resistance when compared to steel, which means that they can be applied in corrosive and chemically aggressive environments, such as wastewater treatment plants [34].

However, some properties of FRP cause challenges that are not present with steel. The main challenges can be defined as:

- **High anisotropy**. This results in a weakness in out-of-plane direction, to ensure a high strength in longitudinal direction.

- **Linear-elastic behaviour**. Steel possesses a high ductility which results in a high deformation prior to fracture. In contrast to this, FRP materials are relatively brittle and therefore susceptible to sudden failure and exhibit low impact resistance [25].
- **Susceptible to delamination**. Delamination is a failure mechanism where different plies, or layers, of a laminate are separated.
- **High costs**. In general, high raw material, fabrication, and assembly costs, result in relatively high costs for FRP composites when compared to steel. However, this does heavily depend on the type of fibers and fabrication process. Innovations and increasing application of FRP will contribute to a cost reduction [25].

2.3 Cold Repair Method

This section of the literature study provides an overview to the Cold Repair method. It introduces the method followed by its implementation on the Galecopper bridge. Moreover, possible failure mechanisms and applications of strengthening OSDs with FRP are presented.

2.3.1 Cold Repair Method with Steel

As described in section 2.1.3 and 2.1.4, many orthotropic steel bridge deck display fatigue cracks and a repair method of applying a HSC overlay was developed. Though this repair method resolves crack type *a* and *b*, as displayed in Figure 1.1, this method does not focus on crack type *c* and *d* which means that these fatigue cracks can still propagate. Section 1.1.2 presented the traditional repair method to resolve these fatigue cracks and highlighted that this method cannot be applied to steel bridges strengthened with an HSC overlay. For this reason, Arup conducted a study into the 'Cold Repair' method. The principle and implemented pilot project of this method were also presented in section 1.1.2 [8].

2.3.2 Introduction to Cold Repair Method with FRP

After the implementation of the Cold Repair method on the Galecopper bridge, a review of the production and implementation process resulted in a discussion about the possibility of including FRP for the strengthening solution. Based on the experience and expertise of involved parties, the decision was made to focus on an FRP composite angle produced by vacuum infusion of fiber fabrics with epoxy resin. The application process would be similar to the Cold Repair method using steel, where the FRP angle would be attached to the bottom of a trough-deck plate detail by an adhesive, in this case by vacuum infusion [8].

As outlined in section 1.1.3, Arup is conducting a research that aims to design the Cold Repair method using FRP. Within this study, there are several design goals which relate to design assumptions and decisions in this thesis. The following design goals related to the OSD are established:

- The application of the Cold Repair must slow down the (root) crack growth, specified as crack *d* in Figure 1.1, in the trough-to-deck plate weld.
- The application of the Cold Repair should not result in adverse effects on other fatigue details.
- The Cold Repair must take over the function of the trough-to-deck plate weld under static loading.

With respect to the Cold Repair itself, the following design goals are established:

- The design life should be thirty years. It should have sufficient static and fatigue strength during its design lifetime.
- It should be relatively easy and quick to install with minimum hinderance to traffic [8].

2.3.3 Failure Mechanisms of Cold Repair Method with FRP

To ensure a verified design, several failure mechanisms of the Cold Repair method need to be considered. In general, there are three loading modes leading to fracture in adhesively bonded joints, which are displayed in Figure 2.11 and characterised by:

- **Mode I**: Opening mode
- **Mode II:** Shear mode where the crack surfaces move perpendicular to the crack tip
- **Mode III**: Shear mode where the crack surfaces move parallel to the crack tip

An adhesively bonded joint can be subjected to one loading mode, resulting in pure mode behaviour, or a combination of two or more loading modes, resulting in mixed-mode behaviour.

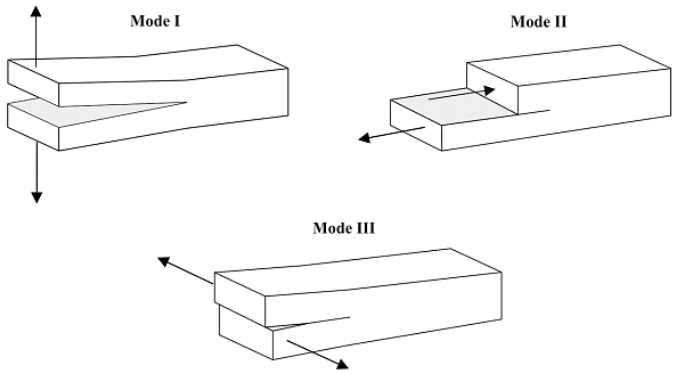

Figure 2.11: Adhesive joint loading modes [66]

In addition to the three loading modes, possible failure modes in an adhesive steel – FRP interface are characterised by:

- **Adhesive failure**: failure of the adherend-adhesive interface, displayed by failure modes *a* and *c* in Figure 2.12;
- **Cohesive failure**: failure inside the adhesive layer, displayed by failure mode *b* in Figure 2.12;
- **Adherend failure**: failure of FRP or steel, displayed by failure modes *d*, *e* and *f* in Figure 2.12 [13, 35] .

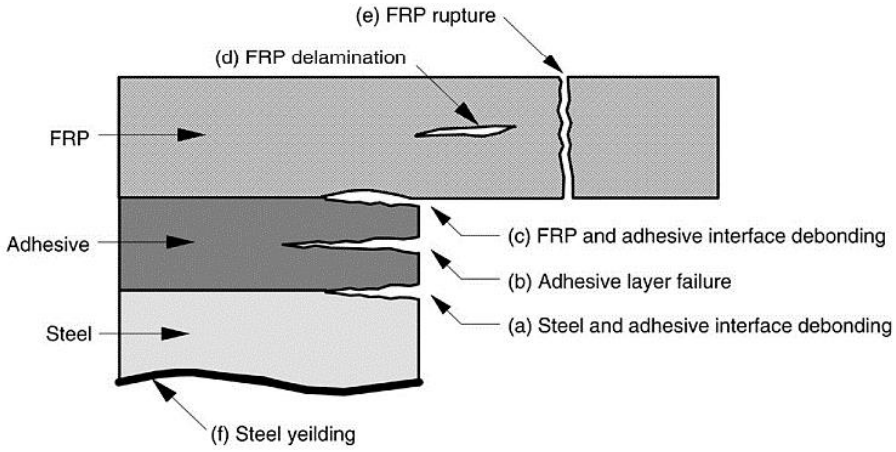

Figure 2.12: Failure modes in a bonded joint [13]

Since the Cold Repair method is a strengthening method which will be applied to existing OSDs, the assumption was made that yielding of steel is unlikely to occur and therefore not considered as a possible failure mode. 'CEN/TS 19101 – Design of fibre-polymer composite structures' indicates that pure adhesive failure, meaning complete failure in either the FRP-adhesive or steel-adhesive interface, should be avoided. This failure mode may be prevented by an appropriate surface preparation and application of a primer to increase the adherend-adhesive bond. In this guideline it is also stated that adhesive failure should cover less than 10 percent of the failure surface in a mixed-mode failure and that the governing failure mechanism of adhesive connections between FRP and steel should be validated by tests [35].

Adherend failure of the FRP can be categorized by FRP delamination and FRP rupture, as displayed in Figure 2.12. These failure modes can be caused or initiated by three types of FRP laminate failure, as displayed in Figure 2.13:

- **Matrix cracking**: resin cracking occurs between fibers.
- **Delamination**: cracks between plies occur. This process is initiated by matrix cracking.
- **Fiber failure**: fiber pullout or breakage occurs. This process is one of the steps towards final failure of a laminate [36, 37].

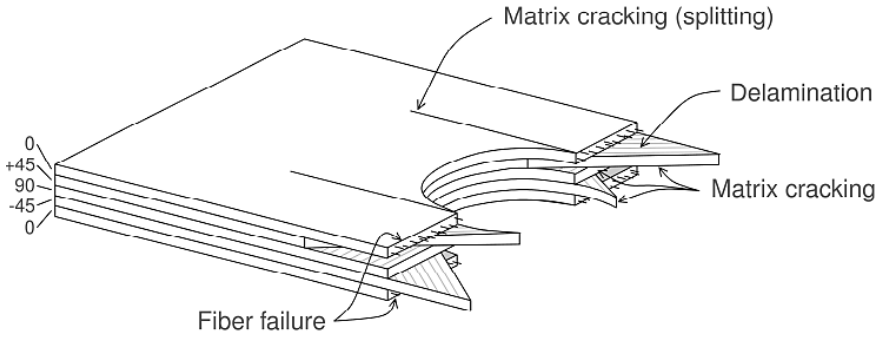

Figure 2.13: FRP laminate failure modes [36]

2.3.4 Applications of Strengthening Orthotropic Steel Decks with FRP

Though the Cold Repair method using CFRP is an innovative approach and not yet applied in the Netherlands, there are references in literature of similar strengthening techniques. In this section, relevant examples will be described.

Liu et al. [6] conducted fatigue tests and numerical studies on seven full-scale OSD specimens strengthened with both CFRP and GFRP angles. The goal of the study was to validate the strengthening technique's effectiveness and to define the effect of different fiber types, adhesives, and angle dimensions. Pultruded FRP angles, illustrated in Figure 2.14, were attached with various adhesives, including epoxy resin, with fibers mostly aligned in X-direction to resist bending stresses. Results showed FRP angles reduced the stress in the strengthening region and distributed stresses to the unstrengthened region in the trough. Detailed FE models analysed the effect on stress intensity factors, which is a parameter used in fracture mechanics to define stress redistribution at crack tips after crack initiation. The following conclusions could be drawn:

- Cold Repair method using FRP angles could significantly increase fatigue life of OSDs. This was mainly caused by the reduction of hot-spot stress in welded connections of strengthened OSDs.
- FRP material, adhesive and angle dimension strongly affect the strengthening effect. Ductile, stronger adhesives and FRP angles with longer plates in transverse direction resulted in better fatigue performance. Since CFRP has a higher stiffness than GFRP, this fiber type is concluded to be more effective.

- Since adhesive debonding, characterized as either cohesive or adhesive failure, occurred in some specimens, resulting in fracture of the OSDs, it is essential that debonding is prevented.
- The observed strengthening effects are supported by numerical analyses. The study was performed at room temperature. However, temperature variation could influence the performance of the Cold Repair [6, 38].

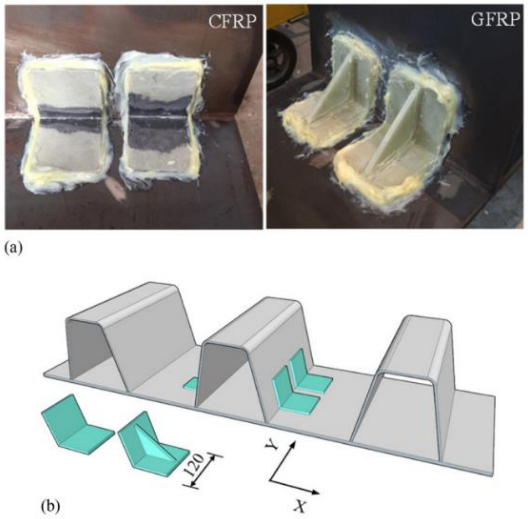

Figure 2.14: Strengthening of OSD with FRP angles: (a) FRP angles; (b) strengthened specimen [6]

Another example is a study performed by Guo et al. that focuses on field measurements of a long-span suspension bridge, the Runyang Yangtze River bridge in China, with OSD, strengthened by GFRP angles with varying dimensions. The GFRP angles were fabricated by pultrusion and bonded to the OSD by applying adhesive, like the implemented Cold Repair method of Arup on the Galecopper bridge. In addition, a numerical study was conducted, in which the stress fields of the trough-to-deck weld were further studied. The following conclusions could be drawn:

- Based on the measured stress ranges, the Cold Repair method using FRP angles could improve fatigue performance of trough-to-deck welds. In addition, FRP angles with longer legs and an increased thickness could further improve fatigue strength.
- The observed strengthening effects are supported by numerical analyses.
- The study was performed at room temperature. However, temperature variation could affect the performance of the Cold Repair [5].

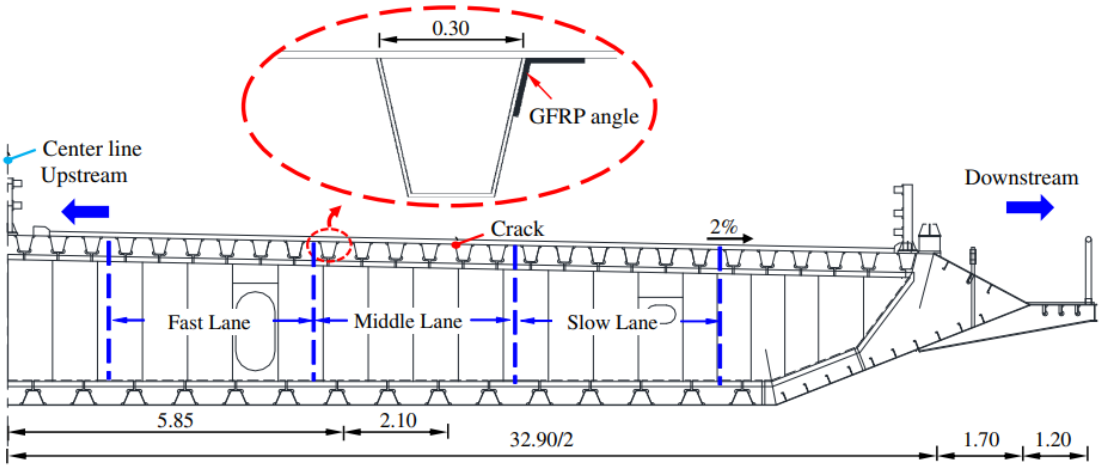

Figure 2.15: Transverse position of GFRP angle (in meters) [5]

2.4 Finite Element Modelling of Adhesive Joints

This section of the literature study provides an overview of FEM of adhesive joints. It introduces several modelling techniques that are used to simulate adhesive interfaces. Implementations of these modelling approaches are provided in section 3.3.

2.4.1 Tied Interface Condition

In a linear model, two elements are generally connected using either merged nodes or with a tied contact definition. This modelling technique implements the concept of infinite stiffness, ensuring that slave nodes or surfaces that are tied to master nodes or surfaces stay tied without allowing movement or failure during the analysis, treating them like one monolithic part.

Limitations of this approach regarding modelling of adhesive interfaces is the infinite stiffness of the interface. This leads to an overestimation of adhesive joints and means that this modelling approach does not allow modelling of failure propagation of bonded joints.

2.4.2 Tie-break Interface Condition

In addition to tied contact definitions, a tie-break contact includes a failure definition that allows the modelling of failure, which is defined as the moment where the non-physical linear spring decouples. This decoupling allows unconstrained movement of the slave node when subjected to tensile stress and results in a traditional compression-only contact between slave and master. In LS-DYNA, failure can be based on either force or stress distribution and there is a wide variety of tie-break contact definitions with corresponding failure definitions. Tie-break contacts can be applied to simulate bonded joints, amongst other applications, and, in contrast to tied contacts, are penalty based [39].

2.4.3 Cohesive Zone Modelling

The third method is the application of solid cohesive elements, commonly referred to as cohesive zone modelling (CZM). This method, which combines cohesive zone models with FE analysis, is employed to predict both static and fatigue behaviour in materials of structural systems, including adhesively bonded joints. CZM relies on spring-like or cohesive elements that create a coupling between 2D or 3D elements of structures to model degradation of cohesive stiffness up to the point of failure. The characteristics of this coupling depend on traction-separation laws that are used to model, for example, adhesive interfaces. Two types of CZM can be categorized, which are the local and continuum approach, as displayed in Figure 2.16. The local approach is used to simulate a zero-thickness interface and is, for example, used for different plies in a composite laminate. On the other hand, the continuum approach is used to simulate a thin strip between two materials, initially not in direct contact and is, for example, employed to model and adhesive bond. Since the local approach takes the effects of external and internal factors into account for assessing the plastic dissipation, this approach provides a more thorough simulation. However, compared to the continuum approach, this method requires more parameters and computations [40–42].

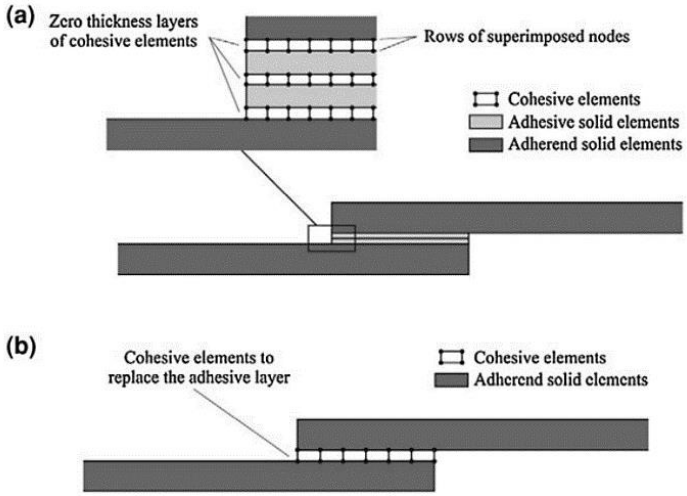

Figure 2.16: CZM: (a) Local approach (b) Continuum approach [40]

2.5 Summary

OSDs are a type of steel deck widely used in long-span bridge engineering since the 1950s. Though their application brings several advantages, one of the major challenges is the sensitivity to fatigue cracking, mainly initiating from trough-to-deck plate welds at the intersection between crossbeam and trough. To mitigate fatigue cracking in existing bridges in the Netherlands, a repair method consisting of the application of an HSC overlay was developed and applied. This strengthening technique results in an extension of the fatigue life of OSDs.

Though this repair method mainly resolves two types of fatigue cracks, it does not prevent further propagation of root-weld cracks. A traditional repair method includes the removal of the existing weld and application of a new welded connection. However, the heating that is required in the welding process will burn the epoxy layer of the strengthened steel deck plate and result in a potential risk for long term damage. For this reason, Arup conducted a study into the effectiveness of the Cold Repair method, which consists of a steel angle, attached to the exterior of trough-to-deck plate detail with adhesive. The strengthening technique was applied to increase the fatigue life of the Galecopper bridge in 2014.

Additional research showed the potentially increased effectiveness of the application of the Cold Repair method with an FRP angle. For this method, carbon fiber fabrics will be attached to the OSD by the process of vacuum infusion with an epoxy resin. The literature review shows that limited knowledge is available on strengthening OSDs with CFRP to slow down root crack growth in trough-to-deck plate welds, especially for applications that include vacuum infusion of fiber fabrics. For this reason, there are several uncertainties and challenges involved with respect to its behaviour, material properties and design.

Moreover, several FEM techniques can be used for simulating adhesive joints. It introduces three main approaches, which are:

- **Tied interface condition**. In this technique, elements are tied with infinite stiffness and strength, treating them as one monolithic part.
- **Tie-break interface condition**. This is a tied contact definition that allows for modelling of joint failure.
- **CZM.** This method applies cohesive elements to simulate degradation and failure in adhesive interfaces through traction-separation laws.

3. Thick-adherend Shear Tests and Numerical Model

To gain knowledge and understanding of modelling and the actual behaviour of the Cold Repair method using FRP, more insight into the bond behaviour of the FRP-steel joint is essential. For this reason, this chapter is devoted to TASTs and corresponding FE model.

3.1 Introduction

Initially, single-lap shear (SLS) and double-lap shear (DLS) tests were proposed to obtain more insight into the bond behaviour of the FRP-steel joint, as displayed in Figure 3.1. However, due to the asymmetry and relatively thin substrate of a single-lap joint specimen, a substantial amount of mixed-mode behaviour is introduced. As described in section 2.3.3, there are three modes that could occur and result in failure of bonded joints. For a single-lap joint, initially mode I behaviour, which is defined as peel or opening of the joint, will be observed, followed by increasing mode II behaviour, characterized as in-plane shear. This results in a more complex evaluation of material properties and is therefore not preferred. On the other hand, DLS tests show less mixed-mode behaviour, making them more suitable for the evaluation of material parameters, such as bond stress. However, due to limitations in the manufacturing process of DLS specimens, these tests could not be performed within this thesis [43].

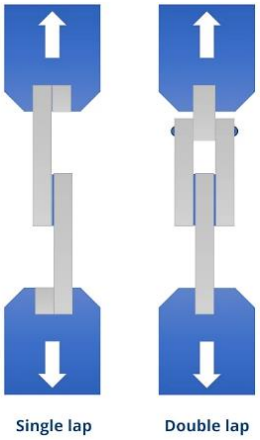

Figure 3.1: SLS and DLS test [67]

3.2 Thick-adherend Shear Tests

This section of the report provides a description of the test set-up and test results of the performed TASTs.

3.2.1 Test Set-up

As an alternative to DLS tests, TASTs of bonded FRP-streel strips were performed in the Stevin II laboratory of the Delft University of Technology. This test method consists of testing thick-adherend shear-lap samples, also referred to as thick-adherend shear specimens and displayed in Figure 3.2, loaded by a tensile load, yet placed in shear. Two substates are connected by a bonded joint, where two notches on either side of the sample result in shear forces in the overlap region, indicated with red in Figure 3.2. Unlike single-lap shear tests, the adherends, which are the components to which the adhesive adheres are thick and therefore rigid, which leads to a minimization of peel forces. TASTs are generally performed to obtain stress-strain properties of adhesives [44].

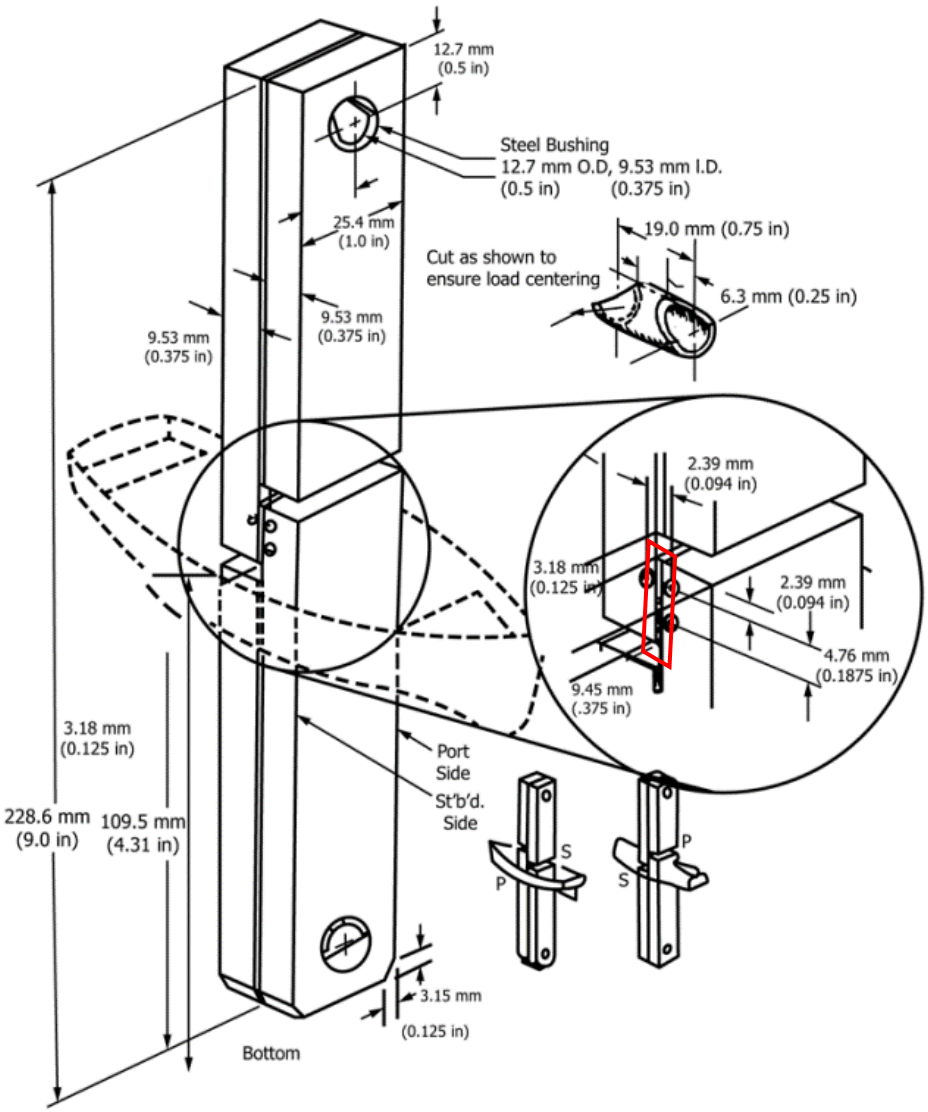

Figure 3.2: Thick-adherend lap shear test specimen [44]

To specify, the performed shear tests are 'modified TASTs' since they are not fully designed according to ASTM D5656-10 [44]. However, for simplicity, the performed small-scale tests will be referred to as TASTs in this thesis. For experiments to be characterized as standardized TASTs and to process the results accordingly, they must comply with the following specifics, as displayed in Figure 3.2:

- Specimens should have specific dimensions, as described in ASTM D5656-10.
- Specimens contain holes through which steel support pins will be inserted, resulting in rotational freedom of the top and bottom of the specimen.

The guideline describes that since bond stresses are not uniform across the overlap regio, they could are influenced by factors like adhesive and adherend stiffness. For this reason, specific dimensions are defined. Nonetheless, to resemble the Cold Repair's full-scale design, the laminate thickness matches the thickness of the Cold Repair. Moreover, to simplify the test set-up and production process of the specimens, considering that drilling holes in the specimens could lead to damage of the materials, the TASTs are performed with clamped top and bottom, as opposed to pinned with support pins [44].

The specimens consist of a 15 mm steel and 18 mm CFRP strip, connected by the process of vacuum infusion with epoxy resin, with applied notches to create an overlap region. A primer is applied to the steel plate to create a better bond between FRP and steel. To observe the influence of the overlap length on the bond strength, specimens with three different overlap lengths are tested, which are 30 mm, 60 mm and 90 mm. The three different types are displayed in Figure 3.3 - Figure 3.5.

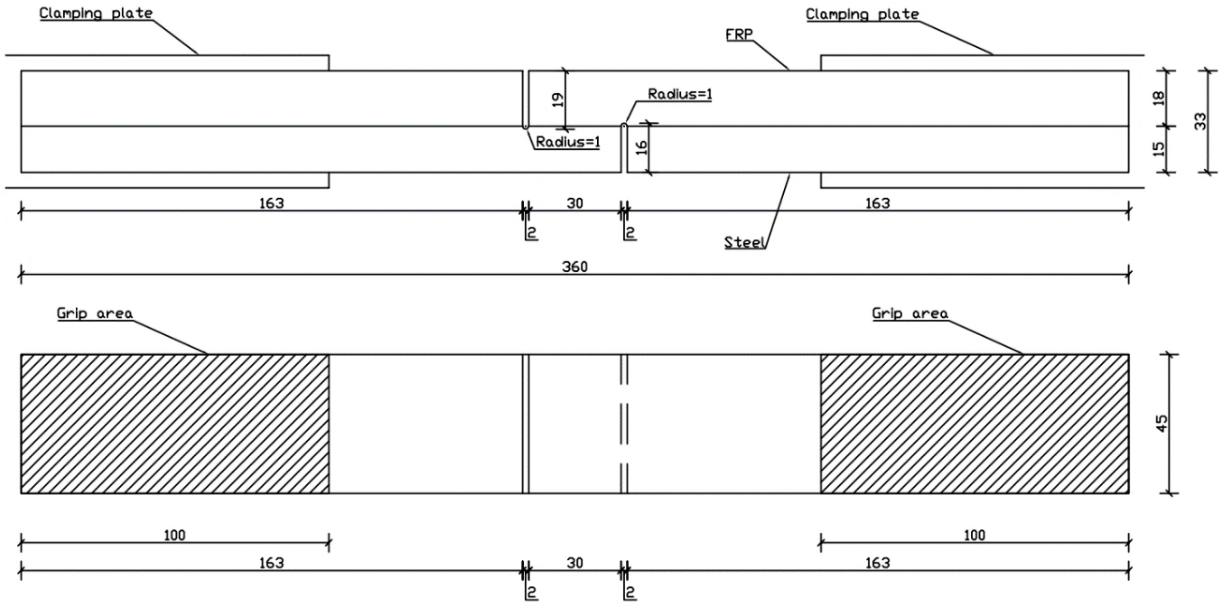

Figure 3.3: Thick-adherend shear test specimen with 30 mm overlap length; dimensions in [mm]

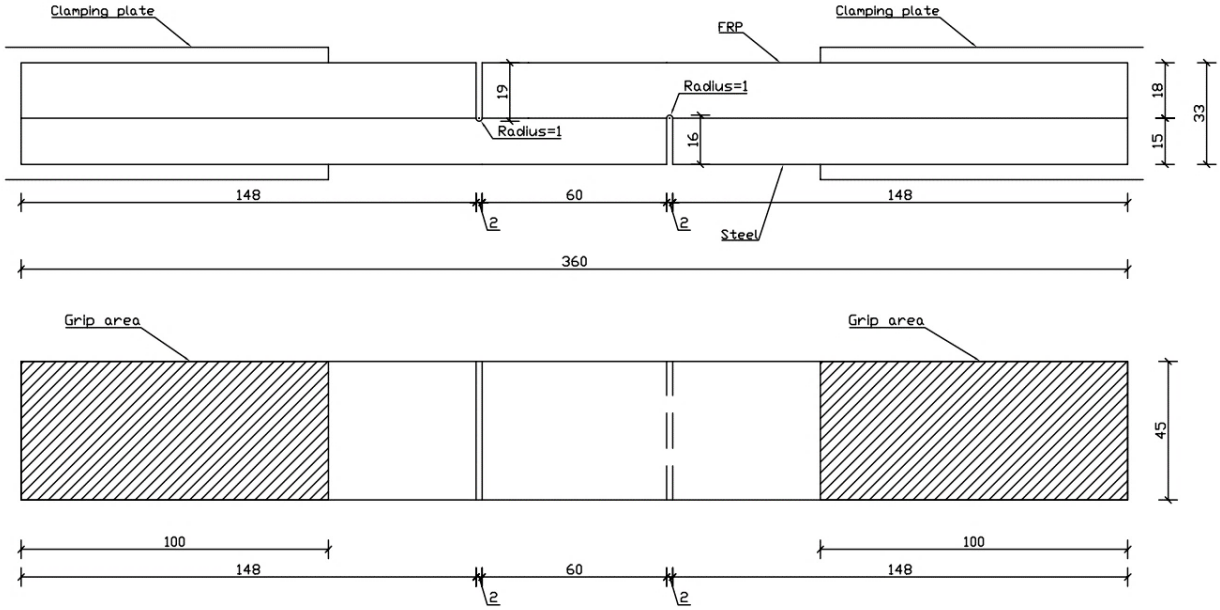

Figure 3.4: Thick-adherend shear test specimen with 60 mm overlap length; dimensions in [mm]

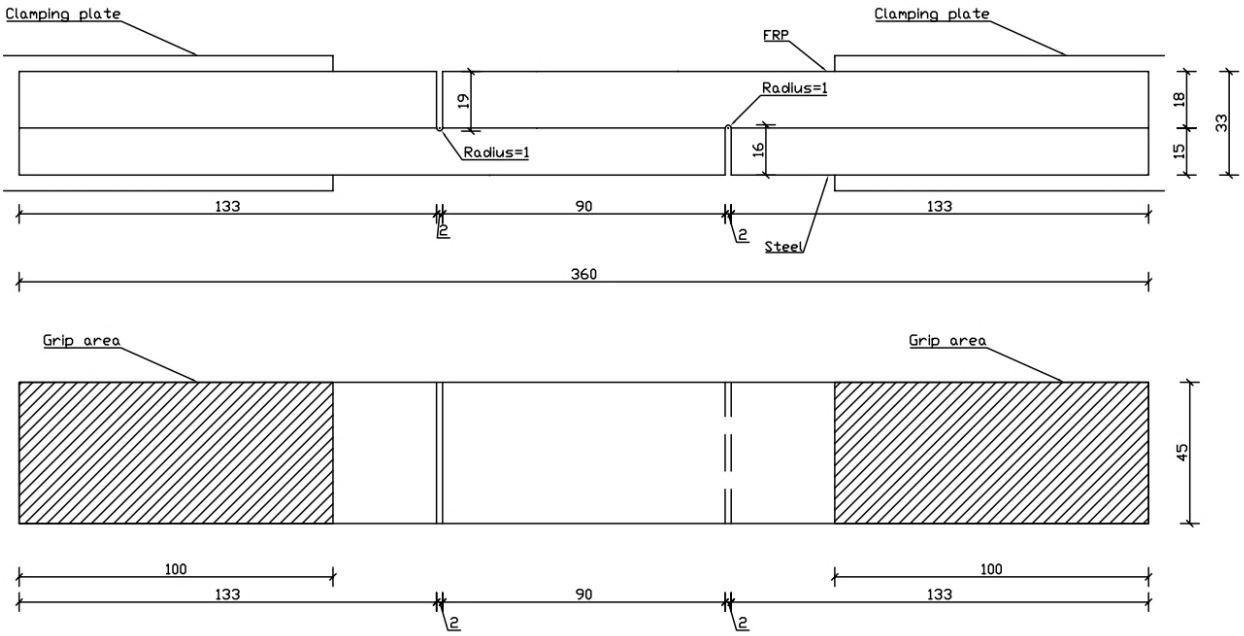

Figure 3.5: Thick-adherend shear test specimen with 90 mm overlap length; dimensions in [mm]

The tested specimens were cut by waterjet from a steel plate with adjacent CFRP on top. The notches were created by waterjet as well. The stiffness difference between the FRP and steel created notch imperfections during the water jetting process. This means that the notch geometry, including width, depth and notch head size, vary over the width of the samples. An example is provided in Figure 3.6, which displays the left and right notch zone of sample TAST 30-3. The image shows a larger penetration and notch head for the steel notch, which is the top notch in this frame, on the left side than the right side. Since the 2D-DIC results are only able to measure strains and crack propagation on one surface, there is a possibility that nonuniform failure and strains occur in the tests, without it being captured by the measuring technique.

(a) (b)

Figure 3.6: Notch zone sample TAST 30-3: (a) left side and (b) right side

In addition to notch geometry imperfections, the FRP itself contains material imperfections. During the vacuum infusion process, the FRP was not fully saturated and post-infusion was performed. Unfortunately, dry patches in several FRP strips were observed after cutting meaning that the laminate was still not fully saturated. The FRP-steel plate before and during post-infusion can be observed in Figure 3.7. Samples TAST 30-1, 60-3 and 90-3 showed the most severe dry patches, as displayed in Figure 3.8. The dry patches could result in a 10-20 percent stiffness reduction for the laminate, as stated by the manufacturer.

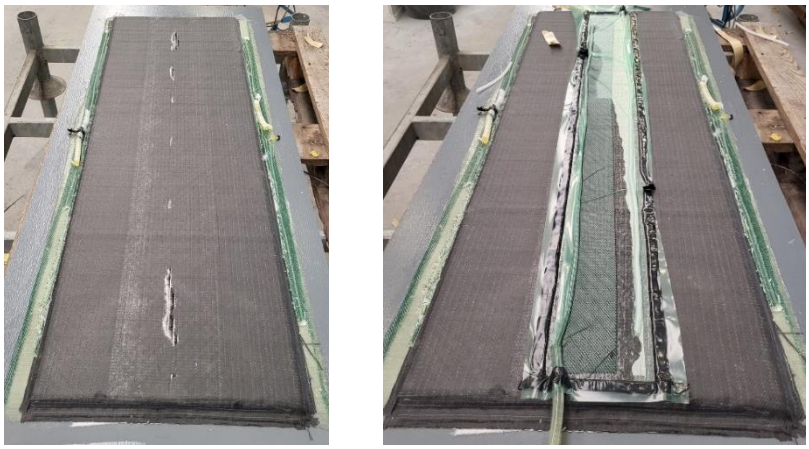

(a) **(b)**

Figure 3.7: FRP-steel plate (a) after vacuum infusion and (b) during post-infusion

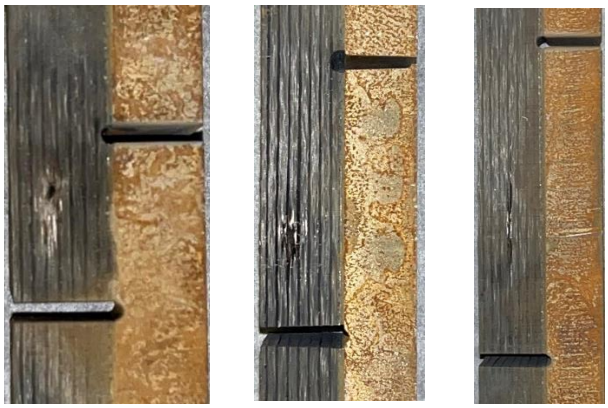

(a) **(b)** **(c)**

Figure 3.8: Dry patch on TAST samples (a) 30-1, (b) 60-3 and (c) 90-3

As described in section 2.2.2, this thesis primarily focuses on carbon fiber fabrics, meaning that the laminate consists mainly of carbon fiber plies. However, due to the potential for galvanic corrosion between the carbon and steel, one layer of GFRP is applied closest to the steel. As a result, the laminate consists of the following fiber fabrics:

- 600 gr/m^2 UD CFRP
- 600 gr/m^2 ±45° CFRP
- 1717 gr/m^2 quasi-isotropic (QI) 0/90/±45 GFRP [12].

The laminate lay-up is symmetric, apart from the first GFRP layer, and consists of 29 layers of CFRP and one layer of GFRP. The UD fabric is used to obtain plies in 0° and 90° direction. Stacking of unidirectional plies is limited to three plies, which results in the following laminate lay-up [QI(GFRP)/0_2/±45/0_3/90/0_3/±45/0_3/±45/0_3/±45/0_3/90/0_3/±45/0_2]. The 0° direction of the FRP is applied in the longitudinal direction of the samples. This lay-up results in the following composition:

- 75.9% UD 0°
- 6.9% UD 90°
- 17.2% ± 45°

Three series of tests with varying overlap lengths were performed, each consisting of 5 specimens. The tests are executed by use of a static tensile machine with a maximum capacity of 600 kN, displayed in Figure 3.9. The tests were displacement controlled and the static load was applied with 0.48 mm/min displacement rate. Relative displacement of the FRP-steel strip was recorded with 2-dimensional 'Digital Image Correlation' (DIC) on one surface of the specimens, as illustrated in Figure 3.10.

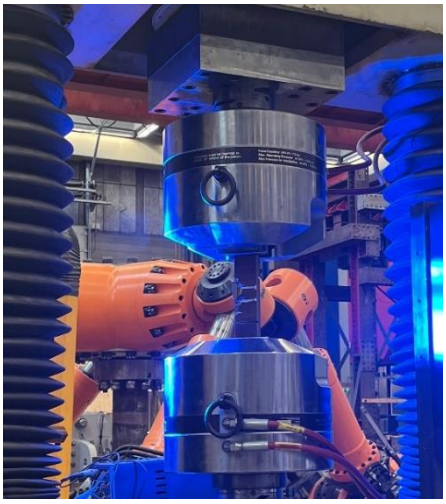

Figure 3.9: TASTs: testing set-up

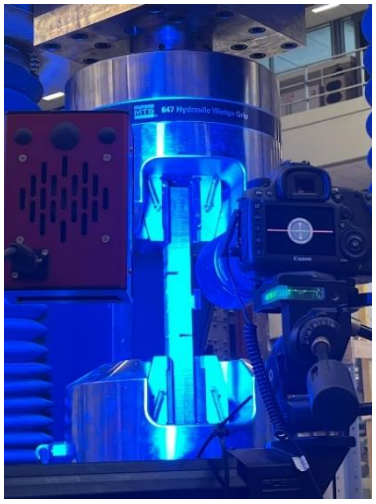

Figure 3.10: TASTs: surface that is measured by 2D DIC

3.2.2 Experimental Results

Table 3.1 displays observed failure pattern per tested specimen. The specimen number is an arbitrary value and not related to the testing order.

Table 3.1: Failure mechanisms of TASTs

Specimen number	Overlap 30 mm	Overlap 60 mm	Overlap 90 mm
Specimen 1	Primer-steel failure	Primer-steel failure combined with delamination of GFRP	Primer-steel failure
Specimen 2	Primer-steel failure	Primer-steel failure	Primer-steel failure combined with delamination of GFRP
Specimen 3	Primer-steel failure	Primer-steel failure combined with delamination of GFRP	Delamination of CFRP
Specimen 4	Delamination of CFRP	Primer-steel failure	Primer-steel failure
Specimen 5	*Removed from results*	Primer-steel failure combined with delamination of GFRP	Primer-steel failure

Observed failure mechanisms are shown in Figure 3.11 - Figure 3.16. Primer-steel failure and primer-steel failure combined with delamination of GFRP ply, is defined based on the observed steel surface area on which GFRP fibers are left after separation. When Figure 3.11 and Figure 3.13 are compared, there is a clear difference in the amount of glass fibers that is bonded to the steel surface. As the adherends are attached through vacuum infusion, the adhesive layer is relative thin. This leads to a complex identification of either adhesive or cohesive failure, as defined in section 2.3.3. The following failure mechanisms can be defined:

- For samples that are categorized as primer-steel failure, either cohesive or adhesive failure between the primer and steel can be defined. Displayed micrographs do not provide additional clarity.
- Figure 3.14 shows that primer-steel failure in combination with delamination of GFRP plies, is a combination of adhesive and adherend failure, as failure between the adhesive layer and steel and failure of the GFRP layer is observed.
- Delamination of CFRP can be defined as adherend failure.

It is important to note that nearly half of the specimens were not completely separated after removing the specimen from the tensile machine, and therefore were separated after the shear test by either gravity or manual force. This could influence the number of glass-fibers left on the steel surface after separation. This is the case for the following specimens: 60-1, 60-3, 60-5, 90-1, 90-2, 90-3 and 90-5.

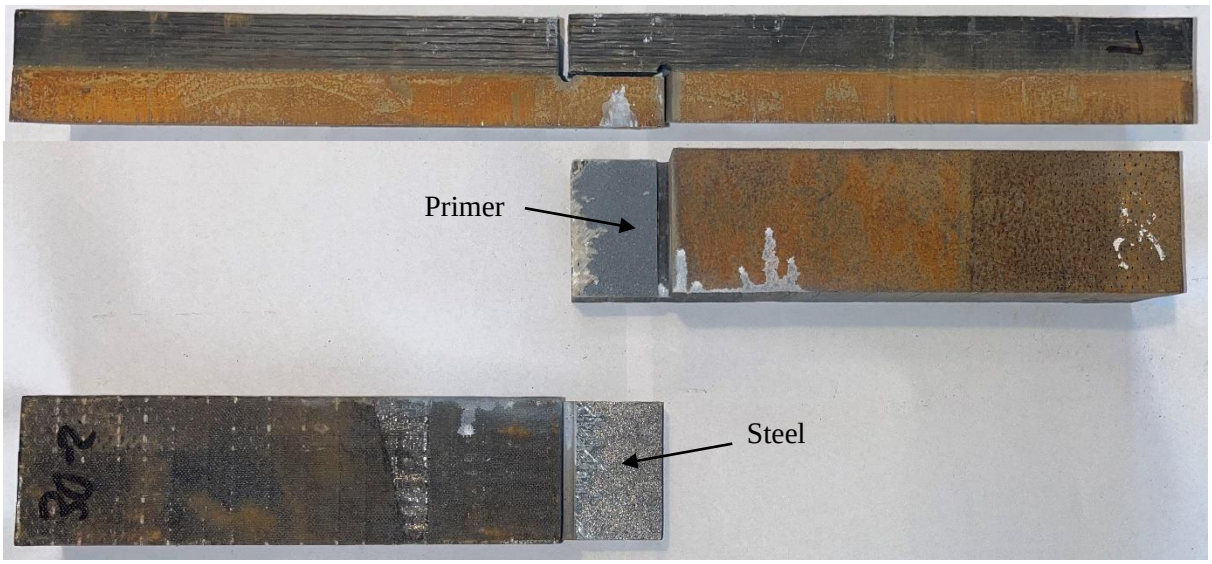

Figure 3.11: Primer-steel failure (TAST 30-2)

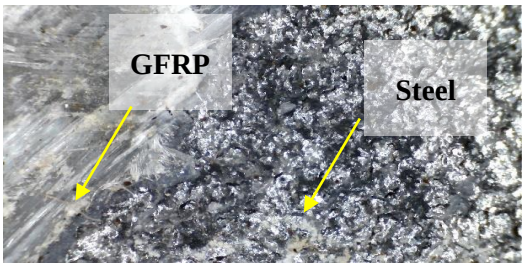

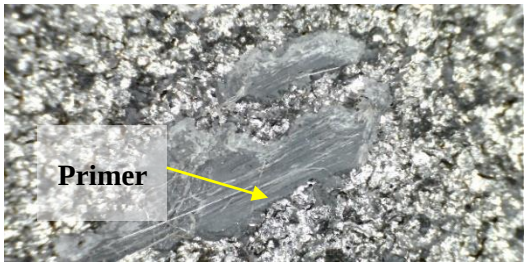

TAST 30-1 **TAST 60-2**

Figure 3.12: Micrographs of primer-steel failure

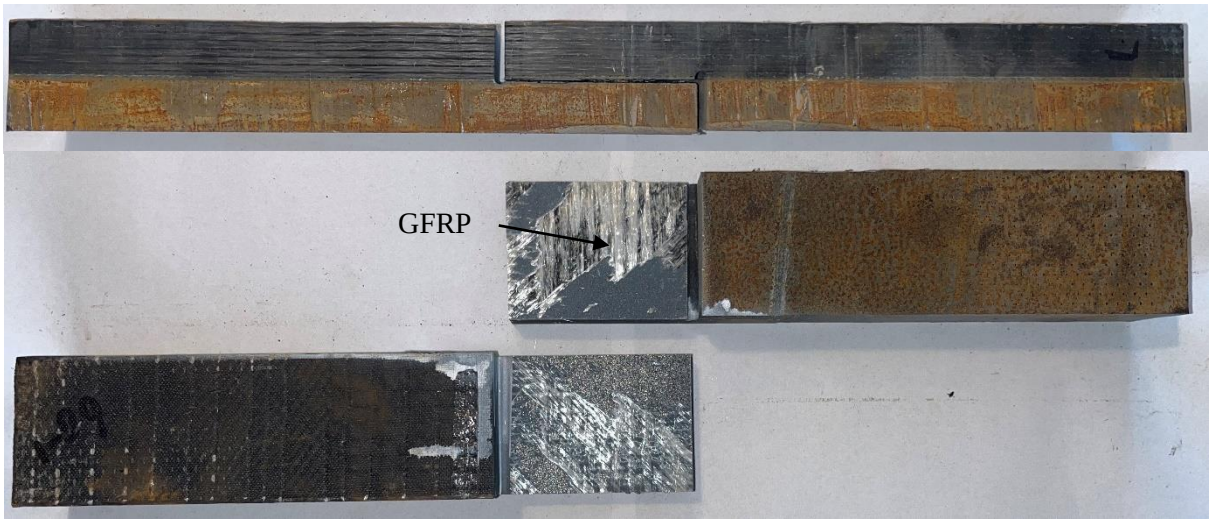

Figure 3.13: Primer-steel failure combined with delamination of GFRP layer (TAST 60-1)

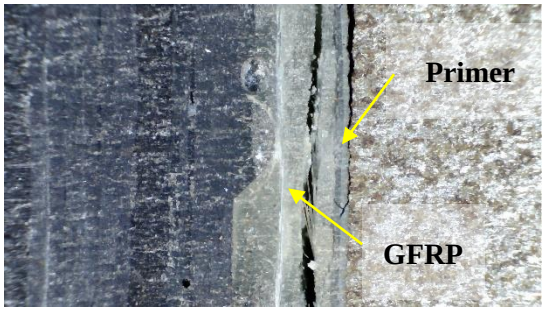

TAST 60-5 **TAST 60-3**

Figure 3.14: Micrographs of primer-steel failure combined with delamination of GFRP

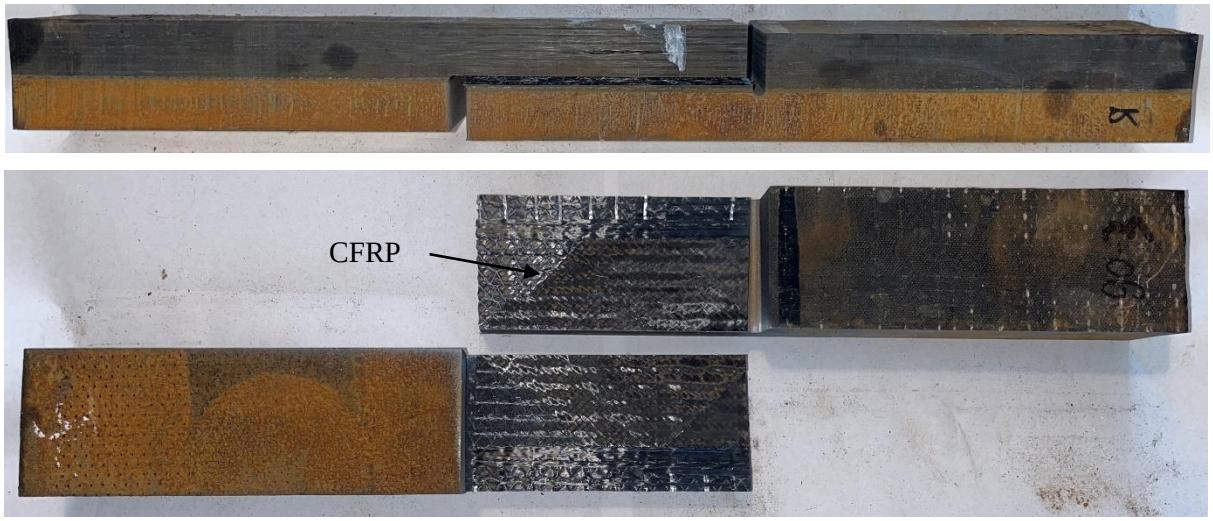

Figure 3.15: Delamination of CFRP (TAST 90-3)

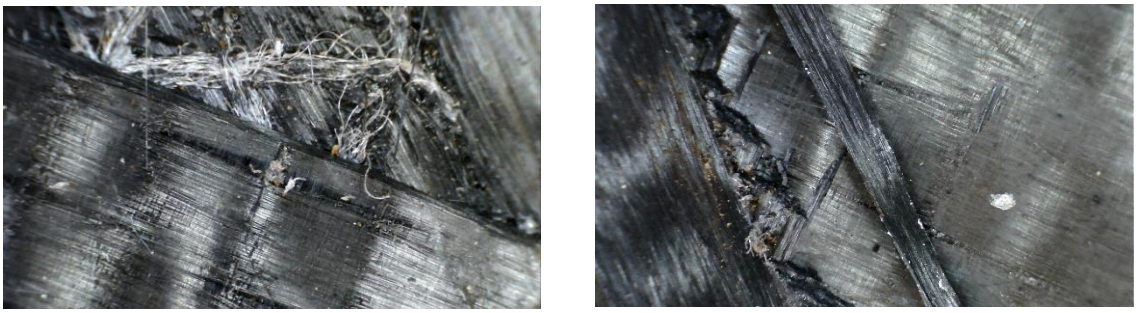

TAST 90-3 **TAST 90-3**

Figure 3.16: Micrographs of delamination of CFRP

Twelve out of fifteen samples suffered failure primer-steel failure with or without additional delamination of GFRP. The following three samples are identified as distinct:

- **TAST 30-4**: The specimen showed delamination of CFRP as the governing failure mechanism. This can be explained by the application of the notch, which is not sawn completely through the CFRP, as shown in Figure 3.17. As a result of this, the CFRP strip is placed in shear as opposed to the bonded FRP-steel joint, resulting in a different loading condition and therefore failure mode.

Figure 3.17: Failure behaviour of TAST 30-4

- **TAST 30-5**: This specimen was first tested and initially loaded by a loading rate of 0.96 mm/min, followed by a loading decrease to 0.48 mm/min during testing. This resulted in a relatively quick failure that occurred at a very low ultimate load. For this reason, the results for this specimen are removed.

- **TAST 90-3:** This sample showed more severe dry patches than the other samples with a 90 mm overlap length, as displayed in Figure 3.8. In combination with imperfections in the notch head size and penetration, this could explain why this sample suffered delamination of CFRP.

During testing, it was observed that all specimens were subjected to sudden failure. Failure is defined by the load drop to 0 kN, after reaching the ultimate load. Therefore, this ultimate load will be defined as the failure load of the experiments, displayed in Table 3.2.

Table 3.2: Failure load for TAST specimens in kN

Specimen number	Overlap 30 mm	Overlap 60 mm	Overlap 90 mm
Specimen 1	31	44	46
Specimen 2	28	40	58
Specimen 3	30	46	51
Specimen 4	21	42	43
Specimen 5	-	44	56

Obtained 2D-DIC results were used to further study local displacements, strains and failure propagation inside the zone of interest. To obtain this data, relative displacements, also known as digital extensometers, were derived from inside the zone of interest. To determine the best position to measure relative displacement, the data is extracted for several distances at different positions on the monitored surface of the sample, which are displayed in Figure 3.18. Their corresponding time-displacement curves for sample 30-1 can be observed in Figure 3.19. From this analysis, the conclusion can be drawn that the approach with a horizontal distance in between the notches provides the most accurate results. That is because this distance is not influenced by the exact positioning of the distance on the occurring fracture, which is the case for the vertical distances, and captures the rotation of the specimens in between the notches. For this reason, the digital extensometers are derived with the horizontal distance in between the notches.

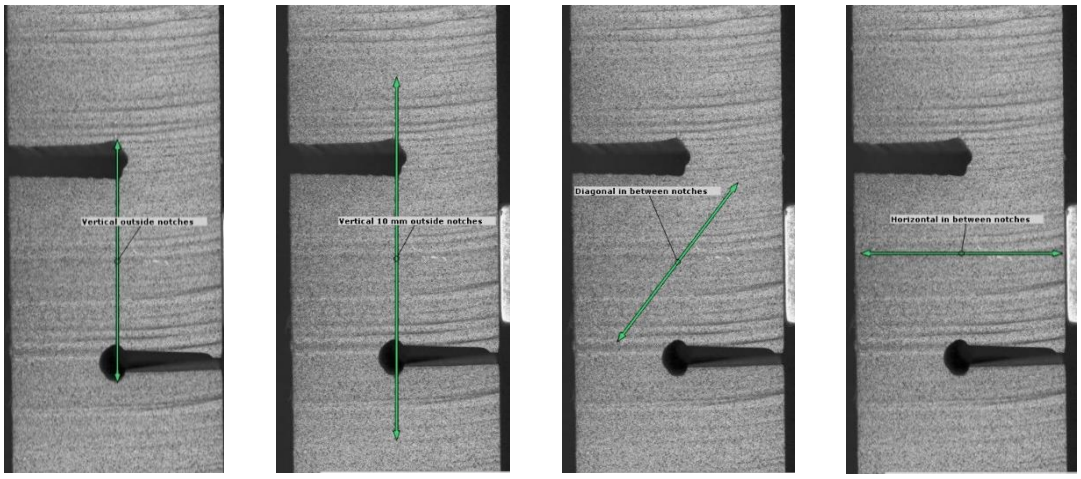

Figure 3.18: DIC digital extensometers

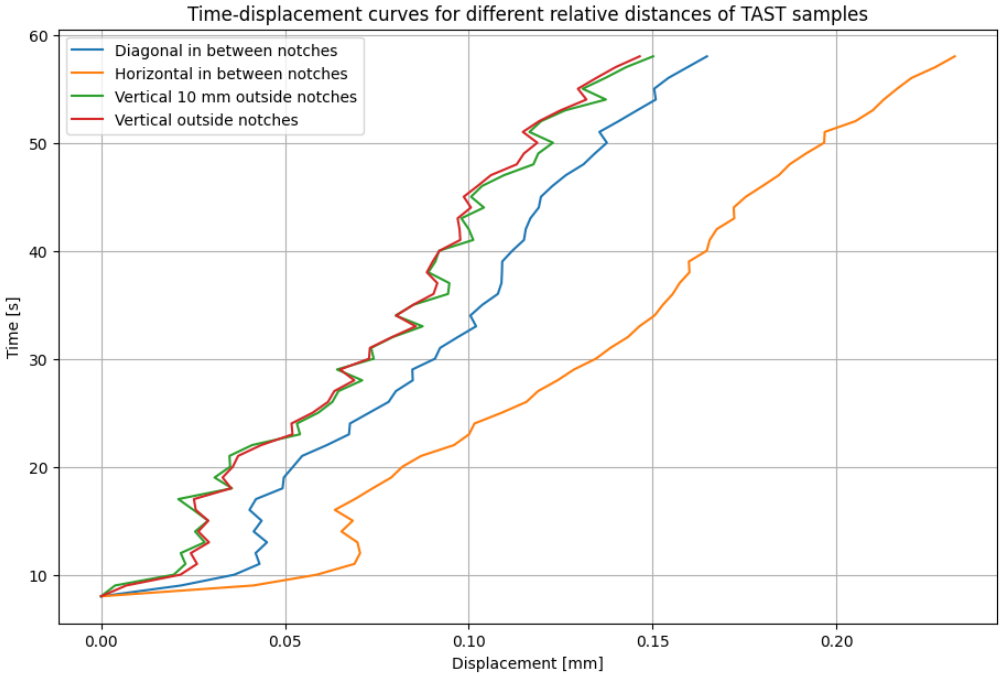

Figure 3.19: Time-displacement curves for different relative distances of TAST 30-2

Relative load-displacement curves, based on the load results from the jack of the test machine and the relative displacements determined from 2D-DIC data, are displayed in Figure 3.20 - Figure 3.22.

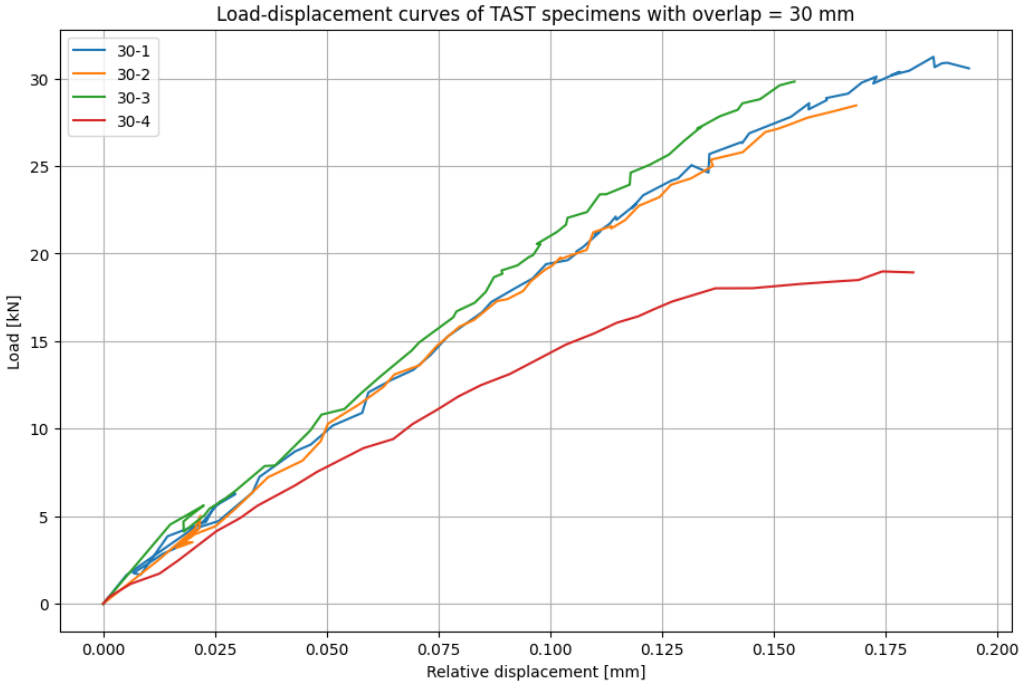

Figure 3.20: Relative load-displacement curves of TAST with overlap length 30 mm

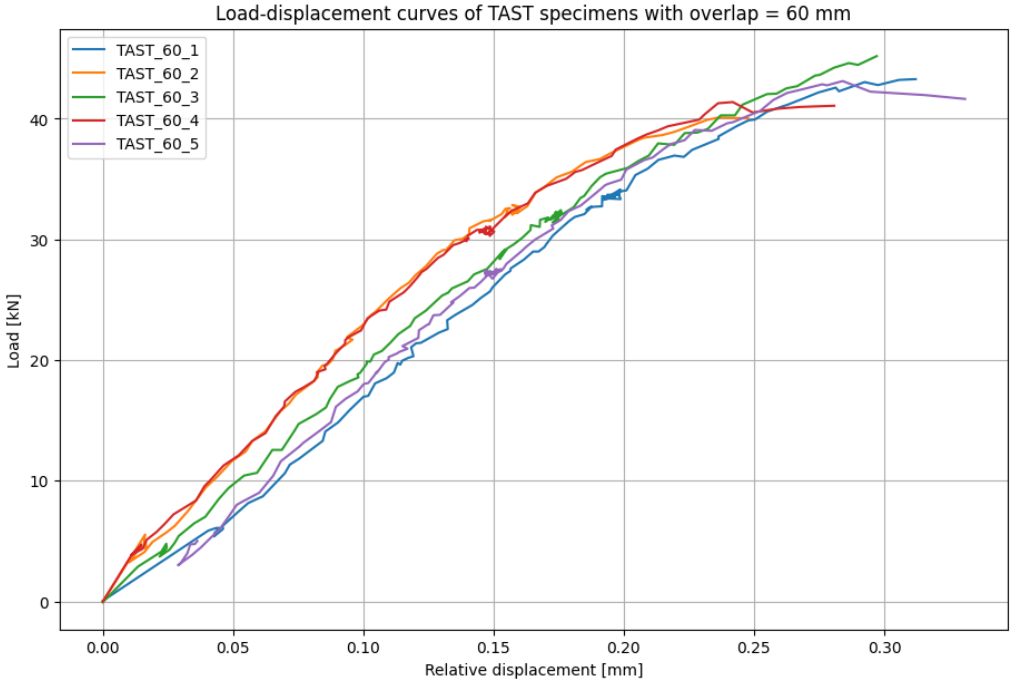

Figure 3.21: Relative load-displacement curves of TAST with overlap length 60 mm

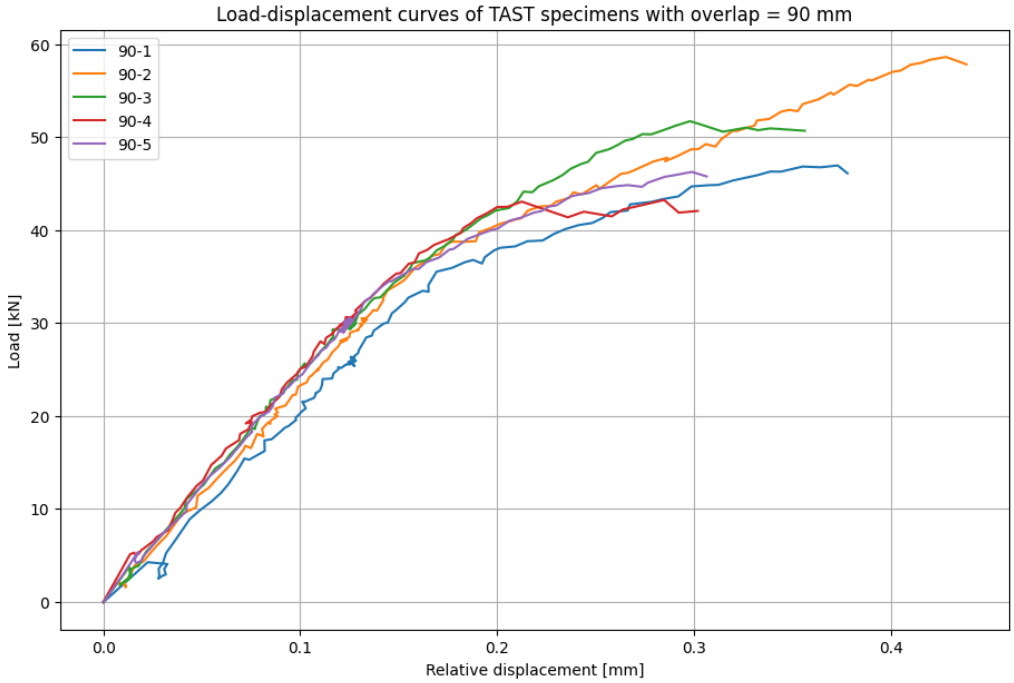

Figure 3.22: Relative load-displacement curves of TAST with overlap length 90 mm

Based on the load-displacement curves displayed in Figure 3.20 - Figure 3.22, the following observations and conclusions can be formulated:

- Specimens with 30 mm overlap length show linear behaviour;
- Specimen TAST 30-4 fails at a load level of 19 kN while the mean failure load level of specimens 30-1, 30-2 and 30-3 is 29 kN. This difference is caused by the notch penetration depth imperfection for sample 30-4, as displayed in Figure 3.17.

- The test series with a 60 mm overlap length displays linear behaviour. Samples 60-4 and 60-5 display a slight platform just before failure where relative displacement increases and the load does not increase further. This behaviour can be explained by crack initiation around the lower notch which resulted in a reduced stiffness of the sample, as displayed in Appendix 0.
- Samples 60-1, 60-3 and 60-5 show a very similar stiffness while the stiffness of samples 60-2 and 60-4 is slightly higher, with a difference of approximately 15 percent between samples 60-2 and 60-5. Unfortunately, this behaviour could not be explained by specimen imperfections or dimensions and deviating behaviour observed from the DIC results.
- Specimens in the test series with an overlap length of 90 mm show bi-linear behaviour where a stiffness decrease can be observed around 37 kN. This behaviour can be explained by crack propagation in the steel-FRP interface, observed at the upper notch, and in the FRP itself, observed at the lower notch, which became clear from the DIC data. Examples of this crack initiation are displayed in Figure 3.23.
- Specimen 90-2 displayed a much higher failure load than other samples in that series. This difference is caused by the notch penetration depth imperfection for specimen 90-2, as described in section 3.2.1. The conclusion can be drawn that subjecting the GFRP ply to shear load, as opposed to the adhesive bond, resulted in a higher failure load.

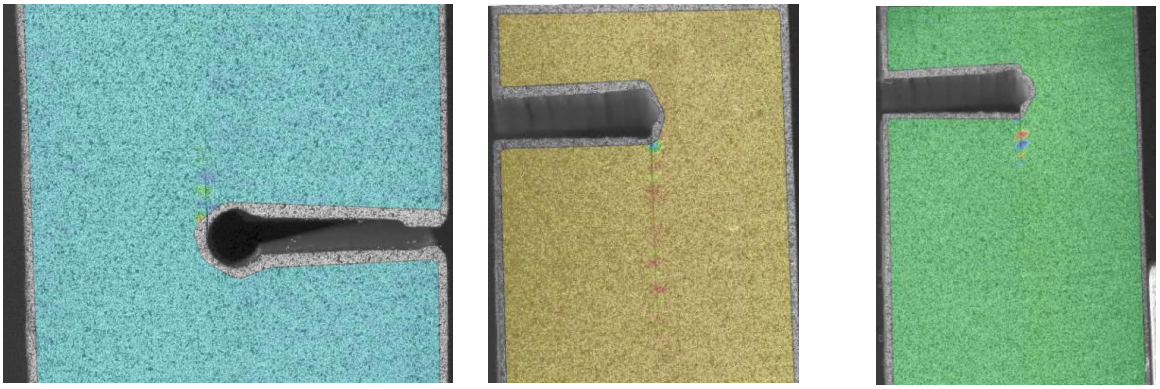

TAST 90-2 at F = 43.5 kN **TAST 90-5 at F = 41.4 kN** **TAST 90-5 at F = 43.6 kN**

Figure 3.23: Crack initiation in TAST samples

The combined results for all three test series, displayed by mean load-displacement curves and standard deviation per test series, can be observed in Figure 3.24. Results of samples 30-4 and 90-2 were excluded from these load-displacement curves since their notch geometry leads to outlying results. Corresponding failure loads and determined stiffnesses are displayed in Table 3.3. An important remark is that the provided stiffness is determined based on the linear phase for all three test series, excluding the bi-linear and non-linear behaviour for series with 60 and 90 mm overlap length.

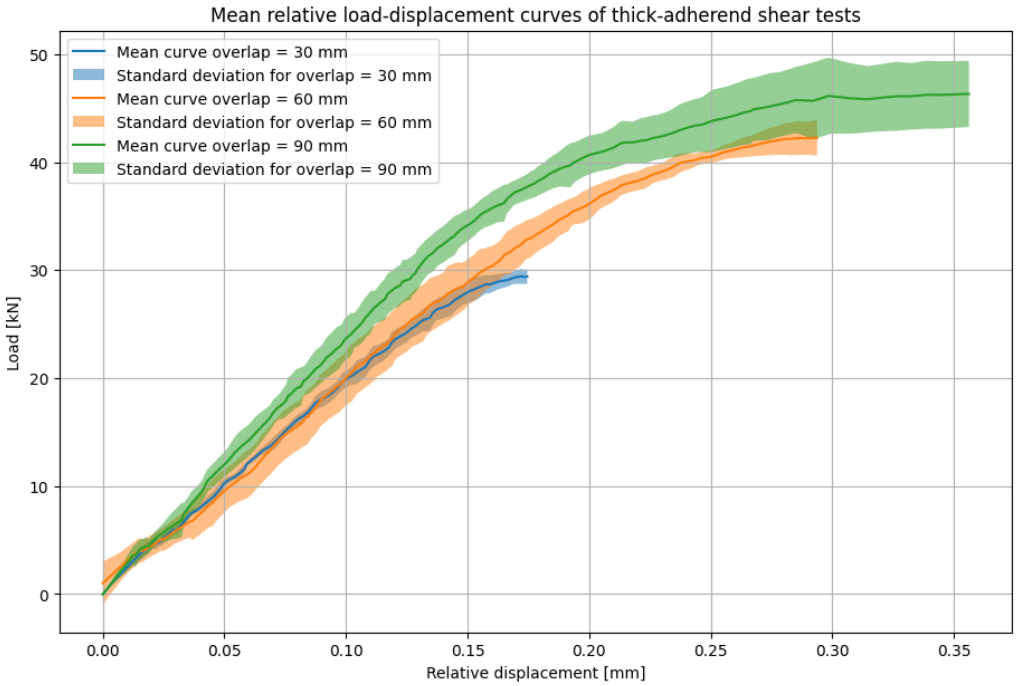

Figure 3.24: Mean relative load-displacement curves of TAST

Table 3.3: Mean failure load and stiffness for TAST series

Property	**30 mm overlap**	**60 mm overlap**	**90 mm overlap**
Mean failure load [kN]	29.0	42.3	46.3
Stiffness [N/mm]	$2.1 * 10^5$	$1.8 * 10^5$	$2.3 * 10^5$

The mean load-displacement curves show that the difference in failure load between test series with 30 mm and 60 mm overlap length is much larger than the difference between test series with 60 mm and 90 mm overlap length. This difference can be explained by the crack propagation for test series with 90 mm overlap, since that leads to a stiffness decrease and therefore to a lower ultimate failure load for these specimens.

Section 3.2.1 identified dry patches in the FRP. For this reason, experimental results of samples with and without visible dry patches were compared and are displayed in Figure 3.25. Table 3.4 highlights that for specimens with overlap lengths 30 and 60 mm, visible dry patches reduce stiffness by 7.2 and 14.9 percent, respectively. However, the samples with 90 mm overlap length show similar stiffness. This is likely a result of the less severe dry patches of sample 90-3 compared to TAST 30-1 and 60-3, as can be observed in Figure 3.8.

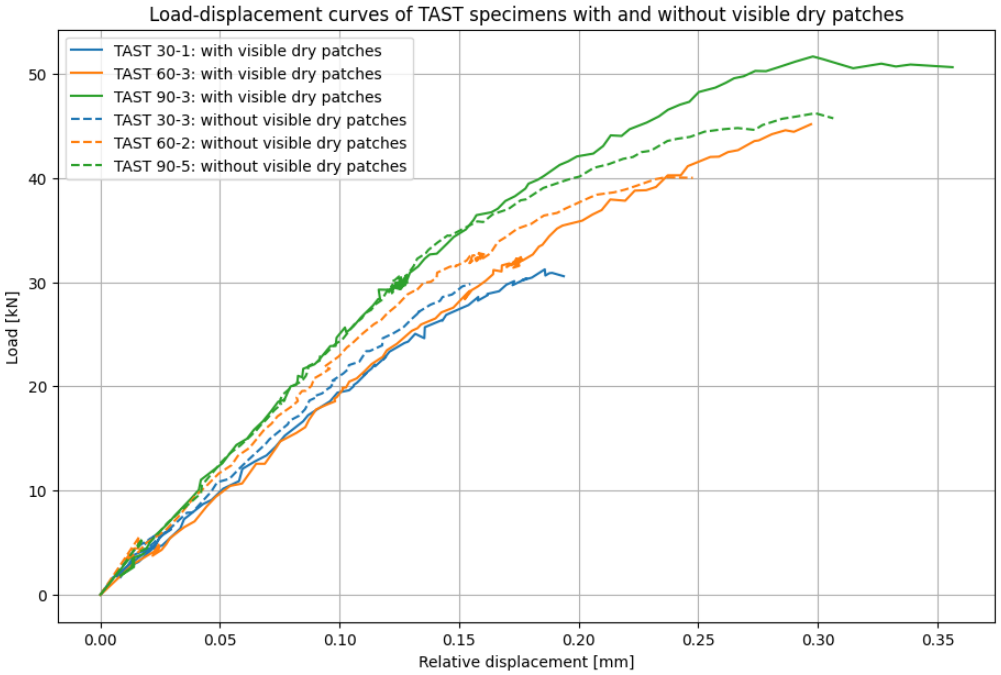

Figure 3.25: Relative load-displacement curves of TASTs with and without visible dry patches

Table 3.4: Difference in global stiffness for TAST samples with and without visible dry patches

Overlap length [mm]	Deviation from sample without visible dry patches
30	- 7.2 %
60	- 14.9 %
90	+ 2.6 %

3.3 Finite Element Modelling of Adhesive Joints in LS-DYNA

This section of the report provides an overview and implementation of two modelling techniques to simulate the adhesive bond, including tied and tie-break contact definitions. A sensitivity analysis was performed to evaluate the performance of the modelling approaches.

3.3.1 Tied Interface Condition

In LS-DYNA, tied contacts can be applied for nodes-to-surface, shell-edge-to-surface, shell-edge-to-solid and surface-to-surface and always include a node-segment pair in which the node is a single point or the node on a surface and the segment is a three- or four-noded surface referencing either a shell element or one of the faces of a solid element. In this principle, the node is generally named as ‘slave’ and the segment as ‘master’, as can be observed in Figure 3.26. Between the slave and master, both tensile and compressive forces are transmitted, resulting in a ‘tied’ contact. Separation of slave and master is resisted by a non-physical linear contact spring. A tied contact definition behaves similarly to merged nodes, where neighbouring solids share the same nodes, and is constraint based [40].

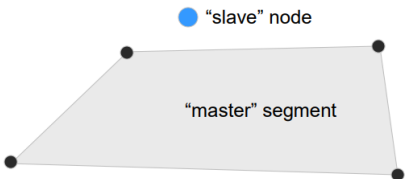

Figure 3.26: Principle of contact treatment in LS-DYNA [39]

3.3.2 Tie-break Interface Condition

In LS-DYNA, there are fourteen options for definition of the failure criterion of the adhesive interface. Input parameters for all options are normal and shear failure stress, NFLS and SFLS, respectively with additional input parameters depending on the failure criterion definition. In this study, the following four built-in tie-break failure criterions were researched and applied:

- **Option 4** – Tie-break is active for nodes which are initially in contact but tangential motion with frictional sliding is permitted. The tie-break failure criterion is defined as

$$\frac{|\sigma_n|}{NFLS} \geq 1. \qquad \text{(Eq. 3.1)}$$

  where σ_n is the peel stress capacity of the interface [45].

- **Option 6** – Tie-break is active for nodes which are initially in contact. Failure stress is required for tie-break to occur. After this criterion is met, damage propagation behaves according to a linear function of the distance between points that are initially in contact. When the critical distance between points is reached, damage is fully developed, and interface failure occurs. The tie-break failure criterion is defined as

$$\left(\frac{|\sigma_n|}{NFLS}\right)^2 + \left(\frac{|\sigma_s|}{SFLS}\right)^2 \geq 1. \qquad \text{(Eq. 3.2)}$$

- **Option 7** – Dycoss Discrete Crack Model, as described in reference [46]. This model implements a softening relationship between stresses and strains to define interface failure. In its application, three states can be identified, which are the elastic or uncracked state, the crack development state and crack open state. The softening relationship and corresponding states are displayed in Figure 3.27, where F_I is the ultimate load for mode I behaviour, G_{IC} is the energy release rate for mode I, A is the crack area represented by the element and $u_{I,ini}$ and $u_{I,ult}$ are the displacements at the end of the uncracked state and crack development state respectively [45, 46].

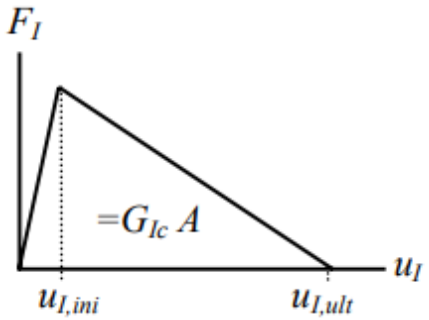

Figure 3.27: Softening behaviour for mode I crack opening in Dycoss Discrete Crack model [46]

This modelling approach allows for a mixed-mode behaviour, as displayed in Figure 3.28.

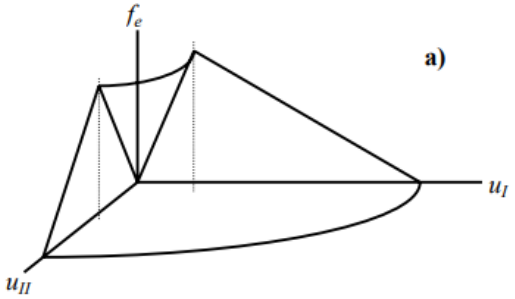

Figure 3.28: 3D representation of softening model in Dycoss Discrete Crack model [46]

For this interface definition, the criterion for crack initiation is defined as

$$\left[\frac{\max(\sigma_n,0)}{NFLS}\right]^2 + \left[\frac{\sigma_s}{SFLS-\sin(PARAM)\min(0,\sigma_n)}\right]^2 = 1 \qquad \text{(Eq. 3.3)}$$

where PARAM is defined as the friction angle [45].

- **Option 9** – Discrete Crack Model with power law and B-K damage models. This tie-break contact definition is based on Material Type 138 in LS-DYNA, which is the material model used to apply solid cohesive elements [45] .

3.3.3 Sensitivity Study for Preliminary TAST Geometry

A sensitivity study was performed to assess the performance of defined modelling approaches for adhesive interfaces. A preliminary FE model of the TASTs was constructed with 3D element formulation and the same boundary and loading conditions as the FE model of the TASTs. The model is displayed in Figure 3.29. As the mesh size and loading rate sensitivity study were performed in parallel with adhesive interface sensitivity study, the mesh size and loading rates of the FE models results show variations.

In the sensitivity study of the four tie-break options, the following parameters were varied:

- Shear failure stress: 24 – 48 MPa
- Normal failure stress: 50 – 100 MPa
- Critical distance parameter: 0.01 – 0.1 mm

Results of the most promising contact definitions for tie-break contacts are displayed in the form of load-displacement curves in Figure 3.30. Corresponding input parameters of the adhesive interface are displayed in Table 3.5 and Table 3.6. Notably, the global stiffness between the two load-displacement curves is different. This is caused by the mesh size difference, as the mesh size is 1.2 mm for model 14.2 and 2 mm for model 11.1.

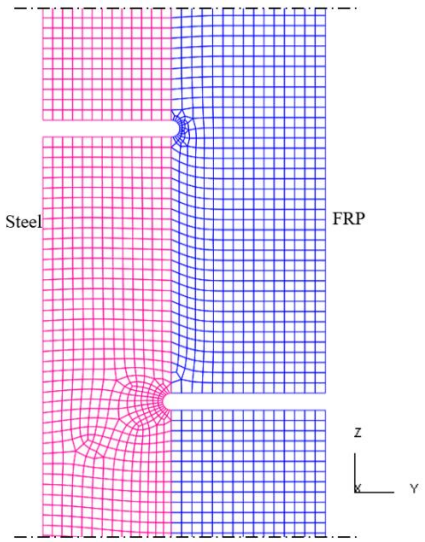

Figure 3.29: Geometry of preliminary adhesive interface sensitivity study

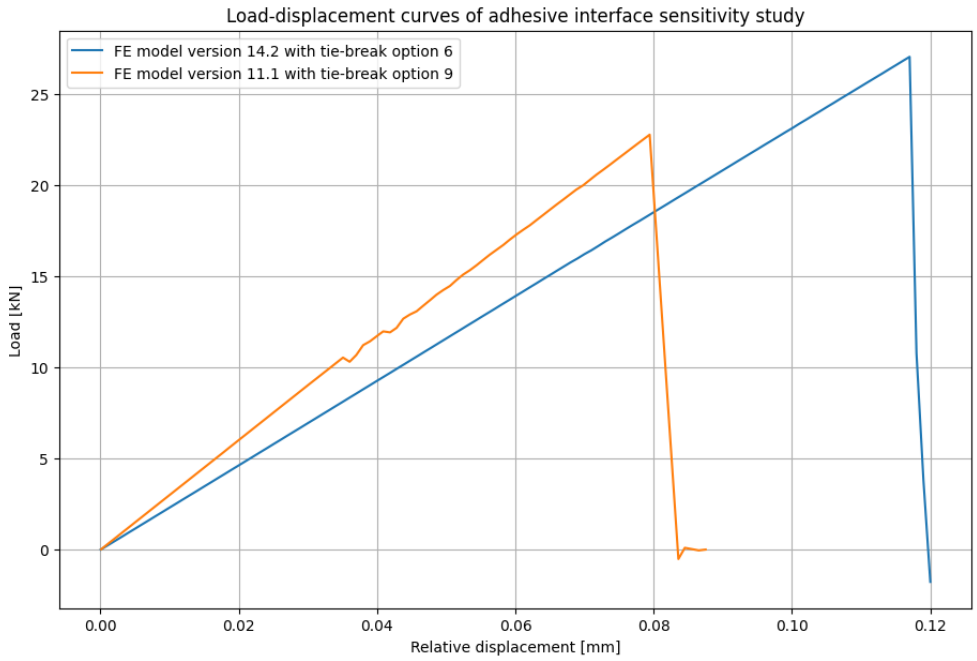

Figure 3.30: Load-displacement curve of model versions 11.1 and 14.2

Table 3.5: Tie-break contact properties of option 6 for model version 14.2

Parameter	Symbol	Value [Unit]	Reference
Static friction coefficient	FS	0.2 [-]	According to [47]
Dynamic friction coefficient	FD	0.2 [-]	According to [47]
Normal failure stress	NFLS	100 [MPa]	Arbitrary value since initial assumption was that peel stresses were negligible
Shear failure stress	SFLS	48 [MPa]	Initial value determined from experimental results, assuming adhesive joint is only subjected to shear load
Critical failure distance	PARAM	0.01 [mm]	Initial arbitraty trial value that influences slope of linear failure propagation

Table 3.6: Tie-break contact properties of option 9 for model version 11.1

Parameter	**Symbol**	**Value [Unit]**	**Reference**
Static friction coefficient	FS	0.2 [-]	According to [47]
Dynamic friction coefficient	FD	0.2 [-]	According to [47]
Normal failure stress	NFLS	70 [MPa]	According to [48]
Shear failure stress	SFLS	112 [MPa]	According to [48]
Exponent in damage model. Exponent < 0 activates B-K damage and an exponent > 0 activates power law.	PARAM	1 [-]	According to [49]
Normal energy rate	ERATEN	0.38 [N/mm]	According to [50]
Shear energy rate	ERATES	0.68 [N/mm]	According to [50]
Tangential / normal stiffness ration	CT2CN	1	Default value
Stiffness	CN	10^6 [MPa]	According to [48]

From this sensitivity analysis, the following conclusions were formed with respect to modelling of the adhesive interface:

- As option 4, does not include the shear behaviour and shear stress in the failure criterion, this tiebreak contact definition is not able to resemble an adhesive interface subjected to shear and peel loading. For this reason, this option was not considered in the final FE model.
- Option 7 and option 9 use a softening relationship that could be to take ductile properties of the adhesive into account. However, as these options result in an increased complexity and number of input parameters, they are more difficult to implement. Despite showing similar global behaviour to option 6, variations led to unrealistic results and failed analysis. This is likely due to uncertainties in adhesive properties, as they were derived from references and not from classic fracture mechanics tests. To avoid unreliable modelling approaches with a high level of complexity, option 7 and 9 were not implemented in the final FE model.
- Option 6 provides the best results considering the load-displacement curves and characteristics of this option. The inclusion of both shear and normal stress in the failure criterion leads to a sufficient approach to model failure progression of the adhesive interface as sudden failure is observed. However, this tie-break approach does not allow modelling of the bi-linear behaviour observed for higher overlaps. Despite this, this modelling technique provides the best approach of all options that were considered in this study, excluding option that were not analysed. In conclusion, tie-break contacts according to option 6 will be applied in the FE model.

3.4 Finite Element Model of Thick-adherend Shear Tests

This section of the report provides an overview of the set-up of the FE models of the TASTs. This includes presenting the geometry and boundary conditions with corresponding mesh sensitivity study. In addition, material models and modelling approaches for the adhesive interface are provided. To conclude, the FE type and analysis are presented.

3.4.1 Geometry and Boundary Conditions

FE models were developed in LS-DYNA R.12 for all three series with varying overlap lengths. To reduce the number of elements, the grip area is not modelled, as it assumed to be perfectly gripped. The notch is modelled as a gap with a rectangular penetration. A symmetry boundary condition is applied in the YZ-face to reduce the number of elements. A fixed boundary condition is defined for the bottom surface of the sample, while a prescribed displacement in z-direction is applied to the top surface. The prescribed displacement is velocity controlled, with a maximum displacement of 0.22 mm, based on an increasing loading rate to 0.1 mm/s. A sensitivity study was performed to determine the loading rate. This study included a trade-off between accuracy of results, in the form of load-displacement curves, the required maximum displacement and total runtime of analysis. The FE models of the TASTs are displayed in Figure 3.31. Degrees of freedom that are not shown in this figure are considered as 'free' in the FE models.

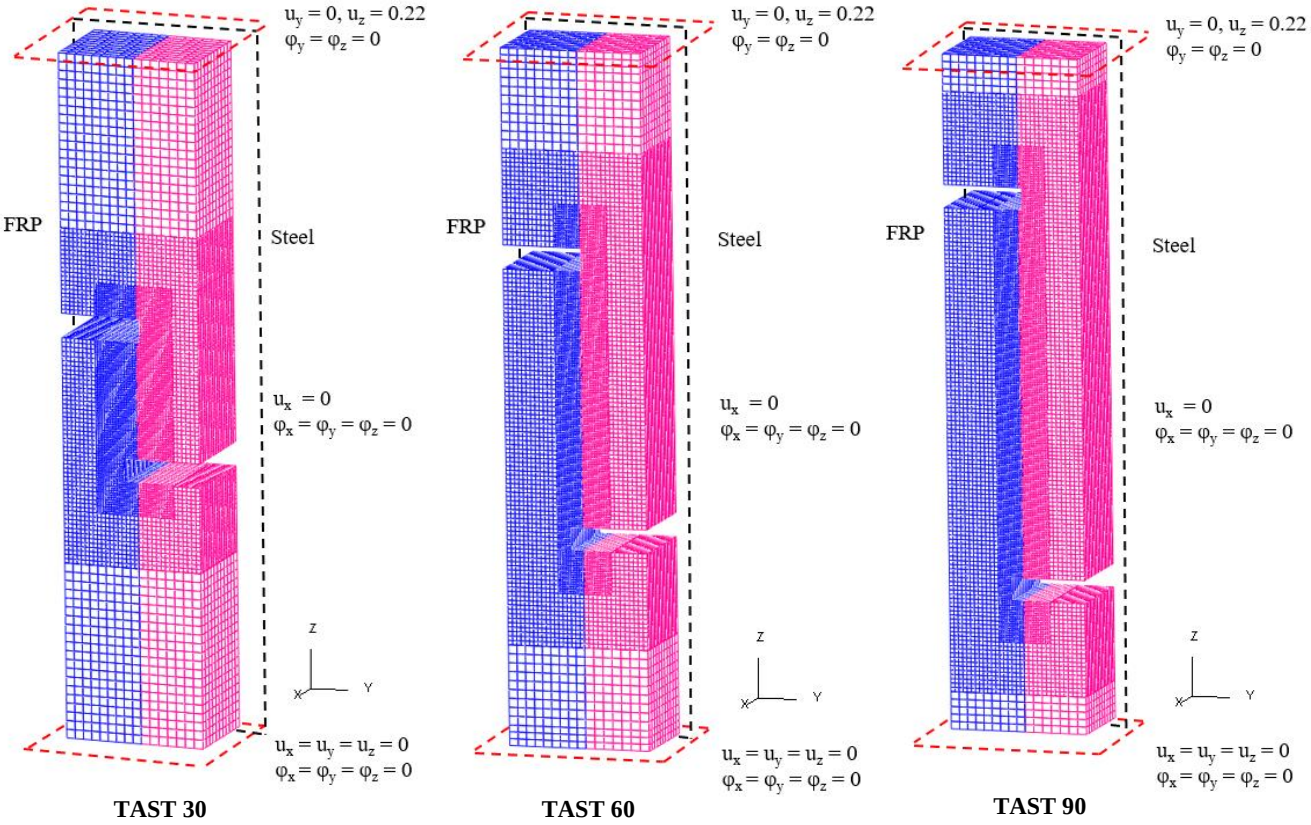

Figure 3.31: Geometry and boundary conditions of 3D FE models of TASTs

3.4.2 Finite Element Type

Eight-noded hexahedron linear solid elements were used for the FRP and steel. Full-integration elements were used for the FRP part and reduced-integration elements were used for the steel part. While crack propagation in the FRP strip was observed during the TASTs, the failure mode of the specimens was related to the adhesive interface. Therefore, the FRP was assumed to behave according to a linear-elastic material model to simplify the FE model. For this reason, linear-elastic material models were applied to both the FRP and steel part. An overview of the FE types is displayed in Table 3.7.

Table 3.7: Overview of FE types in TAST model

Part	Element type	DOF's per node	Interpolation	Stress components	Integration	Hourglass control
Steel	Eight-noded hexahdron solid element	u_x, u_y and u_z	Linear	σ_{xx}, σ_{yy}, σ_{zz}, σ_{xy}, σ_{xz}, σ_{yz}	Reduced	Yes, Belytschko-Bindeman
FRP laminate	Eight-noded hexahdron solid element	u_x, u_y and u_z	Linear	σ_{xx}, σ_{yy}, σ_{zz}, σ_{xy}, σ_{xz}, σ_{yz}	Full	Yes, Belytschko-Bindeman

3.4.3 Material Models

The steel strip is modelled by an isotropic elastic material. Corresponding material properties are displayed in Table 3.8.

Table 3.8: Linear-elastic material properties of steel

Material name	Elastic Modulus [GPa]	Poisson's ratio [-]	Mass density [kg/m^3]
Steel	210	0.3	7859

As described in section 3.2.1, the laminate consists of 29 layers of CFRP and one layer of GFRP, applied closest to the steel. The following lay-up was applied [QI(GFRP)/0_2/±45/0_3/90/0_3/ ±45/0_3/±45/0_3/±45/0_3/90/0_3/±45/0_2]. Since no material failure of the FRP strip was observed during testing, the modelling approach of the composite was simplified to solid elements with homogenized material properties, using an orthotropic elastic material model to take the orthotropic properties of FRP into account. Classic laminate theory was applied, by use of the Classic Laminate Tool [51], to calculate the homogenized properties of the laminate using the elastic material properties of the UD and ±45 plies provided by the manufacturer, displayed in Table 3.9. Test methods ASTM D 3039 and ASTM D 790 have been performed by the manufacturer to ensure these properties. Since there is only one GFRP ply, this was not included in the calculation [51–53].

Table 3.9: Material properties of UD and ±45 CFRP plies

Material name	Elastic moduli [GPa]	Poisson's ratio [-]	Mass density [kg/m^3]
UD CFRP ply	E_1 = 144, E_2 = 8.6, G_{12} = G_{13} = G_{23} = 4.05 [53]	ν_{12} = 0.21 [52, 53]	1520 [52]
±45 CFRP ply	E_1 = E_2 = 14.34, G_{12} = 30.27, G_{13} = G_{23} = 4.05 [52, 53]	ν_{12} = 0.77 [52]	1520 [52]

With these ply properties, the homogenized properties of the composite were determined, displayed in Table 3.10.

Table 3.10: Material properties of CFRP laminate

Material name	Elastic moduli [GPa]	Poisson's ratio [-]	Mass density [kg/m^3]
CFRP laminate with 75.9% 0° UD plies, 6.9% 90° UD plies and 17.2% ±45 plies	$E_1 = 100$, $E_2 = 20$, $E_3 = 6.9$, $G_{12} = 9.2$, $G_{13} = G_{23} = 4.4$ [51]	$\nu_{12} = \nu_{13} = \nu_{23} = 0.34$ [51]	877.88

3.4.4 Mesh Sensitivity Study

A mesh sensitivity study was performed to see with which the FE models reach convergence. The study was partially performed on 2D models to reduce the number of elements, since the large number of solid elements in 3D models could exceed the memory limit of the solver for a mesh size that is too small. The geometry and boundary conditions of the 2D models are displayed in Figure 3.32. In these models, shell elements in the YZ face with a thickness of 45 mm are used.

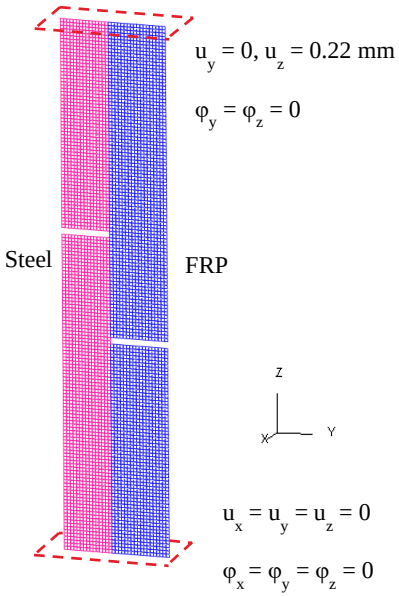

Figure 3.32: Geometry and boundary conditions of 2D FE model of TAST with overlap length of 30 mm

The meshed surfaces were built in 2D in the YZ face and subsequently extruded to create 3D elements. Since this method makes it difficult to include smooth transitions between different mesh densities in x-direction, the transition between mesh densities is employed by tied segment-to-segment contact definition, where a segment is a 2D element on one face of the 3D solids, as described in section 3.4.5. A study was performed to ensure that stresses were distributed correctly from finer to coarser mesh.

The 2D mesh sensitivity study was performed for mesh sizes varying from 2 to 0.25 mm, where the mesh size is divided by factor two for every iteration. In these models, the full geometry was constructed with this mesh size, so no mesh size deviations are used within one model. The load-displacement curves can be observed in Figure 3.33. From these results, the conclusion can be drawn that the models with 0.5 mm and 0.25 mm show negligible difference and therefore, that the 2D models have reached convergence for a mesh size of 0.5 mm.

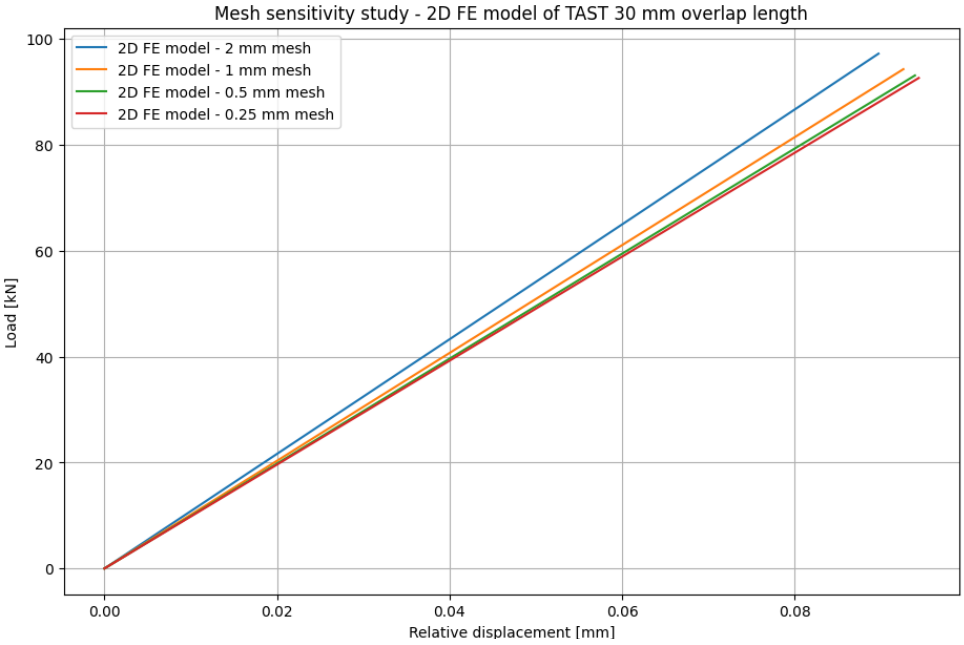

Figure 3.33: Load-displacement curves of 2D mesh sensitivity study

To reduce the computational demand of the 3D FE models, a symmetry boundary condition in x-direction and a finer mesh inside the zone of interest were implemented. Based on the results and conclusion of the 2D mesh sensitivity study, an initial estimation of a mesh size of 0.5 mm was applied to the zone of interest in the 3D FE models.

Due to computational limitations caused by the high number of elements in the 3D FE models, local mesh sizes smaller than 0.5 mm were not applied. A comparison between the 3D local 0.5 mm mesh and coarser mesh sized was performed to analyse whether convergence was reached for the 3D local 0.5 mm FE model. Unfortunately, this study showed that convergence is not reached for a 0.5 mm mesh in the zone of interest. Deviations between the mesh convergence study, based on load – relative displacement curves for the 3D FE models with an overlap length of 30 mm, are displayed in Figure 3.34.

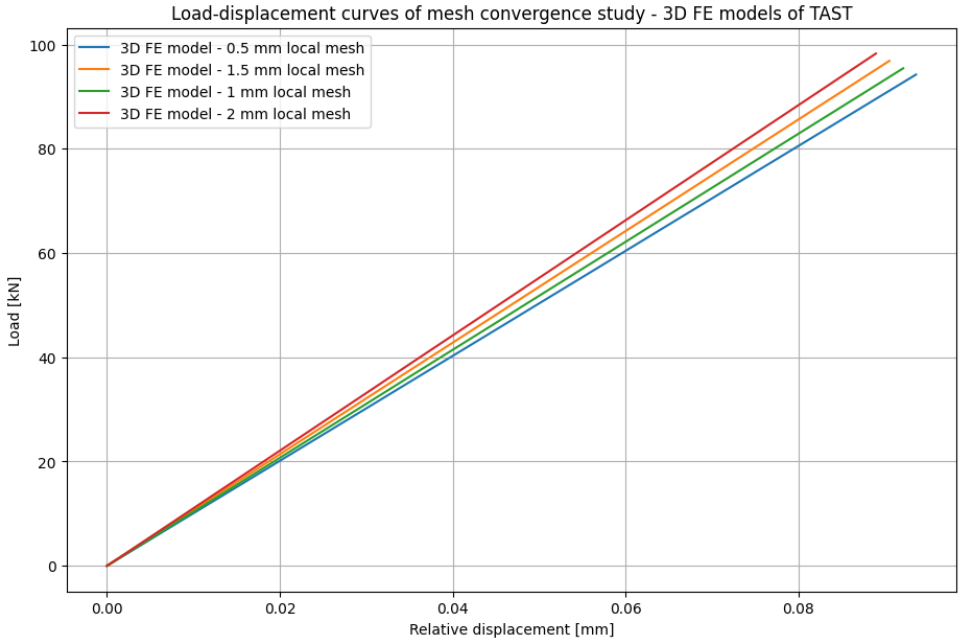

Figure 3.34: Load - relative displacement curves of mesh sensitivity study of 3D FE models of TAST with 30 mm overlap length

In an additional mesh sensitivity study, 3D FE models with a combination of a finer and coarser mesh, as shown in Figure 3.31, were compared with FE models consisting of a uniform element size, to determine the mesh size outside the zone of interest. Based on this study, a combination of 1 mm and 2 mm elements were selected for the constructed mesh outside the zone of interest, where the 1 mm mesh size is implemented directly outside the zone of interest and the 2 mm mesh size is applied on the outer edges of the FE models.

Outside the zone of interest, nine elements for FRP and seven for steel were used in y-direction, increasing to 28 elements for FRP and 23 for steel inside the zone of interest. The total number of solid elements is:

- 189110 for 30 mm overlap length
- 238587 for 60 mm overlap length
- 302656 for 90 mm overlap length

To gain additional insight into the performance of the 3D FE model with 0.5 mm mesh size in the zone of interest, a comparison with the 2D FE model with 0.5 mm mesh size was made. A comparison of the global behaviour is displayed in Figure 3.35, which shows the load – relative displacement curves for the 2D and 3D FE models. Moreover, the maximum global σ_{zz} and global σ_{yz} were used to compare the local behaviour of the FE models, which can be observed in Table 3.11.

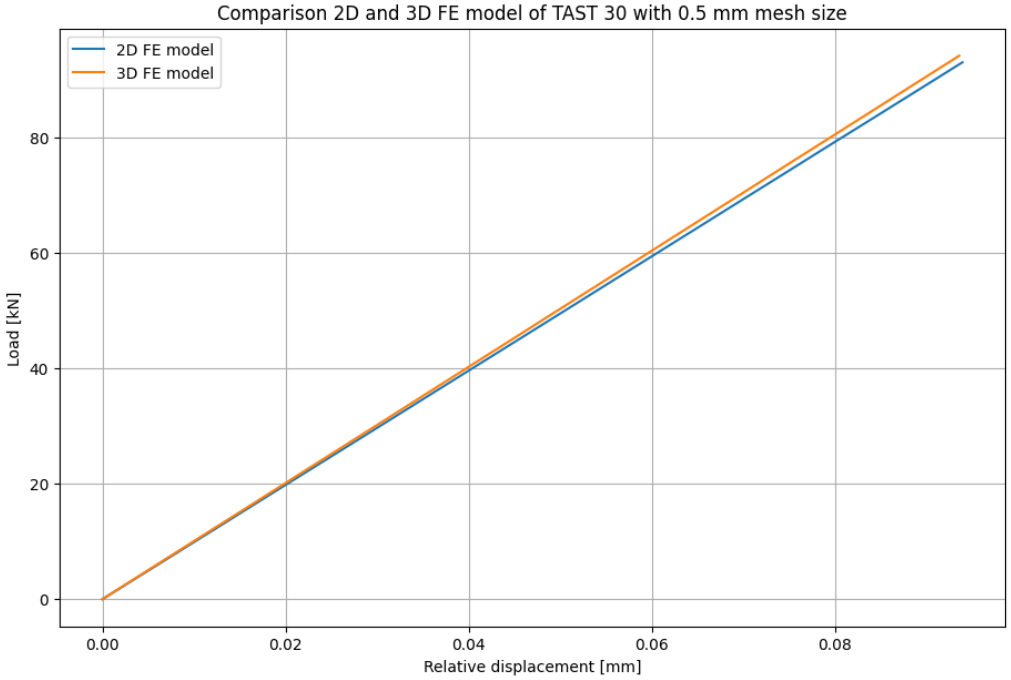

Figure 3.35: Load - relative displacement curves for 2D and 3D FE models of TAST - 0.5 mm mesh

Table 3.11: Local behaviour comparison for 2D and 3D FE models of TAST - 0.5 mm mesh

Results of FE models	**2D FE model – 0.5 mm mesh**	**3D FE model – 0.5 mm mesh**	**Deviation from 2D model**
Max. global σ_{zz} [MPa]	$1.24 * 10^3$	$1.27 * 10^3$	+ 2.4 %
Max. global τ_{yz} [MPa]	253.84	276.05	+ 8.7 %

3.4.5 Steel – FRP Interaction

From the adhesive interface sensitivity study, the conclusion was made to implement tie-breaks and tied interface conditions in the FE model of the TASTs. Three FE models with varying overlap lengths and tied interface definition were constructed. In addition, an FE model with tie-break adhesive interface was constructed for an overlap length of 30 mm.

The properties of the tie-break contact definition were determined based on an iterative process with the objective to obtain a good match between the experimental and FE modelling results. This study resulted in the following properties of the tie-break contact definition:

- Average shear capacity = 48 MPa
- Average peel capacity = 100 MPa
- Critical distance = 0.1 mm

The sensitivity study did not fully lead to physically realistic properties for the tie-break contact definition. Since the TASTs are mainly subject to shear loading, more attention was paid to finetuning the shear capacity than the normal capacity of the tie-break contact. However, this aspect will be further discussed in the FE analysis of the component-level tests.

3.4.6 Finite Element Analysis

For the final 3D FE model, implicit or explicit analysis is performed, depending on the modelling approach for the adhesive interface. For the numerical model of an overlap of 30 mm, an explicit analysis was used as tie-break contacts cannot be analysed in an implicit analysis in LS-DYNA. On the other hand, numerical models of overlap lengths 60 and 90 mm were executed with an implicit analysis, as these models do not include non-linearity, and the runtime of the models is immensely reduced by using implicit analysis. For the implicit analysis, an initial time step size of 0.1 seconds was used. The static load was applied in two steps, starting with an initial increasing velocity and with a maximum velocity of 0.1 mm/s. The applied load is displayed in Figure 3.36.

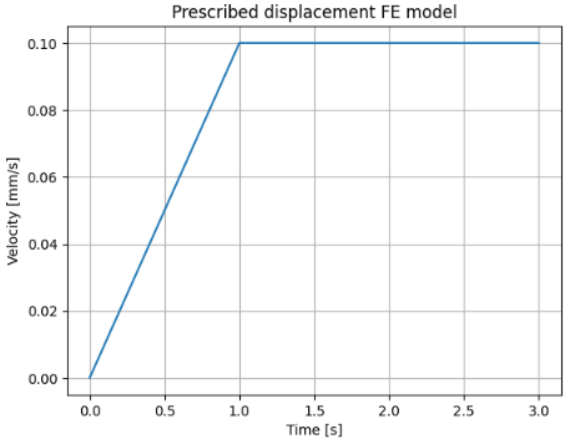

Figure 3.36: Prescribed displacement of FE models

3.5 Discussion of TAST Numerical Models

This section of the report provides a discussion of the 3D FE models with varying overlap lengths. This discussion consists of a comparison of the global behaviour of the FE models and experimental results, in the form of load-displacement curves. Moreover, the influence of observed dry patches on the FRP laminate and notch geometry in the numerical models are displayed.

3.5.1 Load-displacement Curves of Comparison Numerical and Experimental results

The relative displacement of the load-displacement curves is based on the same relative distance, or extensometer, for DIC as numerical results. The relative distance is displayed in Figure 3.37.

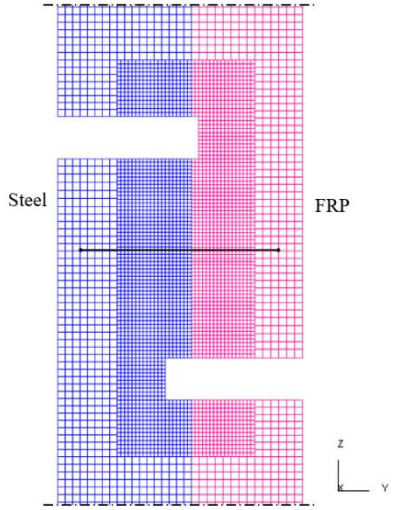

Figure 3.37: Relative distance of TAST FE model with overlap of 30 mm

For every test series with distinct overlap length, the load-displacement curves of the numerical study and experimental results were grouped. To provide a good comparison, the geometry of one specific sample from every series, which are samples TAST 30-2, 60-2 and 90-5, was implemented in the FE models. These samples were selected based on minimizing the deviation from the mean geometry and material imperfections in notch geometry and laminate. The results for 30 mm, 60 mm and 90 mm overlap length can be observed in Figure 3.38, Figure 3.39 and Figure 3.40, respectively.

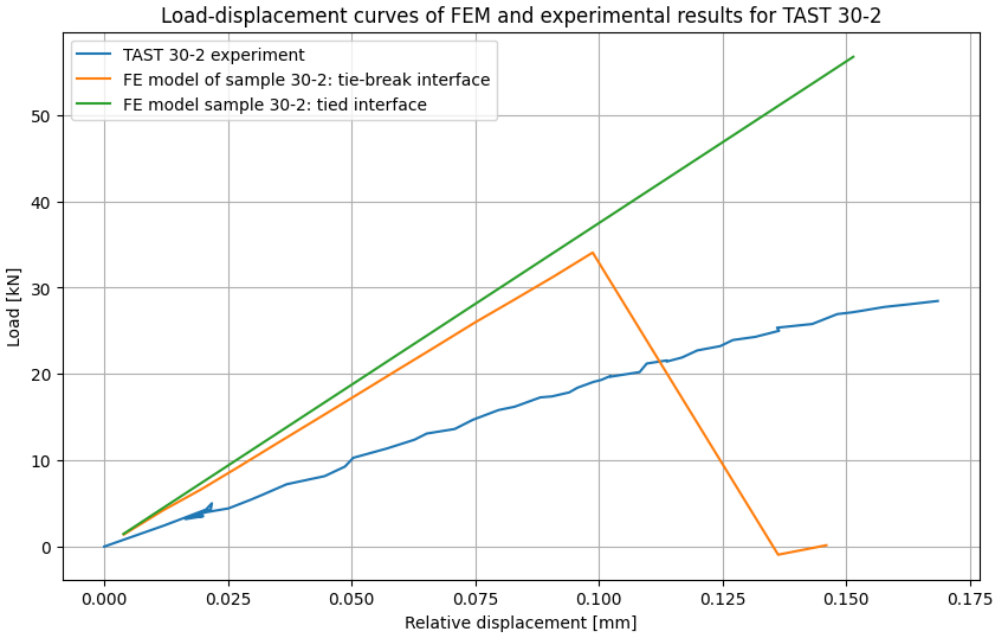

Figure 3.38: Load-displacement curves of FEM and experimental results for TAST 30-2

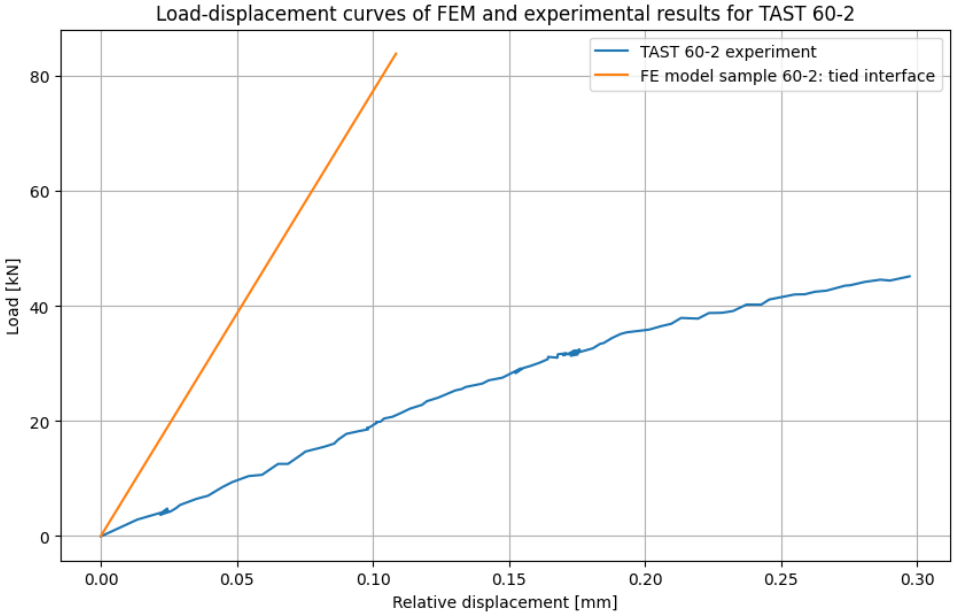

Figure 3.39: Load-displacement curves of FEM and experimental results for TAST 60-3

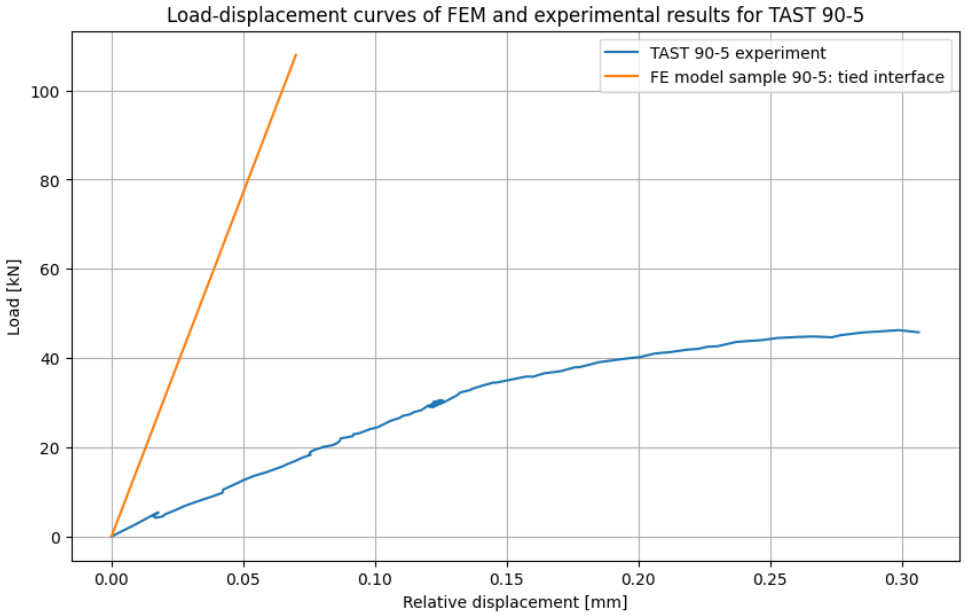

Figure 3.40: Load-displacement curves of FEM and experimental results for TAST 90-5

As can be observed from the load-displacement curves, there are extremely large deviations between the load-displacement curves of the FE models and experimental results. This shows that the FE models highly overestimate the global stiffness of the TAST when subjected to shear force. These deviations increase for increasing overlap lengths, highlighting that the FE models of TAST 60-2 and 90-5 display a higher level of over-performance of the specimens when compared to experimental data. The deviations between the numerical models and experimental results are displayed in Table 3.12.

Table 3.12: Deviation between TAST FE models and experimental data

Model	Stiffness [N/mm]	Stiffness test results [N/mm]	Deviation from test results
30-2 tied interface	$3.75 * 10^5$	$1.92 * 10^5$	+ 95%
30-2 tie-breaks	$3.45 * 10^5$	$1.92 * 10^5$	+ 80%
60-2 tied interface	$7.74 * 10^5$	$1.83 * 10^5$	+ 323%
90-5 tied interface	$15.4 * 10^5$	$2.17 * 10^5$	+ 610%

The implementation of adhesive interface modelling with tie-break contacts allows for failure modelling and will provide interesting insights for the component-level study. For this reason, the model with tie-break contacts will be considered for an overlap of 30 mm. The models with tied interface for 60 mm and 90 mm overlap length will be included in the validation and results.

3.5.2 Influence of FRP Stiffness

Since several samples showed dry patches on the FRP surface of the strips, the elastic stiffness and therefore capacity of the material are likely to be lower than the determined properties with the Classic Laminate Theory. Insights into the influence of these dry patches were provided by the manufacturer, stating that the FRP could have a ten to twenty percent reduction in stiffness. For this reason, a ten and twenty percent reduction in stiffness was applied to the FRP material model and compared to the FE models without this reduction. The comparison was performed on models with tied interface condition. The load-displacement curves for all test series are provided in Figure 3.41 - Figure 3.43.

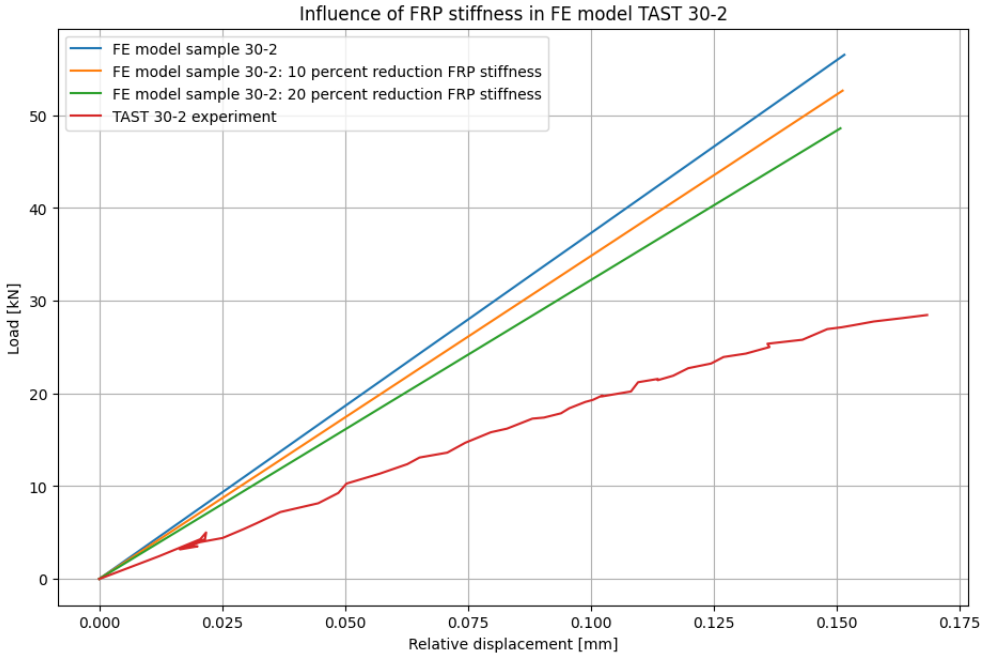

Figure 3.41: Influence of reduction FRP stiffness for TAST 30-2

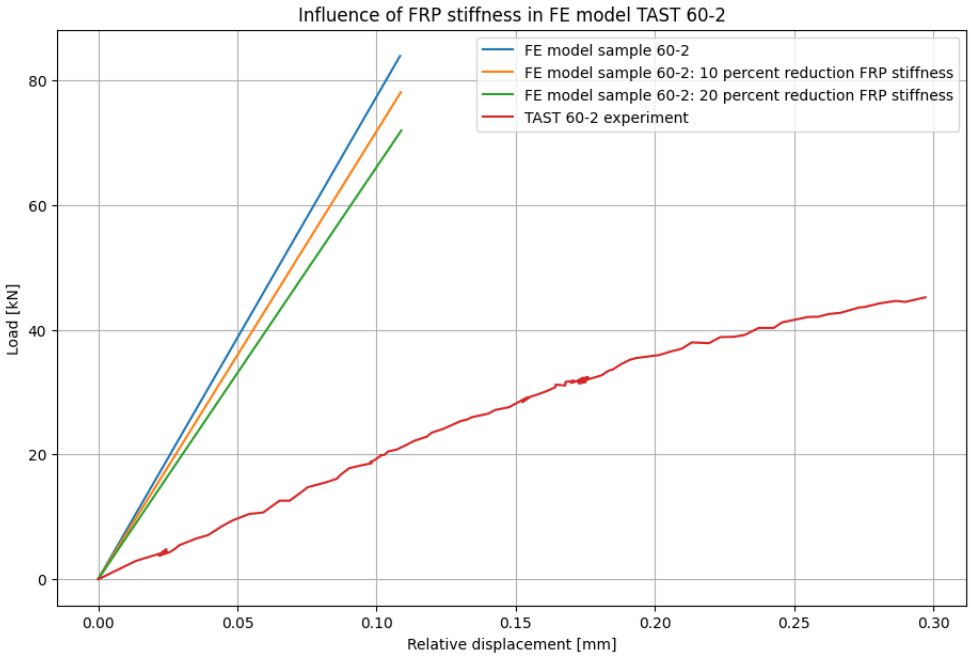

Figure 3.42: Influence of reduction FRP stiffness for TAST 60-3

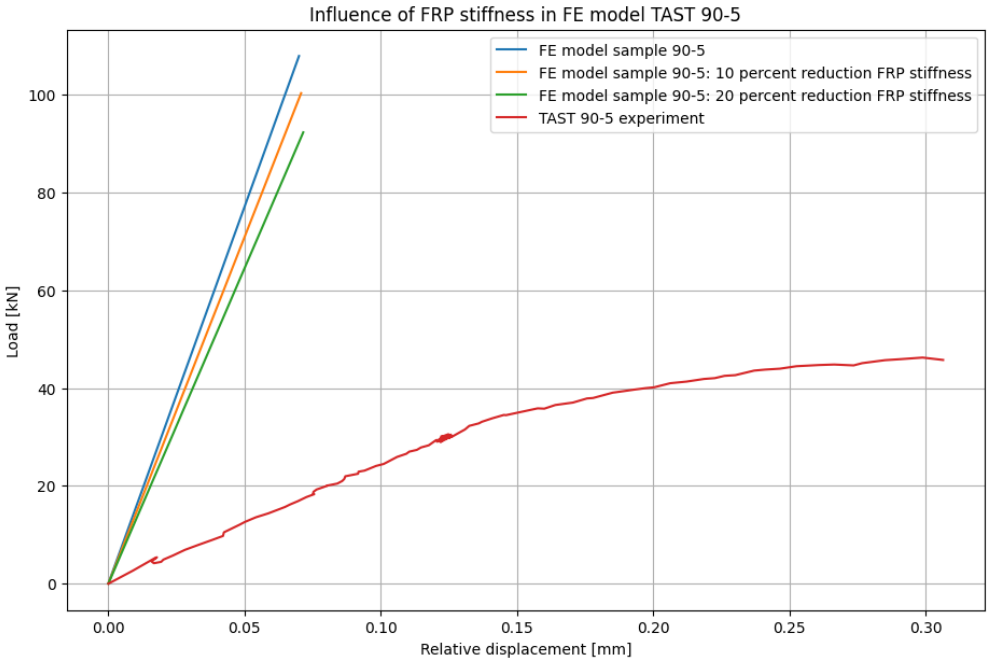

Figure 3.43: Influence of reduction FRP stiffness for TAST 90-5

This comparison shows that even with a ten or twenty percent reduction in FRP capacity, there is still a noticeable difference in global stiffness between the FE models and experimental results. The FRP reduction does indeed lead to a decrease in global stiffness of the FE models. However, this factor alone cannot account for the significant deviation observed between the FE results and experimental data.

3.5.3 Influence of Notch Geometry

In addition to the capacity of the FRP, notch geometry is another factor of which the influence was studied. In section 3.3, the preliminary geometry of the notches was described. In this study, round notches with a penetration of 1 mm were implemented. Due to their sensitivity to meshing around the notches, the decision was made to apply rectangular notches, as displayed in Figure 3.31. However, due to the large stiffness difference between FE results and experimental data, the influence of notch geometry was studied.

A comparison including three models with varying notch geometry, displayed in Figure 3.44, was performed. The analyses were performed on 3D FE models, based on a specimen with an overlap length of 30 mm. A local mesh of 0.5 mm was used inside the zone of interest, while a coarser mesh of 2 mm was used outside the zone of interest. The adhesive interface was modelled with tied contact definitions. Load-displacement curves can be observed in Figure 3.45. Based on this load-displacement curve, it becomes clear that the notch geometry has a large influence on the global stiffness of the FE model. Additionally, the model with round penetrated notches demonstrated a lower global stiffness than the model with sharp penetrated notches.

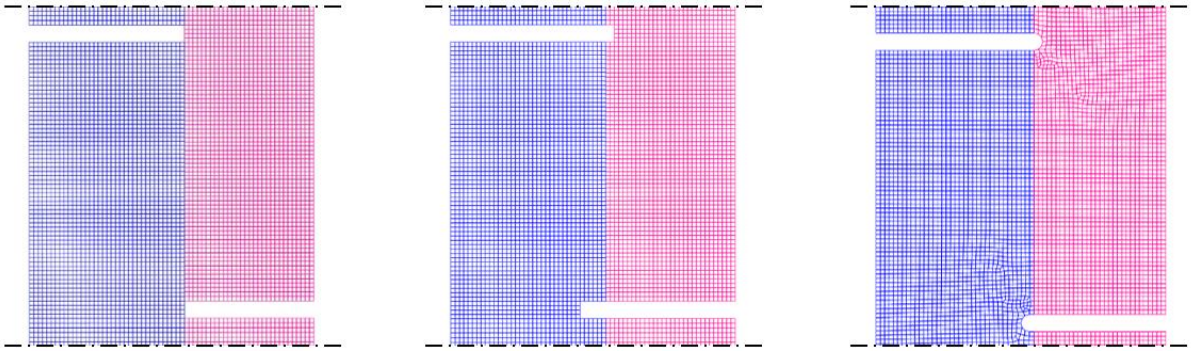

Without penetrated notches **With sharp penetrated notches** **With round penetrated notches**

Figure 3.44: FE models with and without penetrated notches

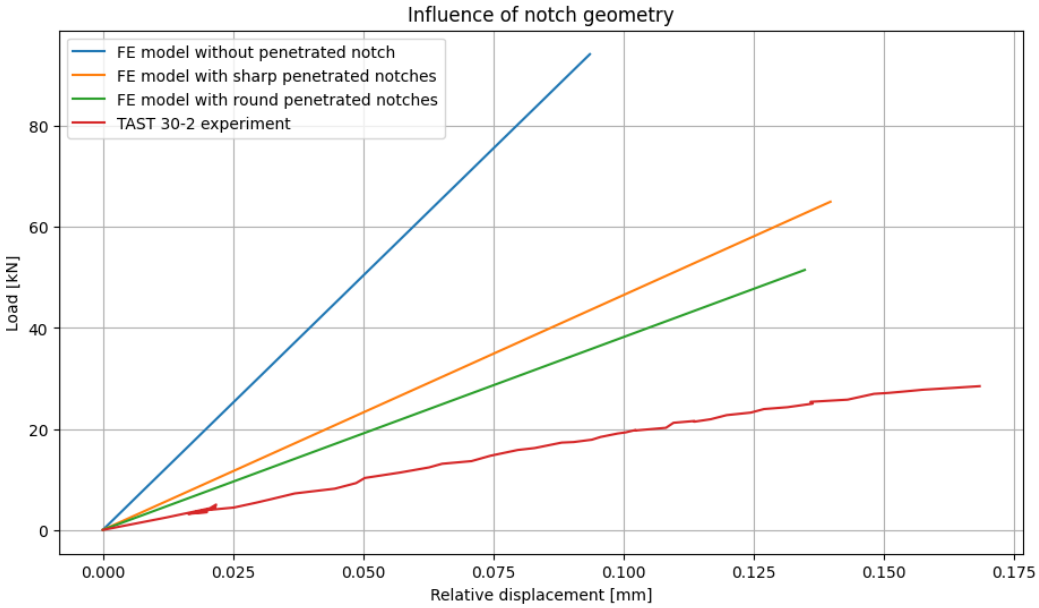

Figure 3.45: Load-displacement curves of FE models with and without penetrated notches

3.6 Results

This section of the report provides results, conclusions and recommendations for the TAST numerical and experimental study. First, a model validation is performed for the three FE models with varying overlap lengths, which is followed by results of the models. In addition, an estimation of design values of the bond strength is provided. To conclude, a discussion of the small-scale study is provided.

3.6.1 Model Validation

For the validation of the three FE models with varying overlap lengths, a comparison between strains based on the DIC results of the experiments and based on the FE models is provided. This comparison includes strains in three directions, which are:

- Global Z-direction, which is in longitudinal direction of the samples.
- Global Y-direction, which is in in-plane transverse direction of the samples.
- Principal direction, which is the direction in which maximum strains occur.

An important remark is that the DIC results do not show strains on the entire surface of the specimens, but of a subsection. To increase the accuracy of the comparison, the same subsection of the surface of the FE model is displayed. In addition, the extreme values of the legend of the FEM results were matched to the extreme values of the DIC plot. Strains of DIC and numerical results for specimens TAST 30-2, 60-2 and 90-5 are displayed in Figure 3.46 - Figure 3.54. Numerical results of the FE models for the TASTs are presented in Appendix B.

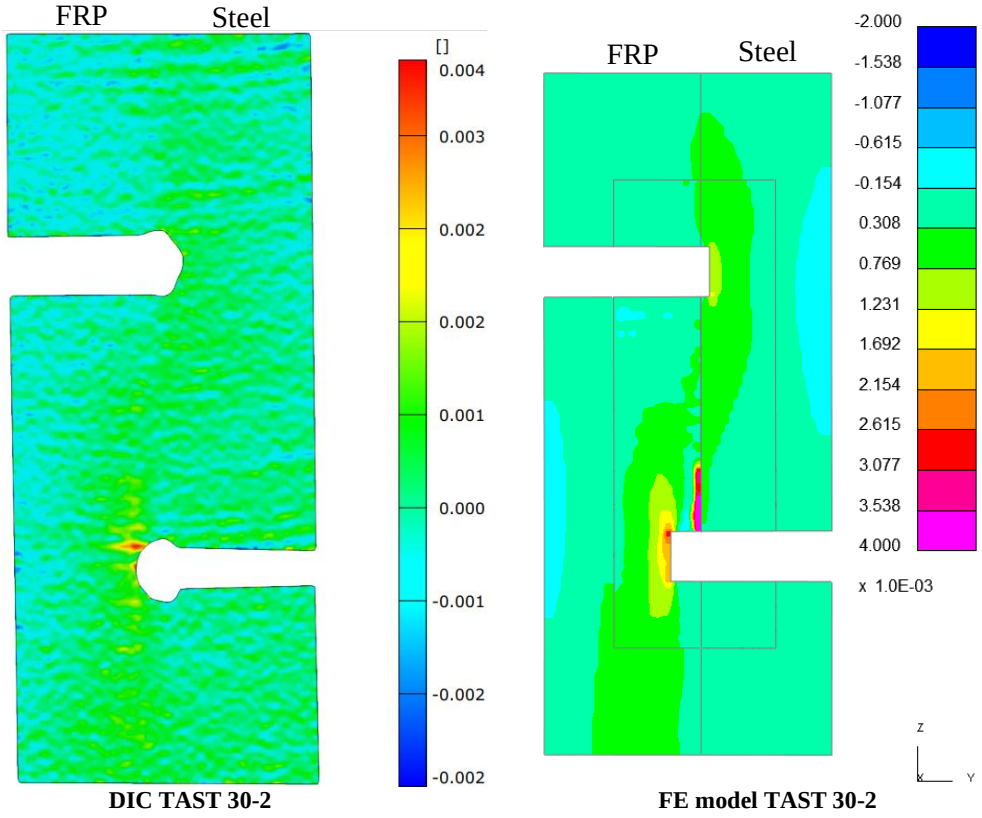

DIC TAST 30-2 **FE model TAST 30-2**

Figure 3.46: Strain in global Z-direction TAST 30-2 at F = 13.6 kN

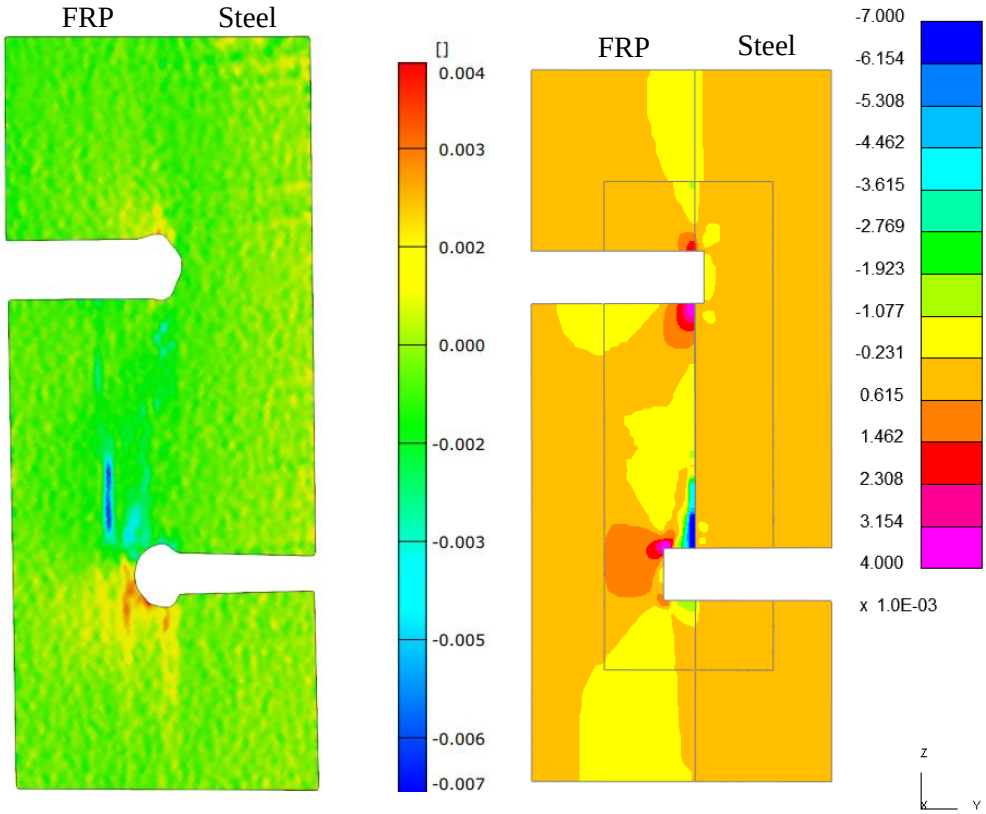

DIC TAST 30-2 **FE model TAST 30-2**

Figure 3.47: Strain in global Y-direction TAST 30-2 at F = 13.6 kN

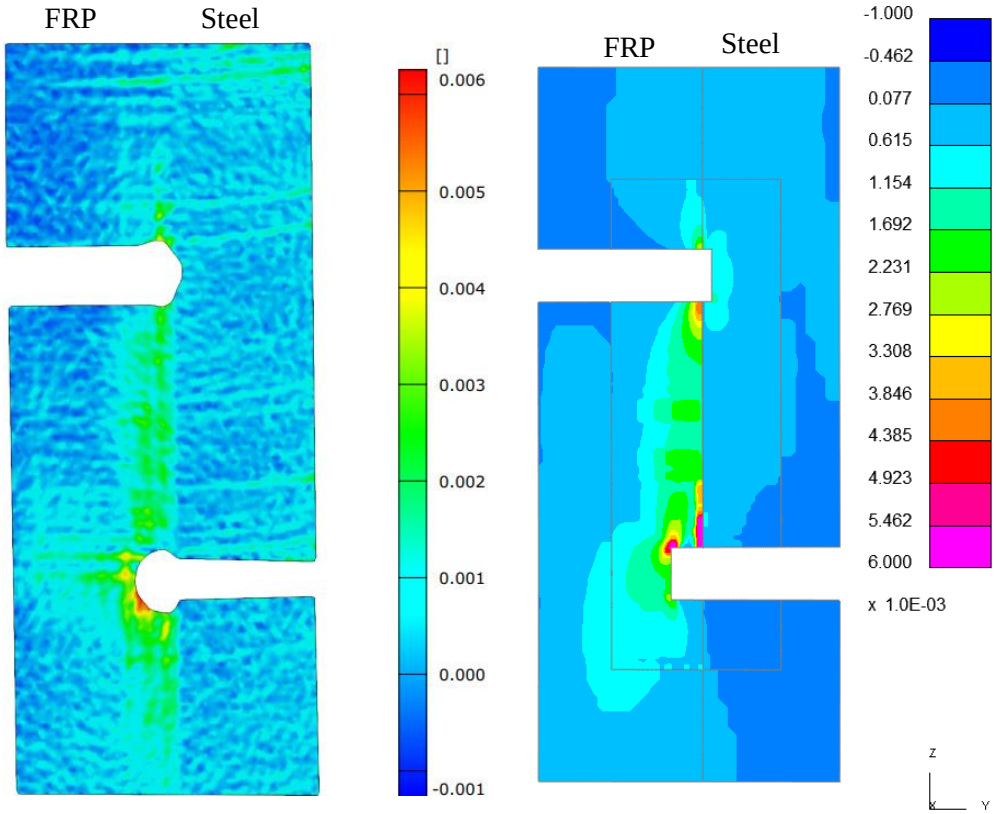

DIC TAST 30-2 **FE model TAST 30-2**

Figure 3.48: Strain in principal direction TAST 30-2 at F = 13.6 kN

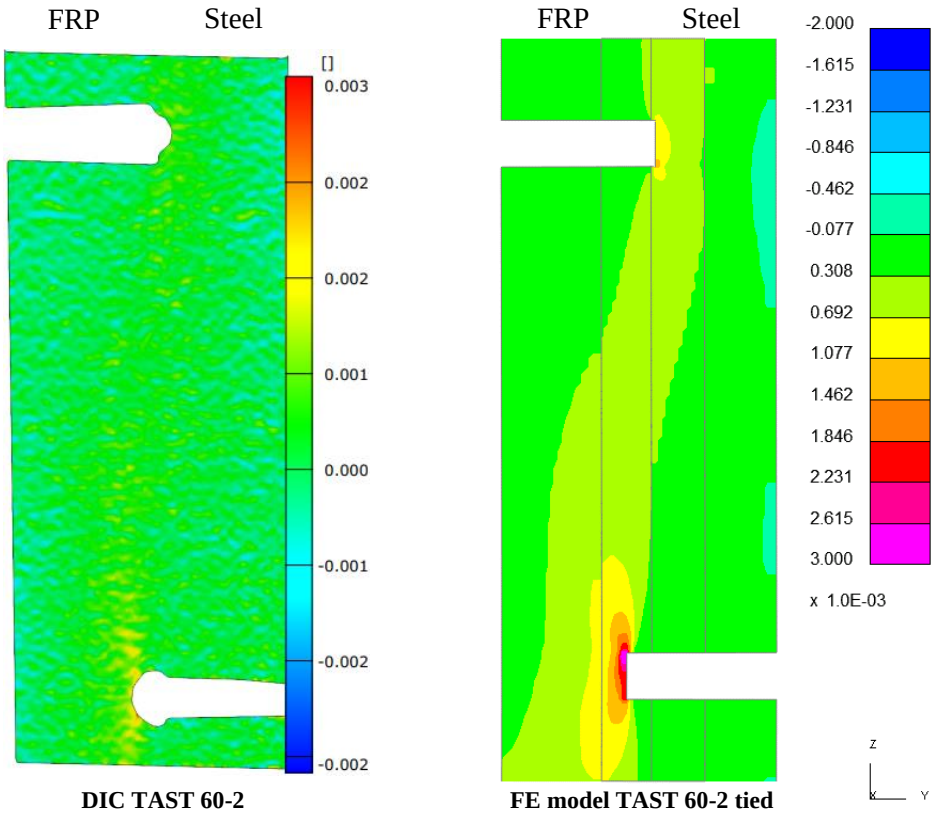

DIC TAST 60-2 **FE model TAST 60-2 tied**

Figure 3.49: Strain in global Z-direction TAST 60-2 at F = 20.0 kN

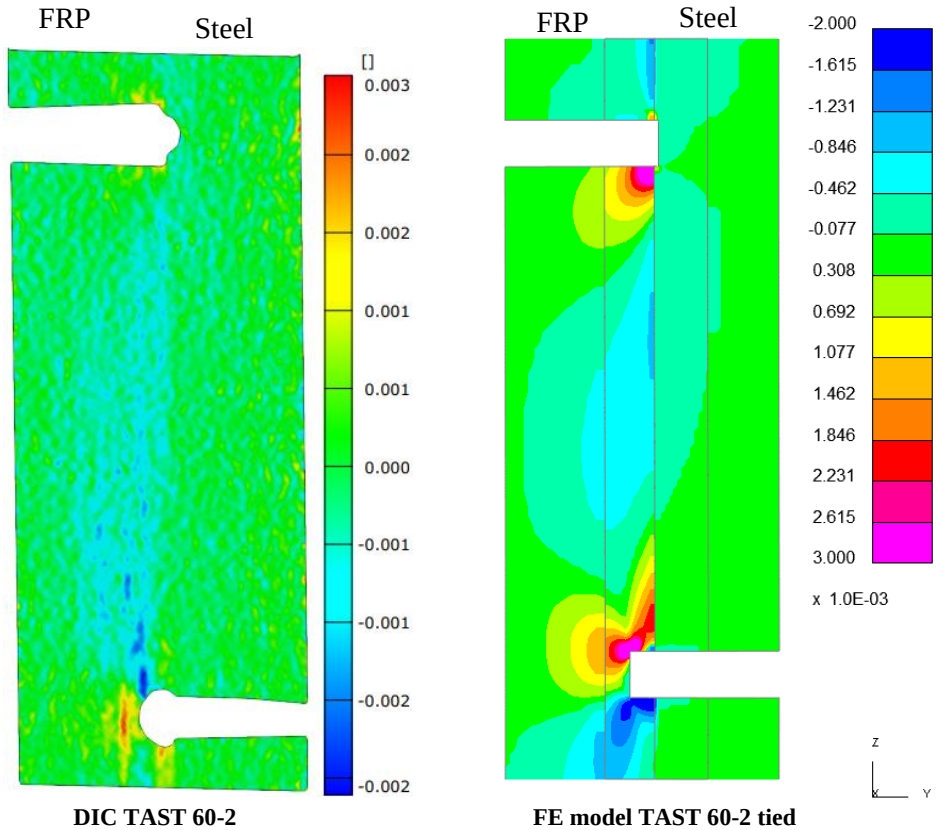

DIC TAST 60-2 **FE model TAST 60-2 tied**

Figure 3.50: Strain in global Y-direction TAST 60-2 at F = 20.0 kN

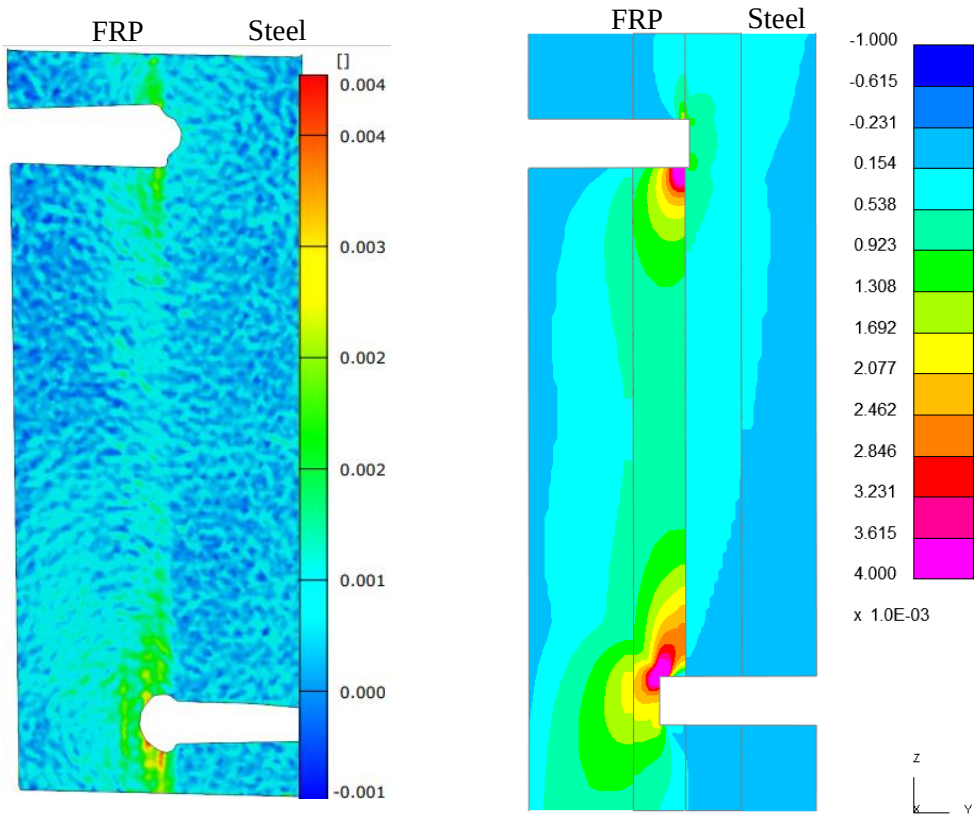

DIC TAST 60-2 **FE model TAST 60-2 tied**

Figure 3.51: Strain in principal direction TAST 60-2 at F = 20.0 kN

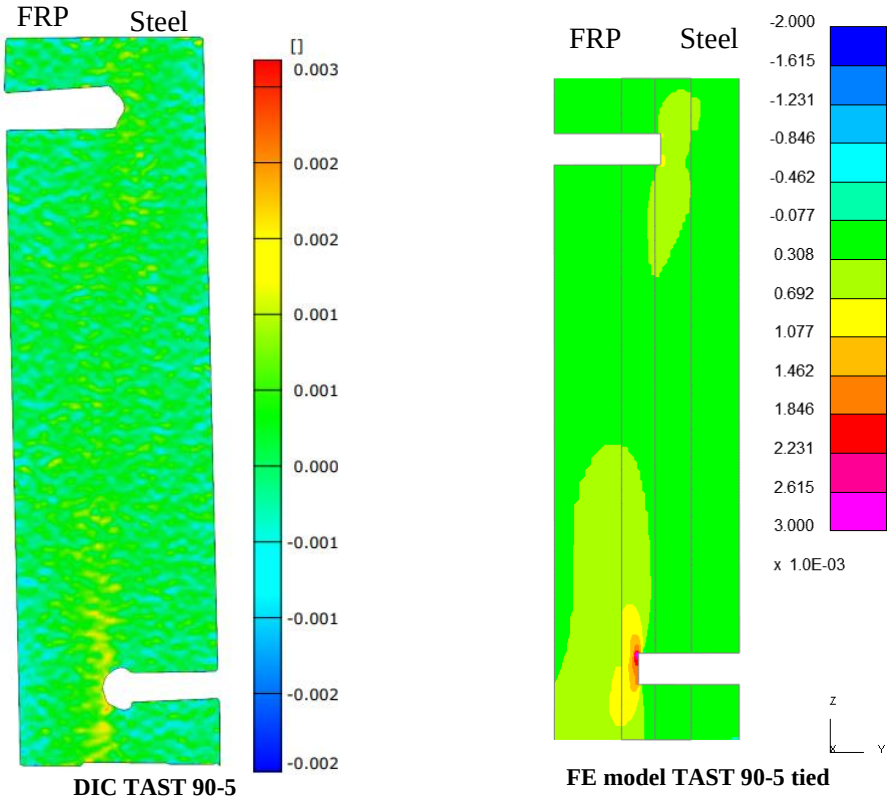

DIC TAST 90-5 **FE model TAST 90-5 tied**

Figure 3.52: Strain in global Z-direction TAST 90-5 at F = 20.5 kN

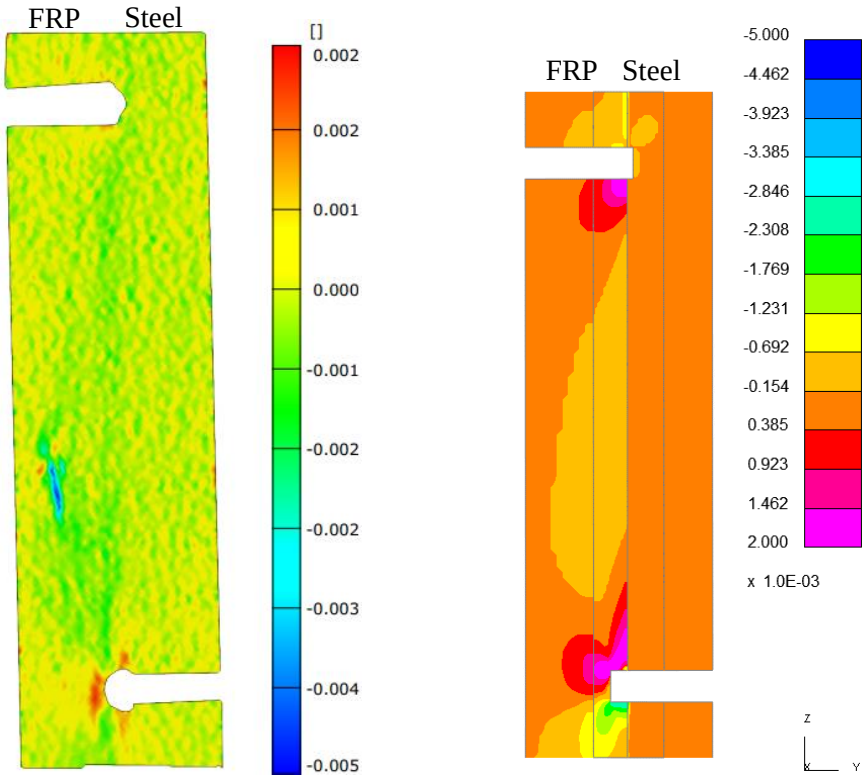

DIC TAST 90-5 **FE model TAST 90-5 tied**

Figure 3.53: Strain in global Y-direction TAST 90-5 at F = 20.5 kN

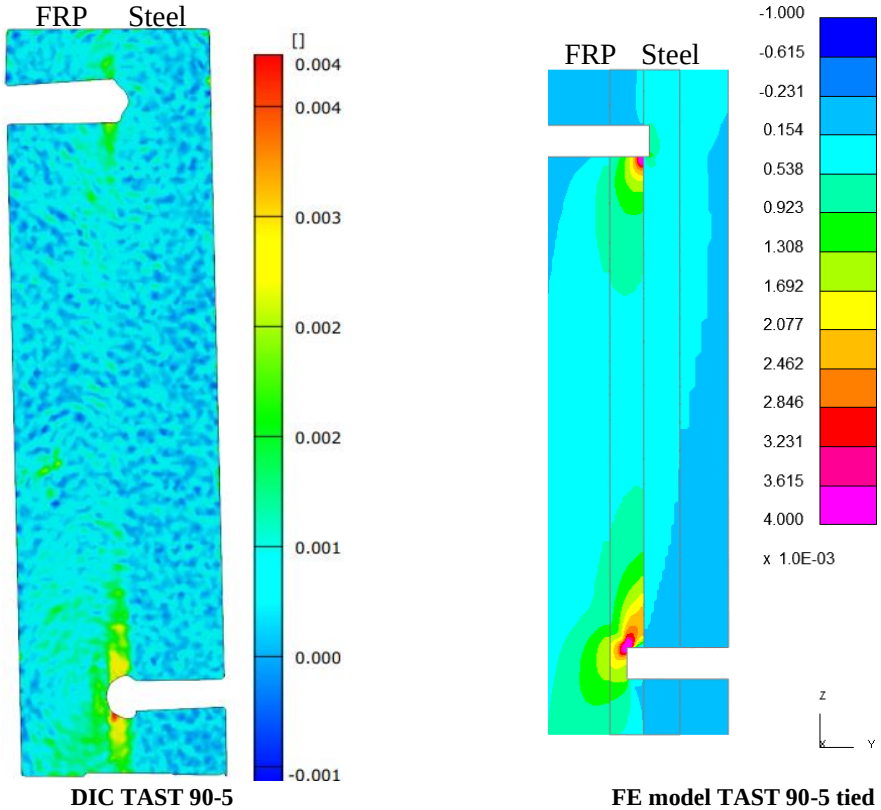

DIC TAST 90-5 **FE model TAST 90-5 tied**

Figure 3.54: Strain in principal direction TAST 90-5 at F = 20.5 kN

From these strain results, the following observations can be formulated regarding validation of the FE models:

- Strain distributions in all three directions show similar qualitatively behaviour for the experimental and numerical results.
- Despite the similar qualitatively results, higher strains are observed for the experimental results than the FE results, with an exception for peak strains around the notches. This is in line what the deviations between the FE and experimental results. These higher strains are mainly observed for strains in z- and principal direction. It is assumed that the stiffness difference is mainly impacted by the longitudinal stiffness.
- All strain plots display maximum positive strain, which corresponds to tensile behaviour, around the lower notch, which is the steel notch. This behaviour is caused by the lower stiffness of the FRP compared to steel, therefore resulting in higher strains. This observation shows that the notch and more specifically, the notch geometry, are an important aspect of the specimens.
- Strains in global y-direction are generally much smaller than those in global z-direction, as observed in the DIC and FE results. However, they are not negligible, indicating the presence of peel stresses.
- In the experimental y-strains, a blue line can be observed for TAST 30-2 and 90-5 where negative strains occur. As specimen 90-5 shows a dry patch at the same position, it is assumed that the dry patch is causing a weakness in transversal in-plane direction of the FRP. The same assumption was mode for sample 30-2, however it is probable that this dry patch is positioned in the middle of the material since it cannot be observed from either surface.
- The numerical model of TAST 30-2 displays substantially large strains in the lower part of the overlap interface. These strains are caused by the tie-break contact definition, which showed partial opening between the two adherends at F = 13.6 [kN]. Experimental results of TAST 30-2 do not display any crack initiation at this stage, showing that the tie-break contact interface displays premature crack initiation.

In conclusion, the FE models demonstrate an accurate qualitative strain distribution along the longitudinal, transverse in-plane and principal direction. However, due to notch geometry, the FE model tends to overestimate peak strains in the notch area. Moreover, the numerical models exhibit generally lower strain levels compared to those observed in experimental results.

3.6.2 Design Values Bond Strength

To gain insight into the design values of the adhesive bond strength, Annex D of Eurocode 1990 was used to determine characteristic and ULS values for the shear bond strength. These values were determined based on the load at failure observed during the TASTs and contact stresses of the FE model of sample 30-2 with tie-break contact definition. This section shows the major steps and conclusions of this evaluation. The full calculation is provided in Appendix F.

Twelve out of fifteen TAST specimens displayed primer-steel failure, with or without a combination of GFRP delamination, with an exception for TAST 30-4 and 90-3. Since primer-steel failure includes failure of the adhesive interface between the FRP laminate and steel, these twelve samples were used in the determination of design values of the bond strength. For these twelve samples, the average stress was computed based on the observed load at failure and average overlap surface for samples with overlap of 30, 60 and 90 mm. Computed average stresses are displayed in Table 3.13.

Table 3.13: Average stress of TAST specimens based on failure load

Specimen number	Average stress for overlap of 30 mm [MPa]	Average stress for overlap of 60 mm [MPa]	Average stress for overlap of 90 mm [MPa]
Specimen 1	25.0	17.1	11.7
Specimen 2	22.6	15.5	14.8
Specimen 3	24.2	17.9	*Not included in design values*
Specimen 4	*Not included in design values*	17.1	10.9
Specimen 5	*Not included in design values*	17.1	14.2

For all three FE models, peak and average bond stresses were extracted at the failure load level, as displayed in Table 3.2. Extracted adhesive interface stresses and derived ratios for average / peak bond stress and average peel / shear stress are shown in Table 3.14.

Table 3.14: Average and peak bond stress from TAST FE models

Property	FE model with 30 mm overlap	FE model with 60 mm overlap	FE model with 90 mm overlap
Peak shear stress [MPa]	29.0	37.0	28.0
Average shear stress [MPa]	26.4	17.2	13.4
Ratio average / peak shear stress	1 / 1.1	1 / 2.2	1 / 2.1
Peak peel stress [MPa]	45.5	61.9	46.8
Average peel stress [MPa]	2.46	2.8	2.0
Ratio average / peak peel stress	1 / 11.2	1 / 22.1	1 / 23.2
Ratio average peel / shear stress	1 / 6.5	1 / 6.1	1 / 6.7

These results show that, compared to the model with 30 mm overlap, the ratio average peel / shear stress decreases for the model with 60 mm overlap and increases for the model with 90 mm overlap. This indicates that the peel stresses show, as expected, a relative increase for 60 mm, but a decrease for 90 mm overlap. This result is in contrast with expectations, as longer overlap lengths are likely to result in higher peel stresses. However, Figure 3.55 shows that the distance from grip area to the zone of interest decreases for higher overlap lengths, resulting in additional stiffness. This leads to a restriction against rotation of the zone of interest, limiting peel stresses. Moreover, these results show that the performed small-scale tests are mainly subjected to shear loading although a certain level of mixed-mode behaviour is observed from the FE model. This leads to the conclusion that failure of the adhesive bond was the result of shear loading, therefore only considering the shear bond strength in evaluation of design values.

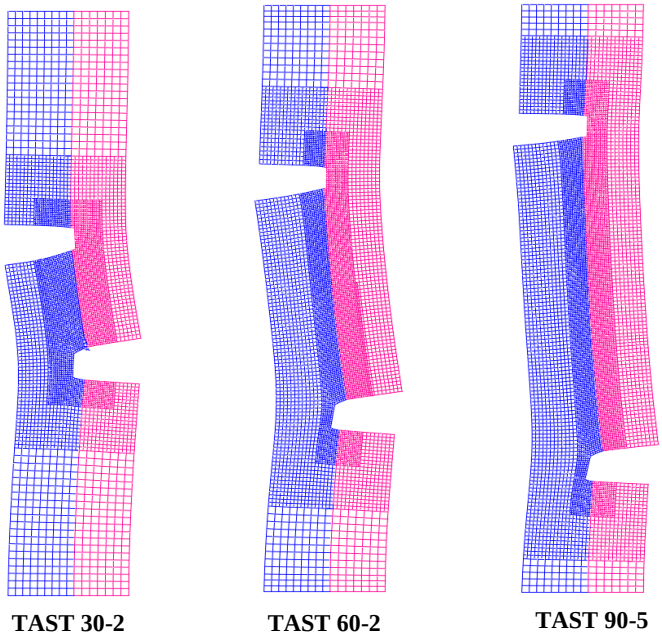

Figure 3.55: Deformed shapes of TAST FE models (magnified 50x)

The average peel / shear stress ratio was applied to the determined average strength observed from experiments. The average shear strengths for all specimens are displayed in Table 3.15.

Table 3.15: Average shear stress of TAST samples at failure

Overlap length [mm]	Average shear strength [MPa]
30	20.7
60	14.6
90	11.2

Annex D of Eurocode 1990 defines two methods to derive properties from tests, which are:

- Method A: by assessing a characteristic value, which is divided by a partial factor and, if necessary, multiplied by a conversion factor
- Method B: by directly determining an ULS design value, implicitly or explicitly accounting for conversion and required reliability of the results [54].

Equations (D.1) – (D.3) and Table D.1 of Annex D of Eurocode 1990 were used to determine characteristic values of the average shear bond strength via method A. In addition, equations (D.4) and (D.5) and Table D.2 of Annex D of Eurocode 1990 were used to determine design values for ULS verifications. Since sufficient knowledge regarding the bond strength is not available, parameters for "V_x unknown" were applied. The ratio of average / peak stress for shear stress was applied to determine peak bond strengths. The values for the bond strength are displayed in Table 3.16 [54].

Table 3.16: Design values bond strength based on TASTs

Bond strength	Characteristic values	Design values for ULS verifications
Average shear strength [MPa]	10.27	5.42
Peak shear strength [MPa]	14.35	7.58

3.7 Discussion

This section provides limitations and uncertainties of the experimental and numerical results of the small-scale study.

Limitations of the experimental results obtained from the TASTs, are presented as:

- **Presence of peel stress**. While TASTs were opted to limit peel stresses, numerical and experimental results highlighted the presence of peel stresses. Therefore, pure mode II behaviour was not observed.
- **Modified TASTs.** As outlined in section 3.2, performed TASTs in this study are, in fact, modified TASTs as they do not follow the specific dimensions and boundary conditions as defined in ASTM D5656-10 [45]. For this reason, this standard could not be used to derive characteristic values of the bond strength.

One of the main objectives of this study was to validate constructed FE models with experimental results. However, from section 3.5, it becomes clear that there are large deviations between global behaviour of experimental and numerical results. There are several factors that could explain why such large deviations were observed:

- **Modelling of FRP**. In this thesis, the FRP laminate is modelled by using solid elements with homogeneous properties. This method does not take the first layer of GFRP plies into account and is not able to compute adherend laminate failure, such as delamination.
- **Material uncertainties of FRP laminate**. Material properties of the FRP adherend were determined by the classic laminate theory and material properties of the plies and resin, as provided by the supplier. Unfortunately, experiments to ensure assumed material properties were not performed, resulting in uncertainties regarding the performance of the FRP laminate.
- **Infinite stiffness interface.** Tied and tie-break contact definitions incorporate the principle of an (initial) infinitely stiff adhesive interface. However, it is likely that the physical adhesive bond displays a more ductile behaviour, therefore reducing the global stiffness of the specimens.
- **Tie-break uncertainties**. Several variations of tie-break contact definitions were used, with the definition presented in the final FE model of TAST 30-2 providing the best results. However, discrepancies between the test results and FE model regarding bond behaviour can be defined by:

- **Insufficient stiffness of the non-physical springs in FE model**. Due to this input property, the models with tie-break contact demonstrated a lower global stiffness than the model with tied contact. Additionally, this resulted in bond stress peaks along the bottom of the adhesive interface, as can be seen in Figure 3.47 and Figure 3.48. This indicates that the tie-break contact interface does not result in a properly tied interface.
- **Inaccurate failure behaviour.** The TAST experiments demonstrated sudden and brittle failure while the load-displacement curve of the FE model with tie-breaks showed a less sudden total failure. This failure behaviour is impacted by the numerical parameter 'critical distance'. Classical fracture mechanics tests, such as DCB and ENF, are required to reliably obtain adhesive properties.

- **Notch geometry.** Section 3.5.3 presented that the notch geometry has a high impact on the global performance of the FE models. While a simplified notch geometry with sharp edges was applied to the FE models, it is highlighted that rounded notches would lead to a decrease in global stiffness.

Section *3.6.2* presents design values for the average shear bond strength, based on the FE models and experimental results. Important remarks with respect to these design values are:

- As the FE models were not validated by experimental results, model imperfections make it challenging to provide an accurate comparison between the models and test results.
- As peak bond stresses are influenced by tie-break properties and mesh size, care must be taken with presented values for the peak strength.
- Values for partial and conversion factors are based on assumptions, as sufficient knowledge is not available.

To further validate the design bond strength, calculated values were compared with values from similar studies, as summarized in Table 3.17. Both reference studies performed TASTs according to ISO 11003-2 standard [55]. It is important to note that within this thesis modified TASTs were performed, which makes presented comparison less precise. The shear bond strength obtained in this study appears realistic and consistent with those reported in literature.

Table 3.17: Shear comparative evaluation between performed TASTs and comparative studies

Adhesive	Average shear bond strength [MPa]	Reference
Prime™ 37 Resin & Ampreg 3X Standard hardener	20.7 for 30 mm overlap length 14.6 for 60 mm overlap length 11.2 for 90 mm overlap length	-
Silkapower® 4720	24.34 ± 0.941	[56]
Araldite® 2015	17.9 ± 1.8	[57]

3.8 Summary

This chapter studies the bond strength and failure mechanisms of adhesive joints between FRP and steel, using TASTs and corresponding FE models. The experimental set-up included three types of thick-adherend shear samples with varying overlap lengths (30 mm, 60 mm and 90 mm) to evaluate the influence of bond surface on shear capacity. Observed failure mechanisms highlighted sudden debonding between primer and steel, in some cases combined with delamination of the GFRP layer, as the primary failure mode.

In addition to the experiments, FE models were developed in LS-DYNA, using both tied and tie-break contact conditions to simulate bond strength and bond failure. A discussion of the numerical models was performed by comparing global load-displacement behaviour across the three overlap lengths. Results showed that both modelling approaches demonstrate large dissimilarities with experimental results, varying from + 80% for an overlap length of 30 mm where tie-breaks are implemented to + 610% for an overlap length of 90 mm where a tied contact is implemented. Possible explanations were provided. Implemented tie-break contacts overestimated the failure load in the FE model with a 30 mm overlap length. This overestimation is assumed to be a result of the physically unrealistic strength properties.

Characteristic and design values of the shear bond strength were derived from experimental and numerical results. An average design bond strength of 5.42 kN was determined. Obtained average bond strength values appear realistic and consistent with those reported in literature.

Findings from this chapter demonstrate the importance of overlap length and notch geometry in bond performance, noting that longer overlaps displayed a reduction in average bond stress caused by crack initiation observed during experiments for 60 mm and 90 mm overlaps. The developed FE models offer a basis for simulating adhesive bond behaviour in FRP-steel applications.

4. Component Experiments and Numerical Model

This chapter presents the component-level three-point bending tests and numerical models. Firstly, it introduces the concept and set-up of the performed three-point bending tests, followed by experimental results. This is followed by the numerical study, which includes FE models of the component strips. A discussion and validation of the FE models is provided. To conclude, a comparison between the component-level and full-bridge FE models is presented, followed by a discussion and summary.

4.1 Introduction

To gain knowledge and understanding into the behaviour of the Cold Repair method using FRP, more insight into the bond and global behaviour of an OSD component strengthened with an FRP angle is essential. Component-level experiments and corresponding FE models contribute to this objective. This series of experiments and FE modelling is a continuation of the TASTs and FE modelling, where mainly the failure mechanisms, obtained shear capacity, and modelling approaches provide valuable information for the component-level study.

4.2 Component Experiments

This section of the report provides a description of the test set-up and test results of the performed component experiments.

4.2.1 Test Set-up

Static three-point bending tests of OSD component strips strengthened with an FRP angle were performed in the Stevin II laboratory of the Delft University of Technology. This test method consists of strips, simply supported on two supports and statically loaded in bending, as displayed in Figure 4.1 and Figure 4.2.

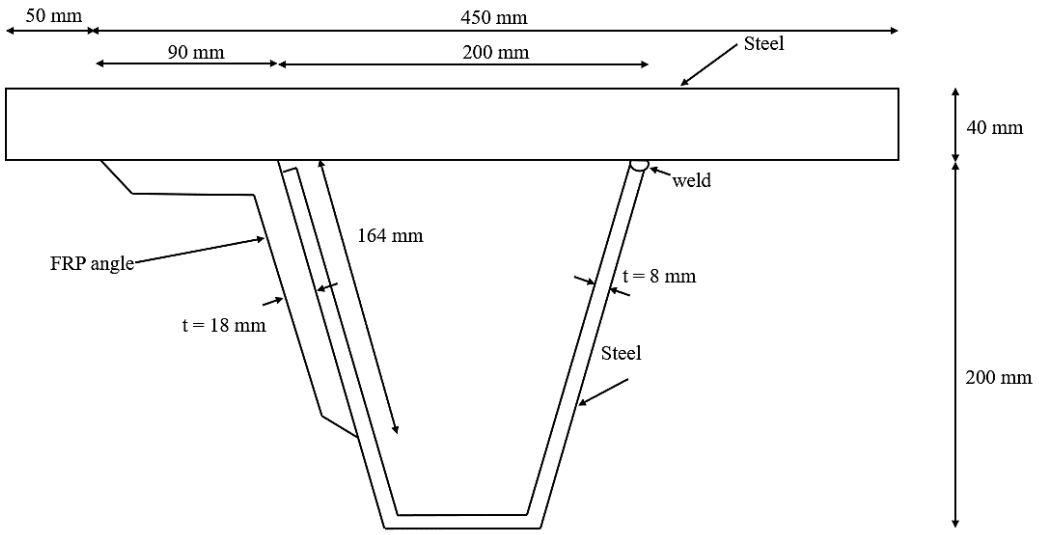

Figure 4.1: Component-level three-point bending test: specimen geometry

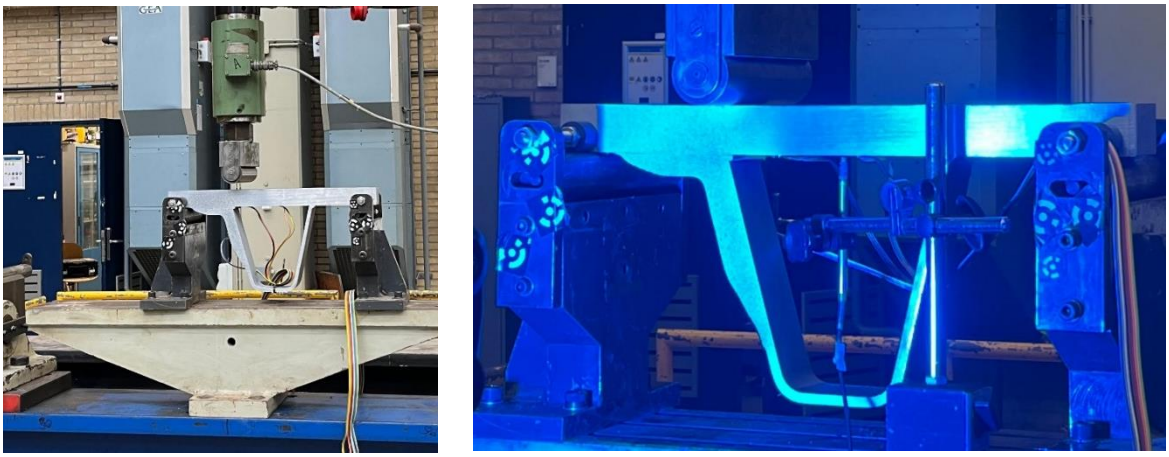

Figure 4.2: Component-level three-point bending test: test set-up

The specimens consist of a deck plate strip with a width of 60 mm and a thickness of 40 mm, to simulate the equivalent stiffness of a OSD with a HSC overlay, as described in section 2.1.4. The deck plate is connected to a trough -with a thickness of 8 mm- with a weld on the opposite side of the FRP angle. The trough leg and deck plate are unconnected on the side where the Cold Repair is attached to the bridge deck component to ensure all loads are distributed through the FRP and it is fully utilized. The CFRP angle is attached to the steel deck component by the process of vacuum infusion with epoxy resin. A primer is applied to the steel plate to create a better bond between FRP and steel. For the component-level tests, an identical FRP laminate to the TASTs was applied. To attain the same percentage of UD plies in the lay-up as for the TASTs, a thickness of 18 mm was implemented in these specimens as well. One series of tests was performed, consisting of 6 samples. A detail of the laminate lay-up is displayed in Figure 4.3. A description of the layers marked by the letters in the detail is provided in Table 4.1

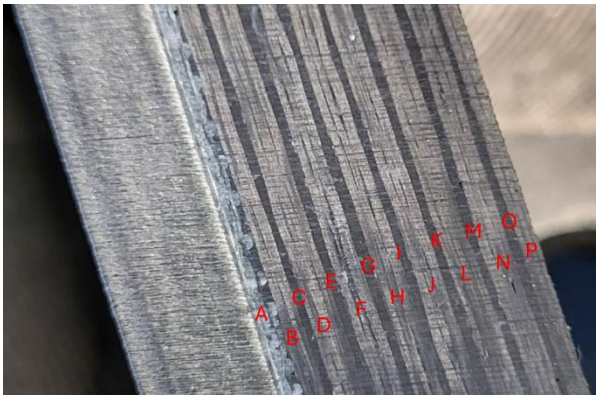

Figure 4.3: Laminate lay-up component samples

Table 4.1: Description of plies in laminate lay-up component samples

Layer	Description
A	GQI1200 + Flow 500 (GFRP layer)
B	2 plies UD 0° 600gr/m²
C	1 ply ±45° 600gr/m²
D	3 plies UD 0° 600gr/m²
E	1 ply UD 09° 600gr/m²
F	3 plies UD 0° 600gr/m²
G	1 ply ±45° 600gr/m²
H	3 plies UD 0° 600gr/m²
I	1 ply ±45° 600gr/m²
J	3 plies UD 0° 600gr/m²
K	1 ply ±45° 600gr/m²
L	3 plies UD 0° 600gr/m²
M	1 ply UD 09° 600gr/m²
N	3 plies 0° 600gr/m²
O	1 ply ±45° 600gr/m²
P	2 plies UD 0° 600gr/m²

The main objectives of these experiments were to measure whether debonding would occur, and, if debonding were to be the governing failure mechanism, when and where it would occur. To measure these objectives, 2D-DIC was used to capture strains in the Cold Repair and occurring failure. Moreover, strain gauges were applied on the deck plate strip in two positions:

- In the middle between the trough legs, in the middle of the width of the strip
- Close to the loaded trough leg, in between the trough legs, in the middle of the width of the strip.

In addition, LVDT, placed in the middle of the deck plate in between supports, was used to measure the global deformation of the deck plate.

4.2.2 Experimental Results

All tested specimens showed a very similar failure behaviour, which initiated in the edge of the horizontal leg of the Cold Repair and propagated in the direction of the trough-to-deck plate joint until failure of the adhesive bond occurred. Observed failure after testing for sample COMP-3, which was the first tested specimen, is displayed in Figure 4.4.

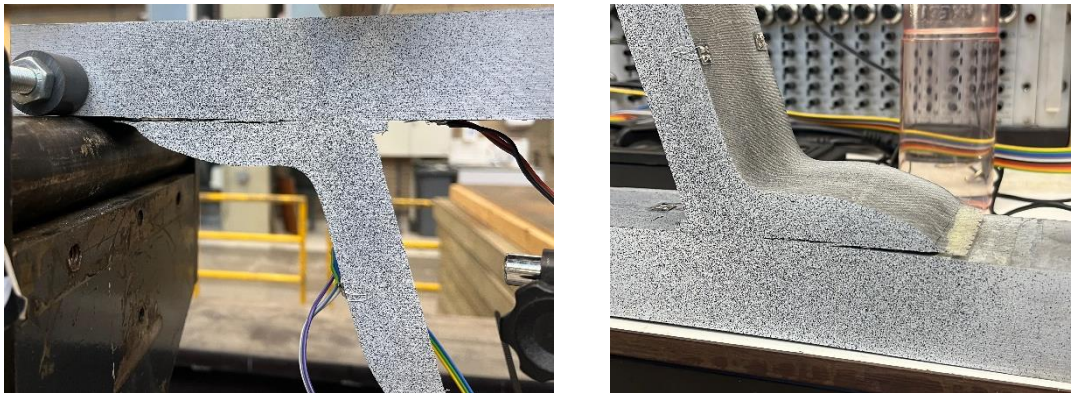

Figure 4.4: Observed failure for specimen COMP-3

As COMP-3 was loaded for a longer time after failure of the adhesive bond, there is a clearly visible gap between the deck plate and CFRP angle. For specimens 2, 4, 5, 6 and 7, this is not the case. For this reason, micrographs of the fracture were taken for all six samples. To be able to identify the different elements of the steel-FRP interface, the photos were taken from the opposite surface as the side of which 2D-DIC measurements were taken. However, for sample COMP-3, DIC paint was already applied on this side, making it difficult to identify the interface elements. For every sample, three micrographs are provided in Table 4.2, including:

- One image of the horizontal leg of the Cold Repair close to the trough-to-deck plate joint
- One image approximately in the middle of the horizontal leg
- One image of the outer edge of the horizontal leg of the Cold Repair

Table 4.2: Micrographs of failure for component three-point bending tests

Specimen number	Close to the trough-to-deck plate joint	Middle of the horizontal leg	Outer edge of the horizontal leg
2			
3		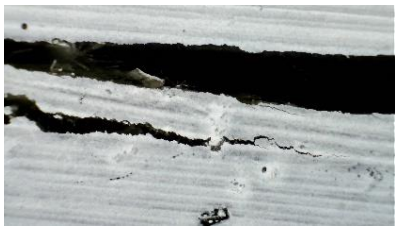	
4		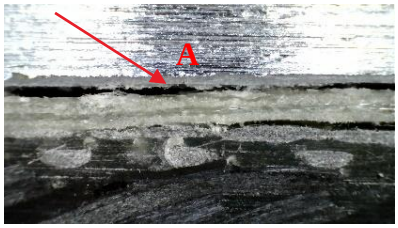	
5			
6	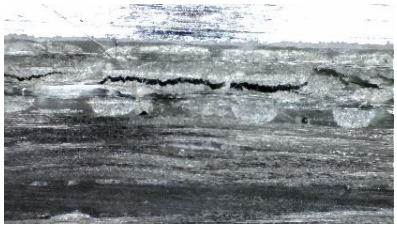		
7			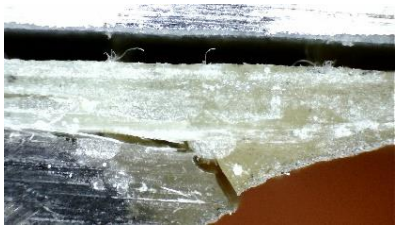

As can be seen from the micrographs, cracks propagated inwards from the outer edge of the horizontal leg of the Cold Repair. A combination of delamination of the GFRP layer, indicated with arrow D, and adhesive failure of the Cold Repair, indicated by arrow A, was observed.

Global load-displacement curves of the experimental tests are displayed in Figure 4.5. The mean curve can be observed in Figure 4.6. The load is based on data from the tensile machine and the displacement was based on the LVDT data.

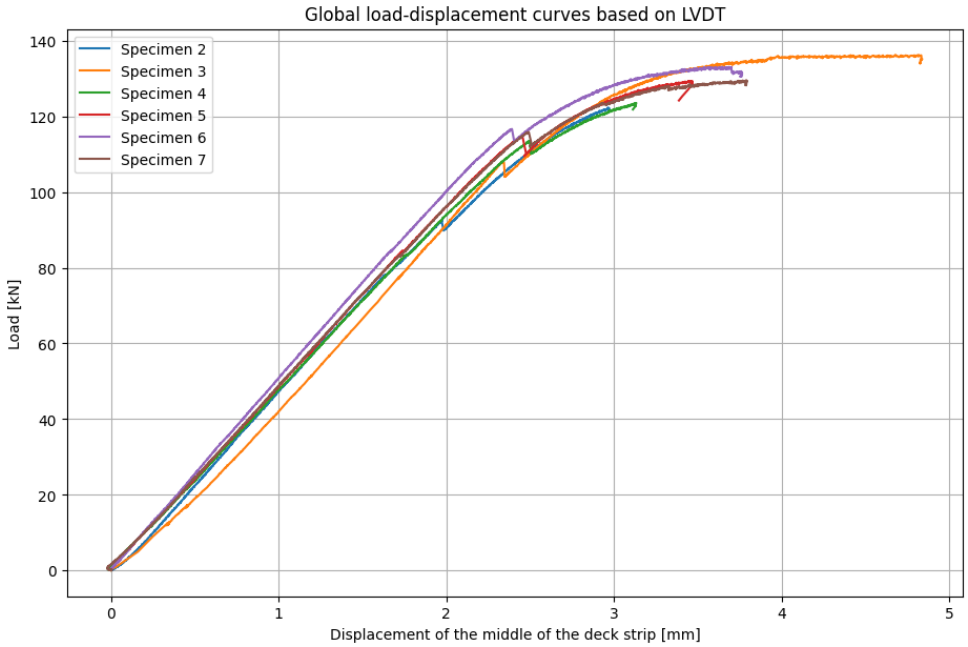

Figure 4.5 Global load-displacement curves of component-level three-point bending tests

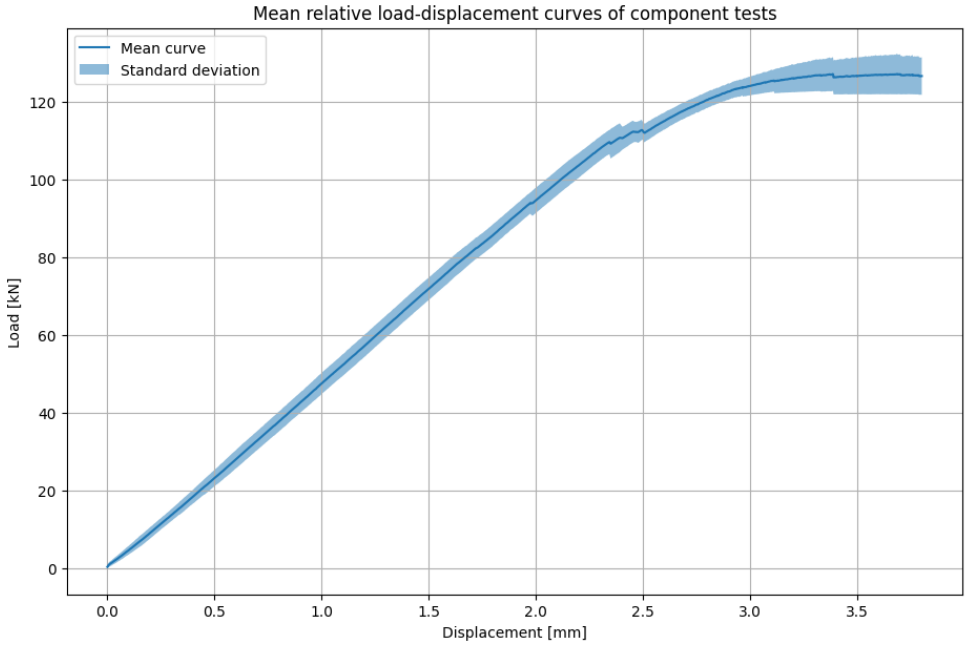

Figure 4.6: Mean load-displacement curve of component tests

From the displayed load-displacement curves, the following observations and conclusions can be formulated:

- All six samples show a linear behaviour with a similar stiffness up to a certain load level, at which the load drops. The load at which this drop occurs, and the magnitude of this drop are displayed in Table 4.3. This load drop was paired by a sudden crack and sound, indicating the full debonding of the Cold Repair. The average load level at debonding is 110.15 kN.

- After this load drop, non-linear behaviour is observed for all specimens. All samples were loaded until the non-linear behaviour was observed after which the loading was slowly removed. However, specimens 3 and 6 were loaded until the non-linear behaviour stabilized and the load no longer increased.
- Before this visible debonding, which occurred between 92.2 kN for COMP-2 and 116.5 kN for COMP-6, a minor kink is visible at a load of level of around 82 kN. 2D-DIC results were used to further study this behaviour.
- Specimen 3 shows a slightly lower stiffness in the linear-elastic phase than the other samples. This can be explained by the deviant testing procedure for this sample. Specimen 3 was initially tested by a machine with an insufficient capacity. Therefore, this specimen was loaded twice. The load-displacement curve of the first test, with the name of COMP-3.1, is displayed in Figure 4.7. The decrease in stiffness and the small load drop at around 80 kN, which was caused by crack initiation, illustrate that the specimen was subjected to some failure, causing a stiffness reduction during test COMP-3.2.

Table 4.3: Load at debonding of component-level three-point bending tests

Specimen number	Load level at debonding [kN]	Magnitude of drop [kN]
2	92.2	2.4
3	107.9	3.8
4	113.5	3.4
5	114.9	4.7
6	116.5	2.9
7	115.9	3.0

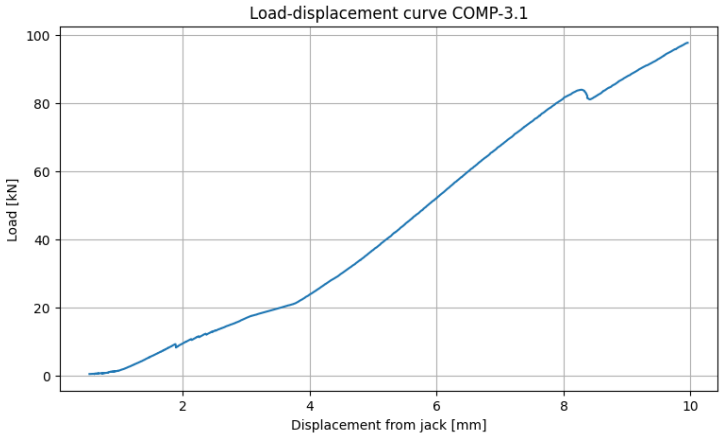

Figure 4.7: Load-displacement curve of COMP-3.1

In addition to global load-displacement curves, load-strain curves from strain gauge 1, which is placed in the middle of the steel deck strip between trough legs, and strain gauge 2, which is applied close to the loaded trough leg, can be observed in Figure 4.8 and Figure 4.9. An inset of Figure 4.9 is displayed in Figure 4.10.

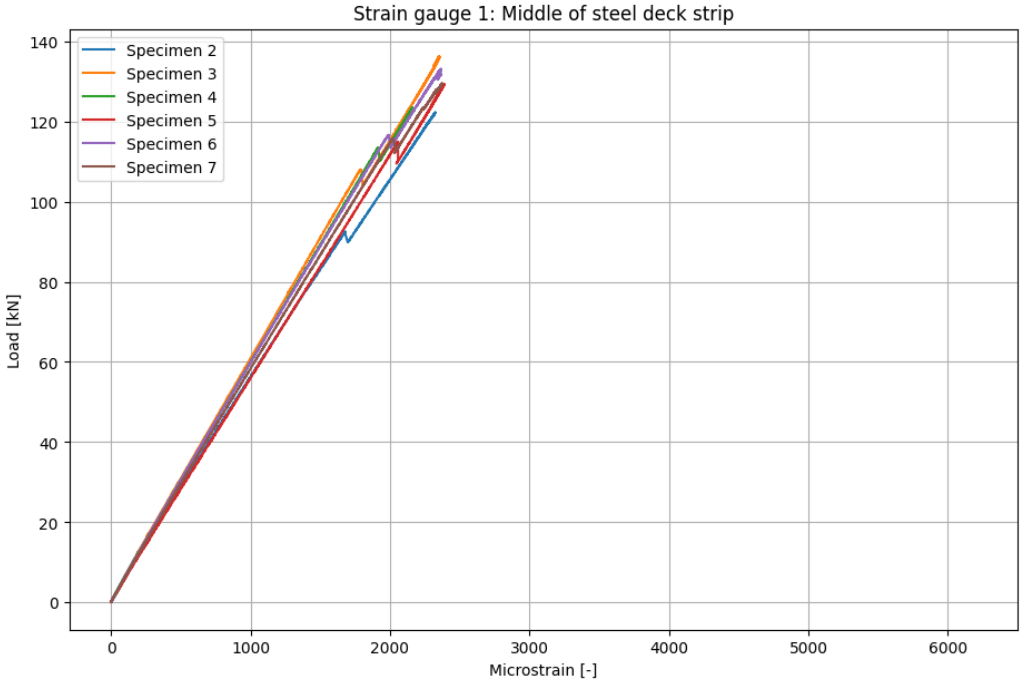

Figure 4.8: Load-strain curves for strain gauge 1

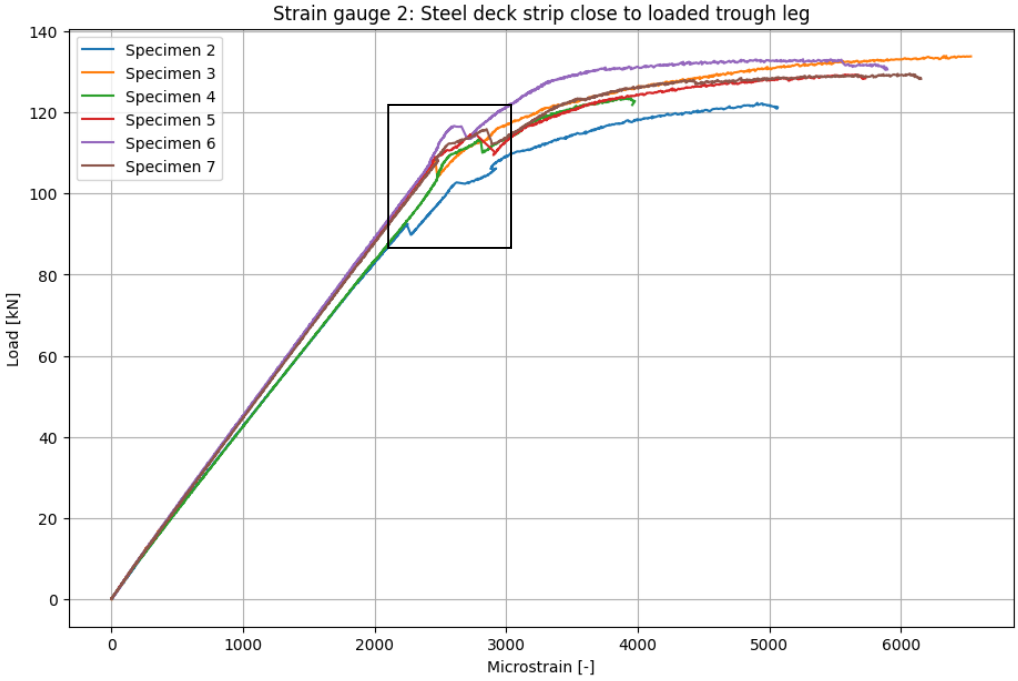

Figure 4.9: Load-strain curves for strain gauge 2

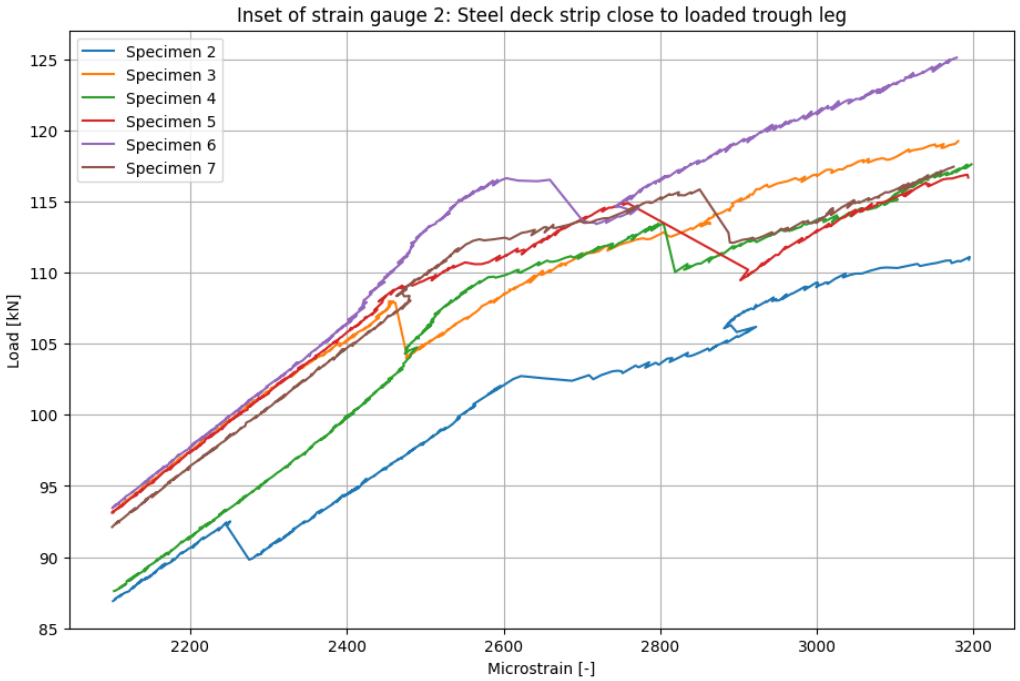

Figure 4.10: Inset of load-strain curves for strain gauge 2

From these load-strain curves, the following conclusions can be drawn:

- Strain gauge 1, which captures strains in the middle of the deck plate in between supports, displays linear-elastic behaviour, meaning that at this point no yielding occurs.
- Strain gauge 2, which captures strains in the deck plate close to the applied load, shows that the deck strip reaches the yielding point. Figure 4.10 shows an overview of the strains at which the onset of yielding is observed, which is the point at which the first non-linear behaviour can be identified. Since the deck plate consists of S460, Hooke's law defines a yield strain of 2.19 * 10^6 when considering a Young's modulus of 210 GPa. As the component strips showed higher strains, the conclusion can be drawn that either the onset of yielding occurred at lower strains but was not captured by the strain gauges or that the steel deck plate has a higher steel grade than the theoretical S460, which is more likely and therefore assumed.
- From the inset of strain gauge 2, two different behaviours can be identified:
    - **Sudden drop in load, followed by non-linear behaviour**. This means that debonding occurred before yielding of the steel deck plate. This is the case for specimens 2 and 3.
    - **Non-linear behaviour with increasing stiffness, followed by a sudden drop in load**. This means that yielding of the steel deck plate occurred before debonding. This is the case for specimens 4, 5, 6 and 7.

  The first defined behaviour can be explained by the divergent behaviour of specimens 2 and 3 observed in Figure 4.5, since these specimens showed debonding at a much lower load level than specimens 4 to 7. The distinct behaviour for specimen 3 is defined by performing the three-point bending tests twice. However, the distinct behaviour for specimen 2 is not as easily identified. 2D-DIC results were used to further study this behaviour.

  Since specimens 4, 5, 6 and 7 display the onset of yielding followed by debonding of the Cold Repair, it is assumed that increasing deformation of the deck plate, caused by the onset of yielding, resulted in debonding of the Cold Repair. However, it is difficult to conclude to what extent the onset of yielding influenced debonding of the Cold Repair.

Table 4.4: Yield strains for steel deck plate in component-level tests

Specimen number	Strain at which yielding occurs [-]
2	$2620 * 10^{-6}$
3	$2700 * 10^{-6}$
4	$2460 * 10^{-6}$
5	$2440 * 10^{-6}$
6	$2420 * 10^{-6}$
7	$2480 * 10^{-6}$

To measure local strains in the Cold Repair and to capture failure, 2D-DIC was used. Digital extensometers, as displayed in Figure 4.11 where the specimen is rotated by 45 degrees, were used to obtain strains in the following positions:

- Horizontal leg of the Cold Repair with $l_0 = 16\ mm$, to measure strain in longitudinal direction of the horizontal leg;
- Vertical leg of the Cold Repair with $l_0 = 40\ mm$, to measure strain in longitudinal direction of the vertical leg;
- Close to the edge of the Cold Repair with $l_0 = 50\ mm$, to measure fracture propagation;
- In the middle of the horizontal leg with $l_0 = 58\ mm$, to measure fracture propagation.

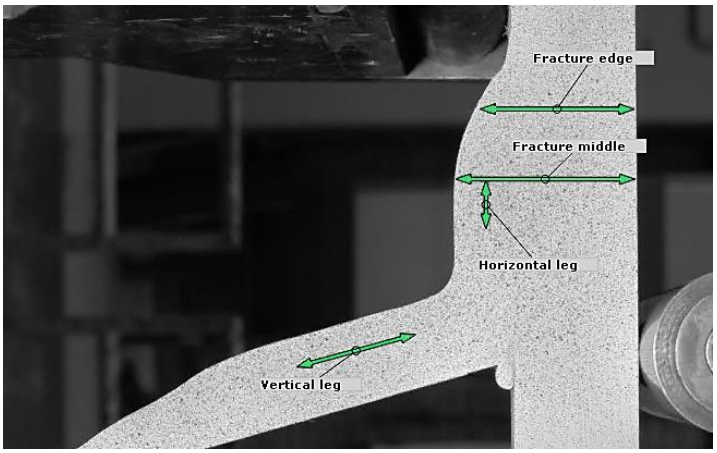

Figure 4.11: Digital extensometers DIC component-level tests

Load-strain curves of the DIC measurements can be observed in Figure 4.13 - Figure 4.14. Some important remarks regarding these results are:

- The 2D-DIC photos for test COMP-6 were out-of-focus and could therefore, unfortunately, not be used to determine strains. For this reason, results of test COMP-6 are not displayed in the load-strain curves.

- Since the first 2D-DIC photo for test COMP-5 was taken at a load level of around 37 kN, strains that occurred before that load level were not measured. This led to inconsistent results between sample 5 and the other samples. For this reason, results of test COMP-5 are not displayed in the load-strain curves.
- The position of the digital extensometers was chosen manually, meaning that small deviations between the positions exist between specimens. Since the results show relatively small strains for the legs of the Cold Repair, these small deviations could lead to relatively large differences in strains in the Cold Repair between specimens.

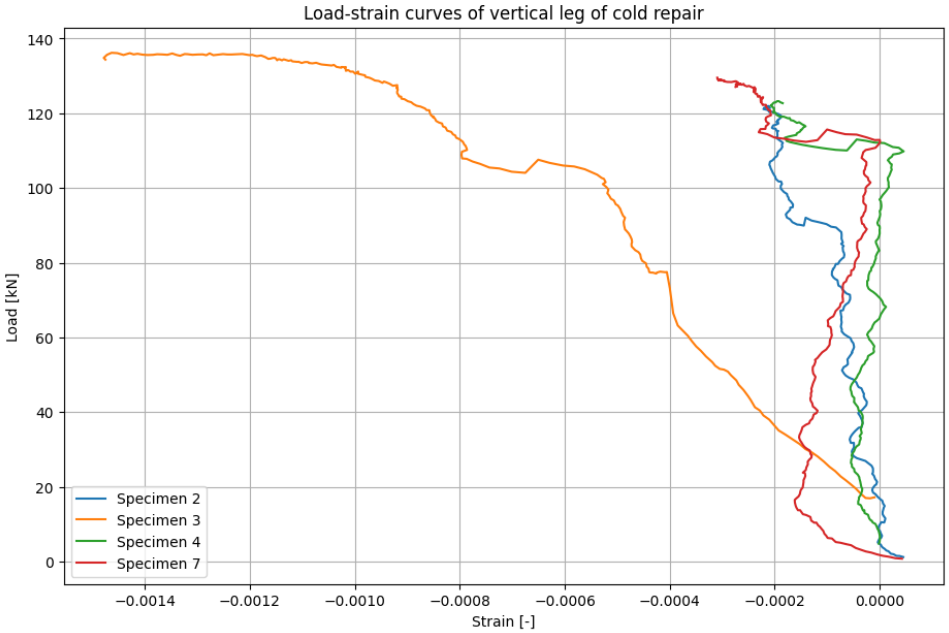

Figure 4.12: Load-strain curves of vertical leg of Cold Repair

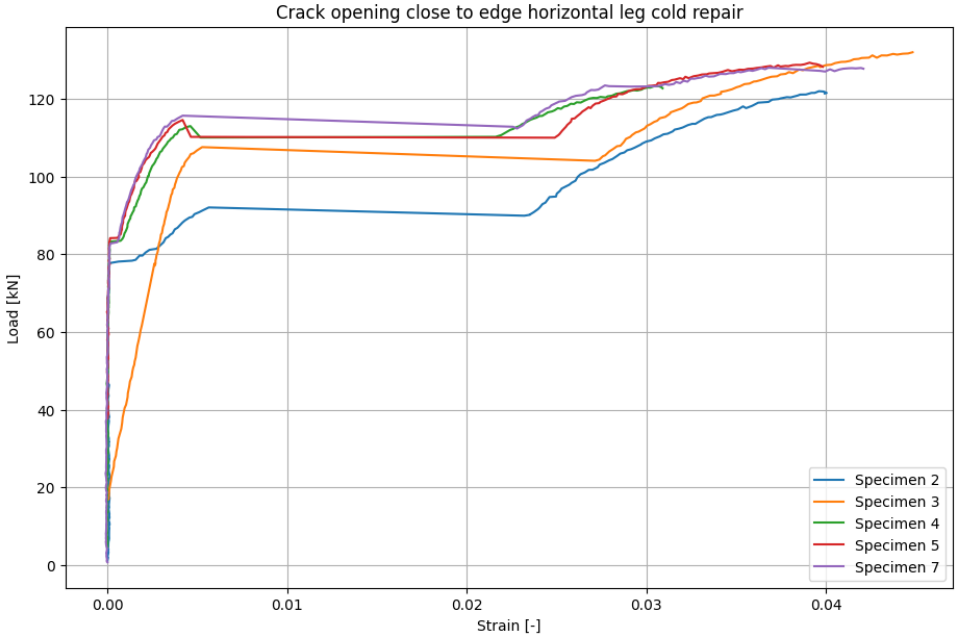

Figure 4.13: Crack opening close to edge horizontal leg Cold Repair

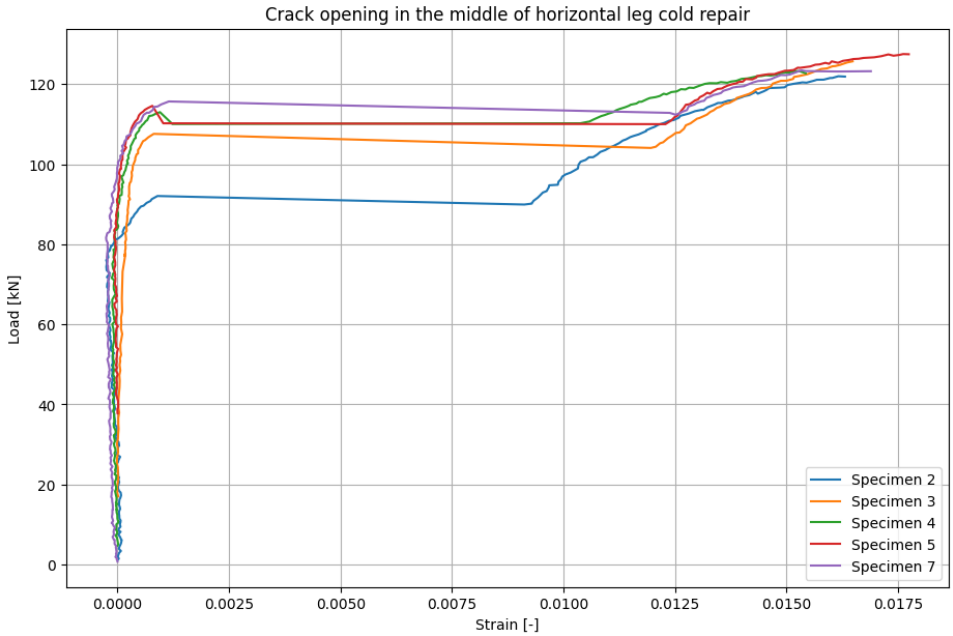

Figure 4.14: Crack opening in the middle of horizontal leg of Cold Repair

From these load-strain curves, the following observation and conclusions can be formulated:

- Especially from Figure 4.13, it becomes clear that test COMP-3.1 caused a stiffness decrease in the Cold Repair since strains in the legs of the Cold Repair are much higher and the crack propagation is initiated much earlier, around 20 kN as opposed to 82 kN, than the other tested specimens.
- In Figure 4.13, opening of the crack close to the edge of the horizontal leg is displayed. This is expressed in terms of strain of the total thickness of the component specimen, including deck plate strip and horizontal leg. It shows crack initiation by a small jump in strain, for which the load levels are displayed in Table 4.5, which is the case for specimens 2, 4, 5 and 7. For all specimens, crack initiation is followed by a slope change in the load-strain curves, indicating crack propagation. These conclusions are supported by the 2D-DIC results which show a clear opening of the crack. Strain plots of specimen 7, before crack initiation, after crack initiation and after debonding are displayed in Figure 4.15. DIC results for all specimens can be found in Appendix D.
- Figure 4.12 shows a jump in strains at the point of full debonding, corresponding with the jumps displayed in Figure 4.13 and Figure 4.14.

Table 4.5: Load levels at which crack initiation of component-level tests is observed

Specimen number	Load level at crack initiation [kN]
2	78.3
3	-
4	83.4
5	84.2
6	-
7	83.1

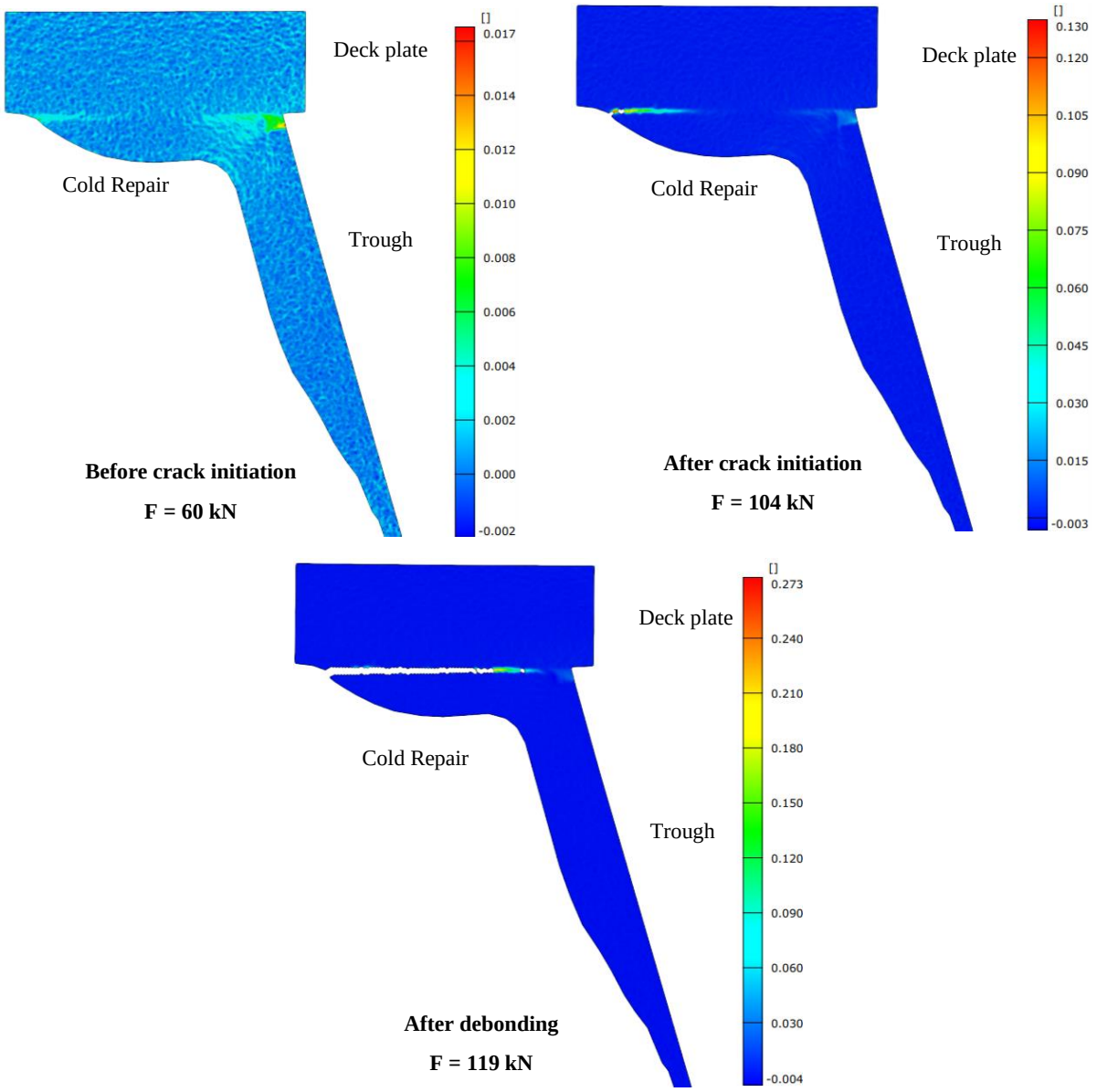

Figure 4.15: Major strain plots of COMP-7

4.3 Finite Element Model of Component Experiments

This section of the report provides an overview of the set-up of the FE models of the component experiments. This includes presenting the geometry and boundary conditions with corresponding mesh size. In addition, material models and modelling approaches for the adhesive interface are provided. To conclude, the FE type and analysis are presented.

4.3.1 Geometry and Boundary Conditions

FE models were developed in LS-DYNA R12. Since the samples are simply supported, a support boundary condition is defined where translation in z-direction and y-direction is constrained. Loading is applied to the deck plate in negative z-direction. Degrees of freedom that are not shown in this figure are considered as 'free' in the FE models. The model of the strengthened OSD component is displayed in Figure 4.16.

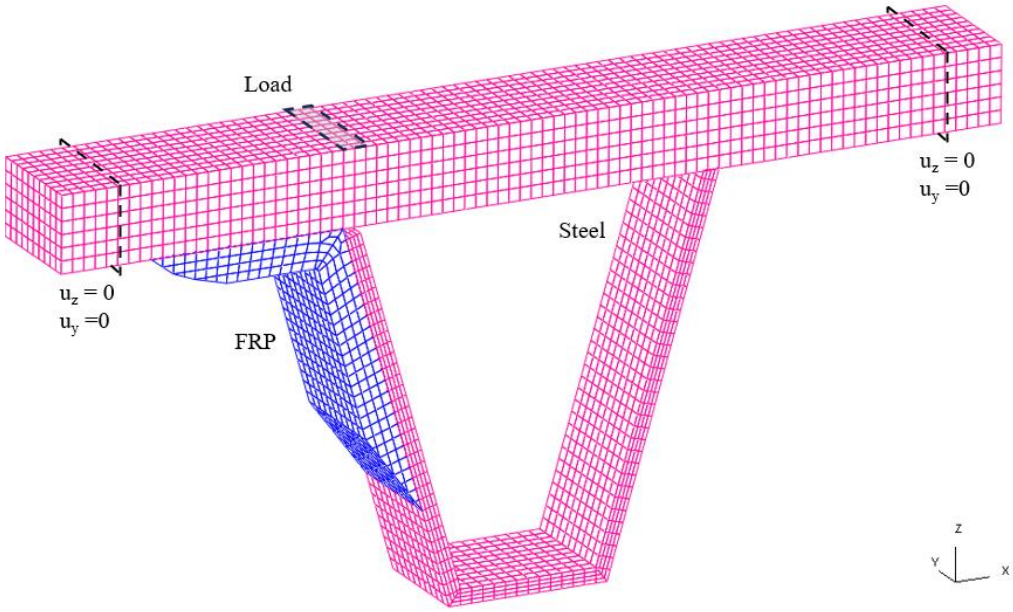

Figure 4.16: Geometry and boundary conditions of 3D FE model of component-level three-point bending test

4.3.2 Finite Element Types

Eight-noded hexahedron linear solid elements were used to model the FRP and steel trough and deck plate. Linear-elastic material models were applied to both the FRP and steel parts. An overview of the FE types is displayed in Table 4.6.

Table 4.6: Overview of FE types in component-level FE model

Part	Element type	DOF's per node	Interpolation	Stress components	Integration	Hourglass control
Steel	Eight-noded hexahdron solid element	u_x, u_y and u_z	Linear	σ_{xx}, σ_{yy}, σ_{zz}, σ_{xy}, σ_{xz}, σ_{yz}	Reduced	Yes, Belytschko-Bindeman
FRP laminate	Eight-noded hexahdron solid element	u_x, u_y and u_z	Linear	σ_{xx}, σ_{yy}, σ_{zz}, σ_{xy}, σ_{xz}, σ_{yz}	Full	Yes, Belytschko-Bindeman

4.3.3 Material Models

For both the steel and FRP in the component-level FE model, identical material models to the TAST FE models were applied. This means that the steel deck plate and trough are modelled by an isotropic elastic material, with properties displayed in Table 3.8. Moreover, the FRP angle is modelled by an orthotropic elastic material model, with properties displayed in Table 3.10.

4.3.4 Finite Element Mesh

For the numerical models of the TASTs, an elaborate mesh sensitivity study was performed to assess the correct mesh size. However, as one of the objectives of the component-level model was to compare the model with the full-bridge model, the same mesh size was implemented, with the smallest element size of 6 mm. Generally, in practice, a mesh size corresponding to the trough thickness is implemented in models of OSDs. The reason for this is the assessment of hot-spot stresses, for which stresses at a distance of 0.5 and 1.5 times the thickness of the trough are required, for a relatively coarse mesh [58]. In conclusion, a mesh size of six mm is applied for the numerical models.

Six elements were used for the thickness of the deck plate, and four elements for the thickness of the trough and cold repair. The FE model contains a total number of 9830 solid elements.

4.3.5 Steel – FRP Interaction

From section 3.3, the conclusion was made to implement both tie-breaks and tied interface conditions in the FE model of the component-level three-point bending tests. One model with tied interface condition and three models with tie-break adhesive interface were constructed.

The properties of the tie-break contact definition were initially determined based on the conclusions of the thick-adherend shear numerical study. An iterative process was performed to obtain a good match between the experimental and FE modelling results. The primary goal was to obtain a realistic load level at which total debonding of the horizontal leg occurred. Properties of several variations are provided in Table 4.7.

Table 4.7: Properties of tie-break contact definition of component FE models

Tie-break variation	Average shear capacity [MPa]	Average peel capacity [MPa]	Critical distance parameter [mm]
Variation A	30	10	0.1
Variation B	40	20	0.1
Variation C	60	20	0.1
Variation D	80	20	0.1

4.3.6 Finite Element Analysis

Explicit analysis was performed for the final 3D FE model, as tie-break contacts cannot be analysed with implicit analysis. A linear static load was applied, as displayed in Figure 4.17.

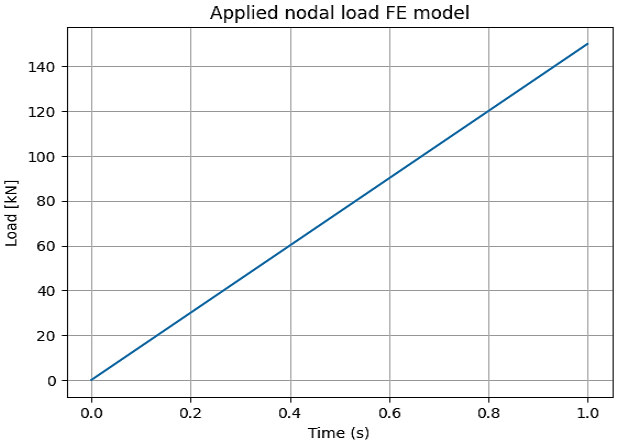

Figure 4.17: Applied load of component-level FE model

4.4 Discussion of Component-level Numerical Models

This section of the report provides a discussion of the 3D FE models. This discussion consists of a comparison of the global behaviour of the FE models and experimental results, in the form of load-displacement curves. Moreover, an overview of the influence of the Cold Repair is displayed.

4.4.1 Load-displacement Curves of Comparison FEM and Experimental results

Discussion of the numerical models involves the comparison of the load-displacement curves from experiments with those obtained by the FE models. The numerical study includes two modelling approaches regarding the FRP-steel adhesive interface, which are:

- Tied contact definition
- Tie-break contact definition: Variation A, B, C and D

Since geometric and material imperfections between the component samples are much smaller compared to the TAST specimens, the FE model was built according to average geometry parameters. For this reason, the mean curve of all tested samples is used for the comparison. The load-displacement curves are displayed in Figure 4.18. Displayed displacements are determined in the middle of the deck plate, which is the same position as the LVDT during experiments. An inset of the FEM results can be observed in Figure 4.19.

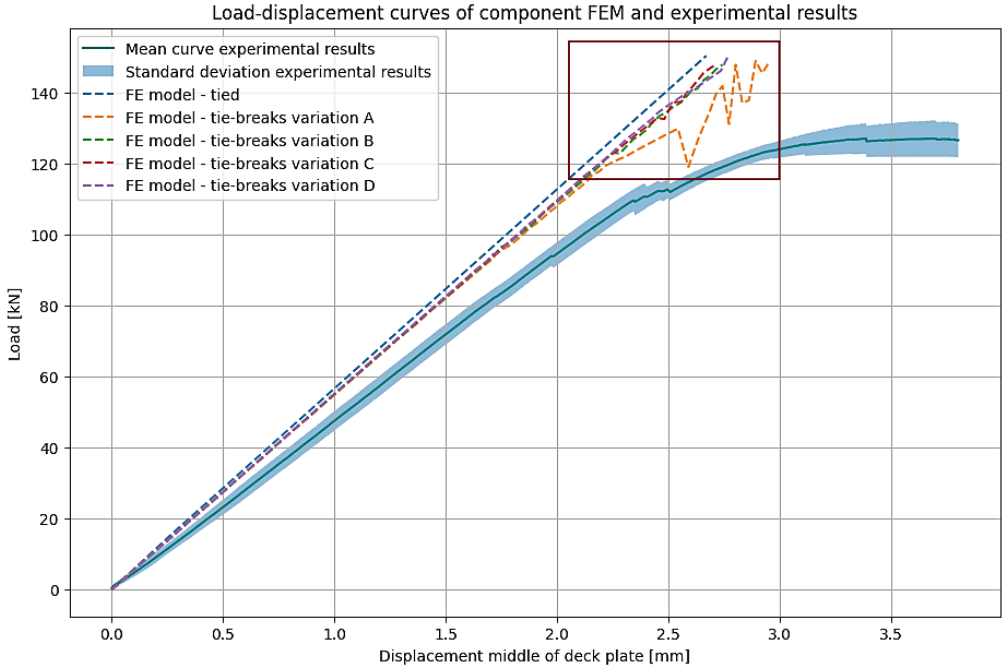

Figure 4.18: Load-displacement curves of FEM and experimental results for COMP-7

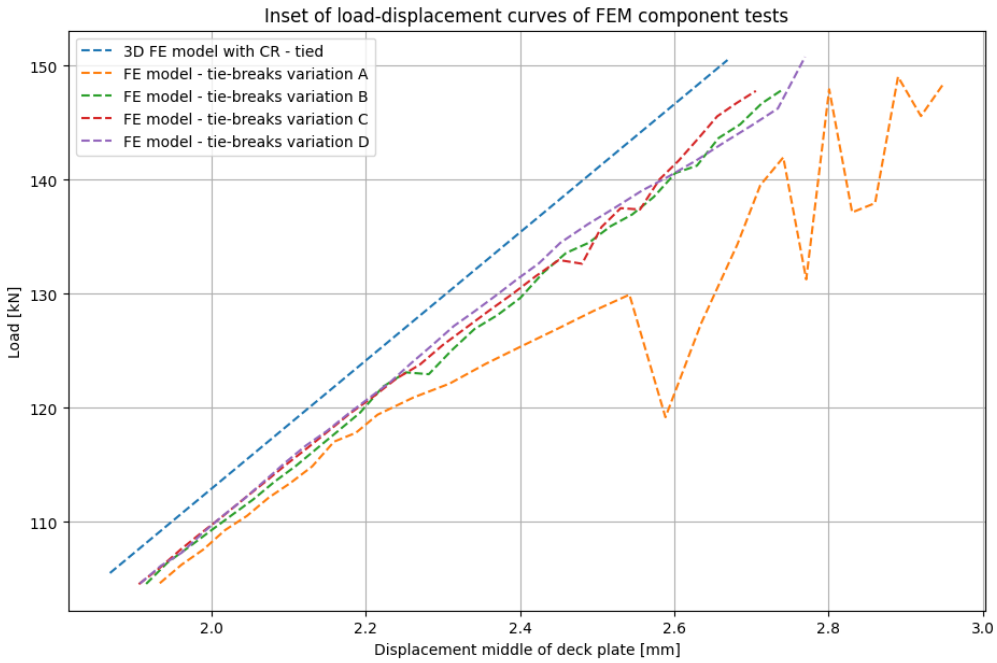

Figure 4.19: Inset of load-displacement curves of FEM component tests

From the displayed load-displacement curves, the following observations can be formulated:

- There is a deviation between the load-displacement curves of the FE models and experimental results of sample COMP-7. This shows that the FE models overestimate the global stiffness of the component specimens when loaded in bending. The stiffness of the linear-elastic behaviour of the mean curve, as displayed in Figure 4.18, is 4.77 * 10^4 [N/mm]. Deviations between the numerical models and experimental results are displayed in Table 4.8.
- Though much less noticeable than the difference between the FE and experimental results, there is difference in global stiffness between the FE models with tied interface condition and tie-break interface conditions. This could be explained by an insufficient stiffness of the non-physical springs in the FE model.
- From the load-displacement curves, it is difficult to observe the specific failure behaviour of the tie-break variations. For this reason, resultant contact forces of the adhesive interface between deck plate and horizontal leg of the Cold Repair are displayed in Figure 4.20.

Table 4.8: Deviation between component FE models and experimental data

Model	Stiffness [N/mm]	Deviation from test results
Tied interface	5.64 * 10^4	+ 18%
Tie-break variation A	5.45 * 10^4	+ 14%
Tie-breaks variation B	5.46 * 10^4	+ 14%
Tie-breaks variation C	5.49 * 10^4	+ 15%
Tie-breaks variation D	5.48 * 10^4	+ 15%

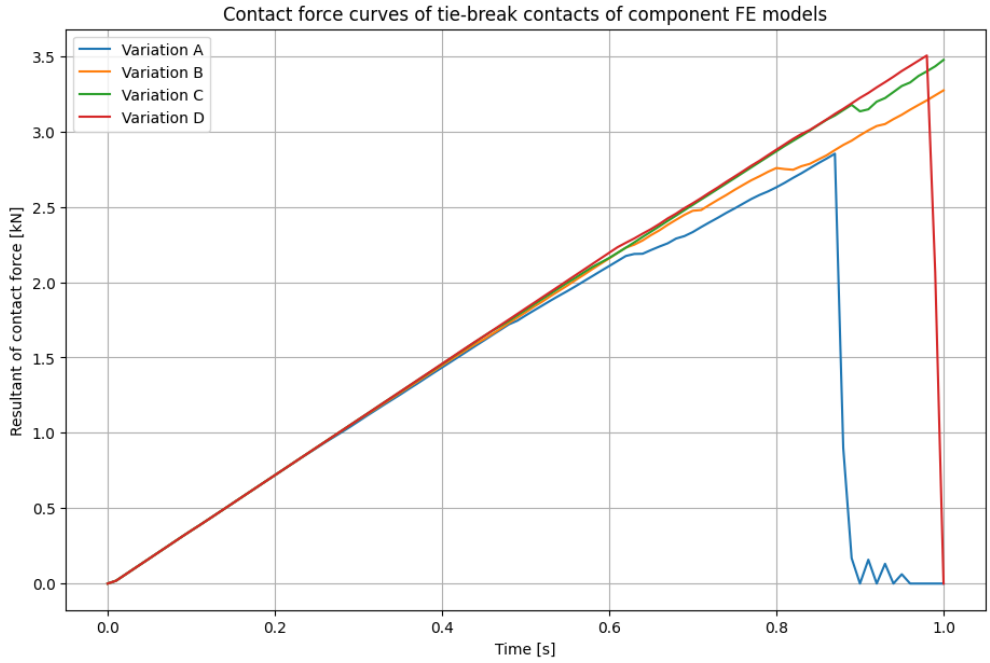

Figure 4.20: Contact force curves of adhesive interface deck plate – horizontal leg of component FE models

Figure 4.20 shows that variations A and D experience total debonding, while variations B and C show partial debonding. As experiments revealed full debonding of the horizontal adhesive bond, variations B and C were excluded from the final FE model. As there is a 30 kN additional capacity between crack initiation and total debonding, variation D, showing debonding without crack propagation, was also not considered. Tie-break variation A, which allows for crack propagation and full debonding of the horizontal leg of the Cold Repair, was selected for the FE model of the component-level tests.

4.4.2 Impact Cold Repair on Global Stiffness Component Specimen

Since there are several uncertainties involved regarding modelling of FRP, two FE models were developed to determine the effectiveness of the Cold Repair. To provide a correct comparison, the initial gap between trough and deck plate was replaced for a tied connection. The reason for this was to ensure the model without Cold Repair would utilize the trough component as well, which is not the case if the trough and deck plate are disconnected. The interface between FRP and the OSD component is modelled as a tied contact. The set-up of both models is displayed in Figure 4.21.

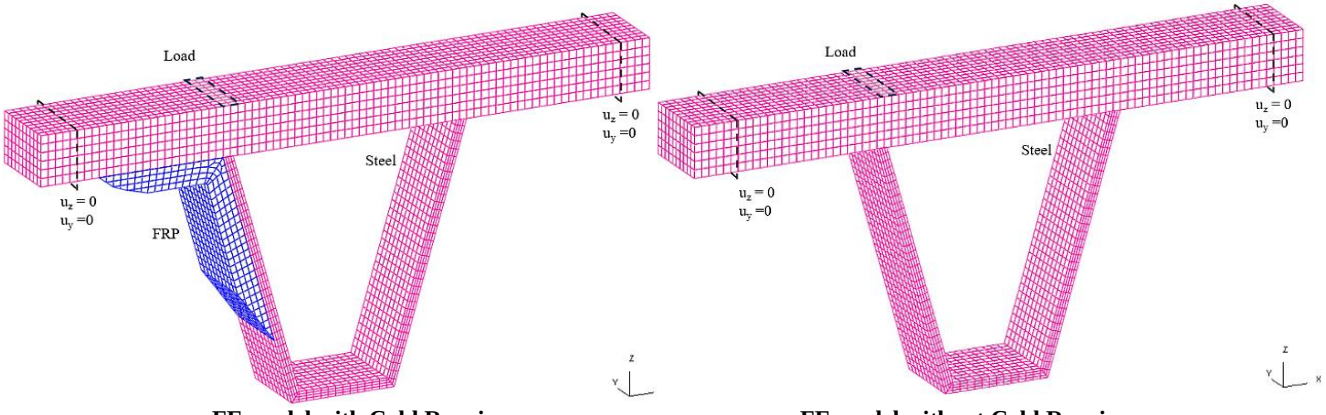

FE model with Cold Repair **FE model without Cold Repair**

Figure 4.21: 3D FE model of OSD component with and without Cold Repair and attached trough-deck connection

Load-displacement curves of both FE models are shown in Figure 4.22. The mean load-displacement curve of experimental results is also displayed to illustrate the performance of these models compared to the component samples. An important remark is that the component strips do not consist of a welded trough-deck joint.

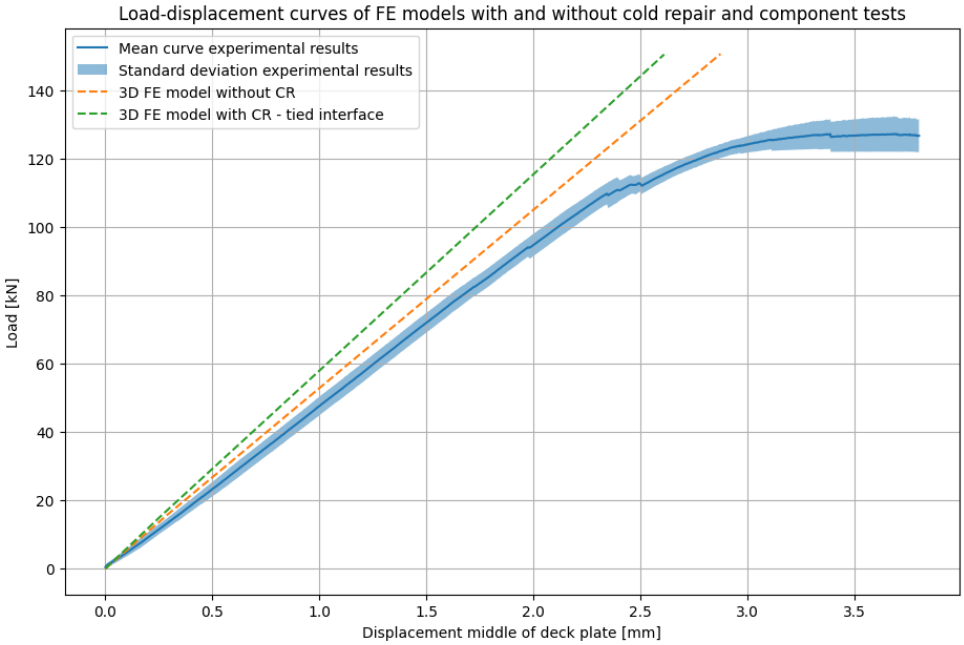

Figure 4.22: Load-displacement curves of FE models with and without Cold Repair and component tests

Based on displayed load-displacement curves, the following observations and conclusions can be formulated:

- The model with Cold Repair provides a higher stiffness than the model without Cold Repair, which is in line with expectations. The model with Cold Repair results in an increase in global stiffness of + 9.9% compared to the model without Cold Repair.
- Both FE models show an overestimation of the global stiffness when compared to experimental results. Theoretically, the FE model without Cold Repair should have a lower performance than experimental results, since the samples are strengthened by the application of the FRP angle. However, this behaviour can be explained by the influence of the tied trough-deck plate connection in the models, which leads to an increase in global stiffness of the entire component.

This last observation sparks interest into the influence of the tied trough-deck connection. For this reason, the 3D FE models with Cold Repair and with and without tied trough-deck joint, as displayed in Figure 4.21, are compared. The interface between FRP and the OSD component is modelled as a tied contact. Load-displacement curves of this analysis can be observed in Figure 4.23.

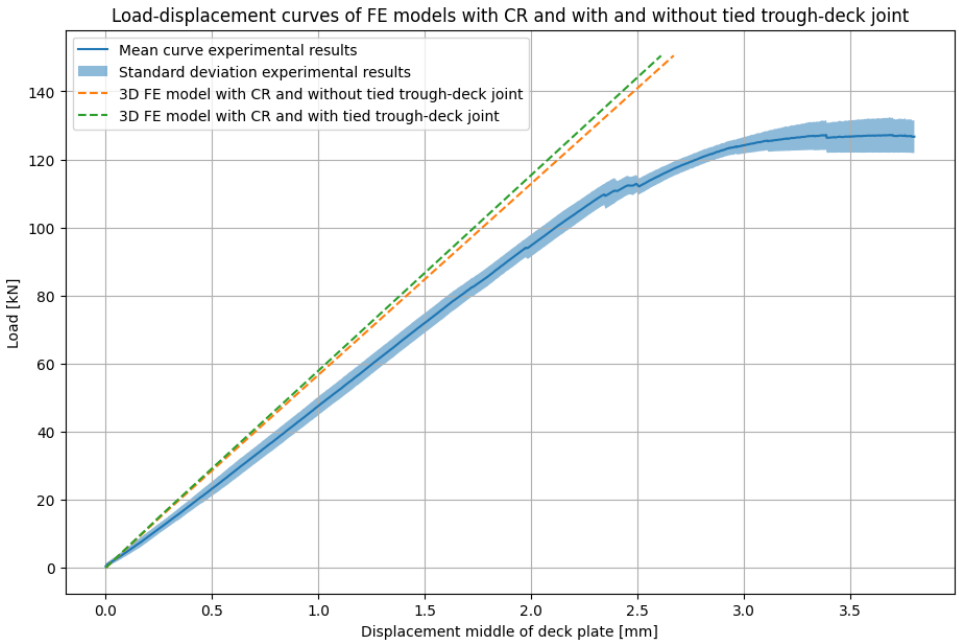

Figure 4.23: Load-displacement curves of FE models with and without tied trough-deck joint

These load-displacement curves show that the influence of the tied trough-deck joint is relatively small, with a deviation of +2.3% for the model with attached trough-deck component. From this result, the conclusion can be drawn that the tied connection alone does not provide a thorough explanation for the stiffness difference between the model without Cold Repair and experimental results.

4.5 Results

This section of the report provides results, conclusions and recommendations for the component-level numerical and experimental study. First, a model validation is performed for the FE model, followed by results of the models. In addition, an estimation of design values of the bond strength is provided. To conclude, a discussion of the component-level study is provided.

4.5.1 Model Validation

For the validation of the FE model, a comparison between strains based on the DIC results of the experiments and based on the FE model is performed. This comparison includes strains in principal direction.

An important remark is that the DIC results do not show strains on the entire surface of the specimens, but of a subsection. To increase the accuracy of the comparison, the same subsection of the surface of the FE model is displayed. In addition, the extreme values of the legend of the FEM results were matched to the extreme values of the DIC plot. Since crack initiation and propagation were observed in the DIC results of the experiments, three significant stages are displayed in the model validation, which are:

- Stage before crack initiation with a load level of 60 kN
- Stage after crack initiation with a load level of 104 kN
- Stage after total debonding of the horizontal leg of the Cold Repair with a load level of 119 kN.

Strains of DIC and numerical results of specimen 7 are displayed in Figure 4.24 - Figure 4.26. Numerical results of the component-level FE models are presented in Appendix E.

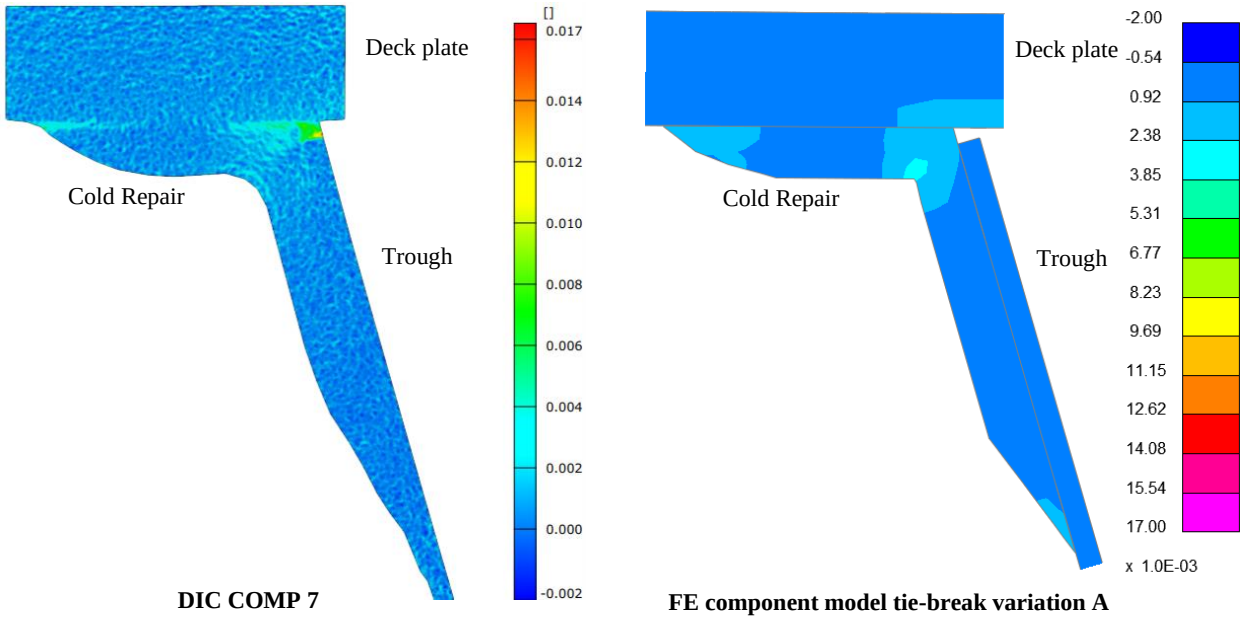

Figure 4.24: Strain in principal direction for DIC COMP 7 and FEM tie-break variation A at F = 60 kN

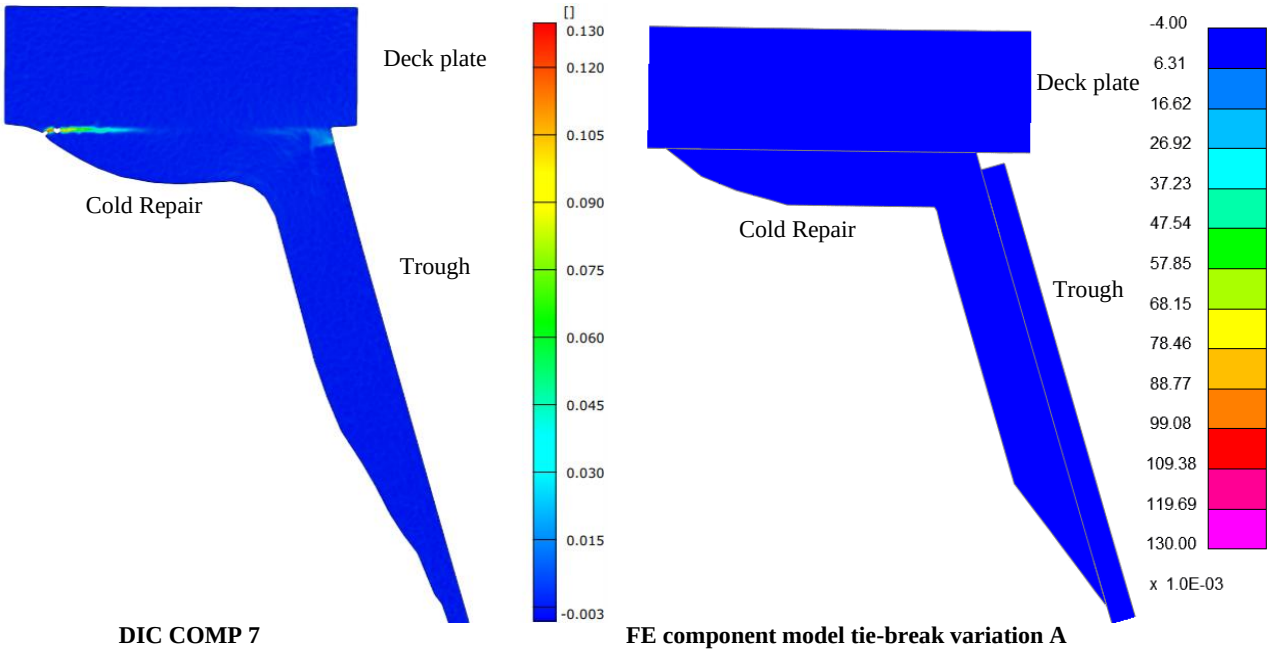

Figure 4.25: Strain in principal direction for DIC COMP 7 and FEM tie-break variation A at F = 104 kN

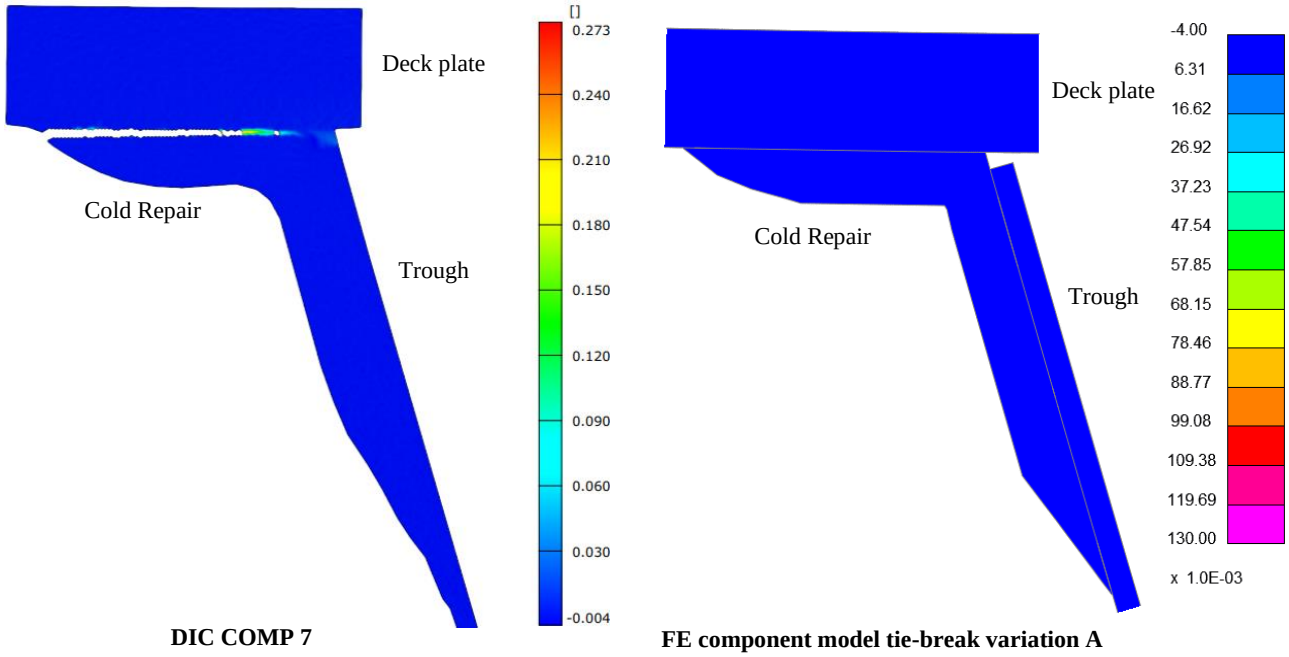

Figure 4.26: Strain in principal direction for DIC COMP 7 and FEM tie-break variation A at F = 119 kN

From these strain and bond contact results, the following observations and conclusions can be formulated regarding validation of the FE models:

- The strain plots indicate negligible strain levels in the steel deck plate and trough for all three load levels. At a load level of 60 kN, strain peaks are mainly observed around the inner and outer edge of the horizontal interface in both the experimental set-up as the FE model. However, the DIC strain plot reveals maximum strains in the trough-deck plate joint. This behaviour aligns with expectations, as the rubber in the specimens is assumed to have a substantially lower stiffness than the OSD component and Cold Repair, leading to higher strains.

- High strain peaks and a visible gap in the horizontal adhesive bond display crack initiation and propagation from the outer edge of the horizontal adhesive joint in the experimental results. The FE model shows crack propagation and initiation as well but this is not visible in displayed figures.

- To display failure of the adhesive interface in FEM, Figure 4.27 - Figure 4.29 can be observed. Figure 4.27 shows the position of horizontal, indicated by yellow, and vertical, indicated by green, adhesive interface. In Figure 4.29, debonding is represented by values between 0 and 1, where 0 indicates full contact and 1 indicates no contact. It is evident that crack initiation and propagation do not follow the same pattern in experimental results, with the following differences:

    - Experimental results of specimen COMP-7 show no crack initiation up to a load of 100 kN with full debonding at around 119 kN. The FE model displayed the first crack initiation around 60 kN. This means that the FE model with tie-breaks underestimates the adhesive bonded joint.

    - DIC results indicate that a crack propagation is initiated from the outer edge of the horizontal adhesive interface. This is in contrast with the FE model, where debonding is mainly propagating from the inner edge of the interface, while the outer edge suffers debonding to a lesser extent. However, the presence of the gap between trough and deck plate in the FE model could provide an explanation of this dissimilarity.

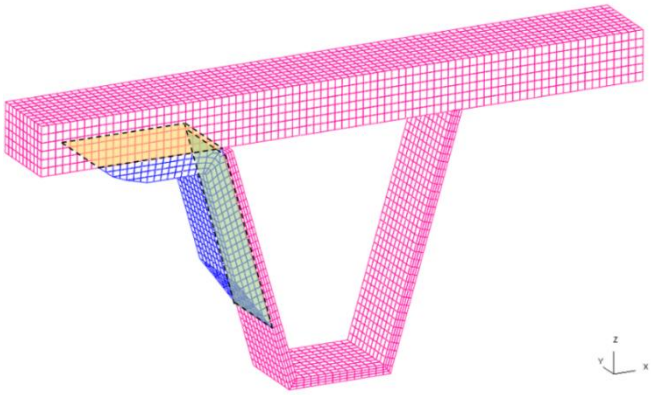

Figure 4.27: Position of horizontal and vertical adhesive interface of component-level FE model

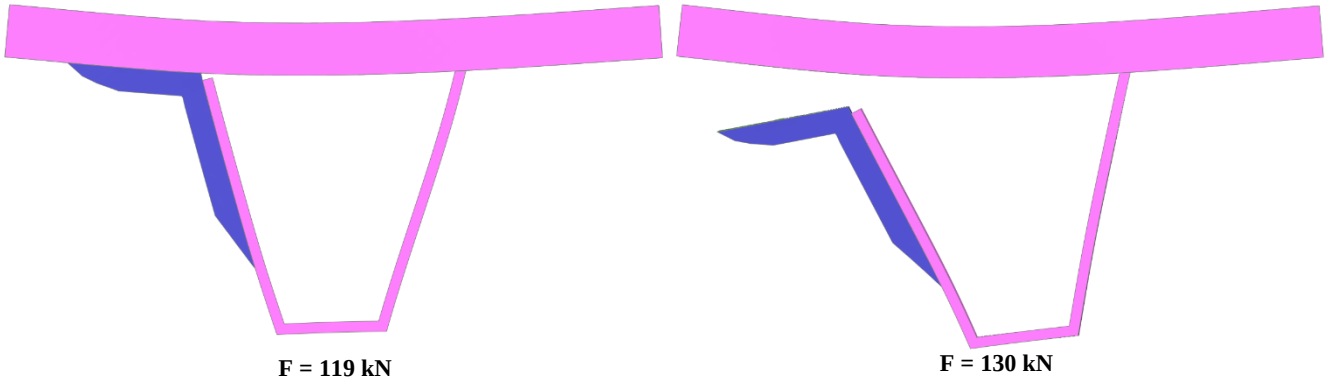

Figure 4.28: Failure of the adhesive interface between Cold Repair and OSD in FEM

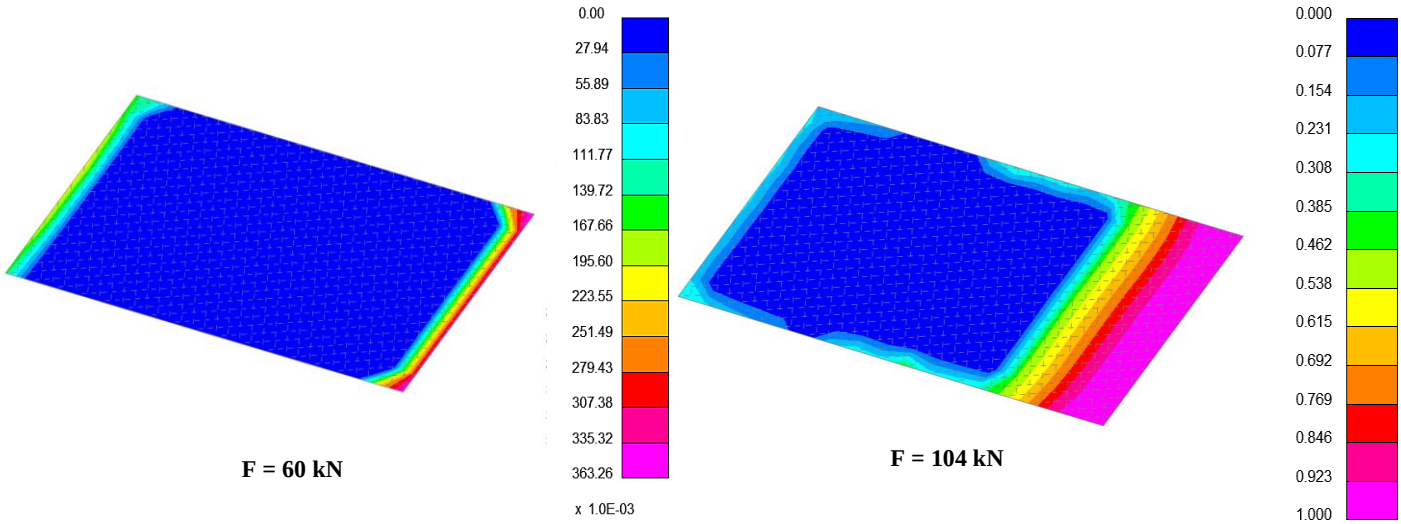

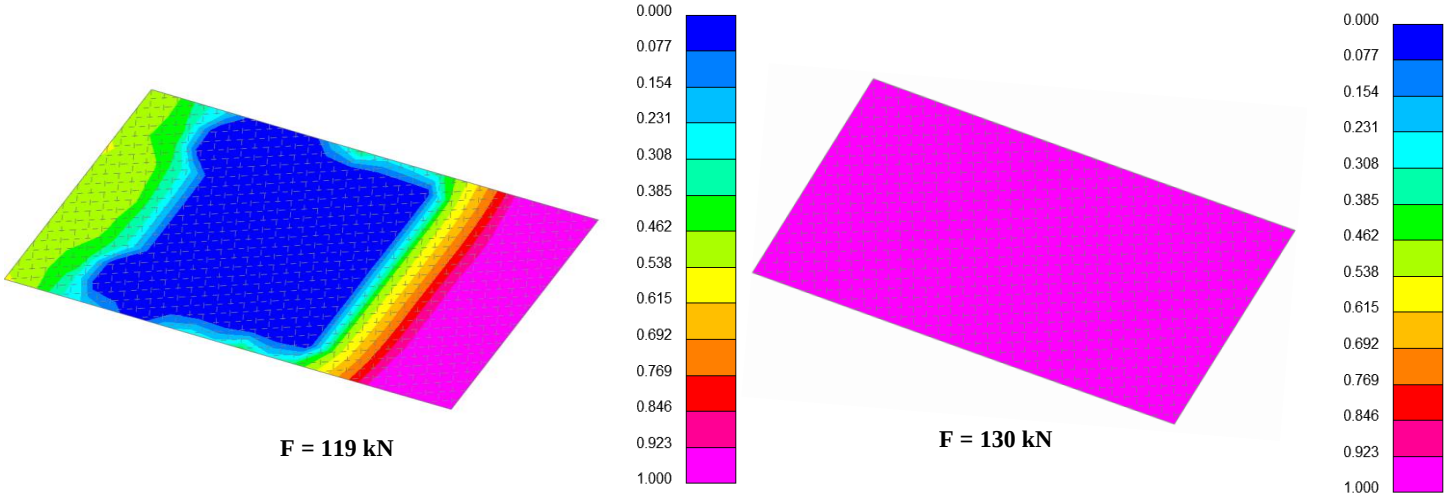

Figure 4.29: Debonding of adhesive interface between deck plate and horizontal leg of Cold Repair

In conclusion, while the FE models demonstrate a reasonable qualitative strain distribution in principal direction, the current tie-break contact interface in the FE model does not fully capture the debonding behaviour observed during experiments, as there is a discrepancy between the experimental and FE model debonding behaviour.

4.5.2 Impact Cold Repair on Stress Distribution in Trough Leg

As outlined in section 4.4.2, the Cold Repair positively impacts the global stiffness of the OSD component, resulting in an increase of 9.9% compared to the model without Cold Repair. However, as the goal of the Cold Repair is not defined as increasing the global stiffness of the OSD, but to take over the function of the weld, the repair method should reduce stress concentrations in the trough-to-deck plate weld. For this reason, a comparison of local stresses in the trough for the model with and without Cold Repair is performed.

To provide a correct comparison, the initial gap between trough and deck plate was replaced for a tied connection. The reason for this was to ensure the model without Cold Repair would utilize the trough component as well, which is not the case if the trough and deck plate are disconnected. The interface between FRP and the OSD component is modelled as a tied contact. Both FE models can be observed in Figure 4.21. Contour plots of stresses in local y-direction (bending stress) are displayed in Figure 4.30. The deck plate is removed to increase visibility of the stress distribution.

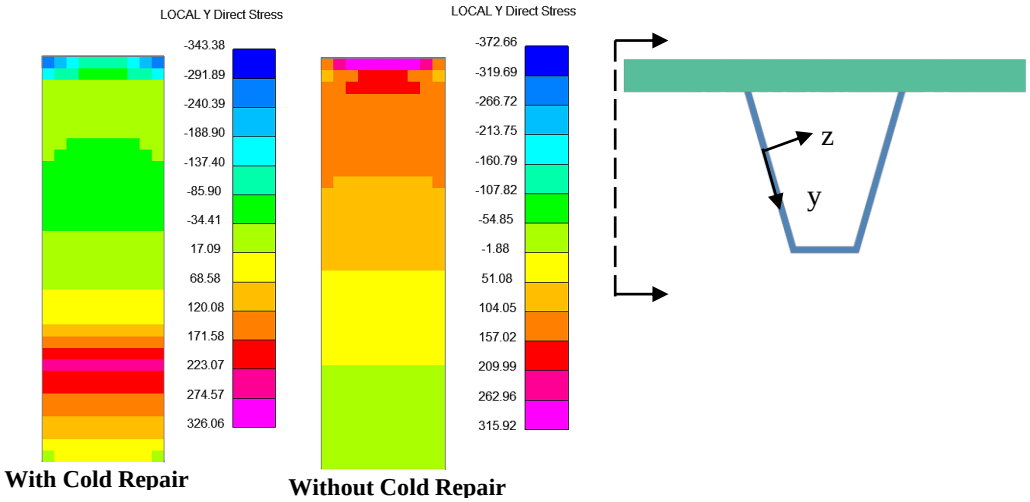

Figure 4.30: Local y-directional stress in trough leg with and without Cold Repair

In Figure 4.31, the mid-plane, read from the top fibers in the second row of elements, and bending stresses in the centre solid elements of the trough leg are displayed. Generally, hot-spot stresses would be indicated at distances of 0.5 and 1.5 times the trough plate thickness from the toe of the weld. However, as the strip models exhibit a mesh size of 6 mm, to match the mesh size of the full-bridge model, and the trough thickness is 8 mm, these stresses cannot be directly obtained from the model.

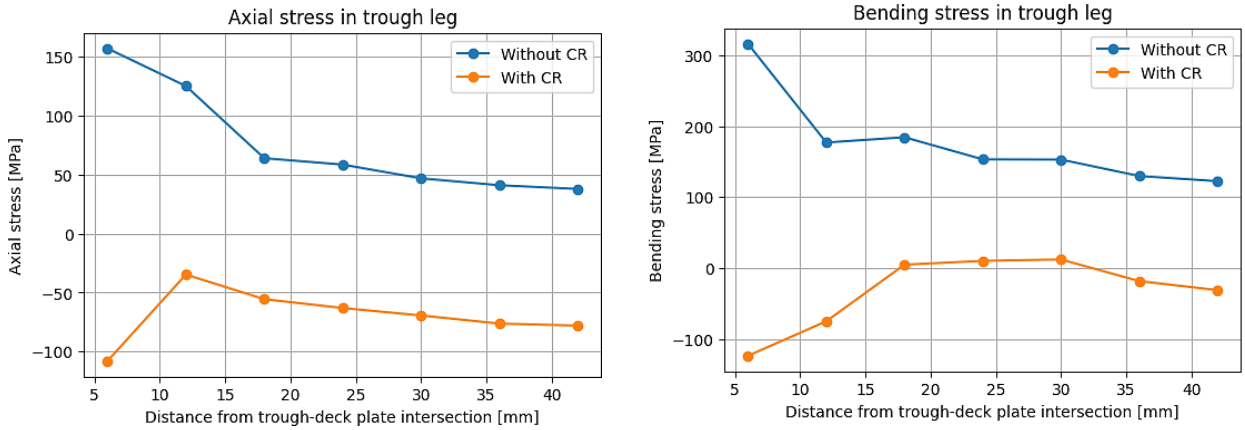

Figure 4.31: Axial and bending stress distribution in trough leg along the length of the trough

As can be seen from the stress distributions, the Cold Repair decreases the bending and axial stress, especially close to the deck plate intersection. Additionally, the Cold Repair leads to compressive stresses in the trough leg while the model without cold repair does not demonstrate any compressive stresses in the upper part of the trough leg. This highlights that the cold repair changes the complete behaviour of the trough leg for this specific component strip. This conclusion is supported by the deformed shape of the component specimen with and without Cold Repair, which exhibits a different behaviour, as can be observed in Figure 4.32.

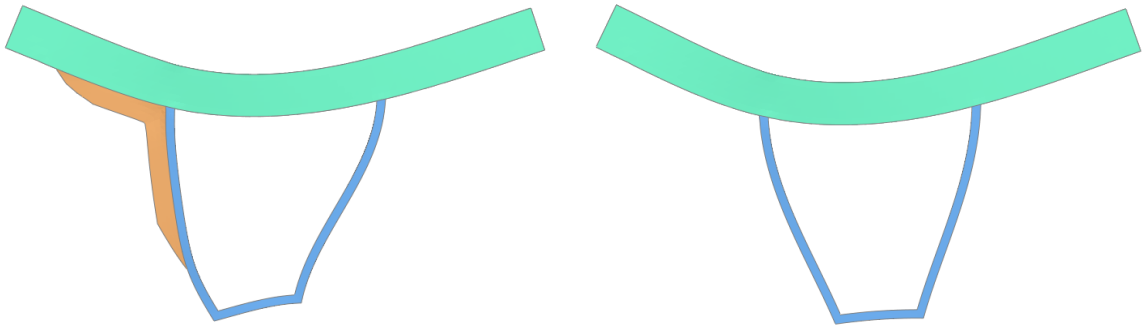

Figure 4.32: Deformed shape of FE model with and without CR (magnified 30x)

4.5.3 Design Values Bond Strength

To gain insight into the design values of the adhesive bond strength, Annex D of Eurocode 1990 was used to determine characteristic and ULS values. This section shows the major steps and conclusions of this evaluation. The full calculation is provided in Appendix F.

Since all six samples of the component tests displayed debonding initiated from the outer edge of the horizontal leg of the Cold Repair, all specimens are included in the determination of design values of the bond strength. The FE model with tie-breaks was used to obtain bond stresses at the outer edge of the horizontal leg of the Cold Repair. For every sample, the bond stresses were taken at the load level at which debonding occurred. Determined bond stresses at the outer edge of the horizontal leg of the Cold Repair are displayed in Table 4.9. These stresses are not the maximum observed stresses but local stresses, making them subject to mesh size and not to be confused with average bond stresses.

Table 4.9: Bond stress at outer edge of horizontal leg of CR for component specimens

Specimen number	Load at debonding [kN]	Shear bond stress [MPa]	Peel bond stress [MPa]
Specimen 2	92.2	16.0	7.5
Specimen 3	107.9	16.3	7.6
Specimen 4	113.5	16.8	6.8
Specimen 5	114.9	16.9	6.5
Specimen 6	116.5	17.0	6.3
Specimen 7	115.9	16.9	6.5

The FE model was used to assess the ratio peel / shear stress for the outer edge of the horizontal interface, which is dependent on the load level. The ratio peel / shear stress at the average failure load of 110.15 kN is 1 / 2.4. This ratio indicates a high level of mixed-mode behaviour. For this reason, and because the obtained ratio peel / shear stress is based on peak stresses and not on average values, no average bond strength values could be derived. However, values for the peak bond strength with a specific ratio of 1 / 2.4 and a mesh size of 6 mm were determined to provide insight into the adhesive bond strength of the Cold Repair and how it compares to the TASTs.

Similarly as for the TASTs, Annex D of Eurocode 1990 was used to determine characteristic and design values for the peak shear and peel bond strength. Values for the peak bond strength are displayed in Table 4.10. As these results are based on peak stresses, they could not be compared to derived peak shear bond strengths from TASTs, as these values were based on a different mesh size.

Table 4.10: Values peak bond strength based on component-level tests at ratio peel / shear of 1 / 2.4 and mesh size of 6 mm

Property	Characteristic value	Design value for ULS verifications
Peak shear strength at outer edge [MPa]	15.80	14.28
Peak peel strength at outer edge [MPa]	5.77	4.16

4.6 Comparison between Component-level and Full-bridge Numerical Model

This section of the report provides a comparative analysis of the component-level strip model, constructed within this thesis, and the full-bridge model, constructed by Arup. It highlights key differences between the models and provides a qualitative and quantitative comparison.

4.6.1 Set-up of Full-bridge Model provided by Arup

Arup has provided an existing FE model of the Second Van Brienenoord bridge. The geometry and boundary conditions of this model are displayed in Figure 4.33. The analysis is focused on governing detail 2, marked red.

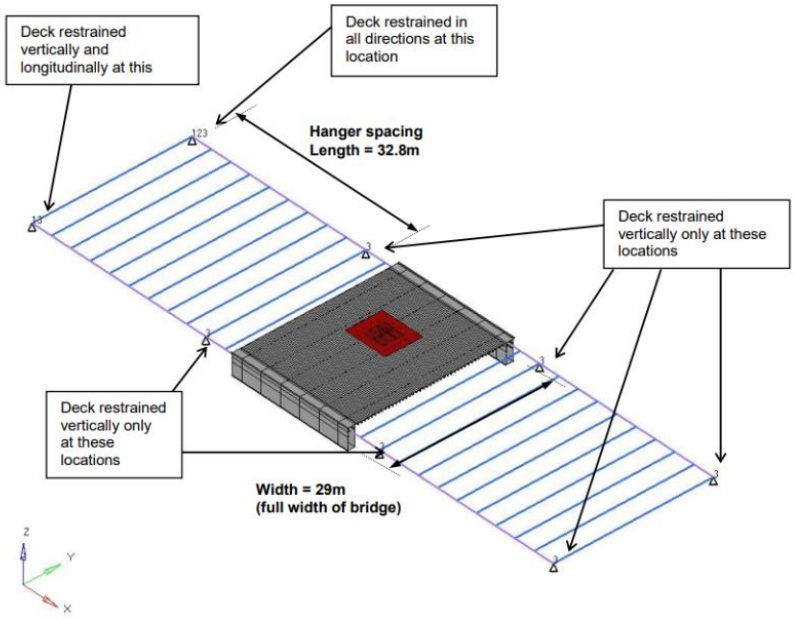

Figure 4.33: Geometry and boundary conditions FE model Second Van Brienenoord bridge (Arup)

Arup's research focuses on the contribution of the Cold Repair by comparison of a FE model with and without Cold Repair. The FE model without Cold Repair exhibits three main elements, displayed in Figure 4.34 and Table 4.11.

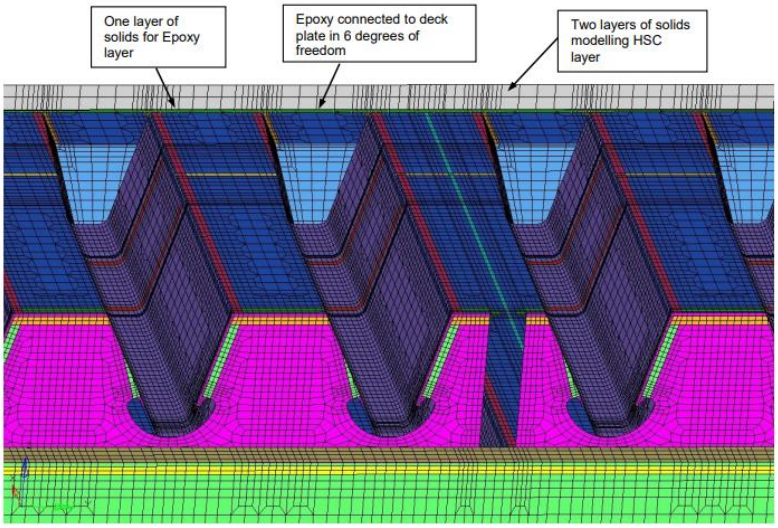

Figure 4.34: Elements in FE model Second Van Brienenoord bridge without Cold Repair (Arup)

Table 4.11: Elements with corresponding element type in FE model Van Brienenoord bridge without Cold Repair

Part	Element type	Thickness [mm]	Young's Modulus [GPa]	Poisson's ratio [-]
Steel OSD	Shell elements	Deck plate = 12 Trough = 6	210	0.3
HSC overlay	Two rows of solid elements	50	22.5	0.2
Epoxy layer between HSC overlay and deck plate	One row of solid elements	3	1.15	0.4

Similar as in this thesis, the OSD is strengthened with the Cold Repair. Several geometries were considered in a sensitivity study with the final geometry modelled according to Figure 4.35. FRP lay-up and properties outlined in this thesis were applied in the full-bridge model as well. A tied contact between the OSD and Cold Repair was implemented.

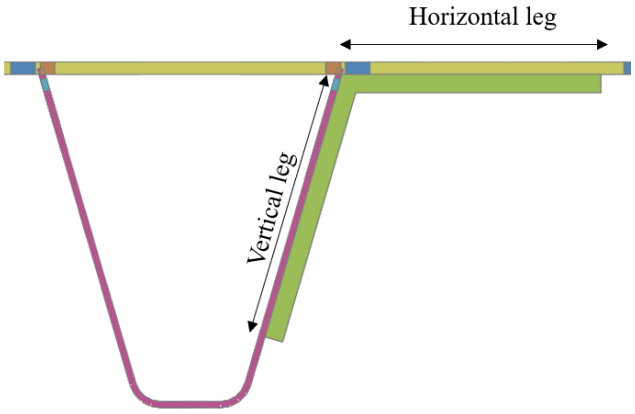

Geometrical parameters	Cold Repair
Thickness	18 mm
Horizontal leg	150 mm
Vertical leg	150 mm
Length	1420 mm

Figure 4.35: Geometry Cold Repair in full-bridge model (Arup)

4.6.2 Comparison of Strip Model and Full-bridge Model

One of the objectives of this thesis research is to assess to what extent the full-bridge model provided by Arup gives comparable results to the component strip model. This comparison relies on similarities with respect to model set-up to provide a proper comparison. However, the full-bridge and strip model exhibit several dissimilarities, making it complex to perform a proper comparison. Identified dissimilarities can be defined as:

- **Loading condition.** In the full-bridge model, a patch load that resembles a tyre load in traffic loading conditions, is applied to the OSD. However, a line load over the entire width of the strip component was applied in the strip model. The impact of the loading condition is verified on a FE model of an unstrengthened OSD component, modelled by shell elements and with a length of 1000 mm, as opposed to the 60 mm of the strip model. The comparison is displayed in Figure 4.36 and shows that the loading conditions impact the distribution of bending stresses in the trough.

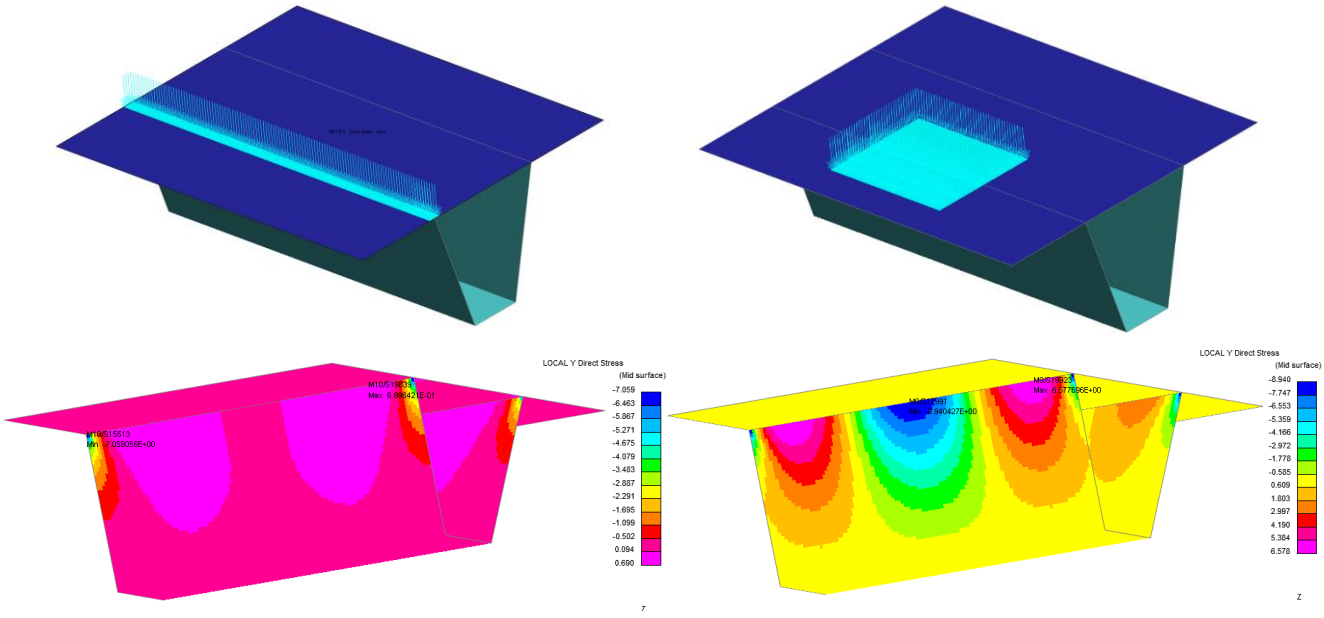

Line load **Patch load**

Figure 4.36: Comparison of loading condition on unstrengthened OSD component

- **Boundary conditions**. The main difference between the strip model and full-bridge model is defined by the boundary conditions. While the strip model is simply supported by supporting the deck plate, the full-bridge model exhibits a supported trough, which is supported by crossbeams, and an increased stiffness of the deck plate supports since the model is extended beyond the displayed detail of strengthened OSD.

- **Dimensions**. Since the strip model is downscaled by a factor 1.5 compared to the full-bridge model, size effects could lead to deviations between results of the component strip and full-scale bridge model. Moreover, the length of the horizontal and vertical leg of the Cold Repair in the strip model is smaller than in the full-bridge model. However, thicknesses are not scaled in the component strip model.

- **Element formulation**. While the full-scale model exhibits shell element formulation for the OSD, the strip model applied solid elements. This difference lies in the presence of the HSC overlay, which is modelled by two rows of solid elements in the bridge model. However, to simulate the additional stiffness of this HSC overlay, the thickness of the deck plate strip in the component specimens was increased. To simulate the experiments, four rows of solid elements were used in the strip model since shell elements are not able to sufficiently take this relatively large thickness into account.

Apart from these dissimilarities, the full-bridge model and component model implement two distinct interface conditions, where the full-bridge model implements tied interface conditions, and the component strip model implements tie-break interface conditions. As outlined in previous sections, the major difference between tied and tie-break interface conditions lies in the inclusion of failure modelling. This means that the full-bridge model is not able to capture debonding of the adhesive interface, as tied contacts are used.

While an accurate comparison of both models is challenging, stress plots for the shear and normal bond stress of both FE models are compared to gain insights into the contribution of the Cold Repair. For the full-bridge model, three cases of tandem loads according to LM1 and LM2 of traffic loading according to Eurocode 1991 [59], as displayed in Figure 4.37, are considered. Occurring bond stresses are displayed in Figure 4.38 and Figure 4.39. To compare, occurring bond stresses in the strip model at a load level of 60 kN are displayed in Figure 4.40.

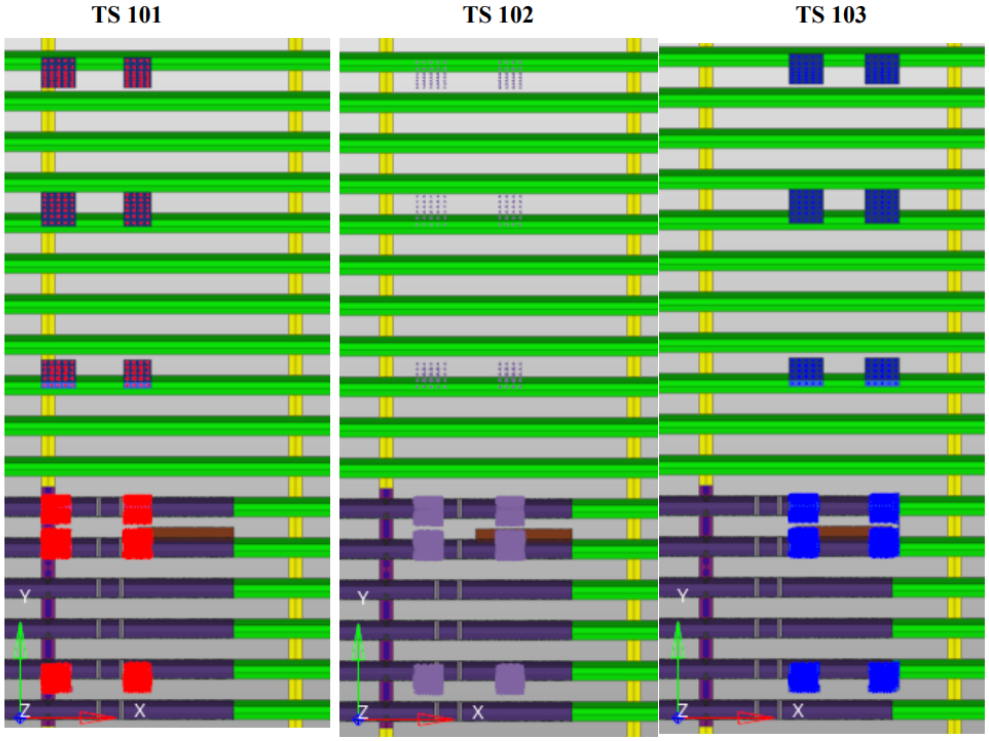

Figure 4.37: Tandem load cases applied in full-bridge model (Arup)

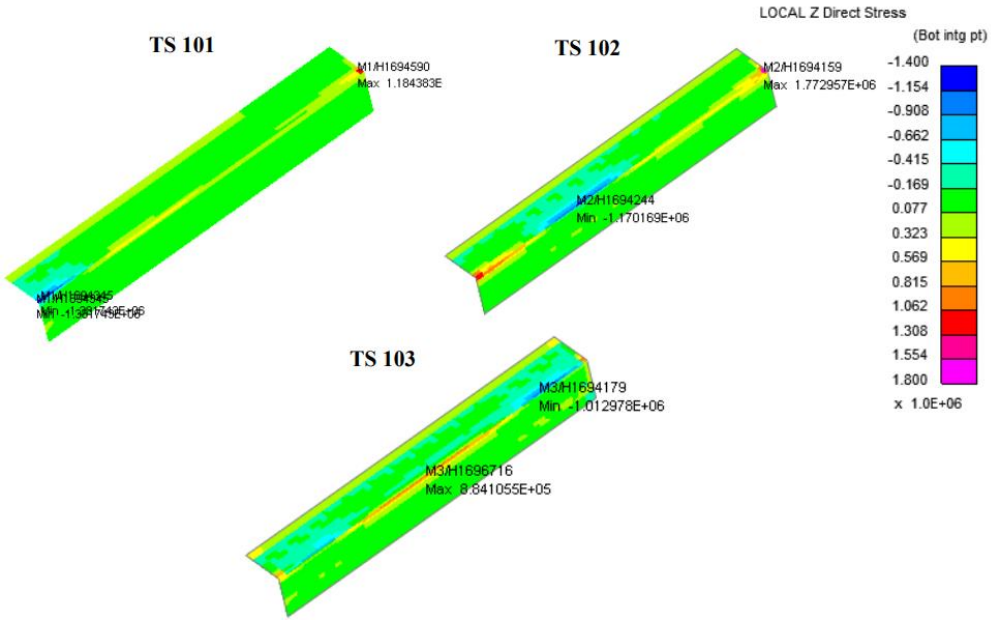

Figure 4.38: Peel bond stress contour plot under characteristic TS cases of bridge model (Arup)

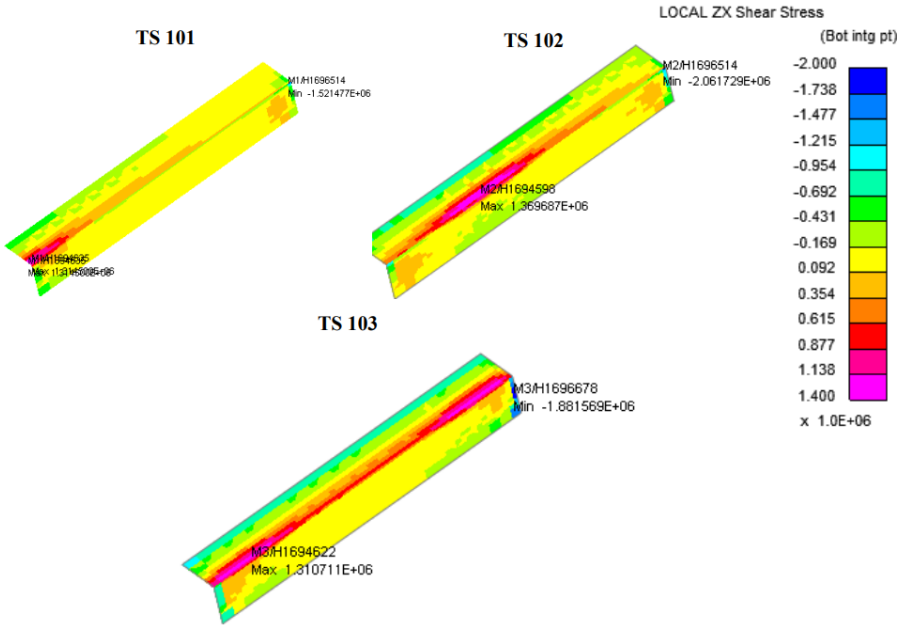

Figure 4.39: Shear bond stress contour plot under characteristic TS cases of bridge model (Arup)

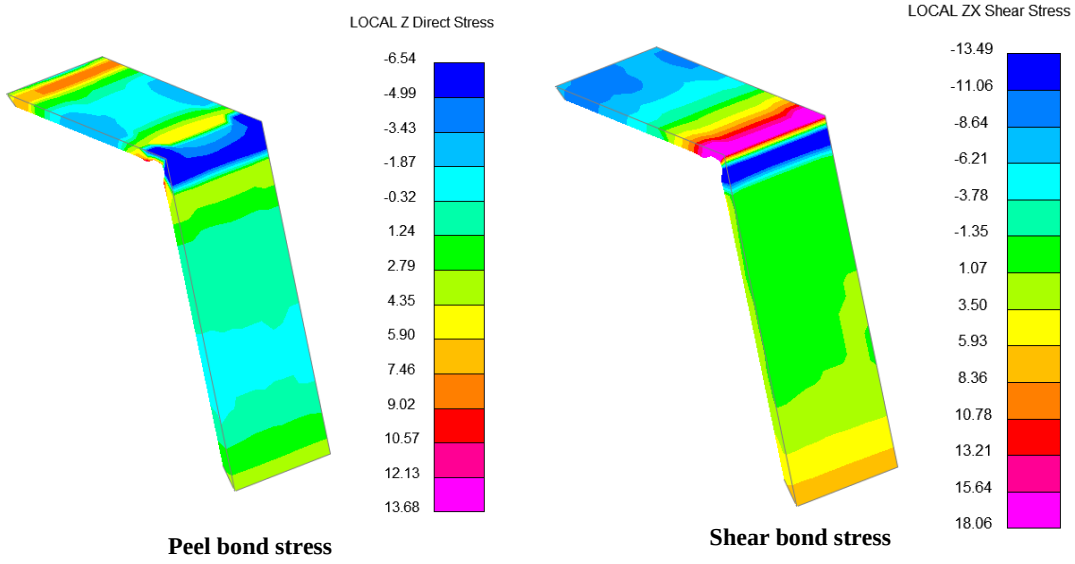

Figure 4.40: Peel bond stress contour plot at F = 60 kN of strip model in MPa

From these contour plots, it is evident that all stress peaks occur in the corner, or inner edges of the Cold Repair. However, while the results from the full-bridge model show substantially lower bond stresses at the outer edges, the strip model shows peel stress concentrations at the outer edge of the horizontal leg. As tapered edges are employed in the component strip model, stress concentrations should be reduced at the outer edges. This dissimilarity could be caused by the separation of the Cold Repair and OSD because of tie-break failure, however there is no additional support for this explanation.

4.6.3 Verification of Cold Repair Design

A verification of the proposed design of the Cold Repair was performed in Arup's study. Assumed average bond strengths were referenced by dolly tests and three-point bending tests conducted for the project of the Suurhoff Bascule bridge. Additionally, design values of observed peak stresses in the full-bridge model were determined, taking temperature loading and LM1 of traffic loading according to Eurocode 1991 into account [59]. These values with accompanying unity checks are displayed in Table 4.12.

Table 4.12: Values for assumed bond strength and design values of bond stress (Arup)

Aspect	Shear [MPa]	Peel [MPa]
Assumed average bond strength (f_{bond})	12	19
Design values of peak bond stress (σ_{design}; τ_{design})	8.9	8.9
Unity check	0.7	0.5

Table 4.12 shows that the ratio peak peel / shear stress in the full-bridge model is 1 / 1. This is in contrast to the ratio of 1 / 6.5, which was derived from the component-level model. As displayed bond stresses are based on different peel / shear ratios and peak stresses, they cannot be accurately compared with derived values in sections 3.6.2 and 4.5.3. Therefore, the design of the Cold Repair as applied in the full-bridge model could not be verified by obtained design values. However, when the average shear bond strength, as assumed by Arup, is compared to the derived average design shear strength, as shown in Table 4.13, it is evident that Arup's design overestimates the shear bond strength.

Table 4.13: Design values of average bond strength from TASTs

Bond strength	Average shear strength [MPa]
Assumed average bond strength (f_{bond})	12
Design values for ULS verifications	5.42

It is evident that bond strength values derived in this thesis cannot be used to verify the Cold Repair design as implemented in the full-bridge model. However, to provide some insights into whether the strengthened component strip could resist loads similar to those in the full-bridge model, the static capacity of the component strips was analysed. Since the component strips represent a small section of a full bridge, the LM1 loading case from Eurocode 1991-2 [59] was applied, as this loading case provides the governing local load. LM1 specifies a tandem load of 300 kN with a tyre contact area of 400 x 400 mm.

The component strips, with a width of 60 mm, displayed crack initiation at an average load of 82 kN and full debonding at 110 kN. Scaling the component strips to a width of 400 mm results in the following load capacities:

- Load at crack initiation: 533 kN
- Load at full debonding: 733 kN

This simplified analysis suggests that the component strips strengthened with Cold Repair, as tested in component-level experiments, could withstand local traffic loads as the defined tyre loads remain below the ultimate load capacity. However, it is important to note the differences between the component-level experiments and the full-bridge model, as discussed in section 4.6.2. These key differences introduce uncertainties to this conclusion, mainly with respect to size effects boundary conditions.

4.7 Discussion

Similarly to the small-scale study, the component-level FE models demonstrate deviations from the global load-displacement behaviour observed in experiments. In addition to described factors in section 5.1, a possible explanation for these dissimilarities could be related to the mesh size, since no mesh sensitivity analysis was performed for this numerical study.

With respect to derived values for peak shear bond strength, uncertainties outlined in section 3.7 also apply to the component-level study. It is also important to highlight that derived values are based on peak stresses and a specific ratio peel / shear stress and mesh size. Therefore, these results are highly case-specific.

4.8 Summary

This chapter studies the component-level experiments and accompanying FEM of reinforced OSD components. It starts with the set-up and execution of static three-point bending tests on OSD strips strengthened with Cold Repair. These tests aim to investigate the bond performance, failure modes and static load-carrying capacity of the specimens. Experimental results demonstrated that crack initiation -at around 82 kN- consistently occurred from the outer edge of the adhesive bond between steel deck plate and horizontal leg of the Cold Repair. The global load-displacement curves displayed linear behaviour during further crack propagation up to the point of debonding. This total failure, at an average load of 110 kN, indicates the point where the horizontal leg of the Cold Repair separates from the deck plate.

The chapter further focuses on the development and discussion of a 3D FE model of the strengthened OSD strips. Similar to the TASTs, the implementation of tied and tie-break contact conditions are studied to simulate bond behaviour and assess their influence on global load-displacement behaviour. Tie-breaks were implemented in the final FE model as they allow for crack propagation followed by debonding of the interface, as opposed to tied contacts. Through an iterative process, the FE model was fine-tuned to approach experimental load-displacement behaviour and observed failure modes, although the model exhibited limitations in capturing the exact global stiffness and debonding behaviour.

A comparative analysis of the full-bridge and component numerical models was performed. While the full-bridge model uses a tied contact for the adhesive interface, the strip model includes tie-break conditions. Key differences in loading conditions, boundary conditions, dimensions (with respect to scaling) and element formulation, challenge direct comparison of both models. Both models show similar bond stress distributions, though the component-level model displays peak peel bond stress at the outer edge of the horizontal leg. While the strip model's load capacity suggests it could withstand local traffic loads employed in the full-bridge model, defined key differences introduce uncertainties.

5. Conclusions and Recommendations for Future Research

This chapter presents the research conclusions, which provide an answer to formulated research questions in section 1.2.3. Based on these conclusions, recommendations for future research are suggested.

5.1 Conclusions

This thesis investigates to what extent non-linear numerical modelling and small-scale and component-level experiments contribute to obtaining an increased reliability using the Cold Repair method with CFRP. Two experimental and numerical studies were performed, followed by a comparison of a full-bridge and component-level model of an OSD strengthened by Cold Repair. First, an answer to the main research question is provided.

This thesis demonstrates that linear numerical modelling provides a sufficient approach to model the Cold Repair method up to the point of failure. Non-linear numerical modelling allows for simulation of the failure behaviour of the adhesive bonded joint between FRP and steel. Performed experiments demonstrate that the samples follow a linear behaviour, and failure of the adhesive bond occurs suddenly. This reduces the necessity to implement non-linear numerical modelling of the adhesive interface when the design of the Cold Repair does not allow for damage.

To support the answer to the main research question, the following conclusions can be formulated:

- Small-scale tests indicate the shear-dominated failure of the adhesive bond between FRP and steel, with a design value of the average shear bond strength of 5.42 kN. Observed failure mechanisms highlight debonding between primer and steel, for four samples in combination with delamination of the GFRP layer, as the primary failure mode.
- Component-level tests demonstrate that crack initiation consistently occurs from the outer edge of the adhesive bond between deck plate and horizontal leg of the Cold Repair. This crack initiation occurs at a load level of around 82 kN. As the crack propagates, the component strips display linear behaviour up to the point of total failure. Total failure is defined by full debonding between the horizontal leg of the Cold Repair and steel deck strip at an average load level of 110 kN. For four of six specimens, full debonding was followed by the onset of yielding of the steel deck strip. As the component strips have additional capacity after crack initiation, non-linear numerical modelling could result in obtaining additional capacity of the Cold Repair design.
- Developed non-linear numerical models do not contribute to additional reliability in the Cold Repair method, for two reasons:
    - Developed non-linear numerical models that implemented tie-break adhesive interfaces are not able to accurately match observed failure behaviour of the FRP-steel bonded joint.
    - As observed during small-scale and component-level experiments, failure of the adhesive bond occurs suddenly. Therefore, non-linear modelling does not provide additional value to results obtained from performed experiments. However, the FE models present valuable insights into mixed-mode behaviour of the tests. The ratio of peel / shear stress, as derived from developed FE models, is equal to 1 / 6.5 for the TASTs, indicating shear-dominating failure, and 1 / 2.4 for the component-level tests, indicating mixed-mode behaviour.

5.2 Recommendations for Future Research

This research could be further improved and extended by studying the following topics:

- **Additional shear tests.** Limitations of the executed TASTs were recognised in this thesis. It is recommended to perform standardized shear tests for which the ratio between peel and shear stresses is known and that do not require application of notches. Examples that fit these criteria include single-lap shear tests and double-lap shear tests.

- **Peel tests to obtain peel strength of adhesive bond.** As mixed-mode and shear-dominant behaviour was observed during component-level tests and TASTs, respectively, the peel bond strength could not be derived. However, it would be valuable to have understanding into the peel strength properties of the FRP-steel adhesive joint. Therefore, it is recommended to perform peel tests.

- **Material testing of FRP laminate.** As outlined in this thesis, uncertainties regarding material properties of the FRP laminate could have contributed to the observed deviations between experimental and numerical results. For this reason, it is recommended to perform material-level tests on FRP laminate in future research to gain confidence into strength and stiffness of the material.

As presented in section 5.1, non-linear numerical modelling allows for modelling of the adhesive bond failure. However, if accurate modelling of failure of the adhesive bond is desired, the following topics could be investigated in extension to this thesis:

- **Modelling of FRP laminate**. Increasing the complexity of the modelling approach of the composite laminate provides additional accuracy, as delamination of the GRP plies was observed in both TASTs and component-level tests. Approaches that take the lay-up of a composite laminate into account are displayed in Figure 5.1 (c) and (d). These modelling approaches implement one row of solid elements per ply or several plies and cohesive solid elements in between to enable the simulation of delamination.

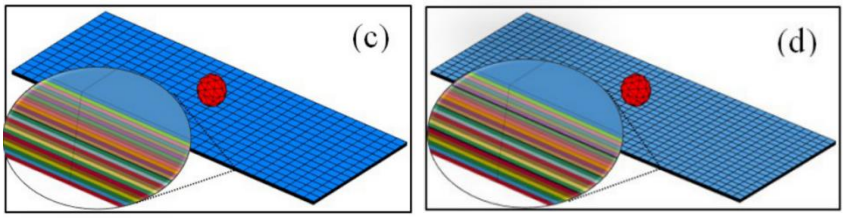

Figure 5.1: FE models of composite laminate plate (c) solid layers (SL) – cohesive zone layer (CZ) - SL and (d) SL - CZ - SL - CZ - SL - CZ – SL (black solid lines are cohesive layers)

- **Fracture mechanics tests**. While several tie-break contact options and basic principles of CZM were studied in this thesis, an improvement could be accomplished by a more complex and extensive analysis of modelling approaches to simulate adhesive interfaces. However, classical fracture mechanics tests, such as double-cantilever beam (DCB) tests or end-notch flexure (ENF) tests are needed to reliably obtain required adhesive properties, such as fracture toughness.

Bibliography

[1] Dr. Romeijn, A. (2006). *Steel bridges Dictaat Deel 1*.

[2] Wu, W., Kolstein, H., & Veljkovic, M. (2019). Fatigue resistance of rib-to-deck welded joint in OSDs, analyzed by fracture mechanics. *Journal of Constructional Steel Research*, *162*. https://doi.org/10.1016/j.jcsr.2019.105700

[3] Wu, W., Veljkovic, M., Kolstein, H., Pijpers, R., & Maljaars, J. (2024). Fatigue behaviour of root crack in stiffener-to-deck plate weld at crossbeam of orthotropic bridge decks. *Engineering Structures*, *306*. https://doi.org/10.1016/j.engstruct.2024.117710

[4] F.B.P. de Jong. (2007, January 9). *Renovation techniques for fatigue cracked orthotropic steel bridge decks*. TU Delft.

[5] Guo, T., Liu, J., Deng, Y., & Zhang, Z. (2019). Fatigue Performance of Orthotropic Steel Decks with FRP Angles: Field Measurement and Numerical Analysis. *Journal of Performance of Constructed Facilities*, *33*(4). https://doi.org/10.1061/(asce)cf.1943-5509.0001308

[6] Liu, J., Guo, T., Feng, D., & Liu, Z. (2018). Fatigue Performance of Rib-to-Deck Joints Strengthened with FRP Angles. *Journal of Bridge Engineering*, *23*(9). https://doi.org/10.1061/(asce)be.1943-5592.0001286

[7] Rikken, M., & Tuinstra, D. (n.d.). De evolutie van renovatiewerkzaamheden aan stalen bruggen. *Bruggen*, *3*.

[8] Arup. (2024). *Cold Repair: Design Basis*. Amsterdam.

[9] Xin, H., Liu, J., Correia, J. A. F., Berto, F., Veljkovic, M., & Yang, F. (2023). Strengthening effects evaluation on fatigue damage of rib to deck joint in orthotropic steel deck. *Engineering Failure Analysis*, *145*. https://doi.org/10.1016/j.engfailanal.2022.107041

[10] Teixeira de Freitas, S., Kolstein, H., & Bijlaard, F. (2010). *Composite bonded systems for renovations of orthotropic steel bridge decks*. *Composite Structures* (Vol. 92). https://doi.org/10.1016/j.compstruct.2009.09.016

[11] Deng, Y., Liu, T., Cao, B., & Li, A. (2023). Fatigue Strengthening for Rib-to-Deck Joint by Bonding Reinforcing Plates on the Deck Surface. *Journal of Bridge Engineering*, *28*(7). https://doi.org/10.1061/jbenf2.beeng-5617

[12] Schnerch, D., Dawood, M., Rizkalla, S., Sumner, E., & Stanford, K. (2006). Bond behavior of CFRP strengthened steel structures. In *Advances in Structural Engineering* (Vol. 9, pp. 805–817). Multi-Science Publishing Co. Ltd. https://doi.org/10.1260/136943306779369464

[13] Zhao, X. L., & Zhang, L. (2007). State-of-the-art review on FRP strengthened steel structures. *Engineering Structures*, *29*(8), 1808–1823. https://doi.org/10.1016/j.engstruct.2006.10.006

[14] Wolters, M. ;, Waltener, C. ;, Koetsier, M. ;, Yang, J. ;, Moreira, M. A., & Pavlovic, M. (2024). *Wrapped Composite Joints For Fatigue Resistant Circular Hollow Section Steel Structures In Wind Energy* (Vol. 1). Retrieved from http://www.treecomposites.com

[15] Arup. (2023). *Cold repair. Nader onderzoek. Offerte (fase 1 t/m fase 3)*.

[16] Kolstein, M. H. (2007). *Fatigue classification of welded joints in orthotropic steel bridge decks.*

[17] Levensduurverlening van vermoeiingsgevoelige orthotrope stalen brugdekken met Engineerd Cementitious Composite (ECC). (n.d.).

[18] Rijkswaterstaat. (n.d.). *Vijftig jaar overbrugd - directie bruggen 1928 - 1978 deel 1*.

[19] Rijkswaterstaat. (n.d.). *Vijftig jaar overbrugd - directie bruggen 1928 - 1978 deel 2*.

[20] Arup. (n.d.). Circulaire economie inspireert tot renovatie van de drukste brug van Nederland, waardoor levensduur met nog eens 100 jaar wordt verlengd. Retrieved 16 June 2024, from https://www.arup.com/nl-nl/projects/van-brienenoord-bridge-renovation

[21] Rijkswaterstaat. (n.d.). Doelen verbetering A27 Houten - Hooipolder. Retrieved 16 June 2024, from https://www.rijkswaterstaat.nl/wegen/projectenoverzicht/a27-verbetering-traject-houten-hooipolder/doelen-en-resultaten

[22] Wu, W., Veljkovic, M., Kolstein, H., Maljaars, J., & Pijpers, R. (2024). Fatigue behaviour of toe and root stiffener cracks in stiffener-to-deck plate weld of orthotropic bridge decks. *Engineering Structures*, *305*. https://doi.org/10.1016/j.engstruct.2024.117740

[23] Wang, Y., Shao, X., Chen, J., Cao, J., & Deng, S. (2021). UHPC-based strengthening technique for orthotropic steel decks with significant fatigue cracking issues. *Journal of Constructional Steel Research*, *176*. https://doi.org/10.1016/j.jcsr.2020.106393

[24] Wijnia, S., Tieleman, O., & van de Voort, M. (2023, February 27). Van Brienenoordbrug vervangen in plaats van gerenoveerd - Land+Water. Retrieved 16 June 2024, from https://www.landenwater.nl/nieuws/van-brienenoordbrug-wordt-vervangen-in-plaats-van-gerenoveerd

[25] Campbell, F. C. (2010). *Structural Composite Materials*. Retrieved from www.asminternational.org

[26] Gurit. (n.d.). *Guide to composites*.

[27] Pavlovic, M., & Csillag, F. (n.d.). *Fibres, resins and cores*.

[28] Jialanella, G. L. (2010). Advances in bonding plastics. *Advances in Structural Adhesive Bonding*, 237–264. https://doi.org/10.1533/9781845698058.2.237

[29] Lugaresi, F., Kotsovinos, P., Lenk, P., & Rein, G. (2022). Review of the mechanical failure of non-combustible facade systems in fire. *Construction and Building Materials*, *361*. https://doi.org/10.1016/j.conbuildmat.2022.129506

[30] Van der Meer, F. P. (n.d.). Influence of the lay-up. *TU Delft - Steel and Composite Structures*. TU Delft.

[31] Pavlovic, M., & de Putter, A. (n.d.). *Composites - Production processes*.

[32] Pavlovic, M. (n.d.). What is FRP? *Steel and Composite Structures*. TU Delft.

[33] Qureshi, J. (2022, March 1). A Review of Fibre Reinforced Polymer Structures. *Fibers*. MDPI. https://doi.org/10.3390/fib10030027

[34] Qureshi, J., Nadir, Y., & John, S. K. (2020). Bolted and bonded FRP beam-column joints with semi-rigid end conditions. *Composite Structures*, *247*, 112500. https://doi.org/10.1016/J.COMPSTRUCT.2020.112500

[35] Technical Committee CEN/TC 250 'Structural Eurocodes'. (2022). *CEN/TS 19101:2022 - Design of fibre-polymer composite structures*. NEN.

[36] Van der Meer, F. P. (n.d.). Lecture 10.1 - Failure Analysis. Delft.

[37] Nur Azrie Bt Safri, S., Sultan, M. T. H., & Jawaid, M. (2018). Damage analysis of glass fiber reinforced composites. In *Durability and Life Prediction in Biocomposites, Fibre-Reinforced Composites and Hybrid Composites* (pp. 133–147). Elsevier. https://doi.org/10.1016/B978-0-08-102290-0.00007-6

[38] Hicks, J. (1999). Fatigue cracking. *Welded Joint Design*, 91–115. https://doi.org/10.1533/9781855738980.91

[39] Bala, S. (n.d.). *Tie-Break Contacts in LS-DYNA*.

[40] da Silva, L. F. M., & Campilho, R. D. S. G. (2012). Advances in numerical modelling of adhesive joints. In *SpringerBriefs in Applied Sciences and Technology* (pp. 1–93). Springer Verlag. https://doi.org/10.1007/978-3-642-23608-2_1

[41] Azevedo, J. C. S., Campilho, R. D. S. G., da Silva, F. J. G., Faneco, T. M. S., & Lopes, R. M. (2015). Cohesive law estimation of adhesive joints in mode II condition. *Theoretical and Applied Fracture Mechanics*, *80*, 143–154. https://doi.org/10.1016/j.tafmec.2015.09.007

[42] Hartlen, D. C., Montesano, J., & Cronin, D. S. (n.d.). *Cohesive Zone Modeling of Adhesively Bonded Interfaces: The Effect of Adherend Geometry, Element Selection, and Loading Condition*.

[43] Jouan, A., & Constantinescu, A. (2018). A critical comparison of shear tests for adhesive joints. *International Journal of Adhesion and Adhesives*, *84*, 63–79. https://doi.org/10.1016/j.ijadhadh.2018.02.035

[44] ASTM International. (n.d.). ASTM D5656 - 10. https://doi.org/10.1520/D5656-10R17

[45] ANSYS. (n.d.). *LS-DYNA ® Keyword User's Manual Volume I*. Retrieved from www.lstc.com

[46] Lemmen, P., Meijer, G.-J., & Rasmussen, E. A. (n.d.). *Dynamic behaviour of composite ship structures (DYCOSS) - Failure Prediction Tool*.

[47] Du, A., Liu, Y., Xin, H., & Zuo, Y. (2016). Progressive damage analysis of PFRP double-lap bolted joints using explicit finite element method. *Composite Structures*, *152*, 860–869. https://doi.org/10.1016/J.COMPSTRUCT.2016.06.028

[48] *Datasheet Epoxy - Prime infusion system*. (n.d.). Retrieved from www.gurit.com.

[49] Santos, M. A. S., & Campilho, R. D. S. G. (2017). Mixed-mode fracture analysis of composite bonded joints considering adhesives of different ductility. *International Journal of Fracture*, *207*(1), 55–71. https://doi.org/10.1007/s10704-017-0219-x

[50] Paliwal, I., Ramji, M., & Khaderi, S. N. (2023). Experimental characterization of CFRP single lap joints under tension at various loading rates. *Composites Part A: Applied Science and Manufacturing*, *173*. https://doi.org/10.1016/j.compositesa.2023.107636

[51] TU Delft. (n.d.). Classic Laminate Theory Tool.

[52] Velds, E. (2024). *Material properties GFRP/CFRP*.

[53] UNIC600-50K TRW40. (n.d.).

[54] Normcommissie 351 001 'Technische Grondslagen voor Bouwconstructies'. (2019). *Eurocode 0: Basis of structural design*.

[55] ISO/TC 61/SC 11. (1993). *Adhesives - Determination of shear behaviour of structural bonds - Part 2: Thick-adherend tensile-test method*.

[56] Monteiro, J. P. R., Campilho, R. D. S. G., Marques, E. A. S., & da Silva, L. F. M. (2015). Experimental estimation of the mechanical and fracture properties of a new epoxy adhesive. *Applied Adhesion Science*, *3*(1). https://doi.org/10.1186/s40563-015-0056-y

[57] Campilho, R. D. S. G., Banea, M. D., Neto, J. A. B. P., & Da Silva, L. F. M. (2013). Modelling adhesive joints with cohesive zone models: Effect of the cohesive law shape of the adhesive layer. *International Journal of Adhesion and Adhesives*, *44*, 48–56. https://doi.org/10.1016/j.ijadhadh.2013.02.006

[58] Normcommissie 351 001 'Technische Grondslagen voor Bouwconstructies'. (2005). *Eurocode 3: Design of steel structures - Part 1-9: Fatigue*.

[59] Normcommissie 351 001 'Technische Grondslagen voor Bouwconstructies'. (2015). *Eurocode 1 - Actions on structures - Part 2: Traffic loads on bridges*.

[60] Wang, D., Xiang, C., Ma, Y., Chen, A., & Wang, B. (2021). Experimental study on the root-deck fatigue crack on orthotropic steel decks. *Materials and Design*, *203*. https://doi.org/10.1016/j.matdes.2021.109601

[61] Bas, J., & den Ridder, H. (2017, July 24). Nieuwe rails op rubber bedje is oplossing voor falende Moerdijkbrug | Moerdijk | bndestem.nl. Retrieved 16 June 2024, from https://www.bndestem.nl/moerdijk/nieuwe-rails-op-rubber-bedje-is-oplossing-voor-falende-moerdijkbrug~aebbedadb/?referrer=https%3A%2F%2Fwww.google.com%2F

[62] IeNw CONTACT. (2022, November 23). Galecopperbrug. *IeNw CONTACT relatiemagazine van IeNw*. Retrieved from https://magazines.rijksoverheid.nl/ienw/ienwcontact/2022/05/galecopperbrug

[63] Rijkswaterstaat. (n.d.). Hagesteinsebrug A27 - Hagesteinsebrug. Retrieved 16 June 2024, from https://beeldbank.rws.nl/

[64] Meeuwsen, F. (2016, June 27). Moerdijkbrug: veiligheid en onderhoud al vele jaren in goede handen Rijkswaterstaat - Omroep Brabant. Retrieved 16 June 2024, from https://www.omroepbrabant.nl/nieuws/2323271/moerdijkbrug-veiligheid-en-onderhoud-al-vele-jaren-in-goede-handen-rijkswaterstaat

[65] Di, J., Ruan, X., Zhou, X., Wang, J., & Peng, X. (2021). Fatigue assessment of orthotropic steel bridge decks based on strain monitoring data. *Engineering Structures*, *228*, 111437. https://doi.org/https://doi.org/10.1016/j.engstruct.2020.111437

[66] Chaves, F. J. P., Da Silva, L. F. M., De Moura, M. F. S. F., Dillard, D. A., & Esteves, V. H. C. (2014, November 2). Fracture mechanics tests in adhesively bonded joints: A literature review. *Journal of Adhesion*. Taylor and Francis Inc. https://doi.org/10.1080/00218464.2013.859075

[67] Costa, M. M. (n.d.). Shear Testing: A Detailed Approach to Methods and Applications. *Biopdi*. Retrieved 26 June 2024, from https://biopdi.com/shear-testing/

A Experimental Results of TASTs

This appendix presents the experimental results of the TASTs. For all samples, strains in y-, x- and major strain direction are displayed at different load levels. Strains in x- and y-direction are displayed for three load levels, where the highest load level is one stage before failure. Displayed major strains include observed failure as the latest stage.

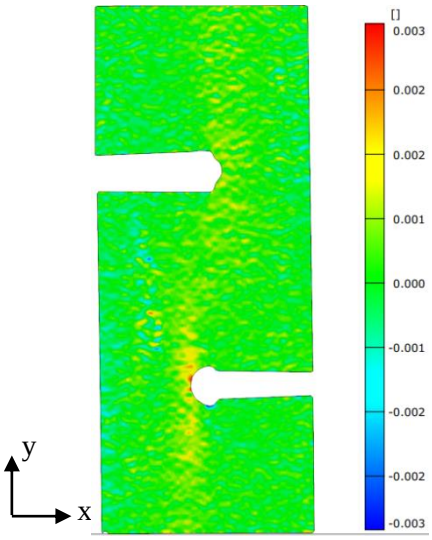

Y-strain TAST 30-1 at F = 20.4 kN

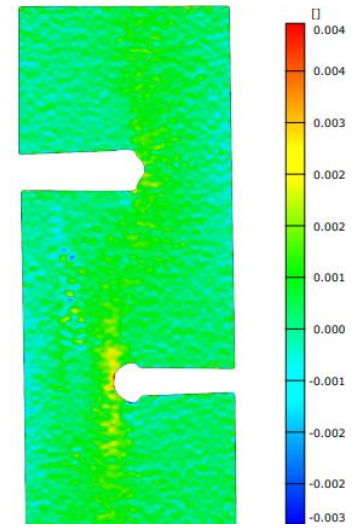

Y-strain TAST 30-1 at F = 28.2 kN

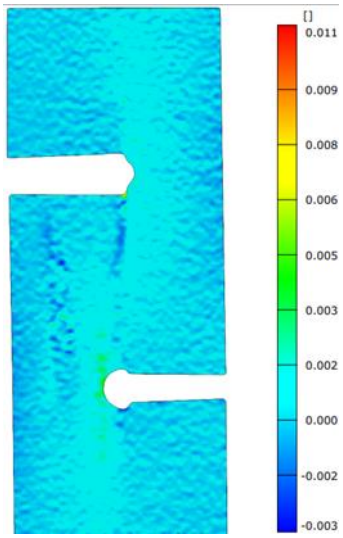

Y-strain TAST 30-1 at F = 30.8 kN

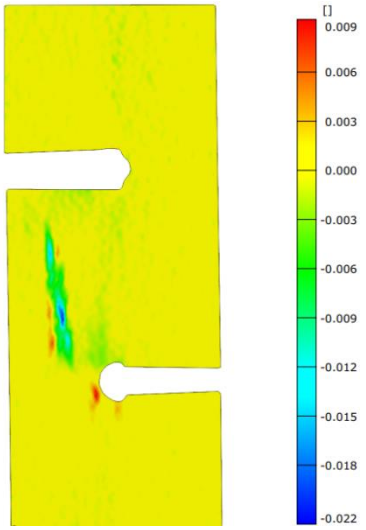

X-strain TAST 30-1 at F = 20.4 kN

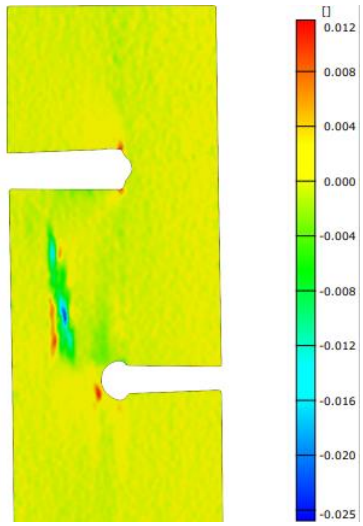

X-strain TAST 30-1 at F = 28.2 kN

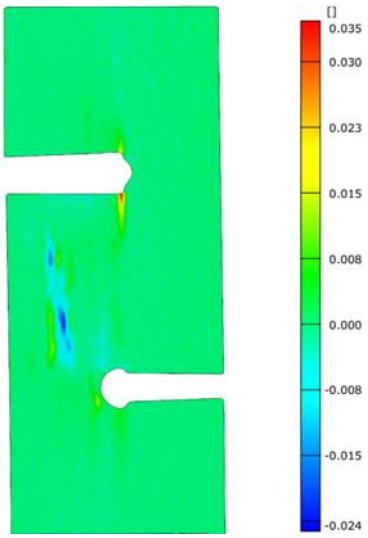

X-strain TAST 30-1 at F = 30.8 kN

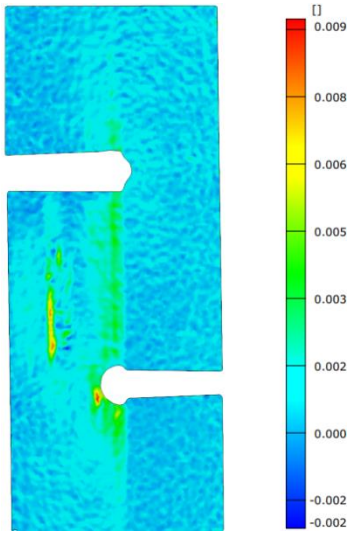

Major strain TAST 30-1 at F = 20.4 kN

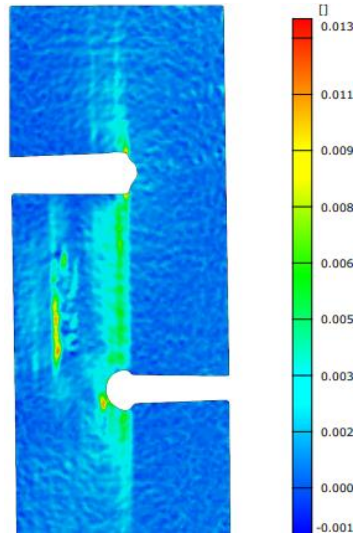

Major strain TAST 30-1 at F = 28.2 kN

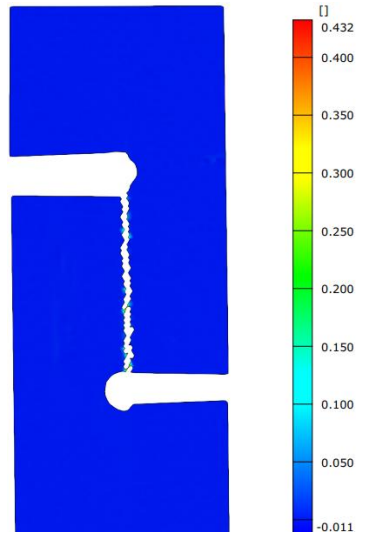

Major strain TAST 30-1 at F = 0 kN

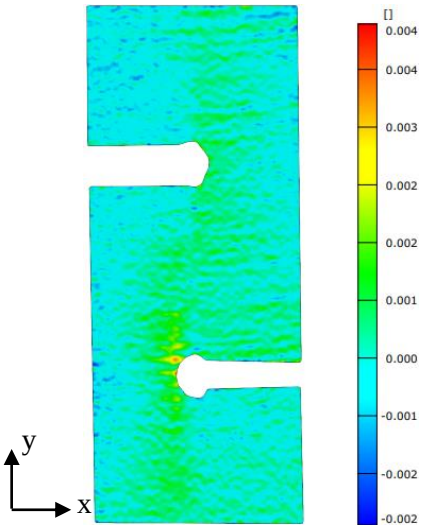

Y-strain TAST 30-2 at F = 17.4 kN

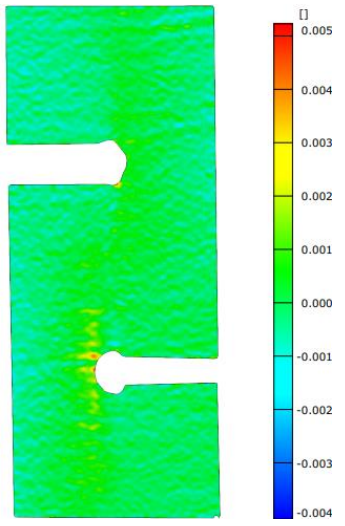

Y-strain TAST 30-2 at F = 21.6 kN

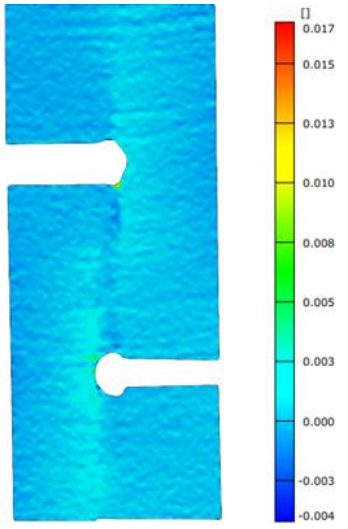

Y-strain TAST 30-2 at F = 28.6 kN

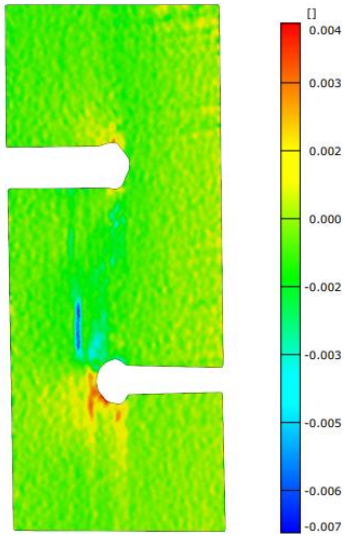

X-strain TAST 30-2 at F = 17.4 kN

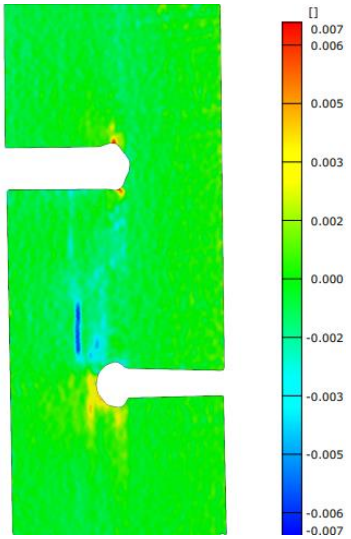

X-strain TAST 30-2 at F = 21.6 kN

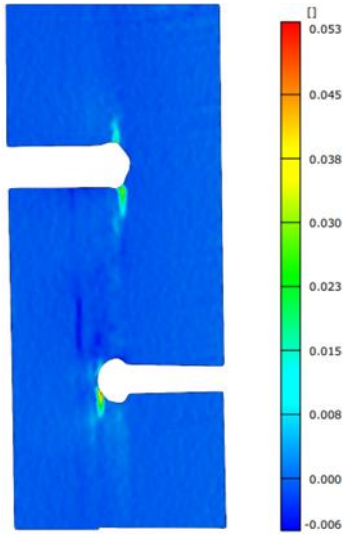

X-strain TAST 30-2 at F = 28.6 kN

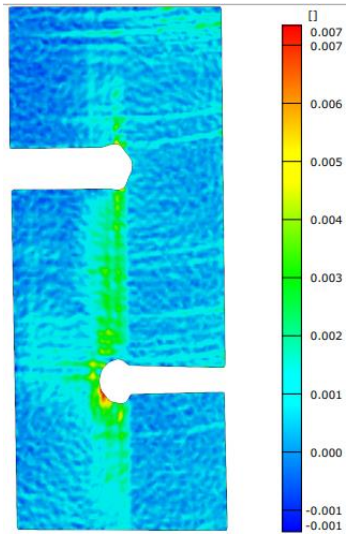

Major strain TAST 30-2 at F = 17.4 kN

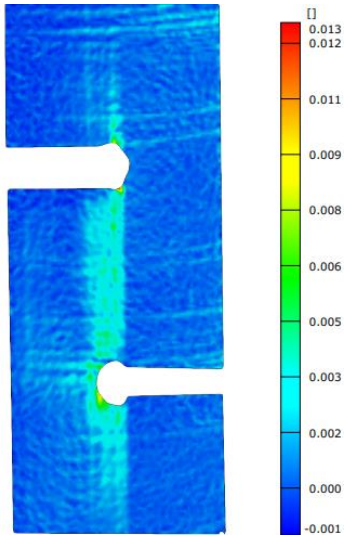

Major strain TAST 30-2 at F = 21.6 kN

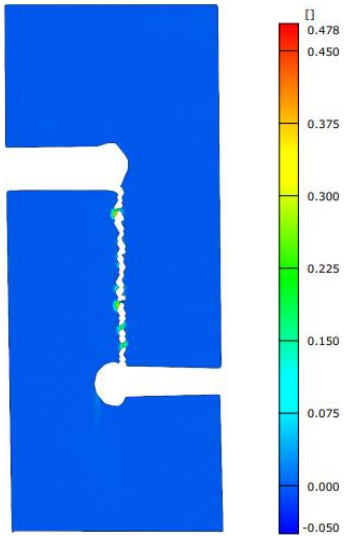

Major strain TAST 30-2 at F = 0 kN

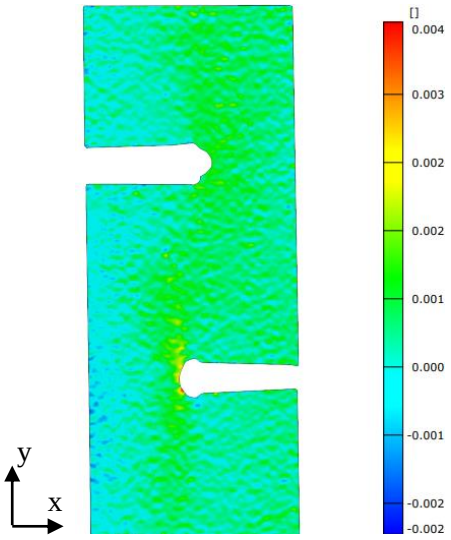

Y-strain TAST 30-3 at F = 18.7 kN

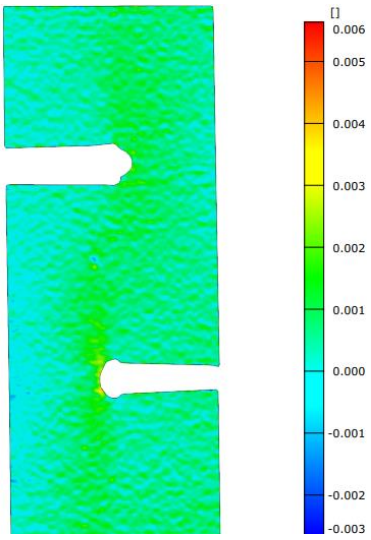

Y-strain TAST 30-3 at F = 24.6 kN

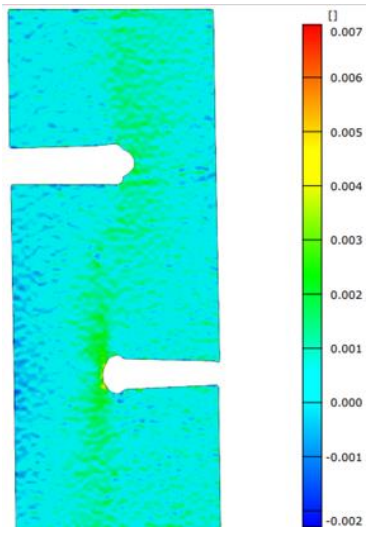

Y-strain TAST 30-3 at F = 29.8 kN

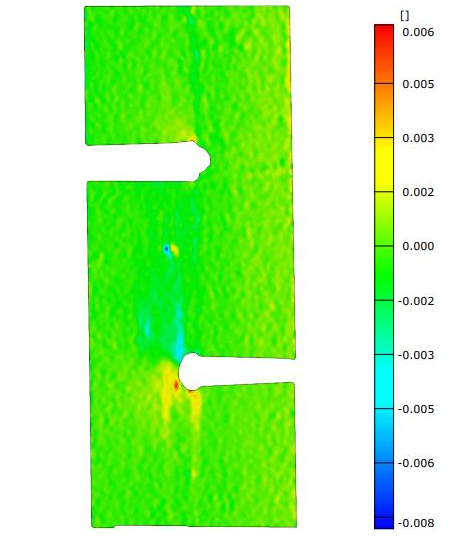

X-strain TAST 30-3 at F = 18.7 kN

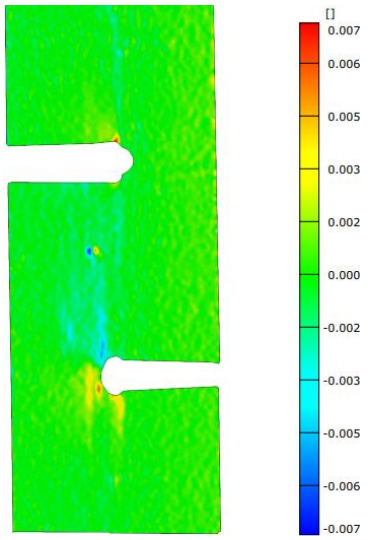

X-strain TAST 30-3 at F = 24.6 kN

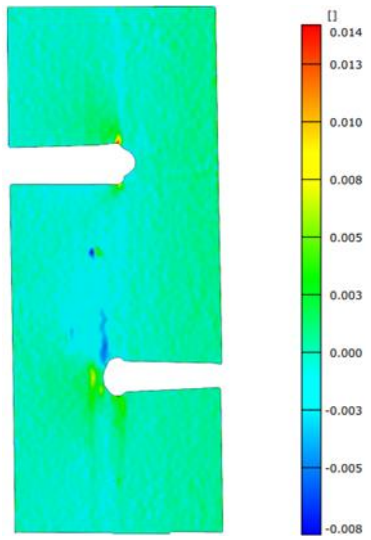

X-strain TAST 30-3 at F = 29.8 kN

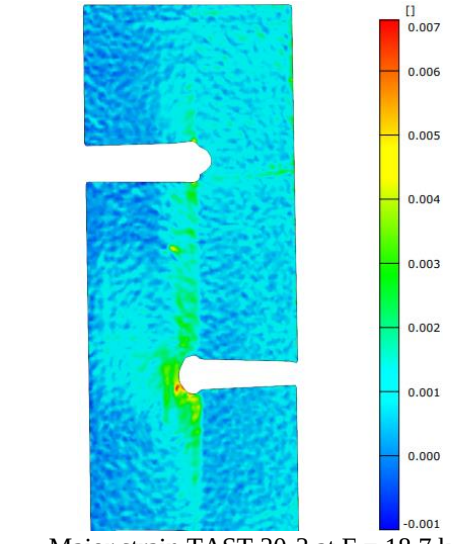

Major strain TAST 30-3 at F = 18.7 kN

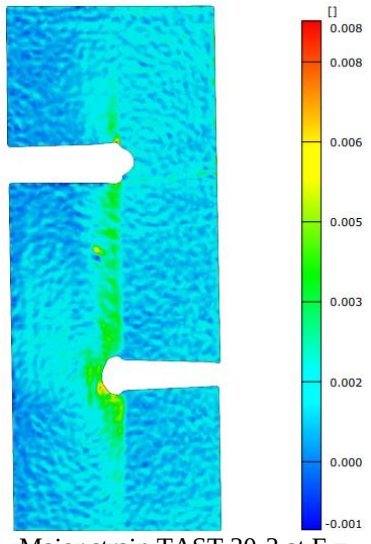

Major strain TAST 30-3 at F = 24.6 kN

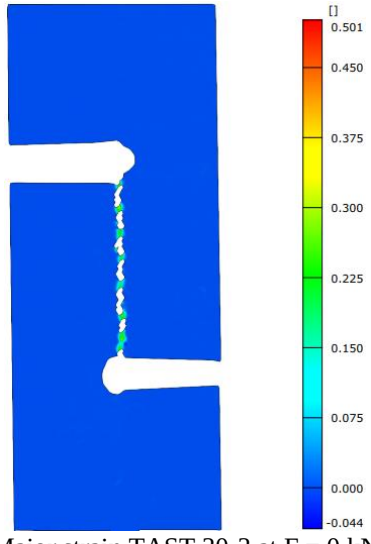

Major strain TAST 30-3 at F = 0 kN

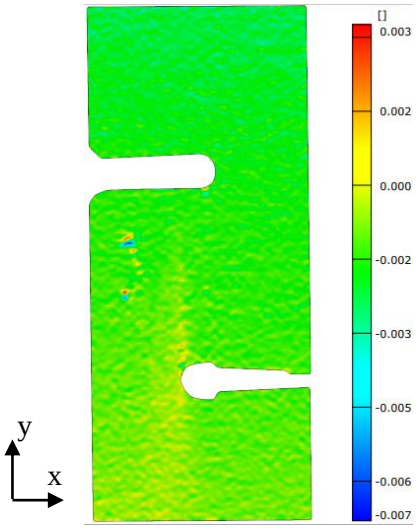

Y-strain TAST 30-4 at F = 6.8 kN

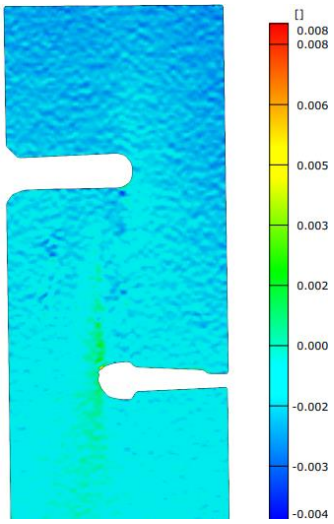

Y-strain TAST 30-4 at F = 12.5 kN

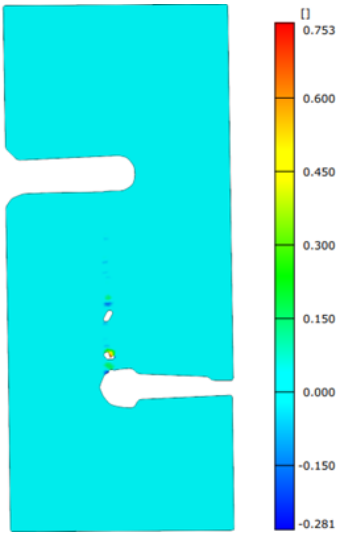

Y-strain TAST 30-4 at F = 19.1 kN

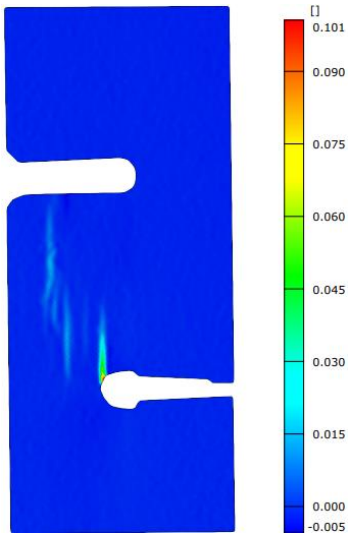

X-strain TAST 30-4 at F = 6.8 kN

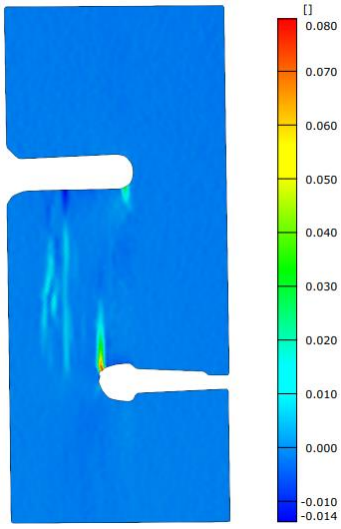

X-strain TAST 30-4 at F = 12.5 kN

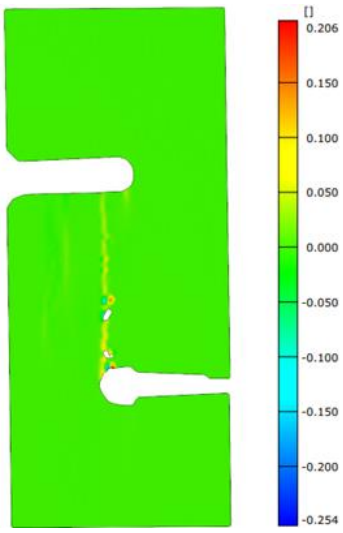

X-strain TAST 30-4 at F = 19.1 kN

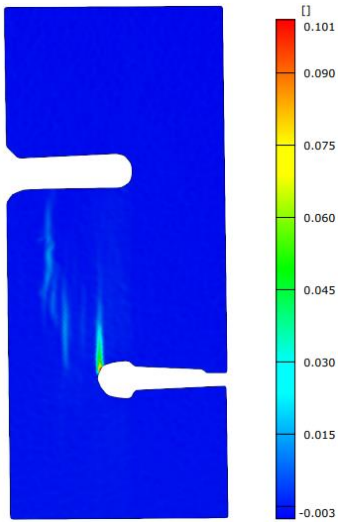

Major strain TAST 30-4 at F = 6.8 kN

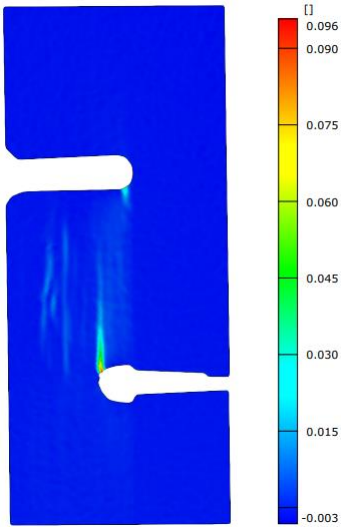

Major strain TAST 30-4 at F = 12.5 kN

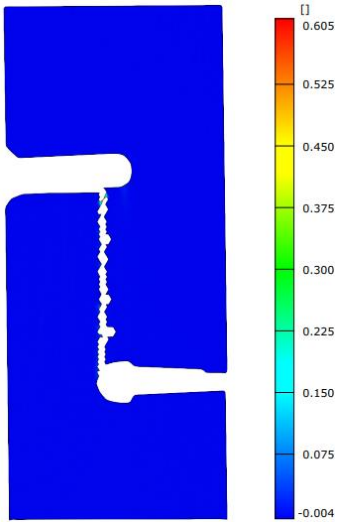

Major strain TAST 30-4 at F = 19.1 kN

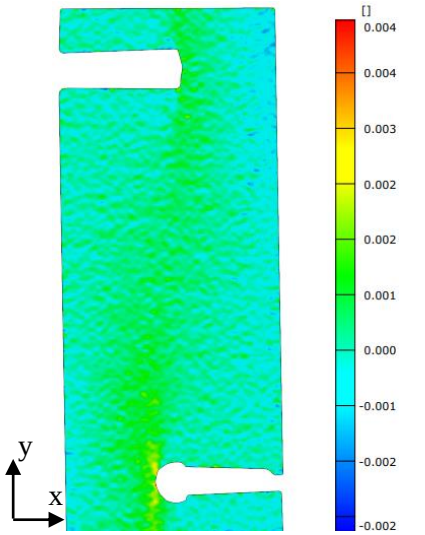

Y-strain TAST 60-1 at F = 29.0 kN

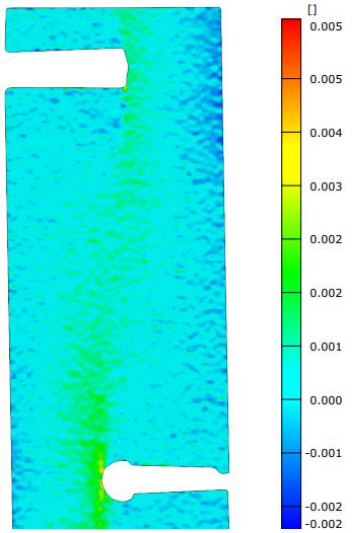

Y-strain TAST 60-1 at F = 33.3 kN

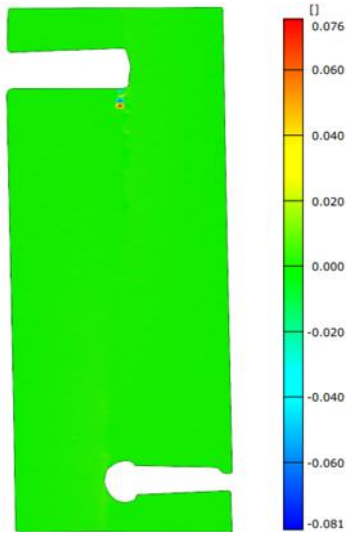

Y-strain TAST 60-1 at F = 43.1 kN

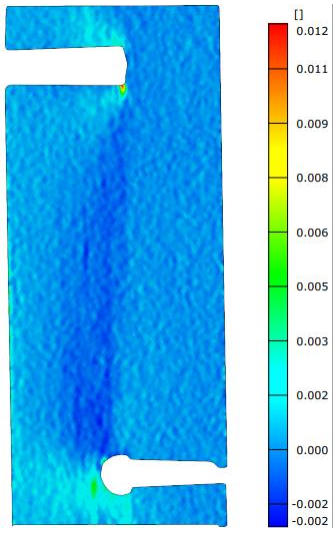

X-strain TAST 60-1 at F = 29.0 kN

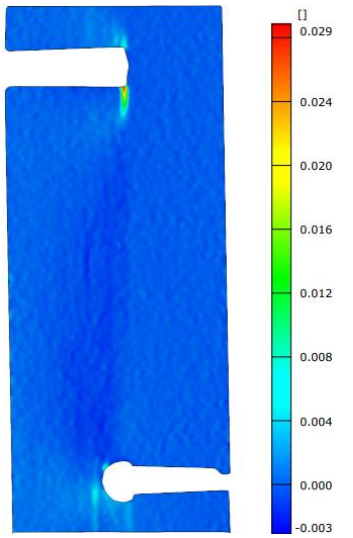

X-strain TAST 60-1 at F = 33.3 kN

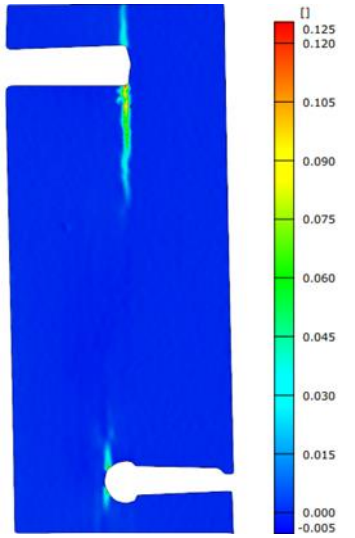

X-strain TAST 60-1 at F = 43.1 kN

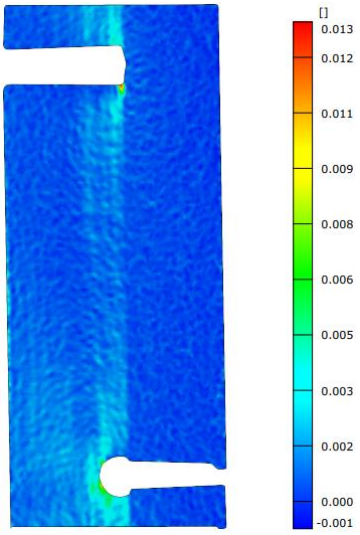

Major strain TAST 60-1 at F = 29.0 kN

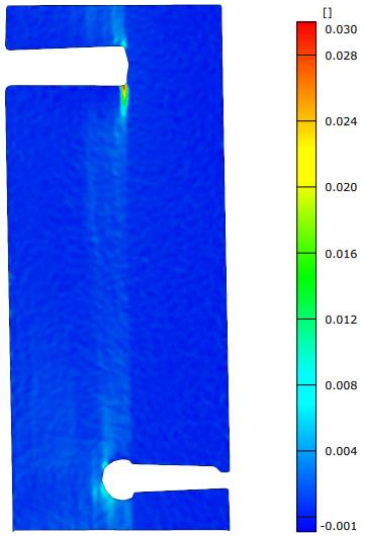

Major strain TAST 60-1 at F = 33.3 kN

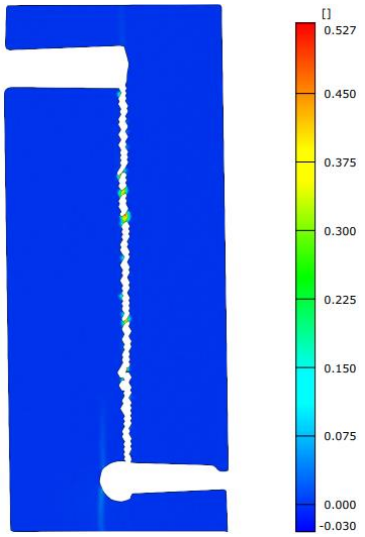

Major strain TAST 60-1 at F = 0 kN

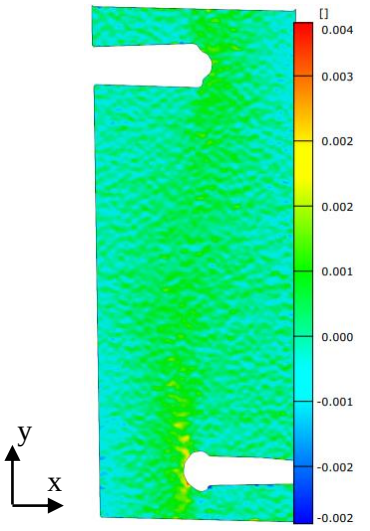

Y-strain TAST 60-2 at F = 26.0 kN

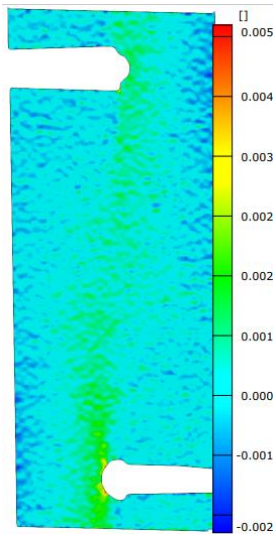

Y-strain TAST 60-2 at F = 32.6 kN

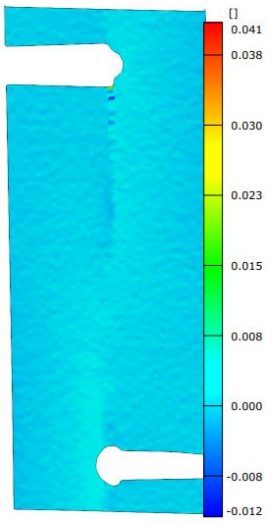

Y-strain TAST 60-2 at F = 40.0 kN

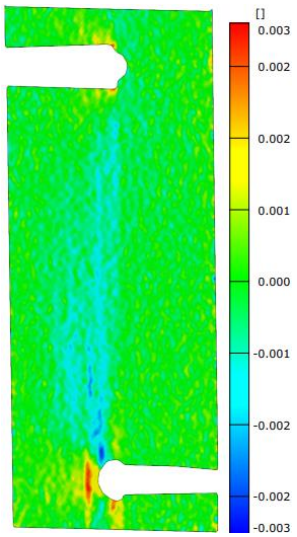

X-strain TAST 60-2 at F = 26.0 kN

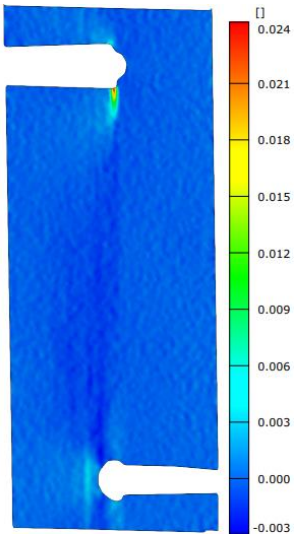

X-strain TAST 60-2 at F = 32.6 kN

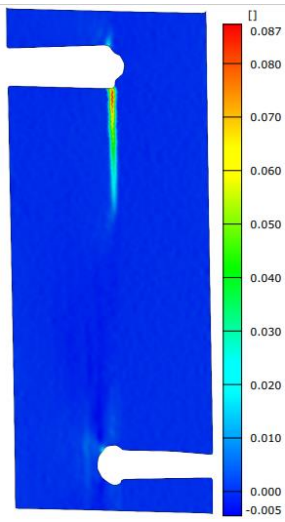

X-strain TAST 60-2 at F = 40.0 kN

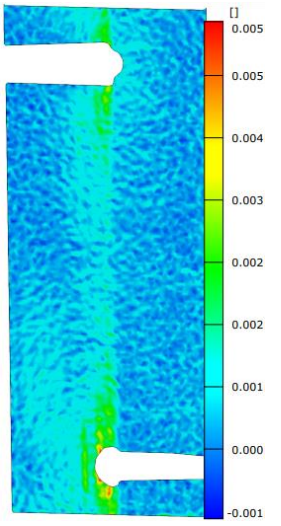

Major strain TAST 60-2 at F = 26.0 kN

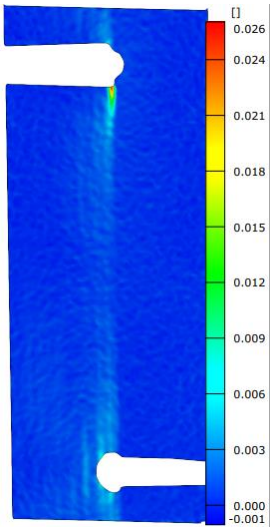

Major strain TAST 60-2 at F = 32.6 kN

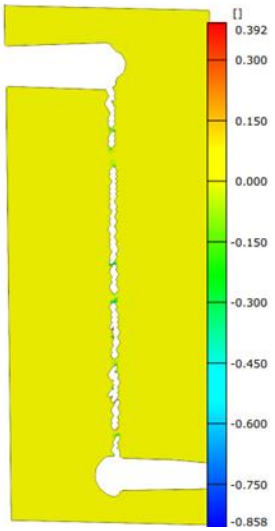

Major strain TAST 60-2 at F = 0 kN

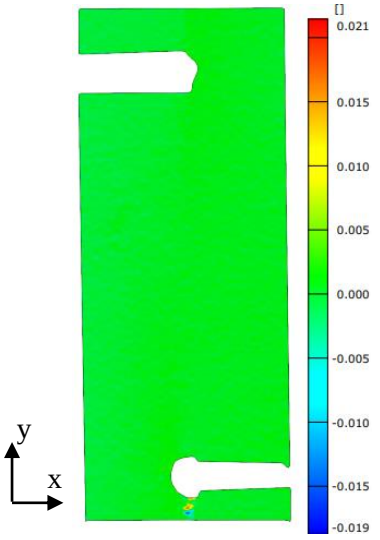

Y-strain TAST 60-3 at F = 28.9 kN

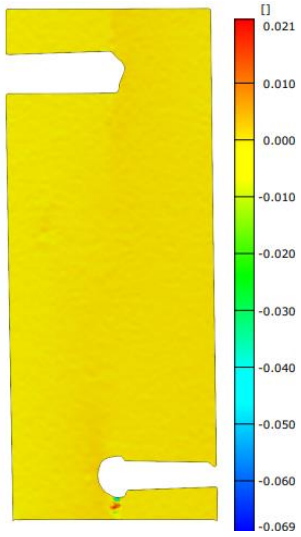

Y-strain TAST 60-3 at F = 32.3 kN

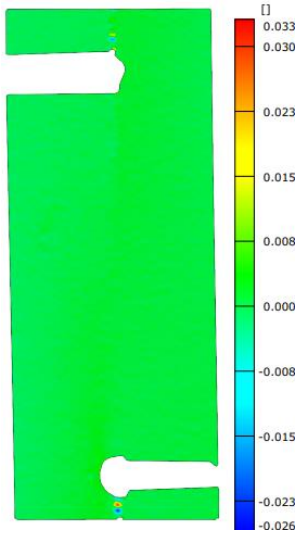

Y-strain TAST 60-3 at F = 45.2 kN

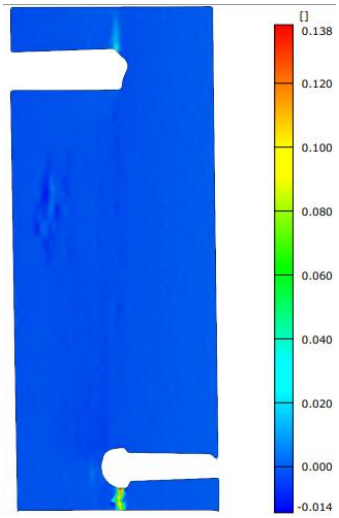

X-strain TAST 60-3 at F = 28.9 kN

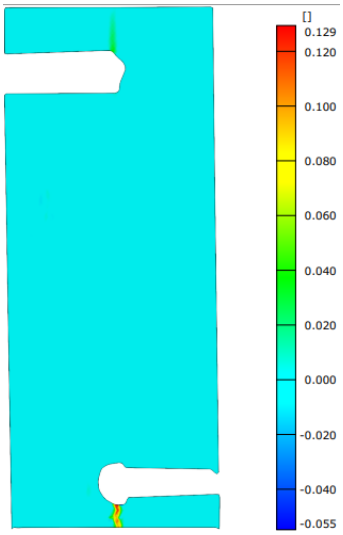

X-strain TAST 60-3 at F = 32.3 kN

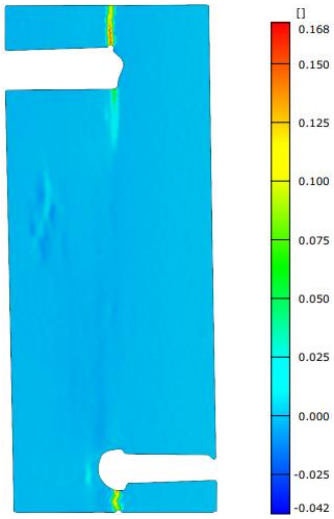

X-strain TAST 60-3 at F = 45.2 kN

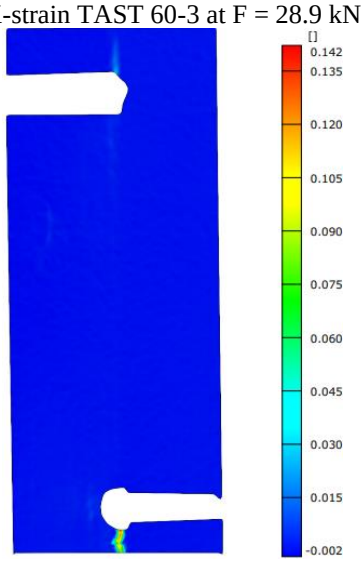

Major strain TAST 60-3 at F = 28.9 kN

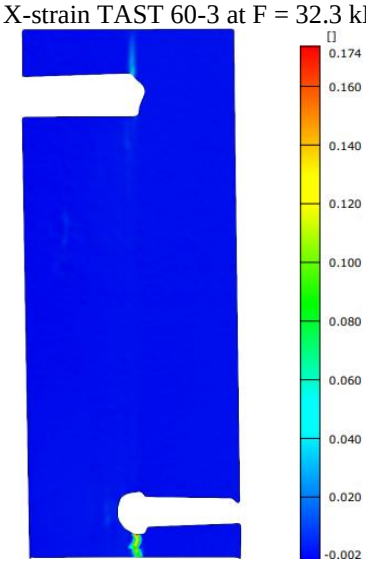

Major strain TAST 60-3 at F = 32.3 kN

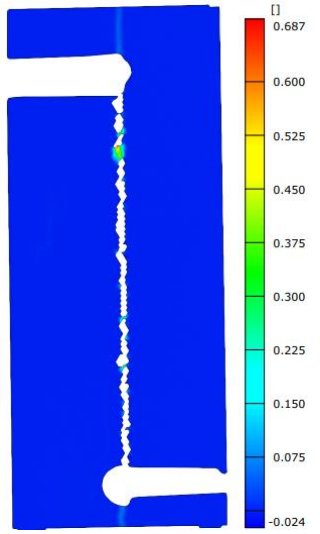

Major strain TAST 60-3 at F = 0 kN

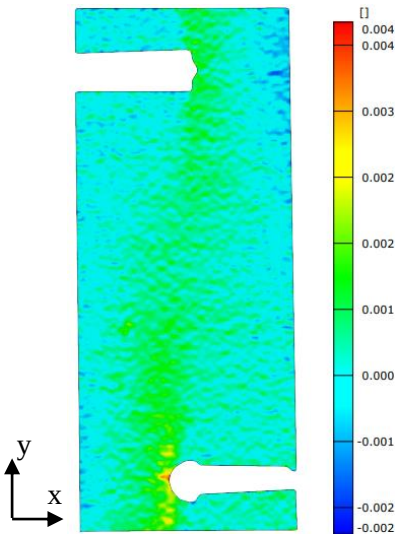

Y-strain TAST 60-4 at F = 29.7 kN

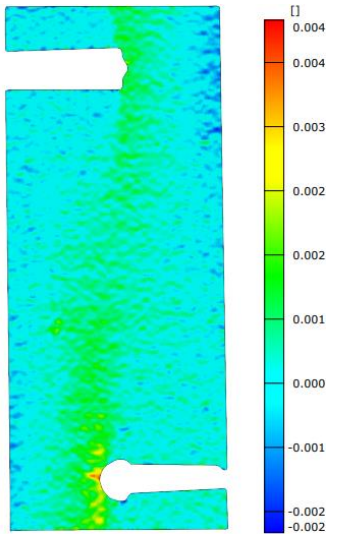

Y-strain TAST 60-4 at F = 30.8 kN

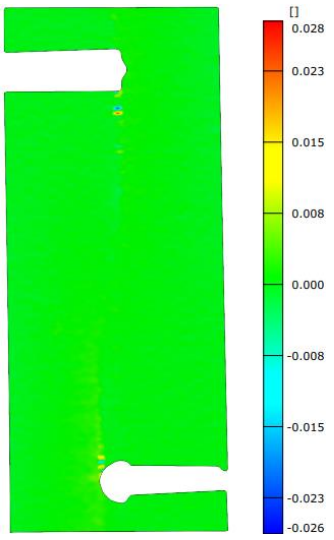

Y-strain TAST 60-4 at F = 41.3 kN

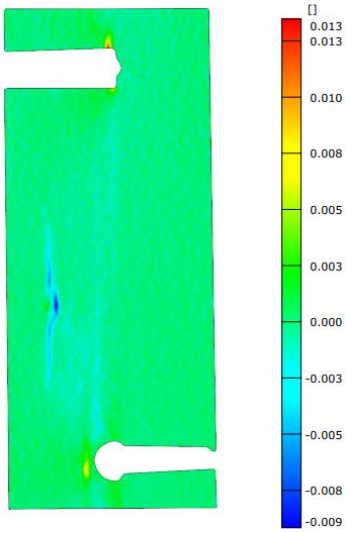

X-strain TAST 60-4 at F = 29.7 kN

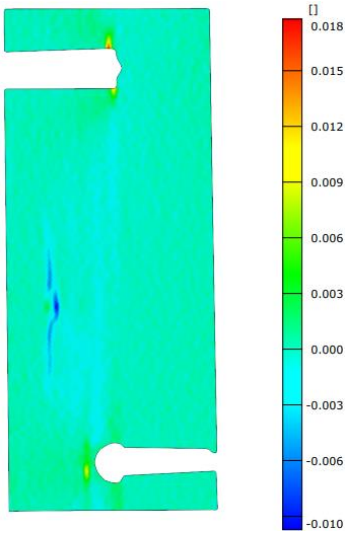

X-strain TAST 60-4 at F = 30.8 kN

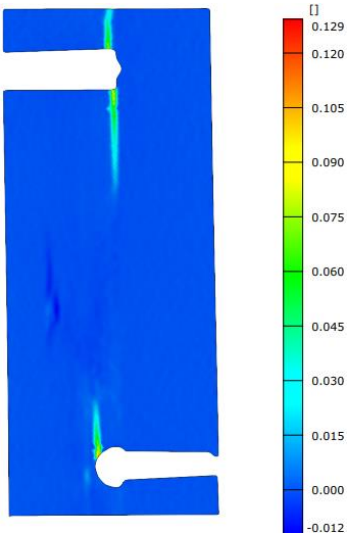

X-strain TAST 60-4 at F = 41.3 kN

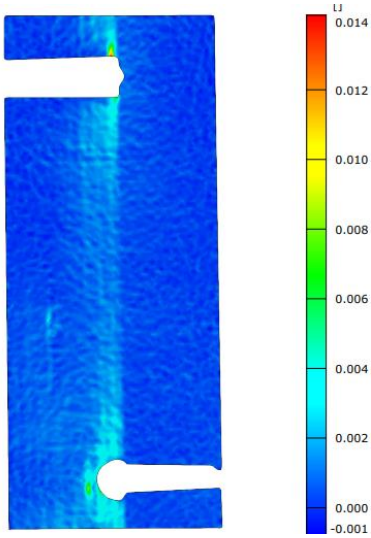

Major strain TAST 60-4 at F = 29.7 kN

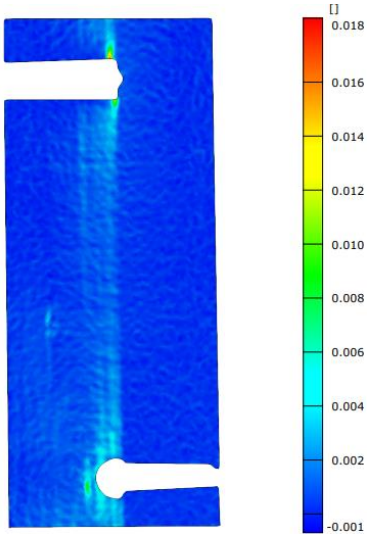

Major strain TAST 60-4 at F = 30.8 kN

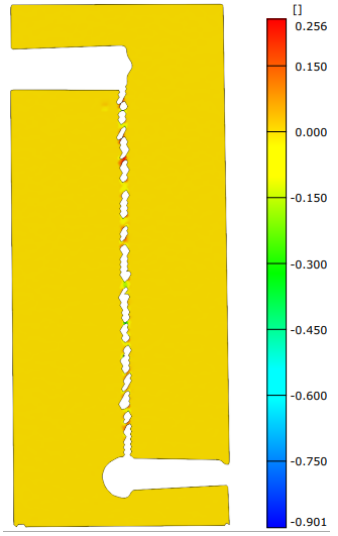

Major strain TAST 60-4 at F = 0 kN

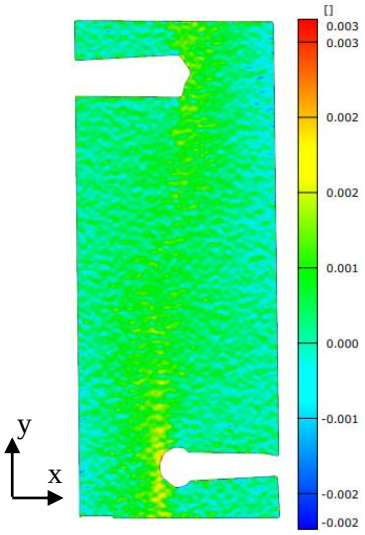

Y-strain TAST 60-5 at F = 24.8 kN

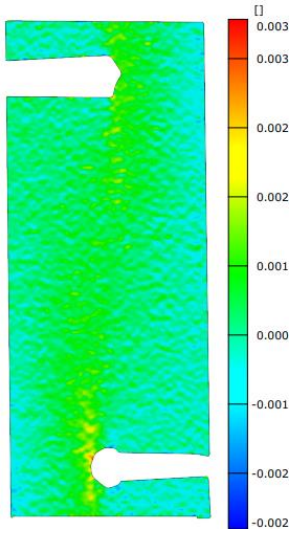

Y-strain TAST 60-5 at F = 27.4 kN

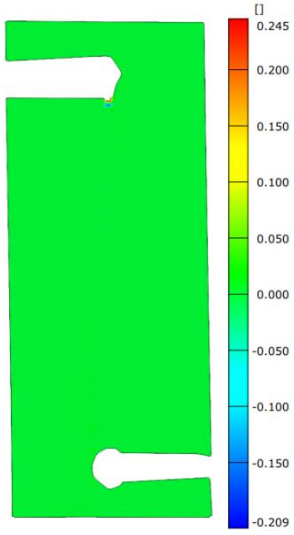

Y-strain TAST 60-5 at F = 41.7 kN

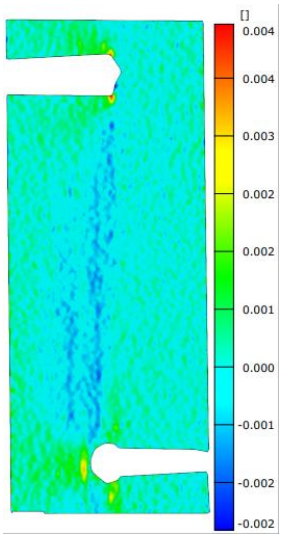

X-strain TAST 60-5 at F = 24.8 kN

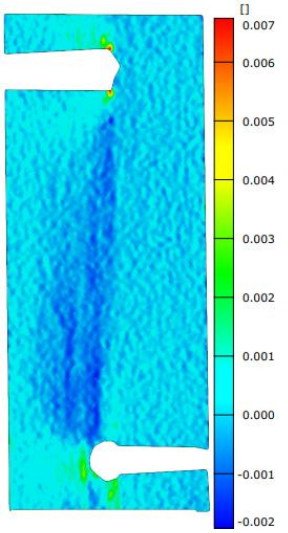

X-strain TAST 60-5 at F = 27.4 kN

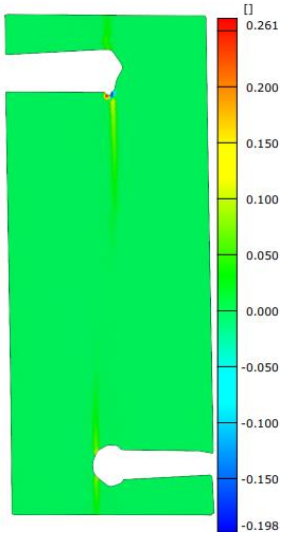

X-strain TAST 60-5 at F = 41.7 kN

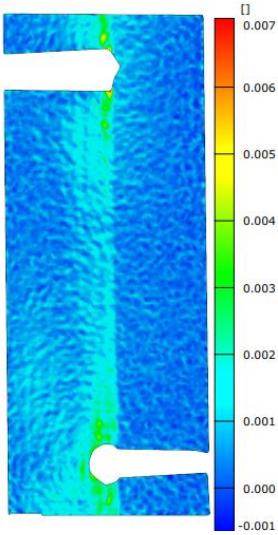

Major strain TAST 60-5 at F = 24.8 kN

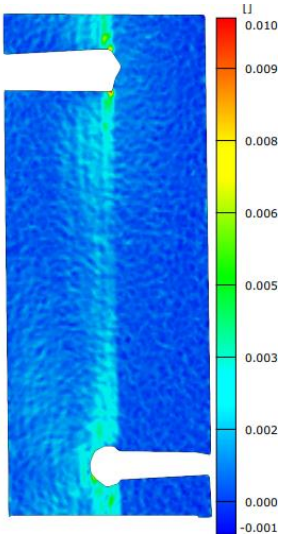

Major strain TAST 60-5 at F = 27.4 kN

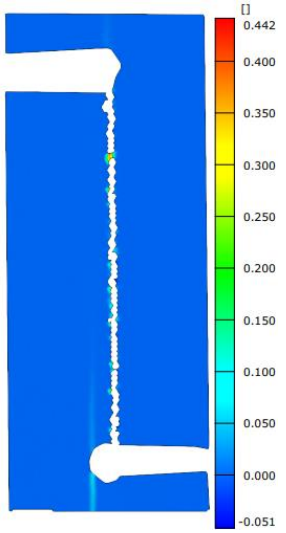

Major strain TAST 60-5 at F = 0 kN

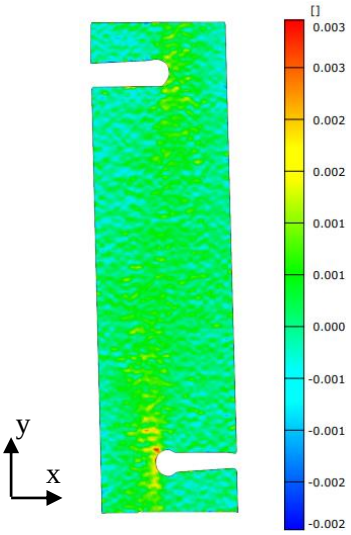

Y-strain TAST 90-1 at F = 25.5 kN

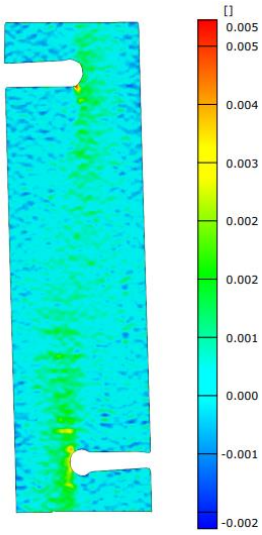

Y-strain TAST 90-1 at F = 36.5 kN

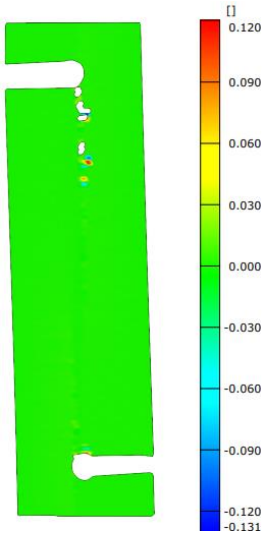

Y-strain TAST 90-1 at F = 41.4 kN

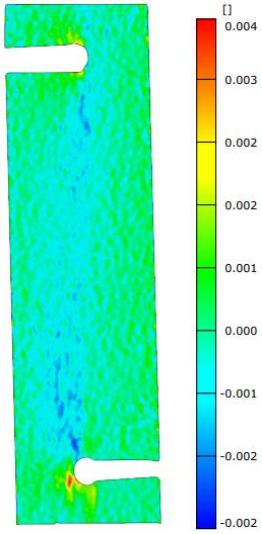

X-strain TAST 90-1 at F = 25.5 kN

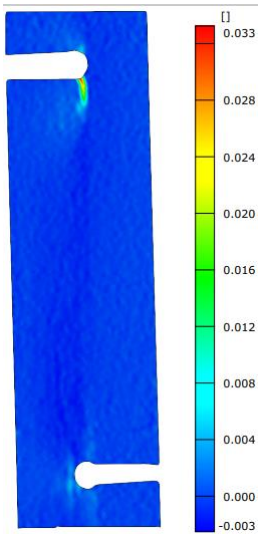

X-strain TAST 90-1 at F = 36.5 kN

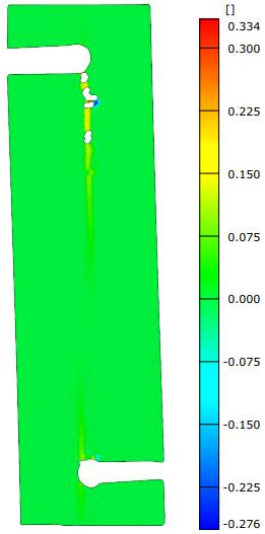

X-strain TAST 90-1 at F = 41.4 kN

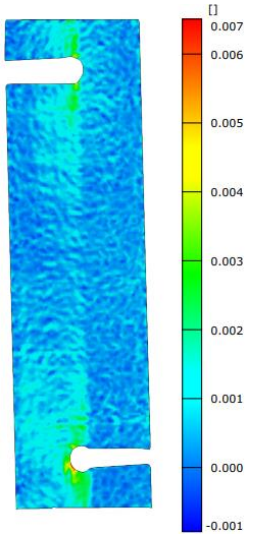

Major strain TAST 90-1 at F = 25.5 kN

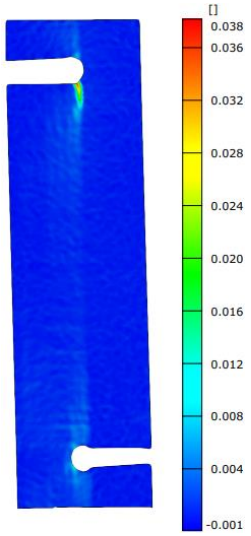

Major strain TAST 90-1 at F = 36.5 kN

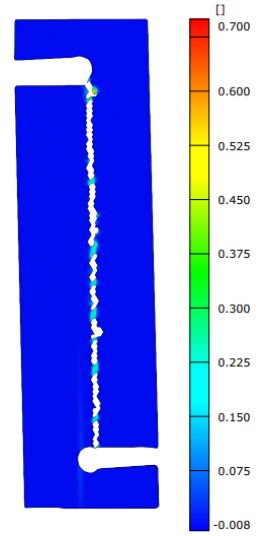

Major strain TAST 90-1 at F = 0 kN

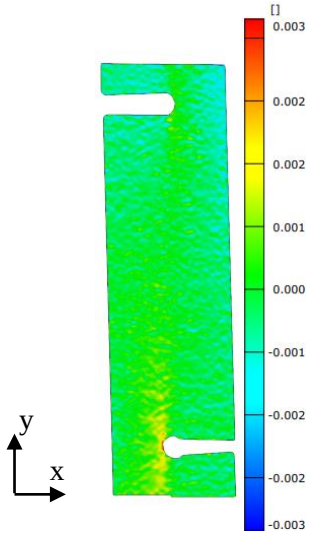

Y-strain TAST 90-2 at F = 30.5 kN

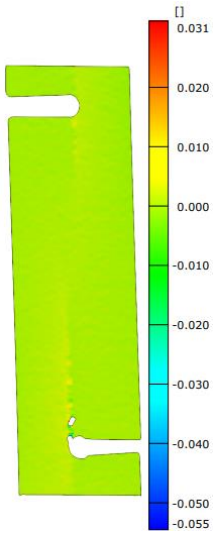

Y-strain TAST 90-2 at F = 49.2 kN

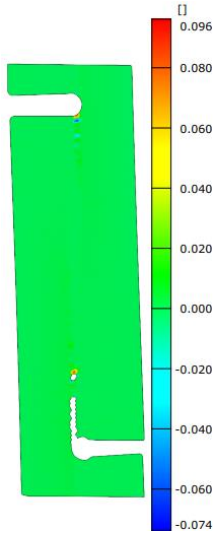

Y-strain TAST 90-2 at F = 57.8 kN

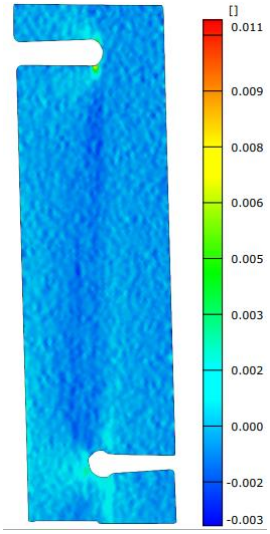

X-strain TAST 90-2 at F = 30.5 kN

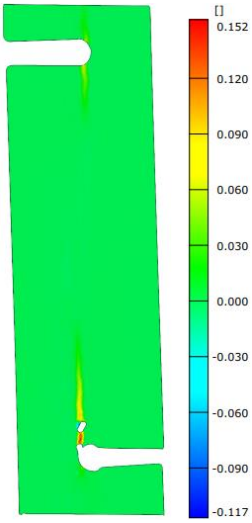

X-strain TAST 90-2 at F = 49.2 kN

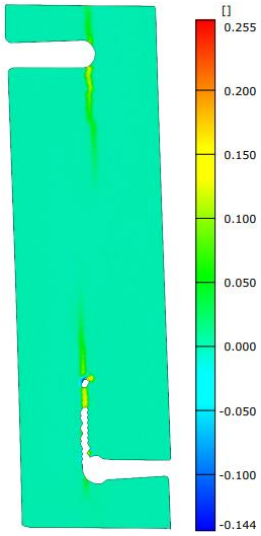

X-strain TAST 90-2 at F = 57.8 kN

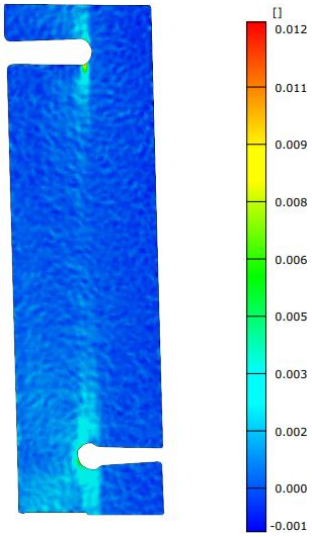

Major strain TAST 90-2 at F = 30.5 kN

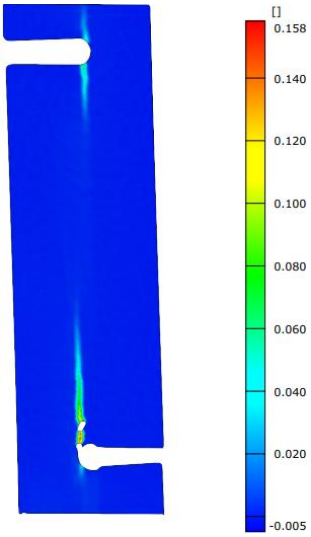

Major strain TAST 90-2 at F = 49.2 kN

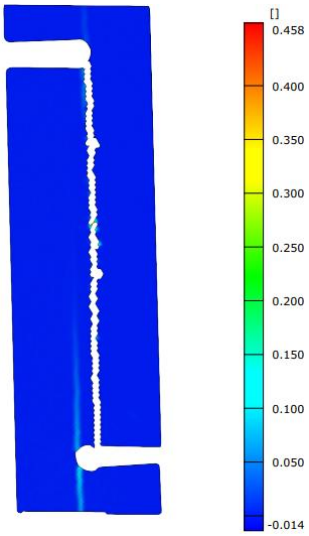

Major strain TAST 90-2 at F = 0 kN

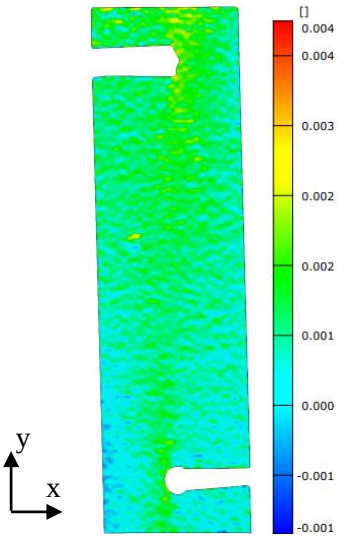

Y-strain TAST 90-3 at F = 30.7 kN

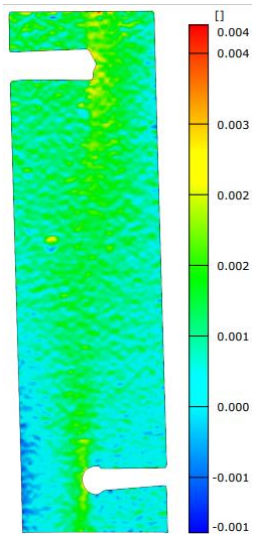

Y-strain TAST 90-3 at F = 39.9 kN

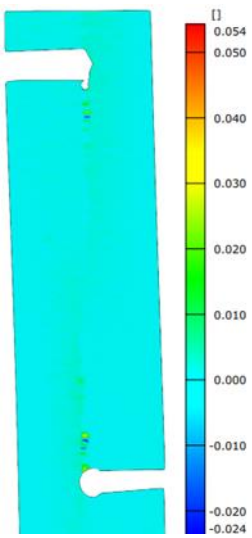

Y-strain TAST 90-3 at F = 50.7 kN

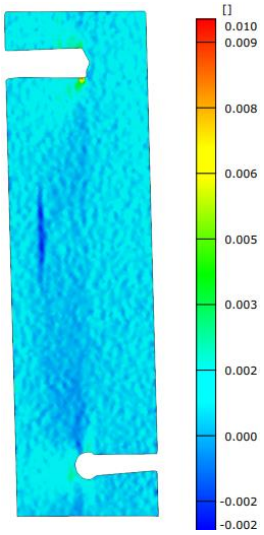

X-strain TAST 90-3 at F = 30.7 kN

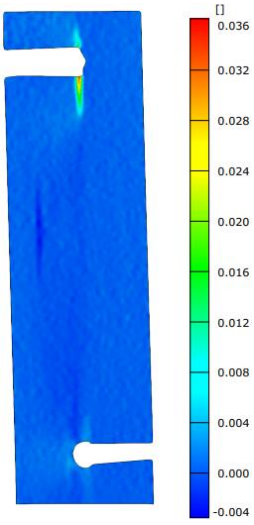

X-strain TAST 90-3 at F = 39.9 kN

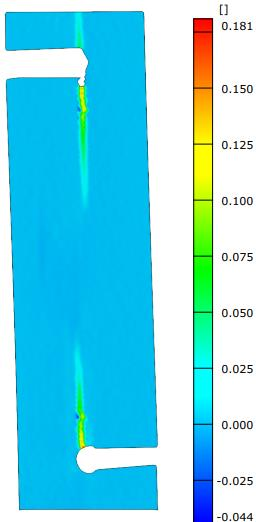

X-strain TAST 90-3 at F = 50.7 kN

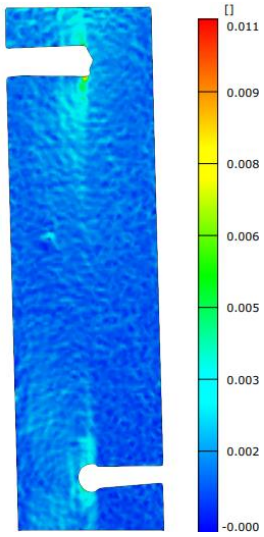

Major strain TAST 90-3 at F = 30.7 kN

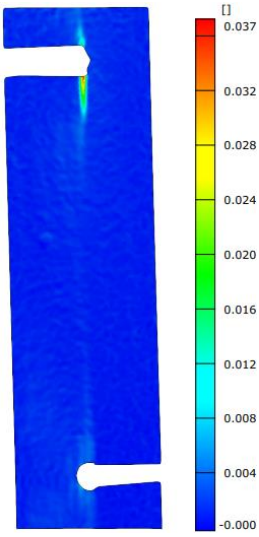

Major strain TAST 90-3 at F = 39.9 kN

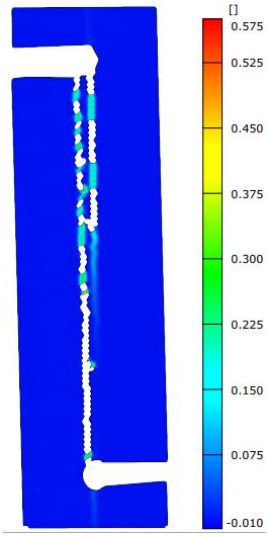

Major strain TAST 90-3 at F = 0 kN

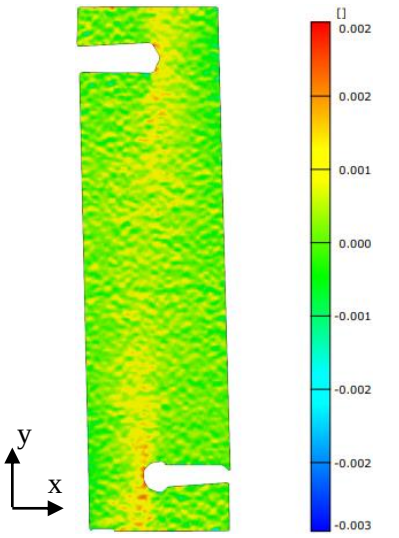

Y-strain TAST 90-4 at F = 29.7 kN

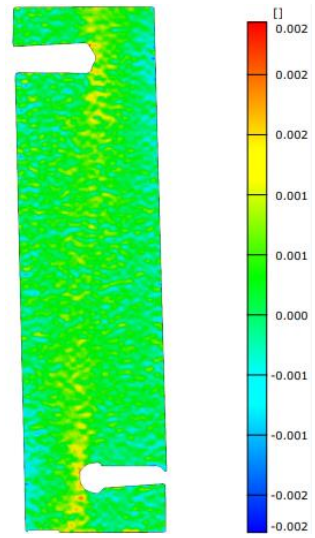

Y-strain TAST 90-4 at F = 31.2 kN

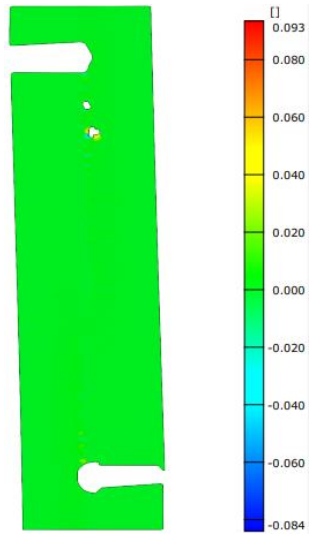

Y-strain TAST 90-4 at F = 41.9 kN

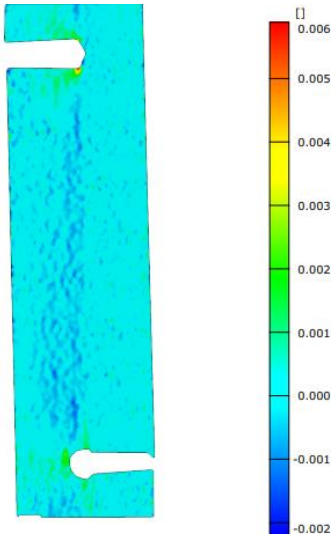

X-strain TAST 90-4 at F = 29.7 kN

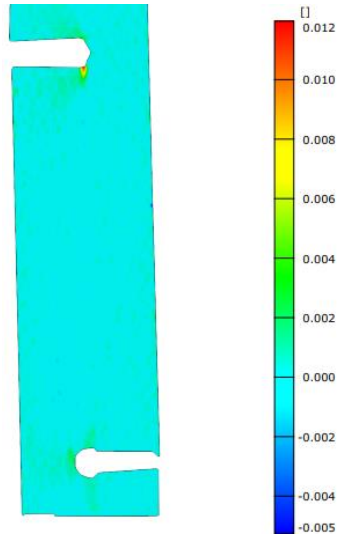

X-strain TAST 90-4 at F = 31.2 kN

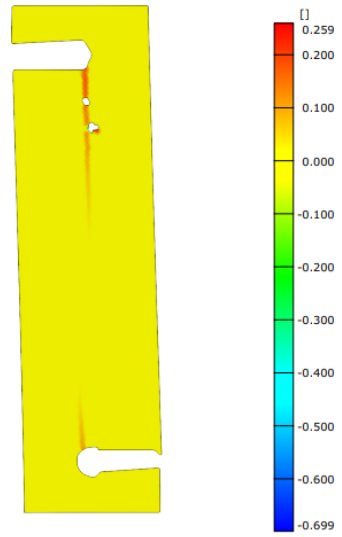

X-strain TAST 90-4 at F = 41.9 kN

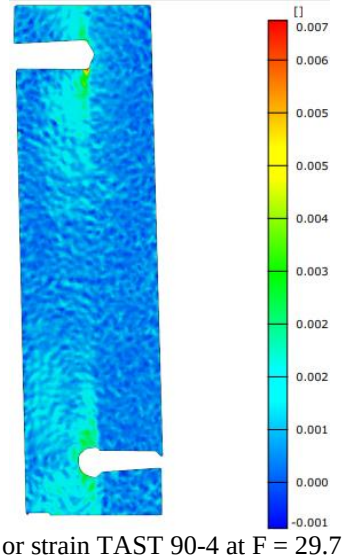

Major strain TAST 90-4 at F = 29.7 kN

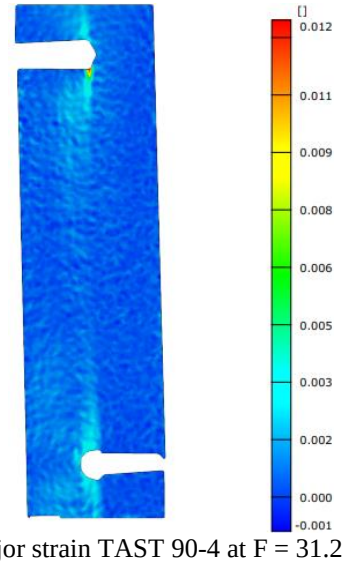

Major strain TAST 90-4 at F = 31.2 kN

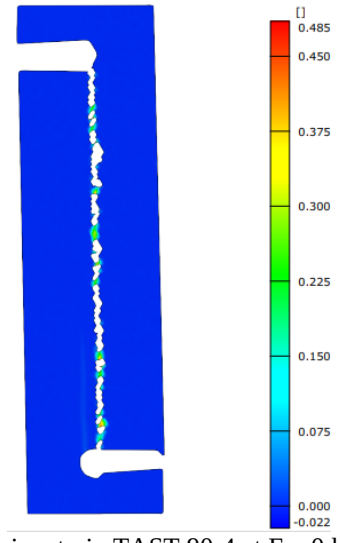

Major strain TAST 90-4 at F = 0 kN

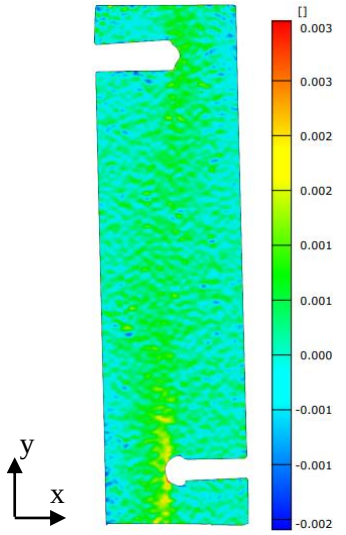

Y-strain TAST 90-5 at F = 30.1 kN

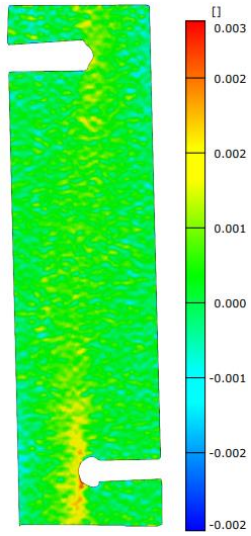

Y-strain TAST 90-5 at F = 33.3 kN

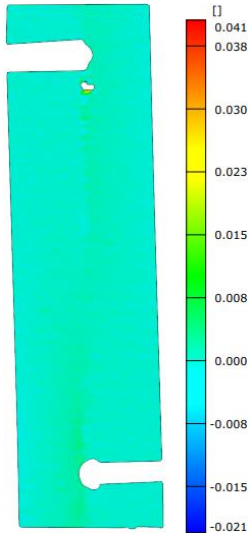

Y-strain TAST 90-5 at F = 44.6 kN

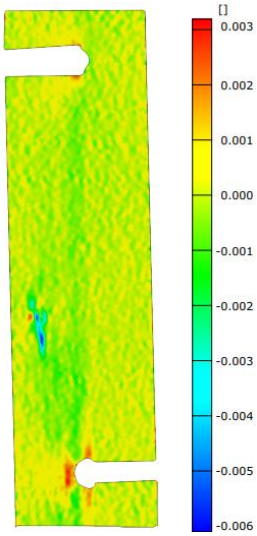

X-strain TAST 90-5 at F = 30.1 kN

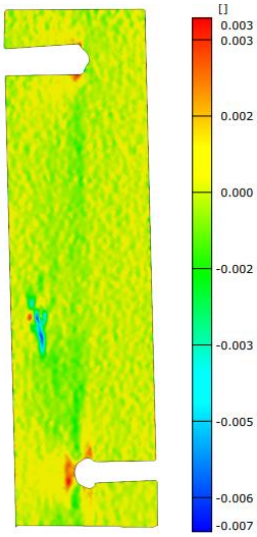

X-strain TAST 90-5 at F = 33.3 kN

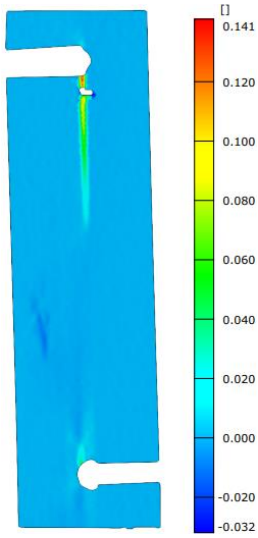

X-strain TAST 90-5 at F = 44.6 kN

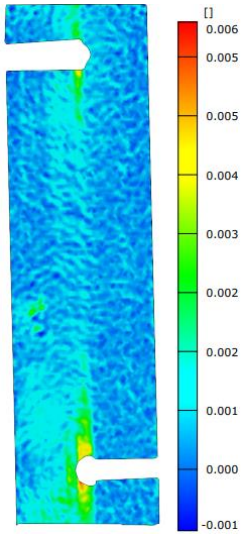

Major strain TAST 90-5 at F = 30.1 kN

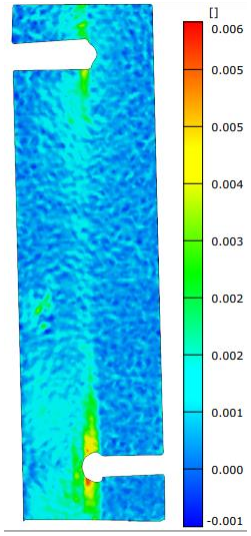

Major strain TAST 90-5 at F = 33.3 kN

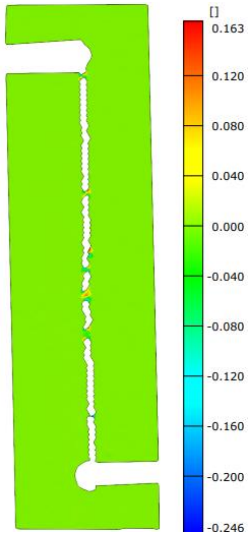

Major strain TAST 90-5 at F = 0 kN

B Numerical Results of TAST FE Models

This section provides results of the FE model for the TASTs with varying overlap lengths. Plots of global stresses, displacements and bond stresses of the FE models are displayed. In FE models of TAST 60-2 and 90-5, the adhesive interface was modelled with tied contact definition. For this reason, bond stresses could not be read from the contact stress. As an alternative, bond stresses were determined from the first row of elements of the FRP laminate. Displayed bond stresses are positioned in the interface between FRP and steel, inside the zone of interest, as indicated by the dashed surface in Figure B.1

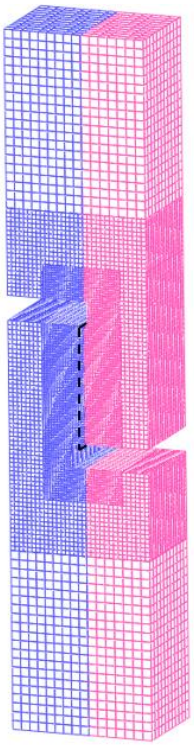

Figure B.1: Position adhesive interface bond stress

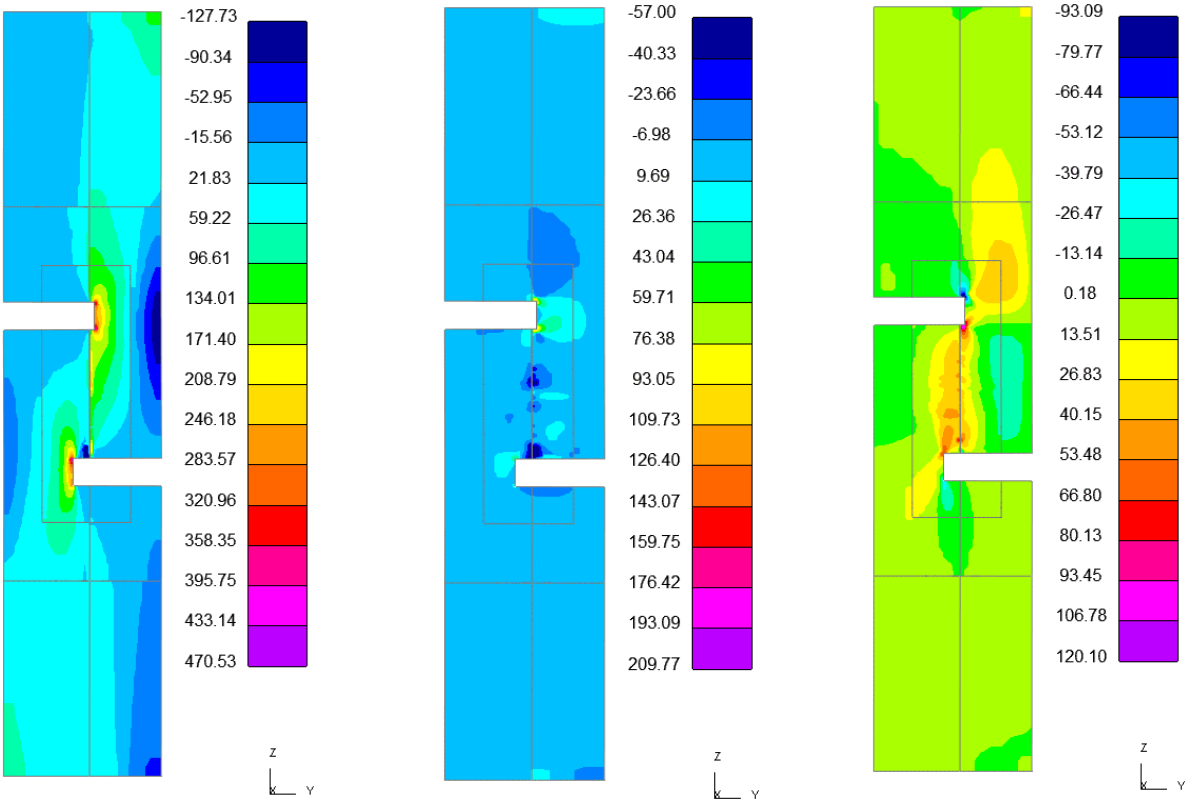

Normal in global Z-direction **Normal in global Y-direction** **Shear in global YZ-direction**

Stress plots in MPa of FE model TAST 30-2 at F = 34.0 kN

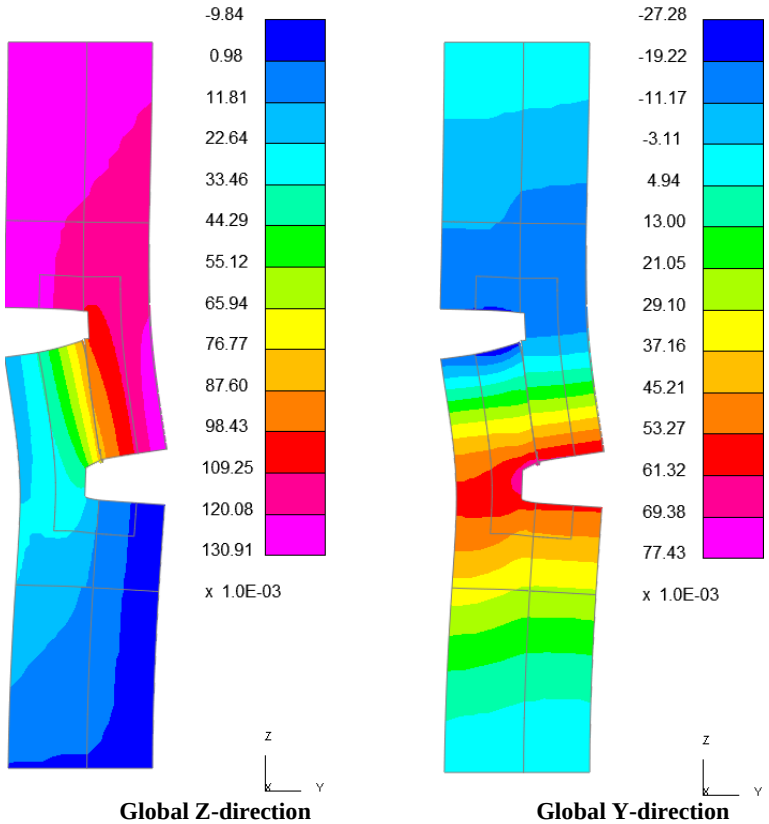

Global Z-direction **Global Y-direction**

Displacement plots in mm of FE model TAST 30-2 at F = 34.0 kN (deformation magnified 50x)

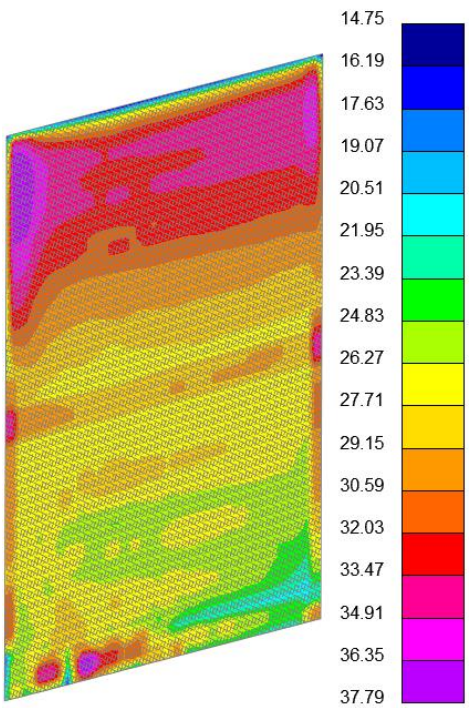

One stage before failure at F = 34 kN

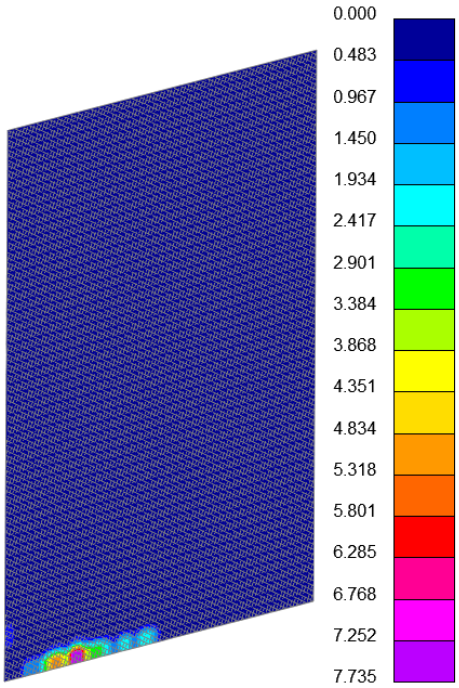

After failure at F = 0 kN

Shear bond stress in MPa of FE model TAST 30-2

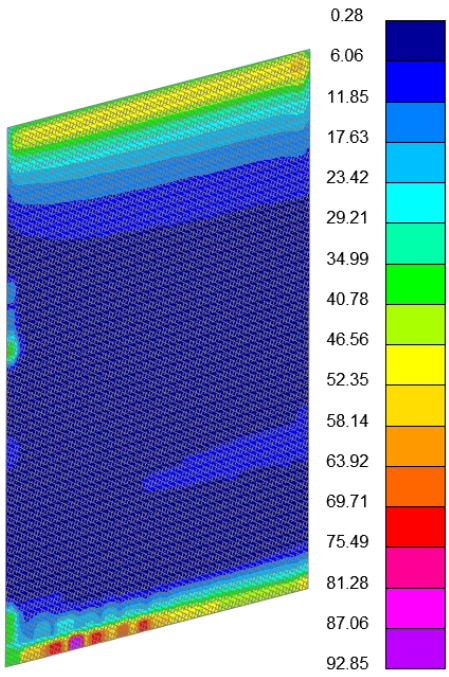

One stage before failure at F = 34 kN

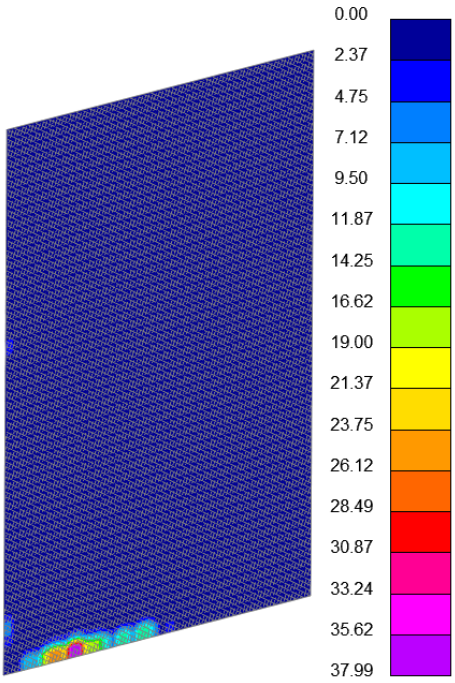

After failure at F = 0 kN

Peel bond stress in MPa of FE model TAST 30-2 [MPa]

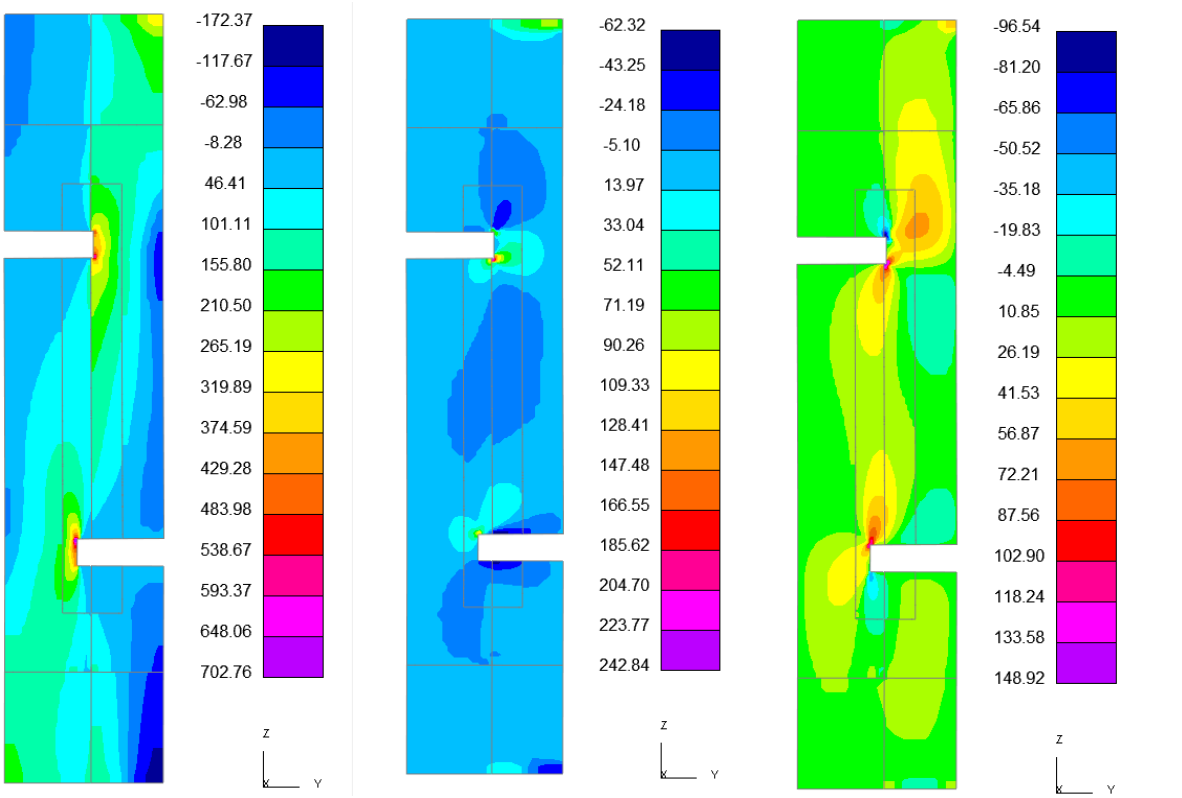

Normal in global Z-direction **Normal in global Y-direction** **Shear in global YZ-direction**

Stress plots in MPa of FE model TAST 60-2 at F = 42.1 kN

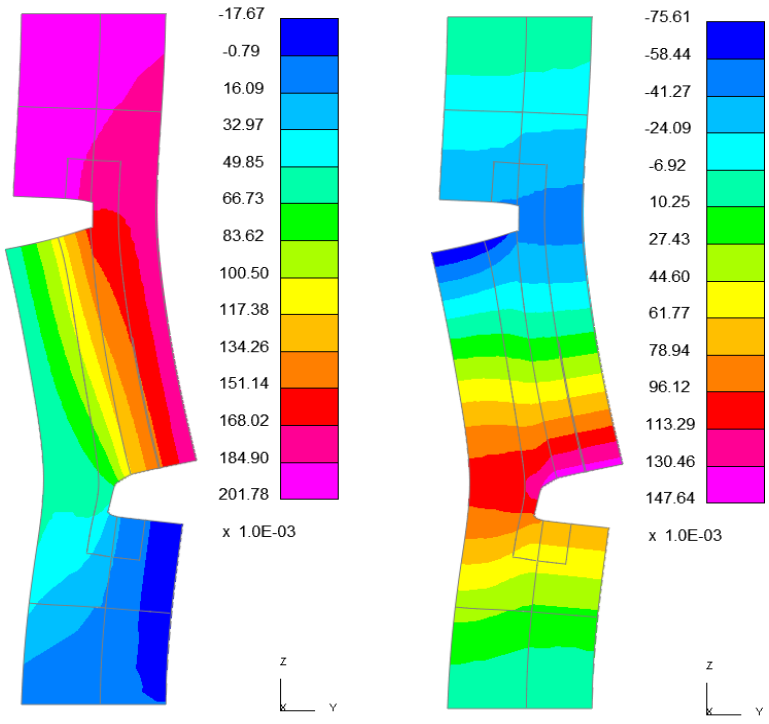

Global Z-direction **Global Y-direction**

Displacement plots in mm of FE model TAST 60-2 at F = 42.1 kN (deformation magnified 50x)

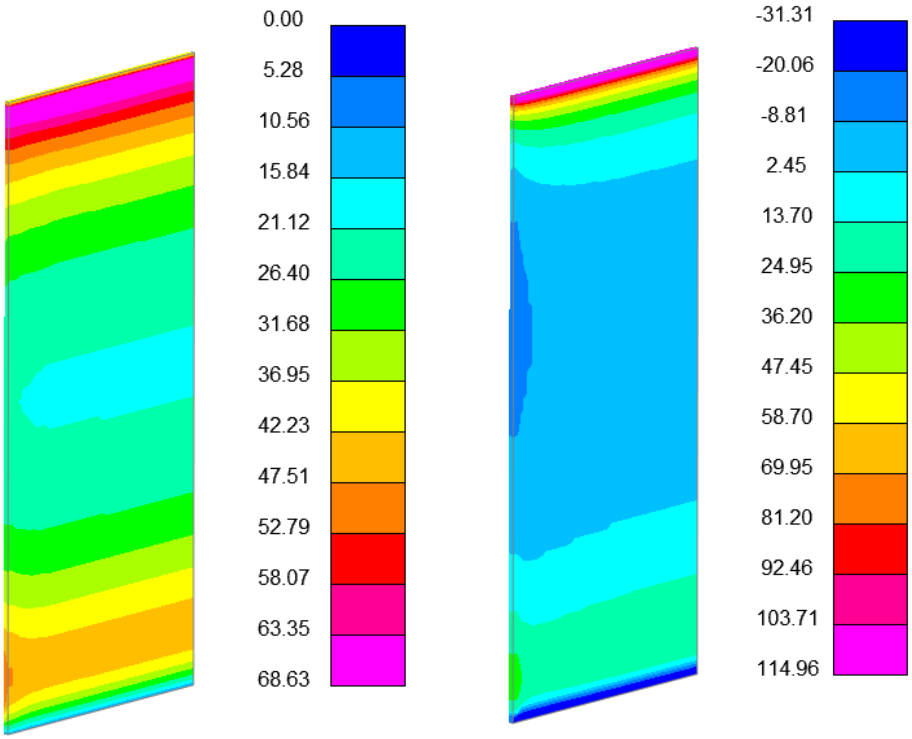

Shear in global YZ-direction **Peel in global Y-direction**

Bond stress plots in MPa of FE model TAST 60-2 at F = 42.1 kN

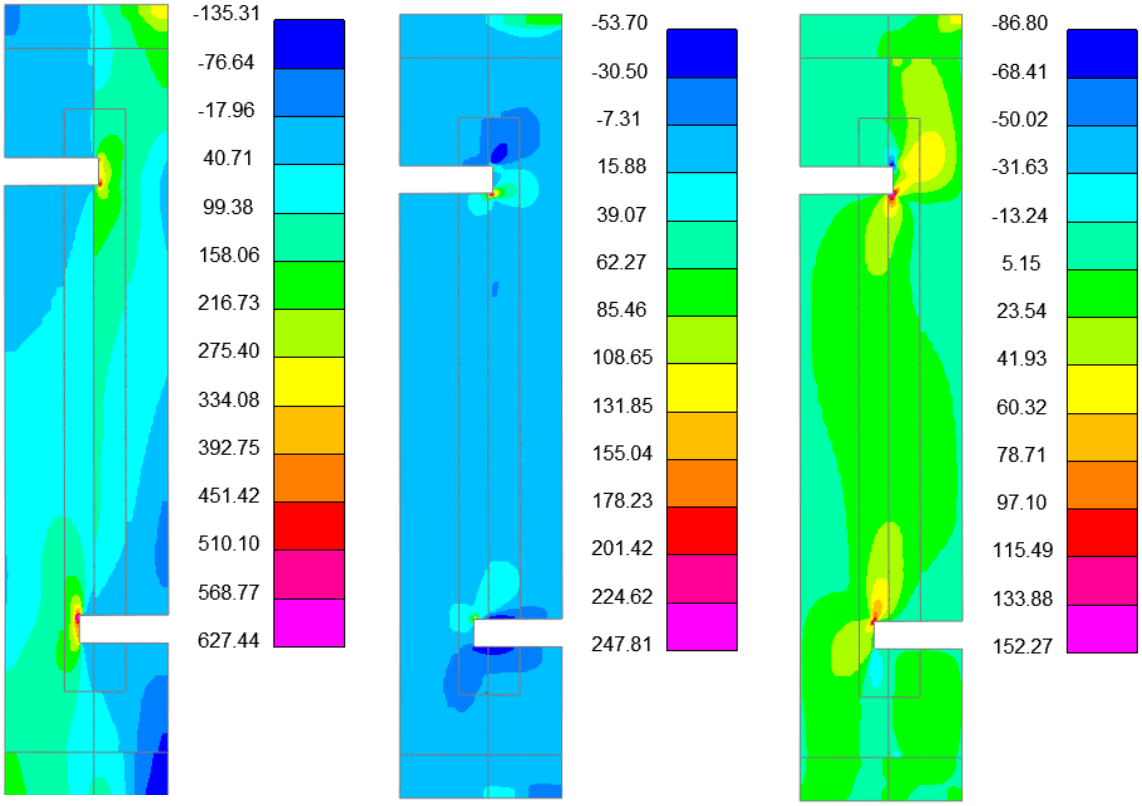

Normal in global Z-direction **Normal in global Y-direction** **Shear in global YZ-direction**

Stress plots in MPa of FE model TAST 90-5 at F = 45.7 kN

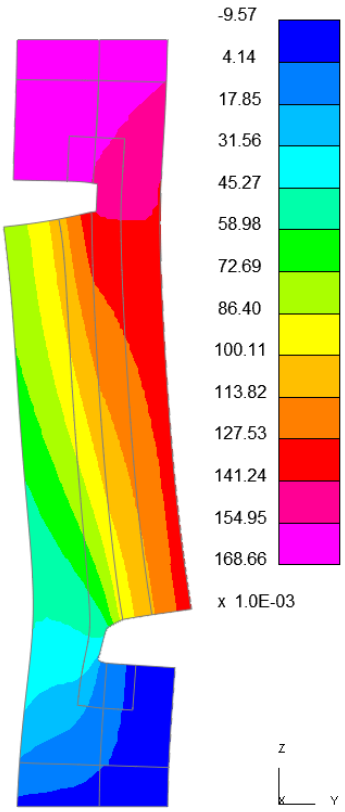

Global Z-direction

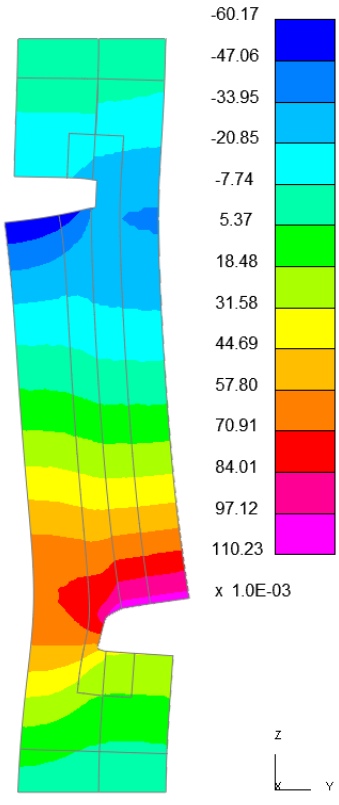

Global Y-direction

Displacement plots in mm of FE model TAST 90-5 at F = 45.7 kN [mm] (deformation magnified 50x)

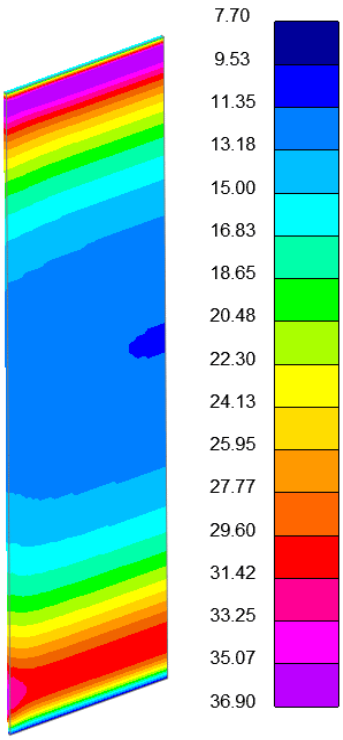

Shear in global YZ-direction

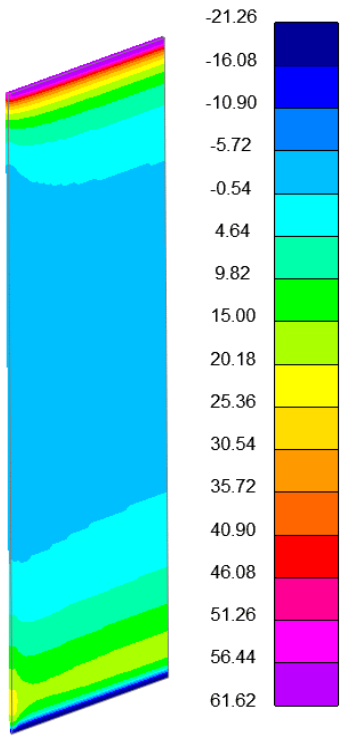

Normal in global Y-direction

Bond stress plots in MPa of FE model TAST 90-5 at F = 45.7 kN

C Determination of Design Values Bond Strength for Thick-adherend Shear Tests

Annex D of Eurocode 1990 defines two methods to derive properties from tests, which are:

- Method A: by assessing a characteristic value, which is divided by a partial factor and, if necessary, multiplied by a conversion factor
- Method B: by directly determining an ULS design value, implicitly or explicitly accounting for conversion and required reliability of the results [54].

First, method A will be applied. With a log-normal distribution, the design value, X_d, should be determined by:

$$X_d = \frac{\eta_d}{\gamma_M} \exp\left[m_y - k_n s_y\right] \quad \text{(C.1)}$$

where

$$m_y = \frac{1}{n} \Sigma \ln\left(x_i\right) \quad \text{(C.2)}$$

$$s_y = \sqrt{\frac{1}{n-1} \Sigma (\ln(x_i) - m_y)^2} \quad \text{if Vx is unknown} \quad \text{(C.3)}$$

η_d is the design value of the conversion factor. This conversion factor is strongly dependent on the type of test and type of material [54]. As sufficient knowledge of the correct value is missing, a value of 1.0 was assumed in the calculation.

γ_M is the partial factor. This partial factor should be selected according to the field of application of the test results. A value of 1.0 was assumed in the calculation.

$m_y = 2.82$ based on experimental results.

n is the number of tested samples. In this case, n = 12.

k_n is based on Table D.1 of Annex D in Eurocode 1990. As insufficient prior knowledge of the coefficient of variation, V_x, is available, V_x is unknown was applied. As n = 12, $k_n = 1.89$.

$s_y = 0.26$ based on experimental results.

This calculation leads to: $X_d = 10.27\ MPa$ where X_d is the characteristic value of the average shear bond strength.

For method B, the following formula is provided to determine basic variable X based on a log-normal distribution:

$$X_d = \eta_d \exp\left[m_y - k_{d,n} s_y\right] \quad \text{(C.4)}$$

where all variables are consistent with method A. However:

$k_{d,n}$ is based on Table D.2 of Annex D in Eurocode 1990. As n = 12, $k_{d,n} = 4.34$

This calculation leads to: $X_d = 5.42\ MPa$ where X_d is the design value of the average shear bond strength for ULS verifications.

D Experimental Results of Component-level Experiments

This appendix presents the experimental results of the component-level three-point bending tests. Sample COMP-6 is excluded from the results since the 2D-DIC photos for this test were out-of-focus and could therefore not be used. For all samples, major strains contour plots are displayed at four load levels:

- Before crack initiation
- After crack initiation, before total debonding
- After total debonding
- At the highest load level, before removing the load.

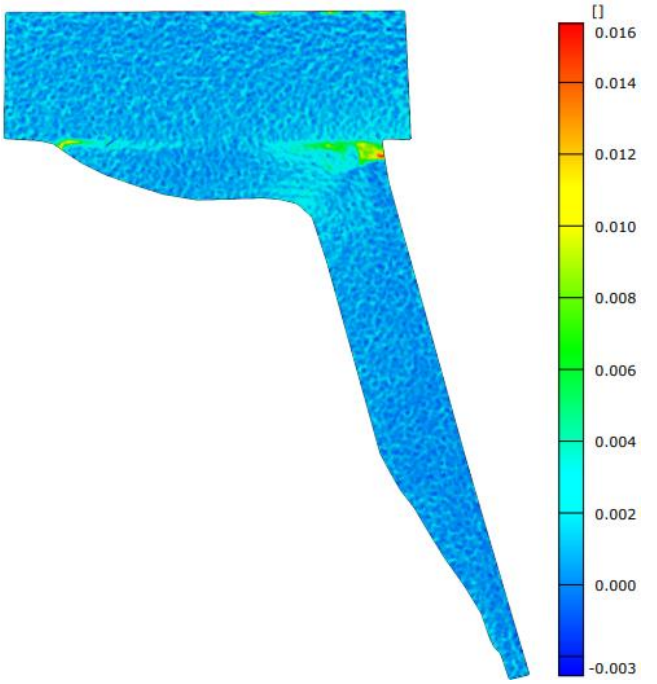

COMP 2 at F = 75.6 kN

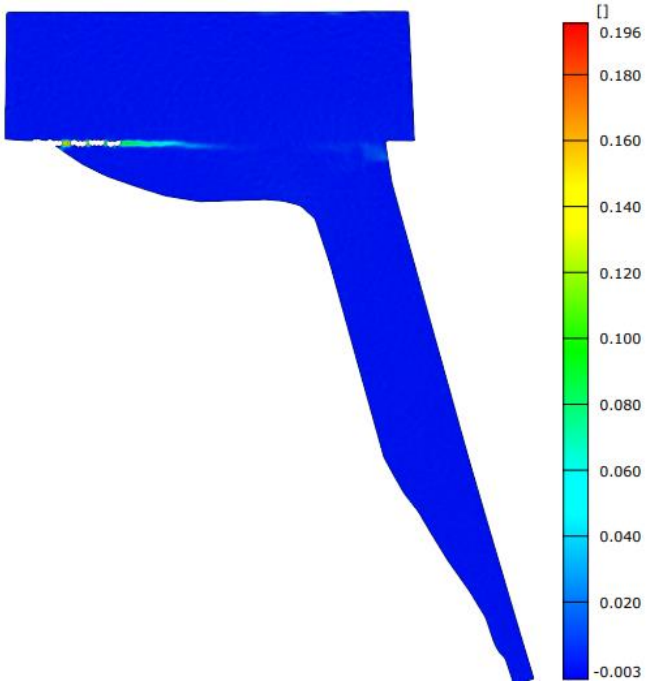

COMP 2 at F = 86.8 kN

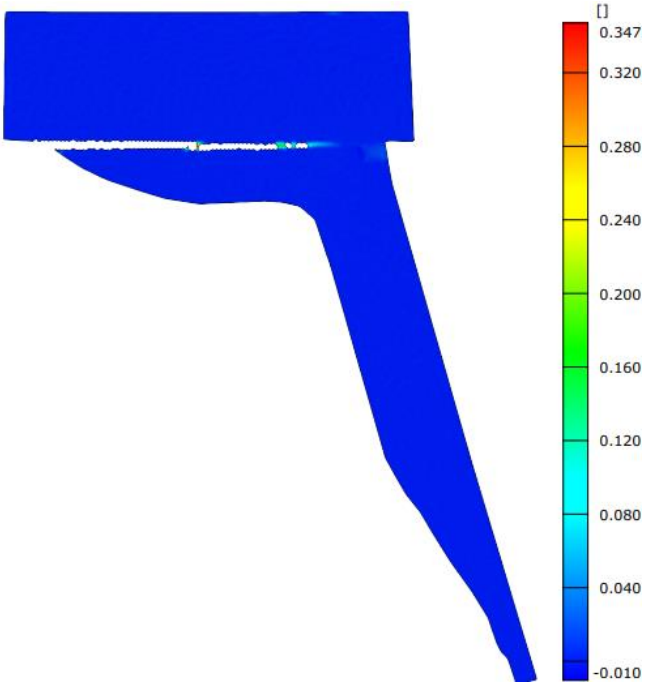

COMP 2 at F = 89.9 kN

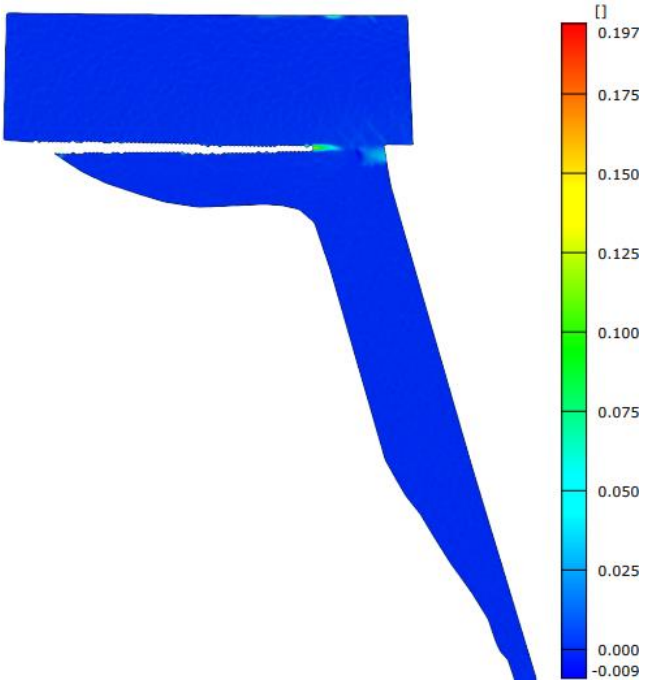

COMP 2 at F = 121.0 kN

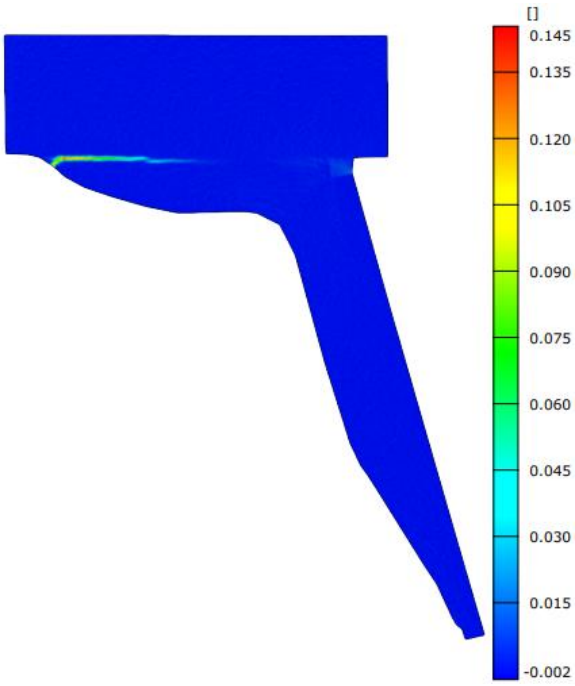

COMP 3 at F = 77.5 kN

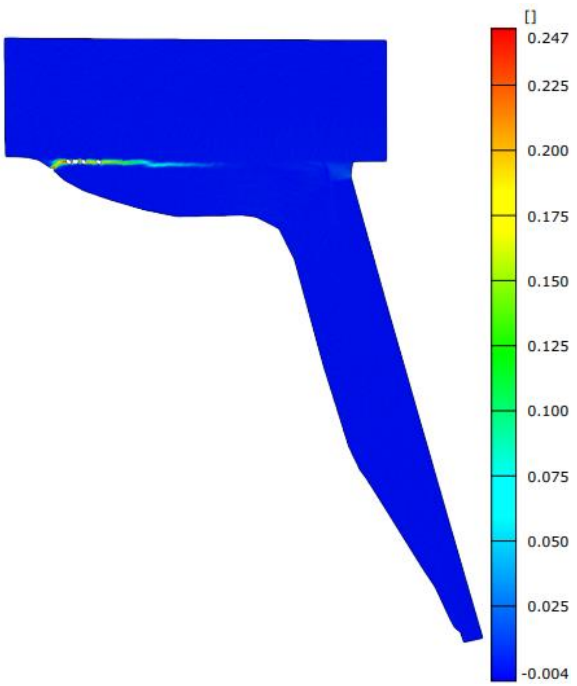

COMP 3 at F = 107.6 kN

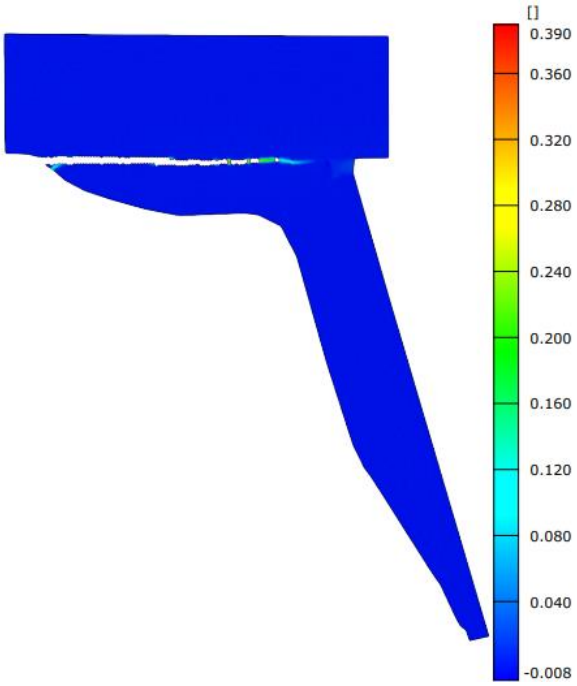

COMP 3 at F = 104.0 kN

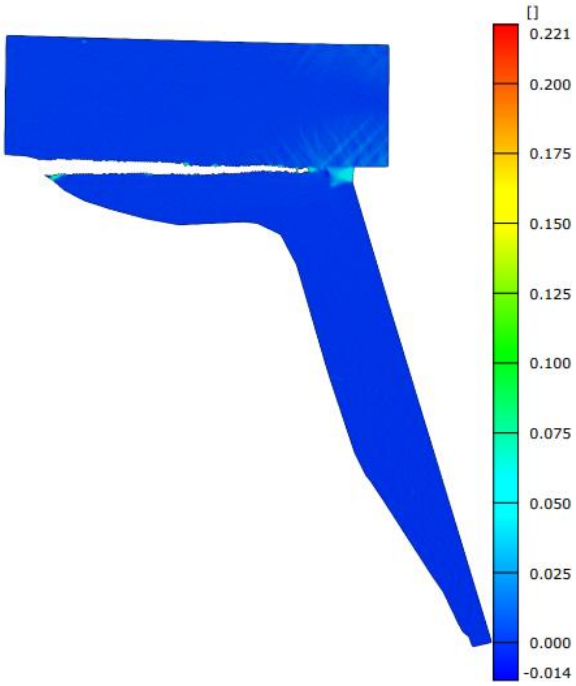

COMP 3 at F = 134.0 kN

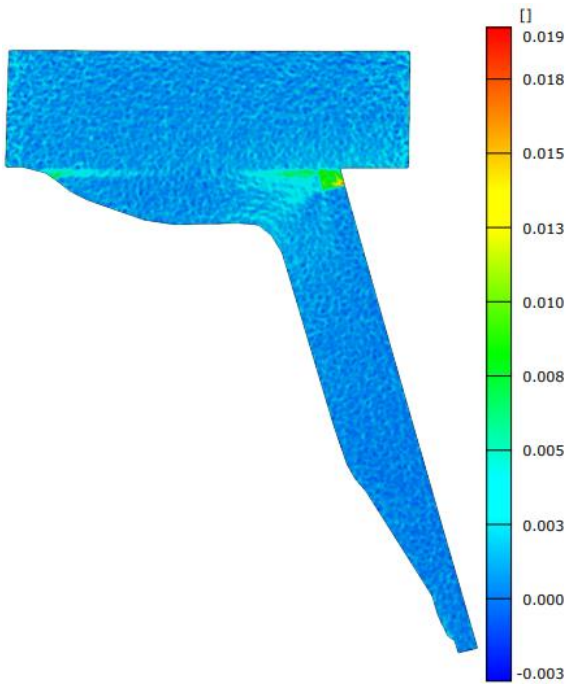

COMP 4 at F = 73.9 kN

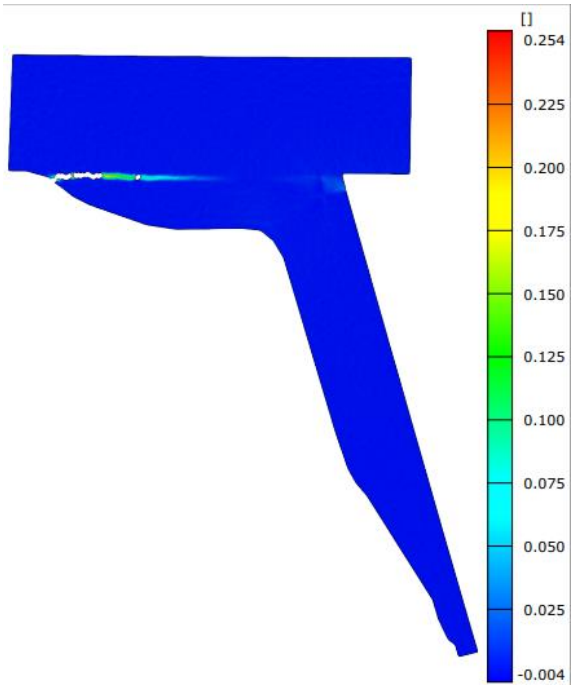

COMP 4 at F = 113.0 kN

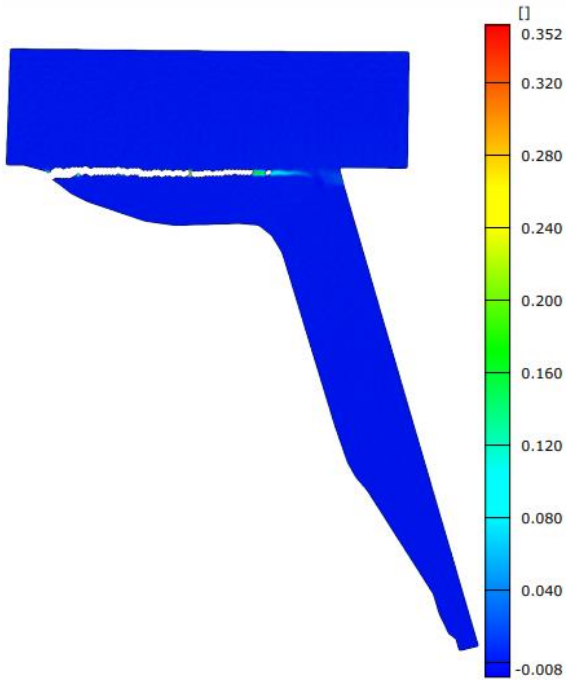

COMP 4 at F = 110.0 kN

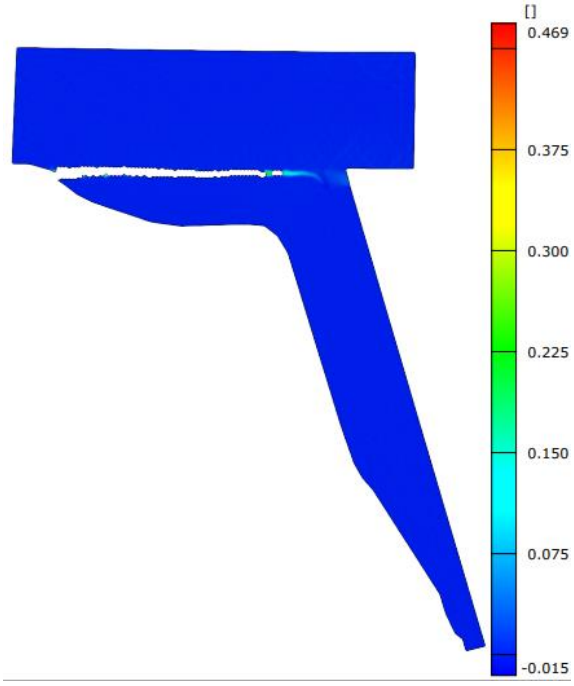

COMP 4 at F = 123.3 kN

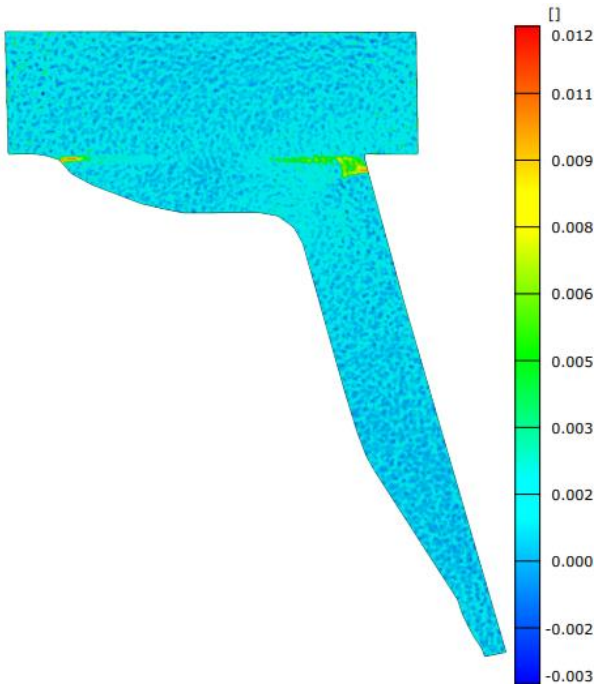

COMP 5 at F = 79.3 kN

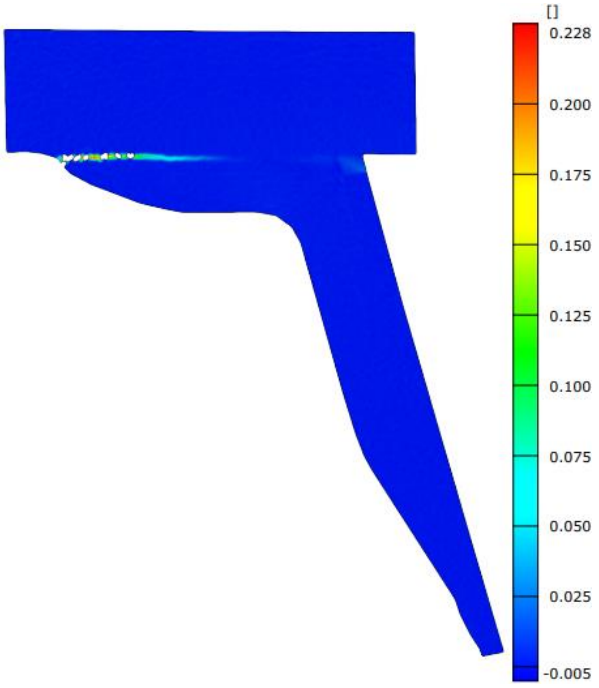

COMP 5 at F = 114.6 kN

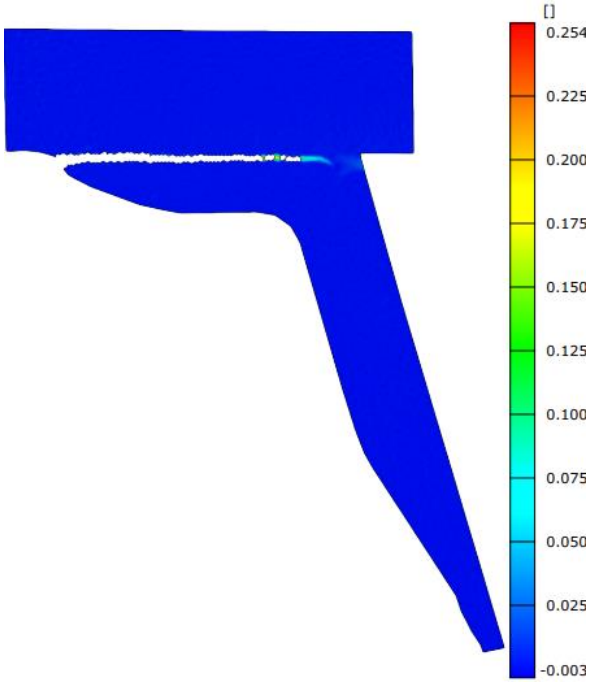

COMP 5 at F = 109.5 kN

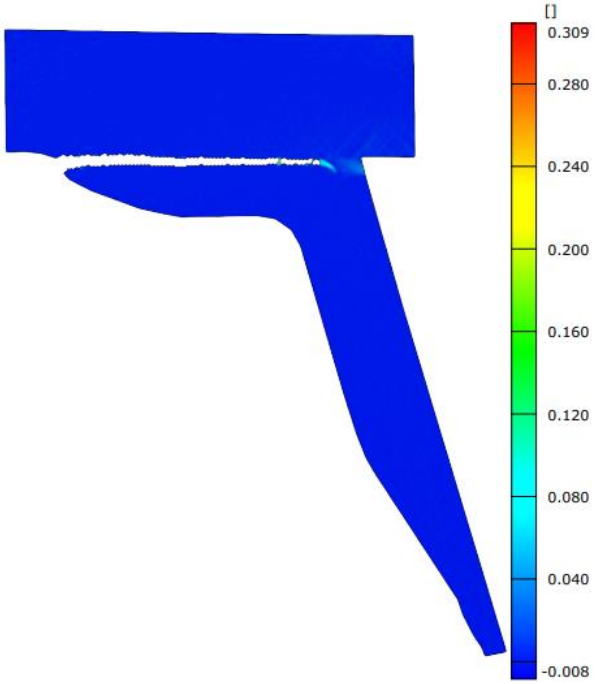

COMP 5 at F = 128.4 kN

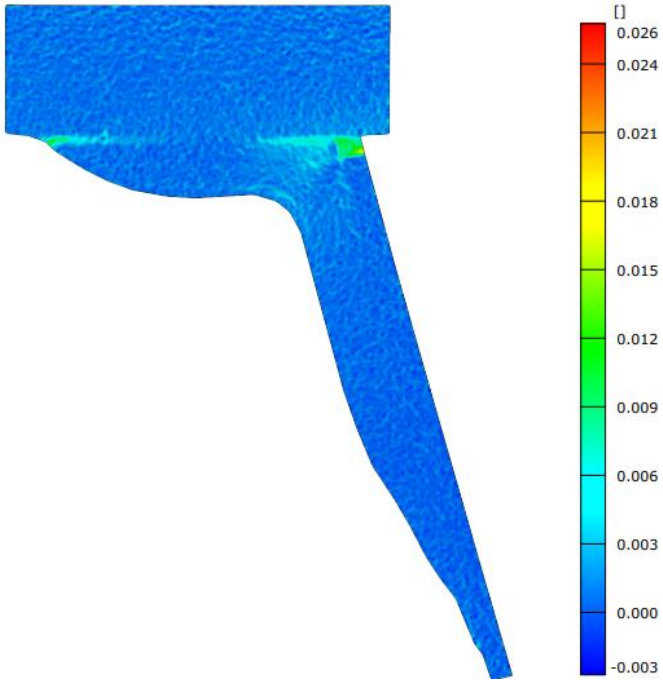

COMP 7 at F = 78.9 kN

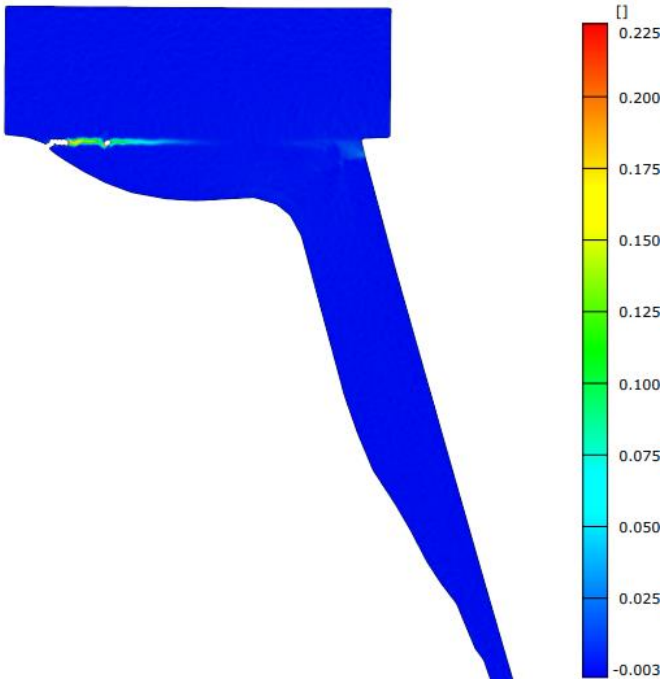

COMP 7 at F = 114.4 kN

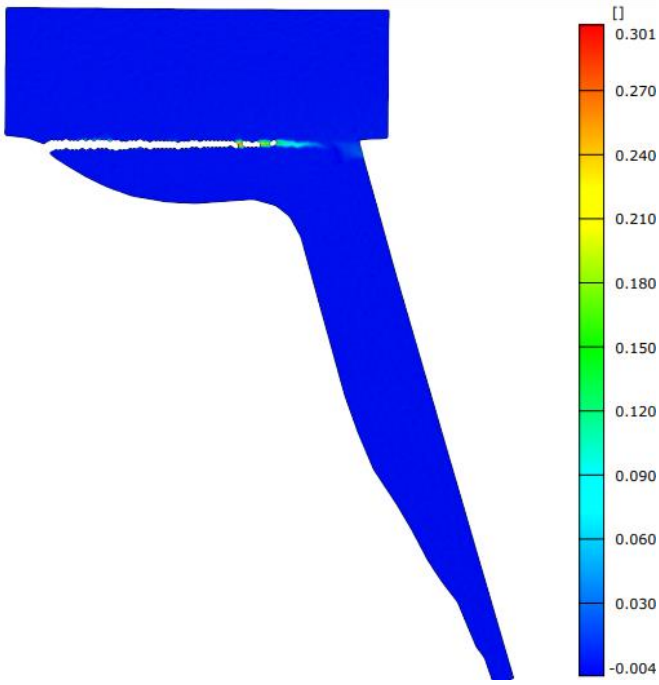

COMP 7 at F = 114.9 kN

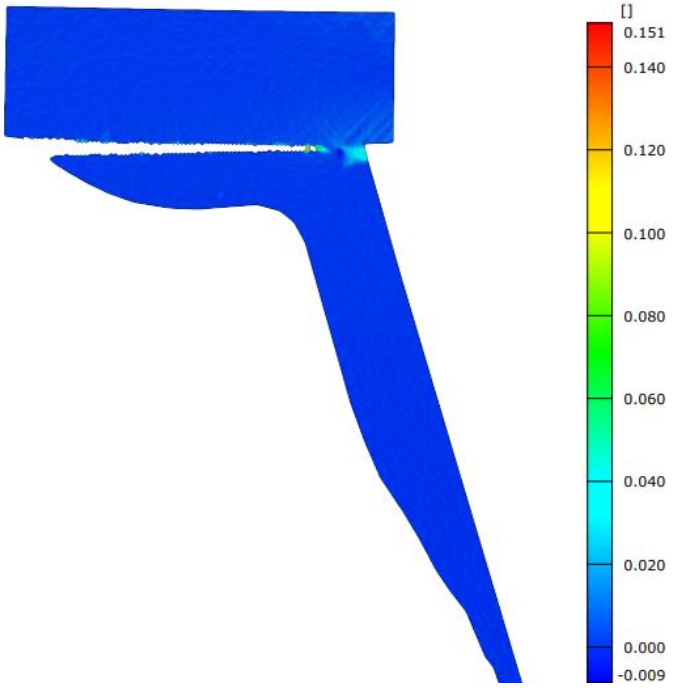

COMP 7 at F = 129.0 kN

E Numerical Results of Component-level FE Models

This section provides results of the FE model for the component-level three-point bending tests. Plots of global stresses and strains, displacements and bond stresses of the FE model are displayed. Since crack initiation and propagation were observed in the DIC results of the experiments, four stages are displayed in the model results, which are:

- Stage before crack initiation with a load level of 60 kN
- Stage after crack initiation with a load level of 104 kN
- Stage after crack initiation with a load level of 119 kN
- Stage after total debonding of the horizontal leg of the Cold Repair with a load level of 134 kN.

Results for the bond stress are displayed for the horizontal and vertical adhesive joint between steel and FRP. Figure 4.27 shows the position of horizontal, indicated by yellow, and vertical, indicated by green, adhesive interface.

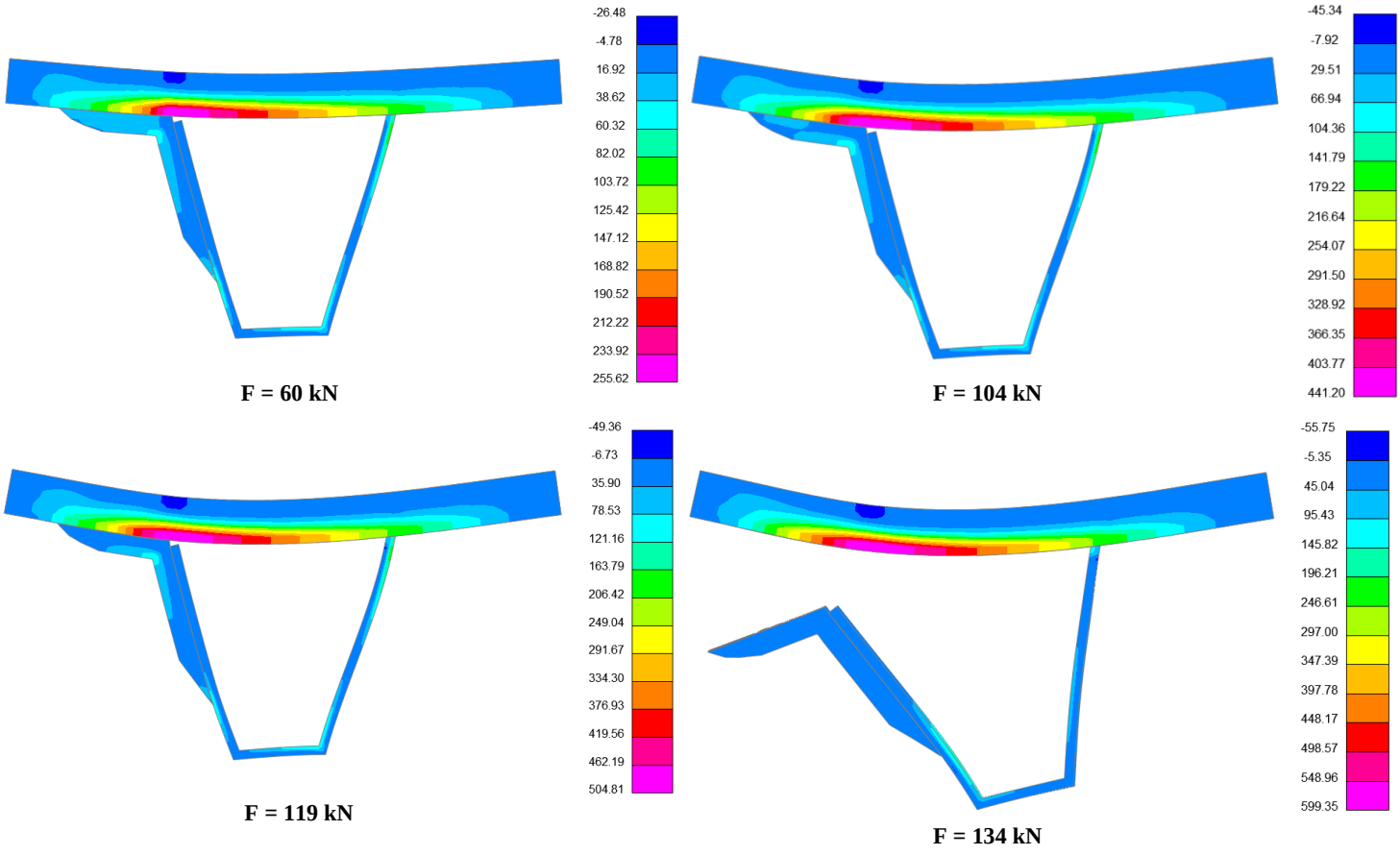

Maximum principle stress in MPa (deformation magnified 10x)

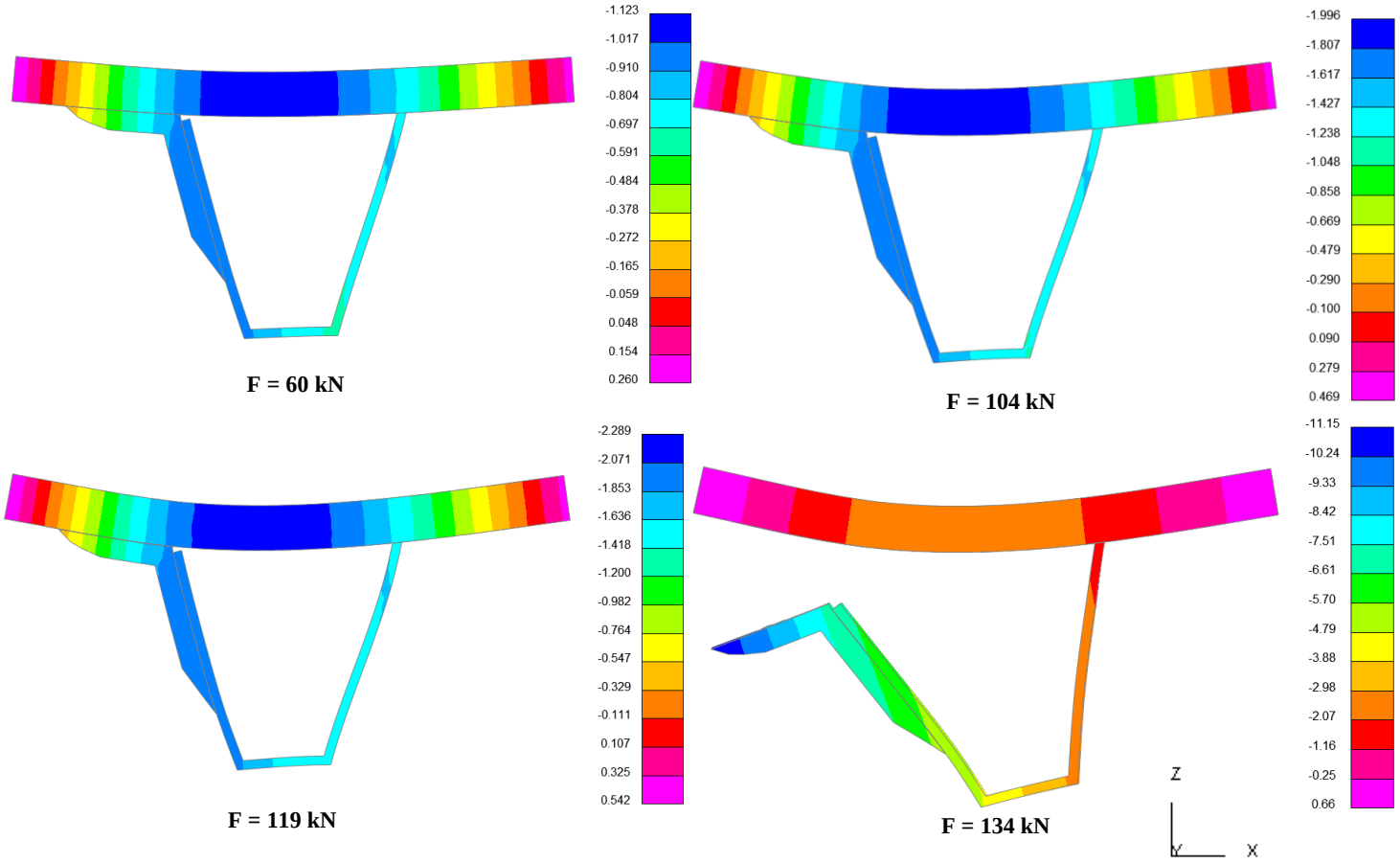

Displacement in mm in global z-direction (deformation magnified 10x)

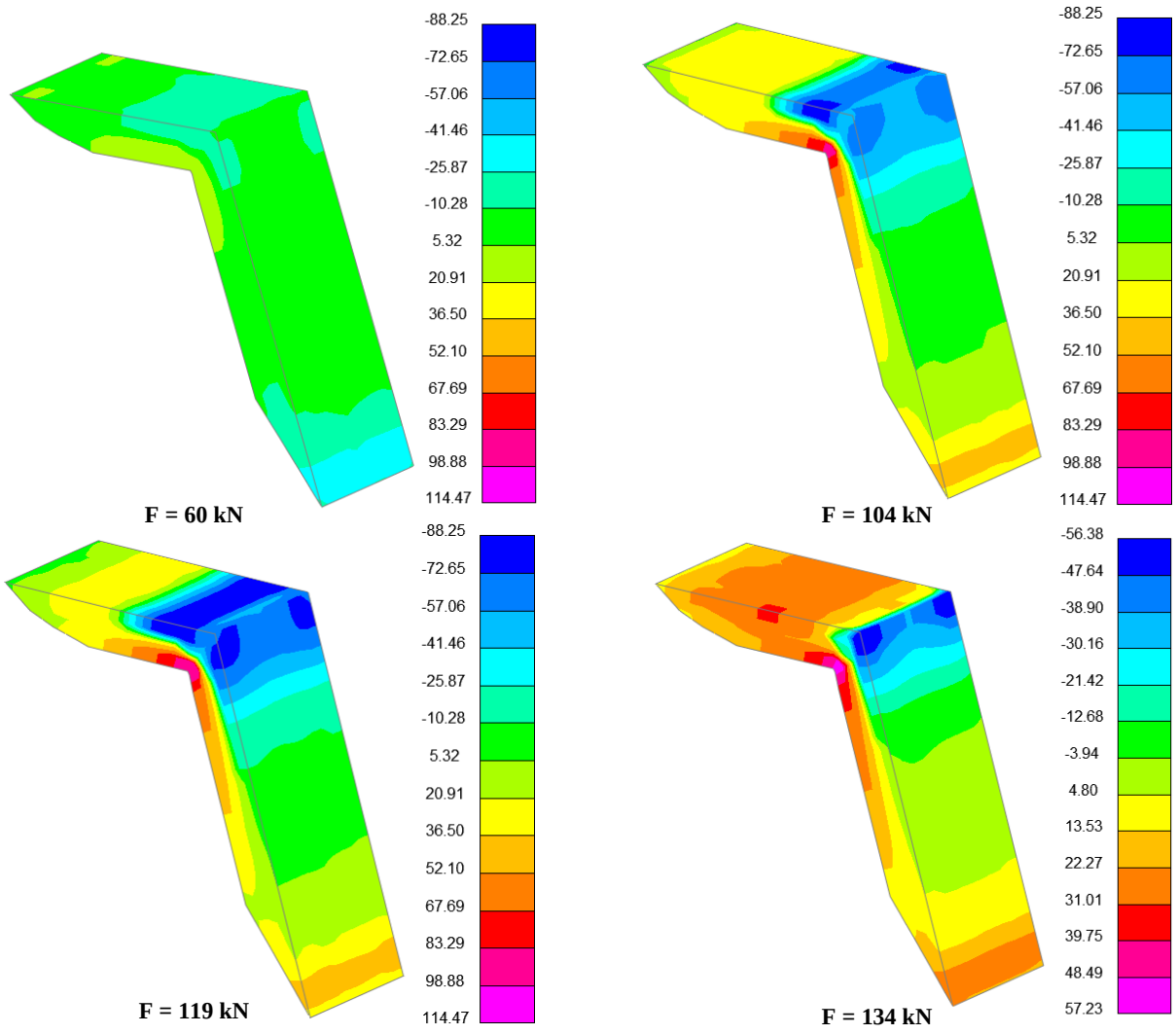

Normal stress in MPa in 0° direction of Cold Repair

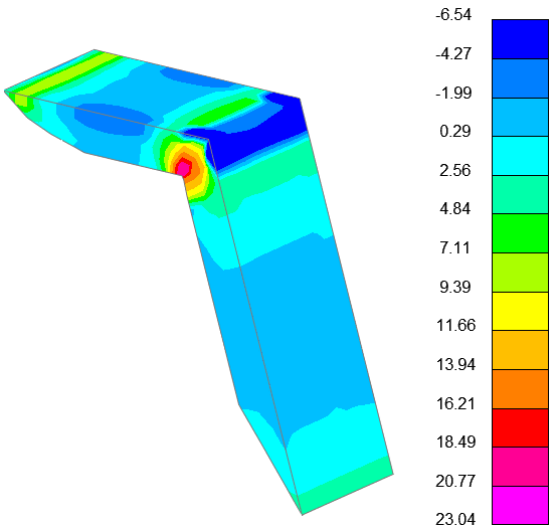

F = 60 kN

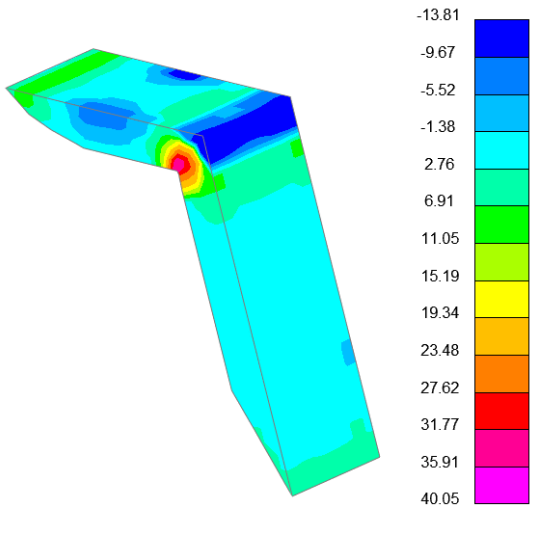

F = 104 kN

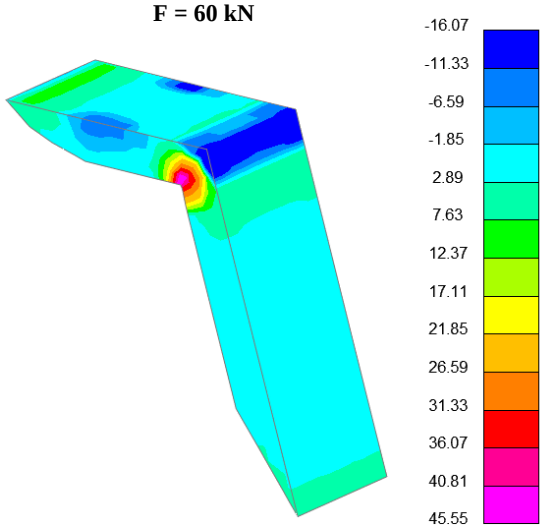

F = 119 kN

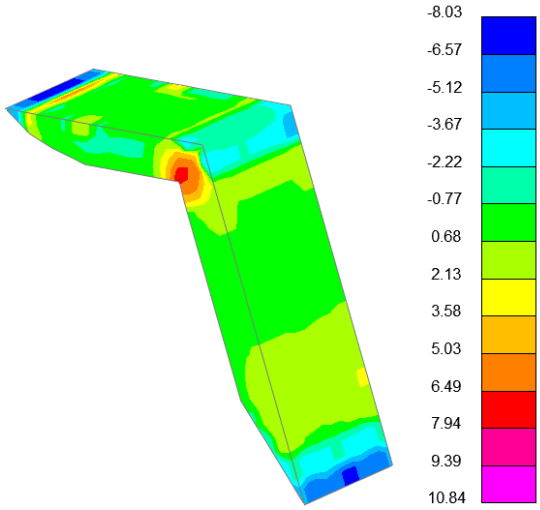

F = 134 kN

Normal stress in MPa in 90° out-of-plane direction of Cold Repair

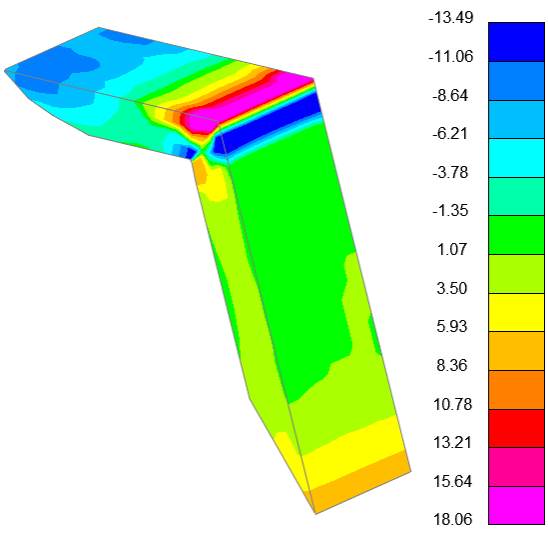

F = 60 kN

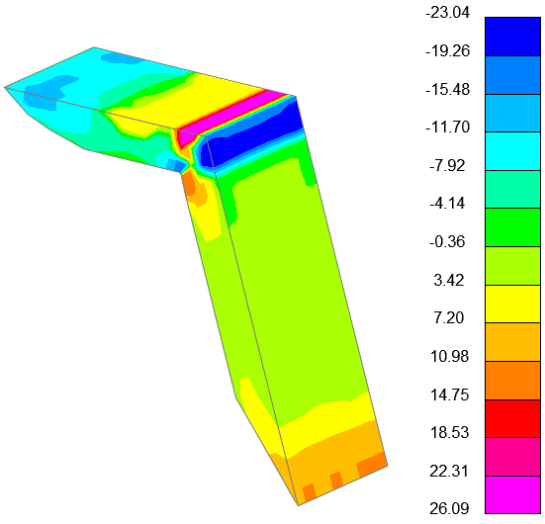

F = 104 kN

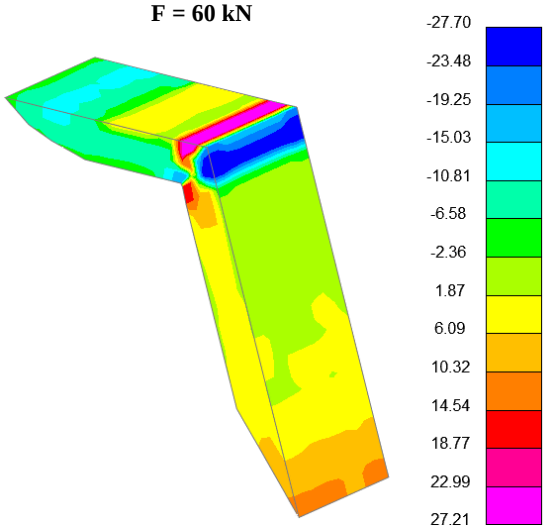

F = 119 kN

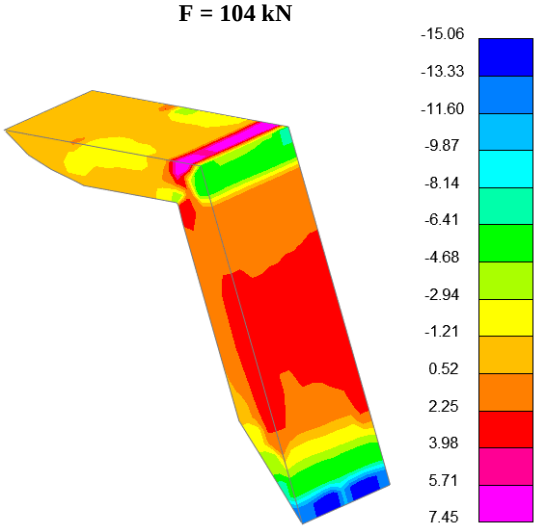

F = 134 kN

Shear stress in MPa in 0° - 90° out-of-plane direction

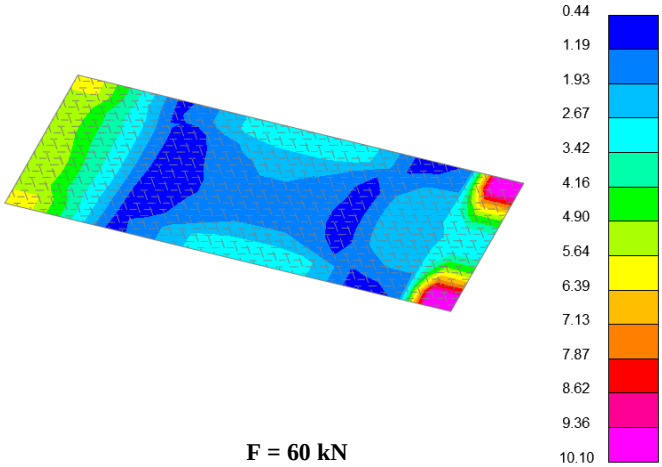

F = 60 kN

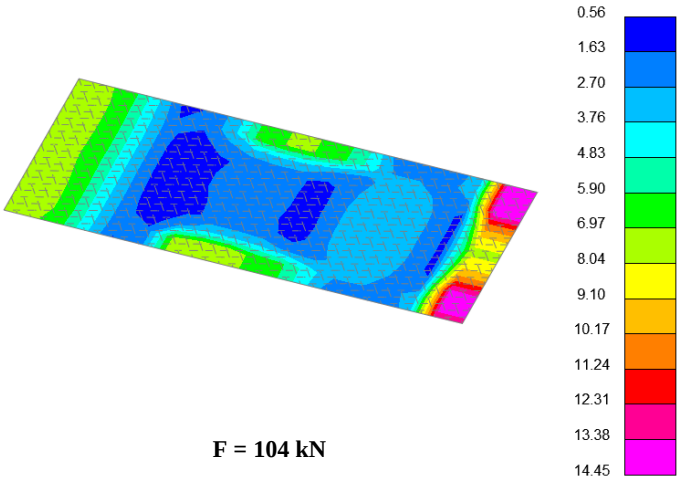

F = 104 kN

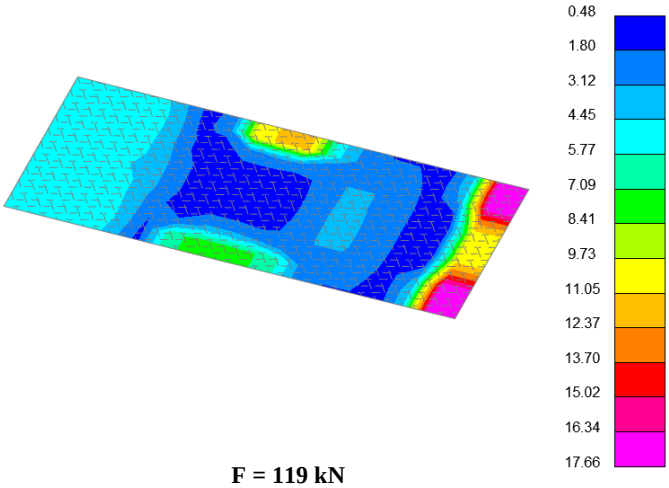

F = 119 kN

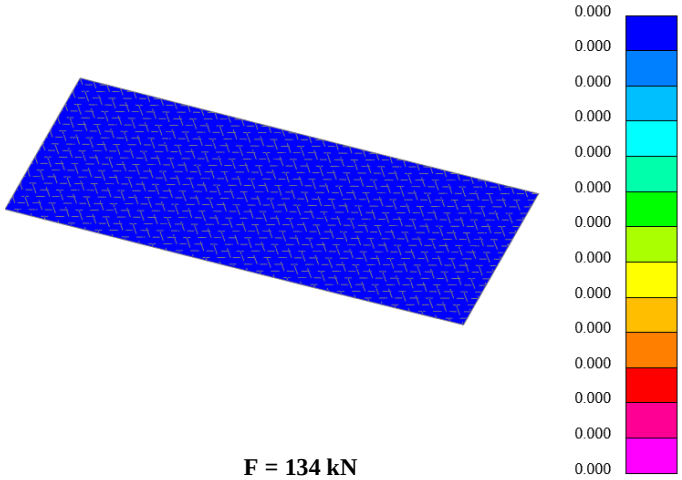

F = 134 kN

Peel bond stress in MPa of horizontal adhesive interface

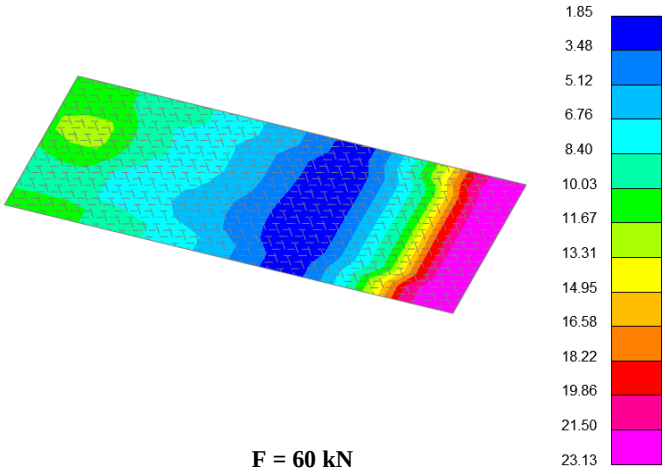

F = 60 kN

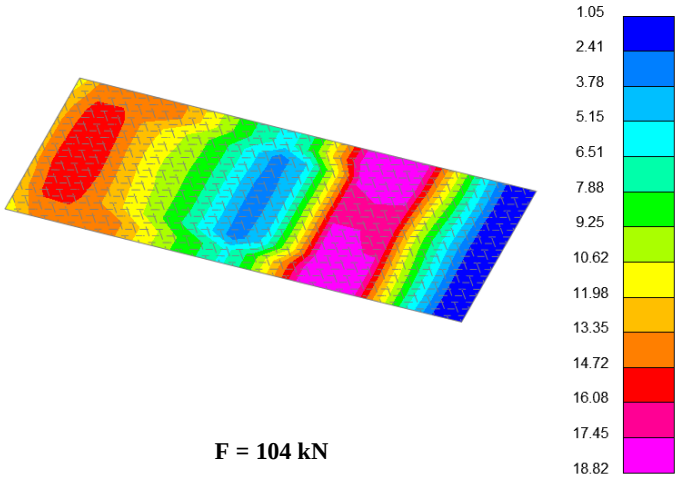

F = 104 kN

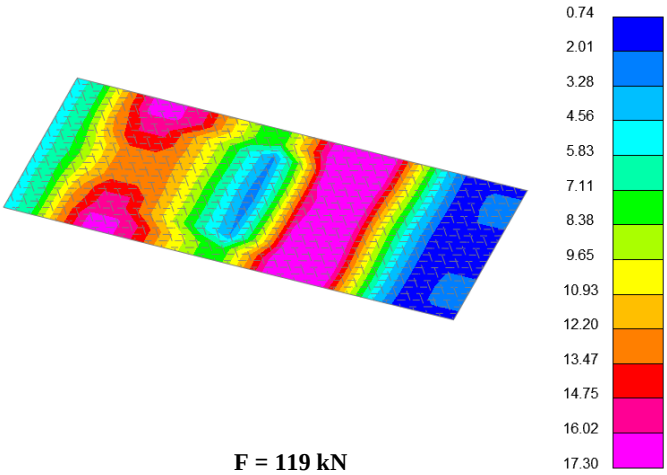

F = 119 kN

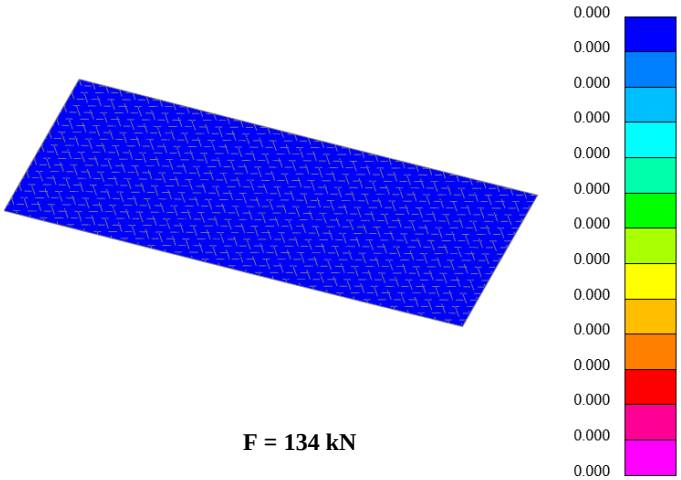

F = 134 kN

Shear bond stress in MPa of horizontal adhesive interface

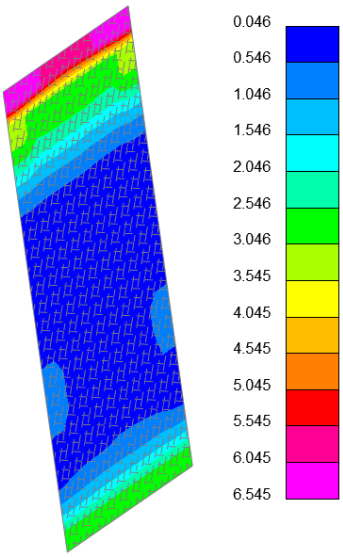

F = 60 kN

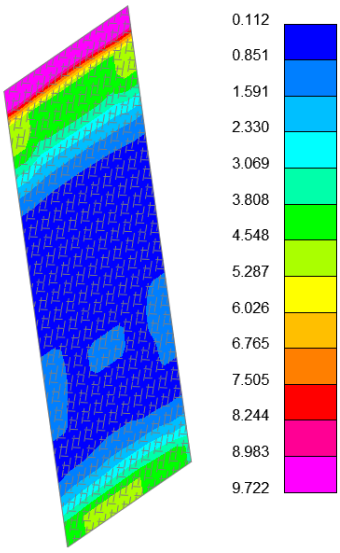

F = 104 kN

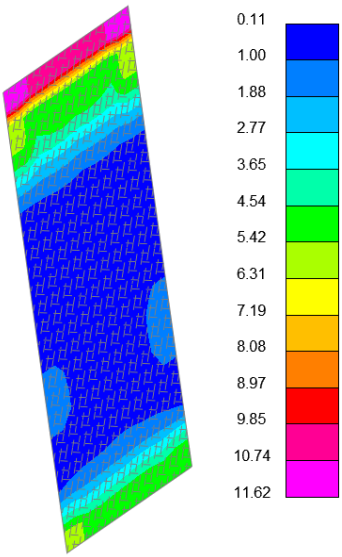

F = 119 kN

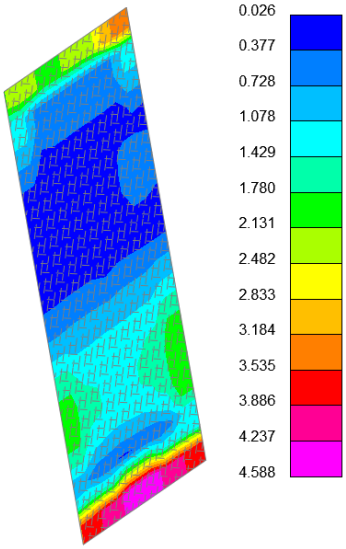

F = 134 kN

Peel bond stress in MPa of vertical adhesive interface

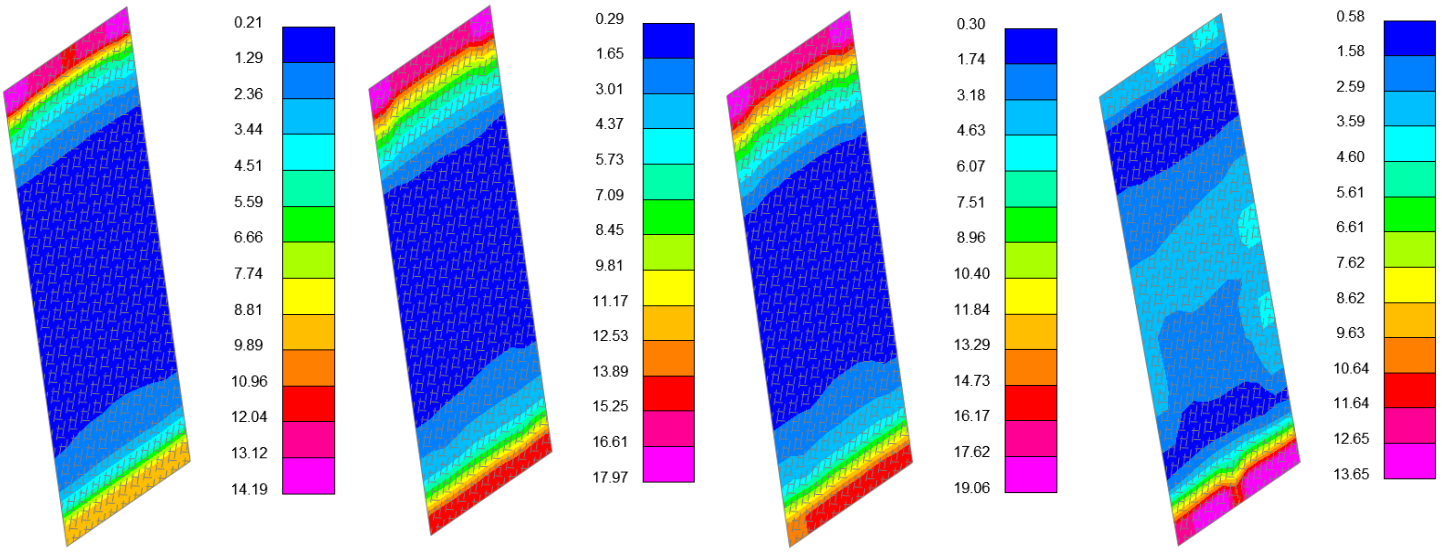

F = 60 kN **F = 104 kN** **F = 119 kN** **F = 134 kN**

Shear bond stress in MPa of vertical adhesive interface

F Determination of Design Values Bond Strength for Component-level Tests

As outlined in Annex C, Annex D of Eurocode 1990 defines two methods to derive properties from tests. Both methods will be used to assess characteristic and design values of lower-bound values of shear bond strength [54].

First, method A will be applied. With a log-normal distribution, the design value, X_d, should be determined by:

$$X_d = \frac{\eta_d}{\gamma_M} \exp\left[m_y - k_n s_y\right] \quad \text{(C.1)}$$

where

$$m_y = \frac{1}{n} \Sigma \ln\left(x_i\right) \quad \text{(C.2)}$$

$$s_y = \sqrt{\frac{1}{n-1} \Sigma (\ln(x_i) - m_y)^2} \quad \text{if Vx is unknown} \quad \text{(C.3)}$$

η_d is the design value of the conversion factor. This conversion factor is strongly dependent on the type of test and type of material [54]. As sufficient knowledge of the correct value is missing, a value of 1.0 was assumed in the calculation.

γ_M is the partial factor. This partial factor should be selected according to the field of application of the test results. A value of 1.0 was assumed in the calculation.

$m_y = 2.81$ for shear stress and $m_y = 1.92$ for peel stress, based on experimental results.

n is the number of tested samples. In this case, n = 6.

k_n is based on Table D.1 of Annex D in Eurocode 1990. As insufficient prior knowledge of the coefficient of variation, V_x, is available, V_x is unknown was applied. As n = 6, $k_n = 2.18$.

$s_y = 0.02$ for shear stress and $s_y = 0.08$ for peel stress, based on experimental results.

This calculation leads to: $X_d = 15.8\ MPa$ where X_d is the characteristic value of the peak shear bond strength with a ratio peel / shear strength of 1 / 2.4 and a mesh size of 6 mm. Additionally, $X_d = 5.77\ MPa$ for the peak peel bond strength.

For method B, the following formula is provided to determine basic variable X based on a log-normal distribution:

$$X_d = \eta_d \exp\left[m_y - k_{d,n} s_y\right] \quad \text{(C.4)}$$

where all variables are consistent with method A. However:

$k_{d,n}$ is based on Table D.2 of Annex D in Eurocode 1990. As n = 12, $k_{d,n} = 4.34$

This calculation leads to: $X_d = 14.28\ MPa$ where X_d is the design value of the average shear bond strength for ULS verifications. Additionally, $X_d = 4.16\ MPa$ for the peak peel bond strength.